Biophysical characterization of the interaction between amyloid-β (1-42) protein and ligands

Inaugural dissertation

for the attainment of the title of doctor
in the Faculty of Mathematics and Natural Sciences

at the Heinrich-Heine-Universität Düsseldorf

presented by

Tao Zhang

from Ganzhou, China

Düsseldorf, May 2019

from the Institut für Physikalische Biologie
at the Heinrich-Heine-Universität Düsseldorf

Published by permission of the
Faculty of Mathematics and Natural Sciences at
Heinrich-Heine-Universität Düsseldorf

Supervisor: Prof. Dr. Dieter Willbold
Co-supervisor: Prof. Dr. Gerhard Steger

Date of the oral examination: 9th July 2019

Declaration

I declare under oath that I have compiled this dissertation independently and without any undue assistance by third parties under consideration of the "Fundamental principles for safeguarding good scientific practice at Heinrich-Heine-Universität Düsseldorf". Furthermore, neither this dissertation, nor a similar work, has been submitted to another faculty. I have not made any unsuccessful attempt to obtain a doctorate.

Düsseldorf, May, 2019 Tao Zhang

This dissertation is dedicated to my family.
献给我的家人。

Learning without thought is labor lost, thought without learning is perilous.

"***Analects***", by Confucius

学而不思则罔，思而不学则殆。–《论语》，孔子

Contents

Acknowledgements

The work presented in the thesis was performed at the Institut für Physikalische Biologie (IPB), Heinrich-Heine-Universität Düsseldorf and the Institute of Complex Systems, Structural Biochemistry (ICS-6) at Forschungszentrum Jülich under the supervision of Prof. Dr. Dieter Willbold and Dr. Luitgard Nagel-Steger. The work received financial support from the Helmholtz Association through the Helmholtz-Portfolio Topics "Technology and Medicine" (D.W. and L.N.-S.) and "Drug Research" (D.W.). In addition, I was supported by a 3-year scholarship from the China Scholarship Council (CSC) and a stipendium from the iGRASP$_{seed}$ program at Heinrich-Heine-Universität Düsseldorf.

First and foremost, I would like to express my deep gratitude to Prof. Dr. Dieter Willbold, for offering me this awesome opportunity to carry out my doctoral study at IPB and ICS-6. I feel very lucky to do research in such a nice, creative and productive team. Thanks to Dieter for being so patient with me on my project, for the insightful discussions and numerous suggestions during my doctoral research. I am also grateful for your considerable effort and input into the manuscripts and my thesis, as well as for supporting me to attend lots of workshops and conferences to expand my horizon and knowledge in science. In particular, I want to thank Dieter for offering me the iGRASP$_{seed}$ stipendium so that I can continue my PhD work.

It has been a great pleasure to be a member of Dr. Luitgard Nagel-Steger's research group and to work with all the group members. I can still remember the moments when we had the interview and met for the first time. Thank you, Luitgard, for guiding me into the field of analytical ultracentrifugation. I appreciate the freedom, patience and continuous support from you very much, which allows me to do research on protein aggregation and protein-ligand interactions. You are always available for discussions and troubleshooting. Thanks for all the things you have done to help me with the experiments, resources, ideas and your trust, without which I could not have gotten here. Besides, you always inspire me to learn new things, not only for the PhD project, but also for my career.

I wish to acknowledge the support and advice from my second supervisor Prof. Dr. Gerhard Steger during my PhD research.

I would like to say thank you to Dr. Christina Decker and Thomas Pauly in our group. Christina instructed me in analytical ultracentrifugation and circular dichroism spectroscopy. Thomas helped me a lot in experiments as well as in my daily life. We worked together to publish our manuscripts and to figure out strange ThT kinetics or AUC profiles. We recommended restaurants and food to each other. We exchanged lots of interesting ideas about our own cultures and experience. Thanks to Dr. Anne K. Braczynski and Rebecca Sternke-Hoffmann, for all the wonderful moments in the office.

It is really enjoyable to work in such a warm-hearted institute. I am very grateful to Dr. Lothar Gremer and Dr. Manuel Etzkorn for teaching me fluorescent labeling and fluorescence polarization, respectively. Dr. Gremer is very kind to provide me with dye labeled materials and gives me valuable suggestions on my experiments. The collaboration with Prof. Dr. Birgit Strodel and her group on MD simulations was very helpful for our project. Thanks to Prof. Dr. Strodel and Jennifer Loschwitz for devoting the computing time to our experiments, and for discussions and corrections. I thank Prof.

Dr. Wolfgang Hoyer, Prof. Dr. Alexander Buell and Prof. Dr. Ingrid Span for the discussions in progress reports and other occasions. My grateful thanks are also extended to Dr. Nan Jiang, Dr. Stefan Klinker, Dr. Thibault Viennet, Dr. Oleksandr Brener, Dr. Mario Schneider, Shanta Elter, Dr. Nadine Rösener, Dr. Michael Wördehoff, Dr. Tamar Ziehm, Dr. Julian Victor, Emil Dandanell Agerschou, Nicola Vettore, Alessia Peduzzo, Marcel Falke, Ci Chu and Filip Hasecke for offering me a number of instructions, discussing the data and helping me with my experiments. Special thanks to Elke, Barbara and Bernd for what they have done to keep the lab running safe and clean. Thank you, Elke, for teaching me the AFM! In addition, I also want to acknowledge the secretaries: Astrid in IPB, Christina, Tugba and Dorothea in ICS-6 for assisting me with all the administration work. I am also thankful to Dr. Sigrun Wegener-Feldbrügge and her colleagues at HeRA for helping me with the visa and related issues.

Many thanks to Dr. Mareike Berleth and Dr. Alexander Hofmann from the Institute for Biochemical Plant Physiology for offering me sufficient measurement time for MST and ITC experiments.

There might be some hard time during the PhD, but I am lucky to have lots of friends, from whom I gain my courage and patience to carry on. Thanks to Haohong for being a close friend of mine. I will remember the talks we had in the evening, the roads we traveled together and all those beautiful photos you shared with me. Chuan, thank you so much for sharing your insightful ideas and thoughts with me, and for being so considerate towards me. Thanks to my dear friends and schoolmates Xin, Jian, Xianlei and Shoupeng. We applied for the CSC scholarship together and started our PhD at the same time, and now it is time to harvest. Thank you, Grace, for those supportive talks. Here in Düsseldorf, I have also made lots of new friends. Thanks to Zeli, Wenxian, Jun and Yuan for the funny basketball time and nice dinners. Dr. Shuai Liu, Dr. Hao Wang, Dr. Zhen Liu, Feng, Chenyin, Haiqian, Xiaopan, Zonghui and Yihan, thank you for involving me in all those gatherings, football games and travels. Dear Wei, I could not imagine where I would be today, had I not talked to you when we were still master students and thinking of our next destinations. Your intelligent words and optimistic attitude toward science and life always cheer me up when I am down. Furthermore, I appreciate some old friends of mine, whom I have known since we were in junior high school, for their encouragement. Thank you, Dr. Daoyuan Chen. To my college roommates Yi, Cong, Shangrong, Rong and Zhipeng, for motivating me to work hard. I would also like to say thanks to Qirong Ke, Changsheng Hua and all the members in the association for their work in making all the things happen. I am thankful to Mr. Dongsheng Han for his help during my stay in Düsseldorf.

I owe a special debt of gratitude to my parents, for their unconditional love and support, for encouraging me to pursue my dreams, and for enduring my ignorance, wilfulness and naiveté. I would not have had the chance to travel so far away from home without my parents' devotion and encouragement. My dear sister Fan, I am proud that you have become a mother and are getting more confident in yourself. A big thanks to Fan and Bin for taking care of the family for such a long time. I would like to say thank you to my grandparents, uncles, aunties and all the family members, for your continued support and love. 感谢爸爸妈妈一直以来的无条件的支持和付出，永远鼓励我去尝试自己的想法。父母独自承受了很多事情，让我能够安心地在外求学。很高兴妹妹组建了自己的家庭，祝愿帆，滨和小外甥喜乐平安。我也谢谢帆和滨在我在外求学时照顾父母和家人。特别感谢我的家人们，爷爷奶奶，外公外婆，叔伯姑舅和所有亲友，一直关心和支持我，无论是精神上还是物质上，你们的支持让我在求学之路上倍感温馨。

List of publications and manuscripts

Publications and manuscripts related to this dissertation

Zhang T, Pauly T, Nagel-Steger L. Stoichiometric Zn^{2+} interferes with the self-association of Aβ42: Insights from size distribution analysis. *Int J Biol Macromol*. 2018 Jul 1; 113:631-639. doi: 10.1016/j.ijbiomac.2018.02.123.
Contribution: experimental design, data collection and analysis, main part of manuscript writing.

Zhang T, Loschwitz J, Strodel B, Nagel-Steger L, Willbold D. Interference with amyloid β nucleation by transient ligand interaction. *Molecules.* 24(11), 2129; doi: 10.3390/molecules 24112129. (Cover story)
Contribution: experimental design, data collection and analysis, main part of manuscript writing.

Zhang T, Nagel-Steger L, Willbold D. Towards the mode of action of the clinical stage all-D-enantiomeric peptide RD2 on Aβ42 aggregation. *Manuscript to be submitted.*
Contribution: experimental design, data collection and analysis, main part of manuscript writing.

Zhang T, Nagel-Steger L, Willbold D. Solution based determination of dissociation constants for Aβ42 binding to antibodies. *Accepted for publication in ChemistryOpen.*
Contribution: experimental design, data collection and analysis, main part of manuscript writing.

Publications not included in the dissertation

Kroeger T, Frieg B, **Zhang T**, Hansen FK, Marmann A, Proksch P, Nagel-Steger L, Groth G, Smits SHJ, Gohlke H. EDTA aggregates induce SYPRO orange-based fluorescence in thermal shift assay. *PLoS One. 20*17 May 4; 12(5):e0177024. doi: 10.1371/journal.pone.0177024.

Bradshaw NJ, Yerabham ASK, Marreiros R, **Zhang T**, Nagel-Steger L, Korth C. An unpredicted aggregation-critical region of the actin-polymerizing protein TRIOBP-1/Tara, determined by elucidation of its domain structure. *J Biol Chem.* 2017 Jun 9; 292(23):9583-9598. doi: 10.1074/jbc.M116.767939.

Cavini IA, Munte CE, Erlach MB, van Groen T, Kadish I, **Zhang T**, Ziehm T, Nagel-Steger L, Kutzsche J, Kremer W, Willbold D, Kalbitzer HR. Inhibition of amyloid Aβ aggregation by high pressures or specific d-enantiomeric peptides. *Chem Commun (Camb).* 2018 Mar 27; 54(26):3294-32 97. doi: 10.1039/c8cc01458b.

Bhatia S, Diedrich D, Frieg B, Ahlert H, Stein S, Bopp B, Lang F, **Zhang T**, Kröger T, Ernst T, Kögler G, Krieg A, Lüdeke S, Kunkel H, Rodrigues Moita AJ, Kassack MU, Marquardt V, Opitz FV, Oldenburg M, Remke M, Babor F, Grez M, Hochhaus A, Borkhardt A, Groth G, Nagel-Steger L, Jose J, Kurz T, Gohlke H, Hansen FK, Hauer J. Targeting HSP90 dimerization via the C terminus is effective in imatinib-resistant CML and lacks the heat shock response. *Blood.* 2018 Jul 19; 132(3):307-320. doi: 10.1182/blood-2017-10-810986.

Falke M, Victor J, Wördehoff M, Peduzzo A, **Zhang T**, Schroeder G, Buell A, Hoyer W, Etzkorn M. α-Synuclein-derived lipoparticles in the study of α-Synuclein amyloid fibril formation. *Chem Phys Lipids*. 2019 Feb 28; 220:57-65. doi: 10.1016/j.chemphyslip.2019.02.009.

Alvarez CE, Bovdilova A, Höppner A, Wolff CC, Saigo A, Trajtenberg F, **Zhang T**, Buschiazzo A, Nagel-Steger L, Drincovich MF, Lercher MJ, Maurino VG. Molecular adaptations of NADP-malic enzyme for its function in C_4 photosynthesis in grasses. *Nat Plants.* 2019 Jul;5(7):755-765. doi: 10.1038/s41477-019-0451-7.

List of symbols, abbreviations and acronyms

Aβ	amyloid-β
AChE	acetylcholinesterase
AD	Alzheimer's disease
ADAM10	α-secretase disintegrin and metalloproteinase domain-containing protein 10
ADDLs	Aβ derived diffusible ligands
AFM	atomic force microscopy
AICD	APP intracellular domains
APOE4	ε4 allele of the apolipoprotein E gene
APP	amyloid precursor protein
AUC	analytical ultracentrifugation
BBB	blood brain barrier
BSA	bovine serum albumin
CAA	cerebral amyloid angiopathy
CD	circular dichroism
ChEI	cholinesterase inhibitor
CSF	cerebrospinal fluid
D	diffusion coefficient
DBS	deep brain stimulation
D_T	thermal diffusion coefficient
DGC	density gradient centrifugation
DLS	dynamic light scattering
DMS	deep magnetic stimulation
DMT	disease modifying treatment
EEG	electroencephalogram
EGCG	Epigallocatechin gallate
EM	electron microscopy
ESI-MS	electrospray ionization mass spectrometry
FAD	familial Alzheimer's disease
F_b	buoyant force
FCS	fluorescence correlation spectroscopy
FDS	fluorescence detection system
F_f	frictional force
f	frictional coefficient
F_g	gravitational force
f/f_0	frictional ratio
H-bond	hydrogen bond
HFIP	1,1,1,3,3,3-hexafluoro-2-propanol
IDP	intrinsically disordered protein
k_B	Boltzmann constant
K_D	dissociation constant
MAP	microtubule-associated protein
MCI	mild cognitive impairment
MD	molecular dynamics
MOPS	3-(N-morpholino)propanesulfonic acid
MRE	mean residue ellipticity
MRI	magnetic resonance imaging
MST	microscale thermophoresis
NFT	neurofibrillary tangle

NMDA	N-methyl-D-aspartate
NMR	nuclear magnetic resonance
NRG1	neuregulin 1
PCAD	preclinical Alzheimer's disease
PEI	polyethylenimine
PET	positron emission tomography
pI	isoelectric point
PICUP	photo-induced cross-linking of unmodified proteins
PSEN	presenilin
R	gas constant
R_g	radius of gyration
R_H	hydrodynamic radius
RMSD	root-mean-square deviation
RP-HPLC	reversed-phase high-performance liquid chromatography
s	sedimentation coefficient (*s*-value)
SAD	sporadic Alzheimer's disease
SANS	small angle neutron scattering
SE	sedimentation equilibrium
SEC	size exclusion chromatography
SPM	scanning probe microscopy
SPR	surface plasmon resonance
S_T	Soret coefficient
SV	sedimentation velocity
$s_{20,w}$	*s*-value in pure water at 20 °C
ThT	thioflavin T
t_{lag}	lag time
$t_{1/2}$	half completion time of the aggregation kinetics
Tw20	Tween 20
TREM2	triggering receptor on myeloid cells 2
Tris	Tris(hydroxymethyl)aminomethane
T-jump	temperature jump
Å	angstrom (10^{-10} m)
ρ	density
η	viscosity
$\bar{\nu}$	partial specific volume
ε	dielectric constant
σ_{eff}	effective charge of a molecule in solution
λ_{DH}	Debye-Hückel screening length
ω	angular velocity
λ_{ex}	excitation wavelength
λ_{em}	emission wavelength
v/v	volume/volume
w/v	weight/volume

List of figures

List of tables

Abstract

It has been a century since the first Alzheimer's disease (AD) patient was described and reported by the German psychiatrist Alois Alzheimer. The disease is receiving increasing attention both due to its complex pathophysiology and the great socioeconomic burden following the global ageing trend. Currently there are around 50 million people suffering from dementia worldwide. AD is the most common cause of dementia, contributing to over 60% of all cases. The aggregation of amyloid-β (Aβ) into toxic oligomers and fibrillar structures in the brain has been recognized as one of the hallmarks of the disease. The accumulation of various Aβ aggregates in the central nervous system occurs early in the progression of AD and induces functional and structural damages to the brain at multiple levels. The central role of Aβ aggregation in the etiology of AD has made it a pivotal target for disease intervention.

A lot of physiological or non-physiological factors have been documented to be able to affect the aggregation pathway of Aβ. For example, zinc ions (Zn^{2+}), the second most abundant trace element in human body, was found to enrich around the amyloid plaque in Alzheimer's brains. However, the detailed influence of Zn^{2+} on the fibril formation of Aβ remains controversial. In chapter I, we investigated the influence of Zn^{2+} on the aggregation of Aβ42, the major toxic isoform of Aβ products in the brain, by applying analytical ultracentrifugation (AUC) and other biophysical techniques. We found that stoichiometric Zn^{2+} shifts the aggregation of Aβ42 toward non-fibrillary aggregates with reduced β-sheet structures and amyloidogenic activity. The interaction between Zn^{2+} and Aβ42 is rapid and can be reversed by adding metal ion chelators such as EDTA. AUC was combined with atomic force microscopy (AFM) to elucidate size distributions and morphologies of Aβ42 aggregates formed with or without Zn^{2+}.

Several non-physiological factors, including two D-enantiomeric peptides (D-peptides) and three commercially available monoclonal antibodies (mAbs) against Aβ were also studied to characterize how they interact with Aβ42 and impact the aggregation process (chapters II-IV). Based on the strategy that stabilizing monomeric Aβ in unstructured conformations could prevent them from the oligomerization and even eliminate existing cytotoxic Aβ species, a series of all-D-enantiomeric peptides were developed and characterized regarding their effects on AD pathology. D3 and RD2 are two of the D-peptides investigated in the present study (Chapters II and III). We first demonstrated that D3 and RD2 bind to Aβ42 monomers with nanomolar affinities via microscale thermophoresis (MST). The high affinity binding leads to the formation of Aβ42 and D-peptides complexes at 1:1 and other stoichiometries, as revealed by fluorescence based analytical ultracentrifugation and molecular dynamics simulations. MST measurements revealed an enhancement in the interaction between D-peptides and Aβ42 when reducing the ionic strength of the buffer, indicating the involvement of electrostatic interaction between these two molecules. By employing thioflavin T (ThT) assay, circular dichroism (CD) spectroscopy and AFM, we demonstrated that D3 and RD2 significantly retard the secondary structure transition and the fibrillation of Aβ42 by interfering with the nucleation process and retaining Aβ monomers in unstructured conformations. Our research showed for the first time that D3 and RD2 are able to interact with monomeric Aβ42, which leads to the formation of highly flexible complexes at various stoichiometries. Our study substantiates the

versatile effects of D-peptides on regulating Aβ aggregation and envisions the promising application of D-peptides in Aβ aggregation related pathologies.

In chapter IV, the interaction between three commercially available anti-Aβ antibodies and Aβ42 was characterized using fluorescence based AUC and MST measurements. All three antibodies, 6E10, 4G8 and 12F4, are able to interact with Aβ42 monomers with low nanomolar affinities, irrespective of the difference in epitopes. The K_D values are consistent with reported values from surface plasmon resonance (SPR) studies on antibodies and Aβ monomers. Besides, the affinity for 12F4 and Aβ42 monomer was quantified for the first time. The results on Aβ42 monomers and antibodies also validate that fluorescence based AUC and MST are useful and rigorous methods for the study of the interaction between aggregation-prone proteins and their binding partners.

To summarize, this work characterized how several binding partners interact with Aβ42 and further affect its fibrillation process. In particular, our study figures out that the interaction and complex formation between D-peptides and Aβ monomers could be an important and early event of the whole interaction process, and that D-peptides play a diverse role in modulating the aggregation of Aβ through interfering with Aβ nucleation and eliminating toxic Aβ assemblies. These findings demonstrate that both Aβ monomers and oligomers can be involved in the interaction with D-peptides and highlight the potential of D-peptides as drug candidates for the intervention of AD. Our study may also aid to understand the interaction between small ligands and intrinsically disorder proteins.

Introduction

Alzheimer's disease, a general introduction

Epidemiology and risk factors

The continuous increase in the quality of life owing to dramatic improvements in modern science and technologies helps us live longer and healthier than before. The increase in the average life expectancy comes with the growth of the global geriatric population. A report from the National Institute of Ageing showed that currently there are about 8.5% of people worldwide (~620 million) aged 65 and above [1]. As shown in Fig. 1, the percentage is estimated to double by 2050, leading to approximately 1.6 billion people over the age of 65 [1]. The gradually ageing world is followed by an increasing prevalence of dementia. The population of people affected by dementia is over 50 million and the total number keeps rising [2, 3]. Alzheimer's disease (AD) accounts for the majority of dementia cases in the world. It is believed that 50% - 75% of the dementia cases are caused by AD [4]. The prevalence of AD increases along with the global ageing trend and has caused great socioeconomic impacts.

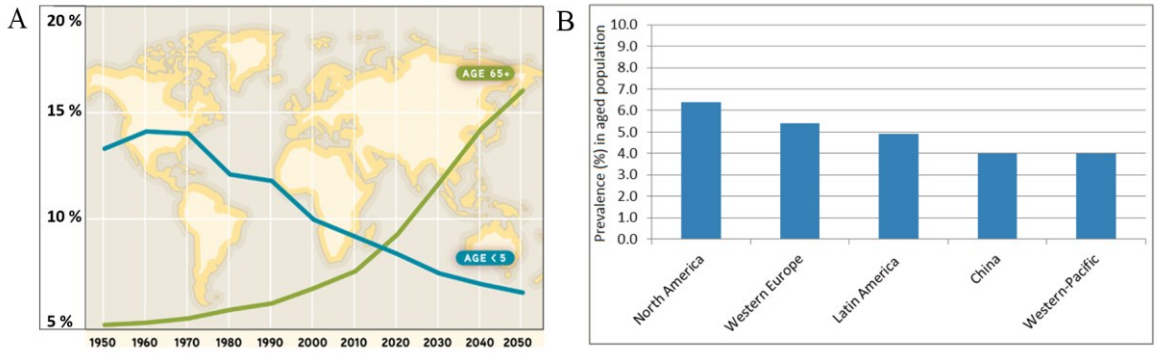

Figure 1. Global ageing and the prevalence of dementia worldwide. Percentage of population aged 65 and over and children under 5 (A), modified from He et al., 2015 [1]. These two age groups will continue to change in opposite directions. The global ageing trend is featured by an increasing prevalence (%) of dementia among aged population worldwide (B), modified from Reitz et al., 2014 [5].

Alzheimer's disease was first described by the German psychiatrist Alois Alzheimer. He observed brain atrophy, neuronal loss, the formation of amyloid deposits and neuronal argyrophilic fibrillary tangles in the brain autopsy following the death of his patient Auguste Deter, who had paranoia and memory loss [6, 7]. The pathological signs, together with the clinical symptoms, were soon termed as "Alzheimer's disease" [8]. Numerous research studies have been accumulated in the past century to deepen our understandings on this disease. AD is a chronic neurodegenerative disease characterized by progressive decline in memory and cognitive abilities associated with behavioral functions [9, 10]. In addition to these clinical symptoms, there are two typical histopathological changes in AD (Fig. 2), namely amyloid plaques formed by amyloid-β (Aβ) proteins and neurofibrillary tangles (NFT) composed of hyperphosphorylated microtubule-associated protein (MAP) tau [11]. A variety of other pathologies, such as synaptic dysfunction, the depletion of

cholinergic neurons in basal forebrain, cerebrovascular impairments, oxidative stress and neuroinflammatory response, and calcium dysregulation are also present in the central nervous system of AD patients [11, 12]. AD can be divided into two categories according to the age of onset. A small fraction of the AD cases (~10%) shows clinical phenotypes such as memory impairments and neurological symptoms under 65-year old. This type of AD is called early-onset Alzheimer's disease (EOAD) [13]. While most of AD cases display memory dysfunction after the age of 65, and have complex etiologies. This is termed as late-onset Alzheimer's disease (LOAD). AD could also be categorized into familial Alzheimer's disease (FAD) and sporadic Alzheimer's disease (SAD). FAD is most likely caused by gene mutations closely related to AD [13]. It is usually early-onset and highly heritable among the family, but affects only a small group of population. The sporadic form accounts for more than 90% of all AD cases and is thought to be induced both by genetic and environmental factors [14].

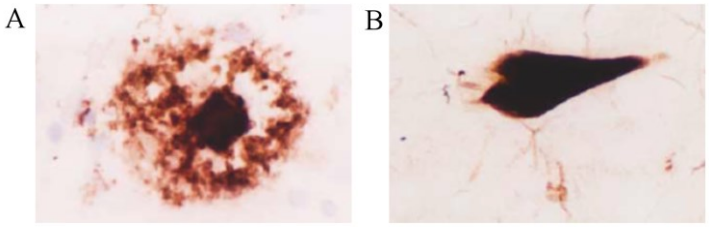

Figure 2. Typical pathological changes in brains of Alzheimer's patients. AD is histologically featured by the deposition of neuritic plaques (A) which consist of amyloid-β proteins, and the formation of neurofibrillary tangles (B) containing paired helical filaments of hyperphosphorylated tau proteins in the central nervous system. Neuritic plaques were stained by an anti-human Aβ protein monoclonal antibody using diaminobenzidine and hematoxylin counterstain. Neurofibrillary tangles were visualized by Gallyas silver stain. 2500-fold magnification, taken from Cummings et al., 2002 [15].

There is increasing evidence that AD is a complex and multifaceted syndrome. The complexity of the disease makes it difficult for researchers to identify exact etiologies, however, multiple risk factors have been found to participate in the pathogenesis of AD. Ageing is the most significant risk factor as the incidence rate of AD is positively correlated with the advance of age in the elderly population [16, 17]. Other non-modifiable risk factors include the presence of ε4 allele of the apolipoprotein E gene (*APOE4*) [5, 18], mutations in amyloid precursor protein (*APP*) and presenilin (*PSEN*) genes [5, 19]. ApoE protein transports cholesterol to neurons via interacting with apoE receptors in the brain [20]. The *APOE* gene has three alleles and is able to produce ε2, ε3, and ε4 isoforms, respectively [21]. Epidemiological studies demonstrated that more than 40% of the AD patients are *APOE4* allele carriers [22-24]. The risk for individuals with one and two *APOE4* alleles will increase by three-fold and eight- to twelve-fold, respectively [5, 25]. APP and presenilins are closely involved in the production of Aβ proteins and are commonly found to have mutations in FAD patients [5]. Other genes have also been revealed to participate in the pathogenesis of AD (Fig. 3). Triggering receptor on myeloid cells 2 (TREM2) is a transmembrane protein responsible for microglial phagocytosis in the central nervous system [26, 27]. The function of TREM2 highlights its role in regulating CNS immune response and the clearance of Aβ species [28, 29]. The mutation

of TREM2 is rare, nevertheless the common mutation (R47H) increases the risk of SAD by two-fold [30]. Other genetic risk factors identified by genome wide association studies include CR1 and CD33 which are related to immune response; PICALM and BIN1 that play roles in the endocytosis; CLU and ABCA7 which encode lipoproteins and deliver lipids [19, 31].

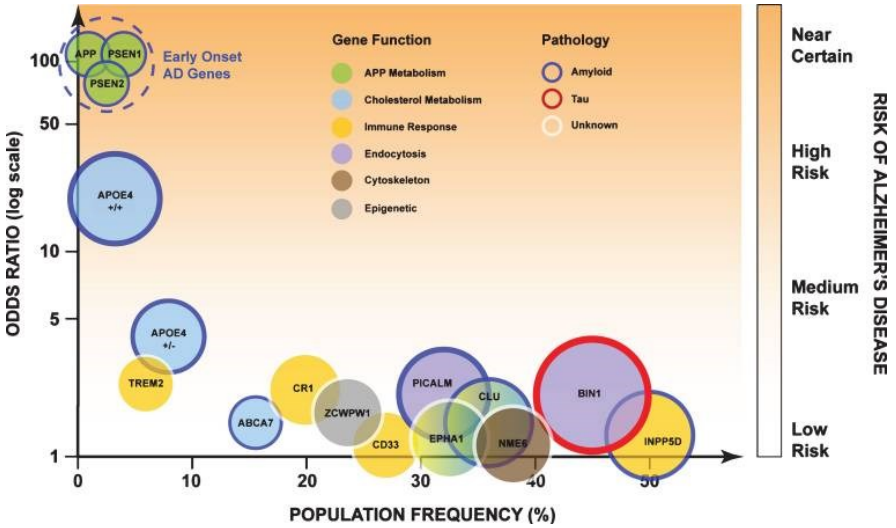

Figure 3. Genetic risk factors for AD and their population frequency. Many of the genes have physiological functions in human beings, while they may also increase the severity of the disease or advance the onset of AD, depending on their roles in AD related pathologies. The area of each circle is correlated with the gene's population attributable fraction. The larger the area, the stronger the gene will influence the population. Taken from Robinson et al., 2017 and Guerreiro et al., 2013[19, 31].

Non-genetic risk factors are mostly linked with the lifestyle or the physical health of individuals. Elderly people with cerebrovascular disease, traumatic brain injuries, high blood pressure or with obesity are more likely to develop AD than those without such conditions [5, 32]. Individuals suffering from type II diabetes, hyperlipidemia, hyperhomocysteinemia or other metabolic syndromes confer a higher risk of dementia [33, 34]. Lifestyle factors like physical exercise, smoking, intellectual activities and social engagement might also influence the risk of developing Alzheimer's disease [35, 36].

Pathological changes of Alzheimer's disease

Owing to advances in clinical imaging techniques and novel tracers, scientists have been able to determine how diverse pathological events of AD develop temporally and spatially during the progression of the disease. As depicted in Fig. 4, the abnormal accumulation of Aβ starts at early ages and might be the first detectable AD-related pathology [37, 38]. Tau pathology occurs almost at the same time as Aβ pathology and could be accelerated by elevated Aβ levels and the existence of misfolded Aβ species [39-41]. The development of Aβ pathology and tauopathy will further induce oxidative damages and inflammation in the central nervous system, leading to cholinergic dysfunction and synaptic toxicities [42]. Aβ aggregates and hyperphosphorylated tau proteins might also directly impair neuronal functions via multiple pathways [42]. At this stage the brain might show significant Aβ deposits and (or) neurofibrillary tangles, while individuals could still maintain their

cognitive functions [43, 44]. This stage is generally recognized as preclinical Alzheimer's disease (PCAD) [43]. The gradual loss of neurons in brain regions like hippocampi and prefrontal lobes is irreversible and will finally reduce the gray matter density [45]. The cortical atrophy, which can be accurately assessed by magnetic resonance imaging (MRI), can be detected in patients with mild cognitive impairment (MCI) [46, 47]. Individuals at this stage start experiencing memory problems. Recent research proposed that MCI patients with positive AD-related biomarker profile (Aβ and tau pathologies) can be diagnosed as prodromal AD [48]. It is an intermediate stage between the PACD and AD type dementias and has been regarded as a vital time window for the diagnosis and intervention of AD [49]. Without effective interventions, most of the prodromal AD patients will proceed to AD type dementia [49]. The disease will not only continue exacerbating cognitive functions, but also induce psychiatric disorders at late stages [50, 51]. The rates of progression of AD vary among individuals and show high heterogeneities depending on the genetic backgrounds of the patients and the involvement of interventions [52, 53].

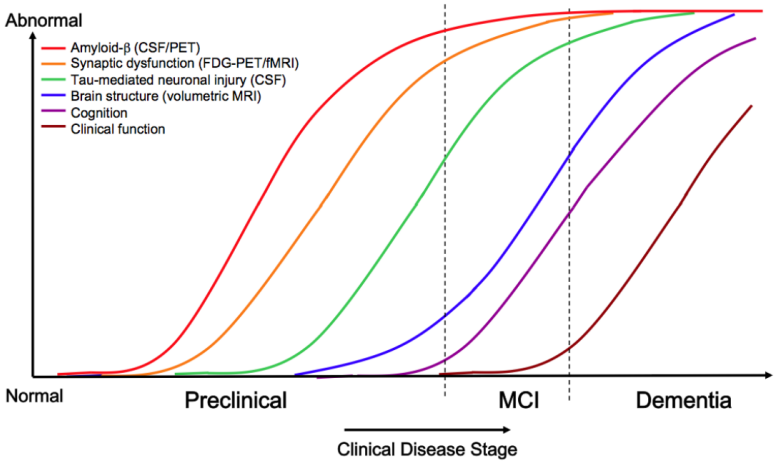

Figure 4. A model showing dynamic biomarkers of AD pathological cascade and clinical disease stages. Aβ is detected by measuring cerebrospinal fluid (CSF) content or positron emission tomography (PET) imaging. Abnormal Aβ accumulation is followed by synaptic dysfunction and tau induced neuronal damages. All pathologies contribute to subsequent changes in brain structures and morphologies which can be measured by magnetic resonance imaging (MRI). Finally, clinical symptoms such as cognitive impairments and behavioral alterations manifest in patients. Taken from Sperling et al., 2011[43].

The prevalence of AD worldwide and its massive socioeconomic influence have made it a global priority to develop both diagnostic and interventional strategies to slow down the progression of AD, or even to cure the disease [54]. The cognition and behavioral abilities can be evaluated by neurological examinations and mental status tests [55]. Various genetic tests can be performed to evaluate the susceptibility of an individual to develop AD, as well as to complement the clinical diagnosis [56, 57]. Aβ pathologies and tauopathies can be measured by analyzing the CSF, or by applying non-invasive imaging techniques like PET [57]. The morphological and functional changes in the brain can be determined via MRI and electroencephalograms (EEG) [58, 59]. Nevertheless, the confirmatory diagnosis of Alzheimer's disease can only be made based on the post-mortem autopsy of patients' brains [60].

Interventions for Alzheimer's disease

Nowadays there are only five agents that have been approved by the Food and Drug Administration to treat AD induced memory and cognitive problems [61]. Three of the five agents, namely donepezil, galantamine and rivastigmine, are cholinesterase inhibitors (ChEIs) [62]. These drugs were developed on the basis of a loss of cholinergic neurons and a deficiency in acetylcholine activity in AD patients [63]. By inhibiting the activity of acetylcholinesterases (AChEs) in synaptic clefts the concentration of acetylcholine will be preserved, thus leading to an improvement in cognitive functions in AD patients [62]. Memantine is an N-methyl-D-aspartate (NMDA) receptor antagonist. It has been found that several Aβ species and abnormal tau proteins are able to modulate NMDA receptors and produce the widely known neuronal excitotoxicity [64]. Memantine interacts with NMDA receptors and blocks the neuronal calcium overload triggered by excess glutamate in synaptic clefts, thus protecting neurons from Ca^{2+} induced cellular damages [65, 66]. The fifth agent is a combination of donepezil and memantine and has been approved for mild to moderate AD [67]. It has to be mentioned that all the approved agents can only temporarily rescue the cognitive and behavioral symptoms and have modest clinical effects [68].

The ongoing clinical trials can be grouped into symptomatic treatments and disease modifying treatments (DMTs) according to their mechanisms of actions (Fig. 5) [69]. A lot of symptomatic treatments are developed based on the dysregulation of neurotransmitters in Alzheimer patients' brains and target primarily the cognitive and behavioral symptoms [70]. The disease modifying treatments cover a wide range of mechanisms and aim directly on key events in the pathogenesis of AD [71]. Agents that can modulate the metabolism or the aggregation of Aβ proteins have been widely investigated [72]. Therapies aiming on hyperphosphorylated tau proteins also attract lots of research interests [72]. Other ongoing DMTs include neuroprotective agents which could promote the neuronal regeneration, or chemicals that can suppress neuroinflammation and oxidative stress [73]. Aβ and tau immunotherapies are particularly attractive because of their promising outcomes in animal studies and some clinical trials [74, 75]. However, the clinical efficacy of these immunotherapies is still debatable since up to now there is no successful phase III clinical trial. Additionally, the safety and tolerability of antibodies and vaccines are also of high importance [74]. Scientists and pharmaceutical companies are now putting more emphasis on the preclinical and prodromal stages of AD, hoping that immunotherapies could slow down the progression of the disease [72]. Several physically based interventions are also proposed and evaluated in animals or in AD patients. High frequency deep brain stimulation (DBS) was originally introduced to treat movement disorders [76]. This treatment requires the patients to be implanted with a neurostimulator at specific brain regions. The electrical impulses generated by the neurostimulator will be transferred to the targeted brain regions and modulate local neuronal activities [77]. Now it is also applied to AD subjects to investigate its efficacy on memory and cognition. Nir et al. developed a non-invasive DBS method in 2017 to regulate neurons at depth by using temporally interfering electric fields [78]. Recently a novel non-invasive deep magnetic stimulation (DMS) approach designed by a Chinese research group showed positive effects on AD mouse models. Their animal studies demonstrated that low field magnetic stimulation was capable of improving overall AD pathologies in AD mice

[79]. Regardless of the exciting benefits, these physical approaches still require in-depth research to elucidate their effects on AD.

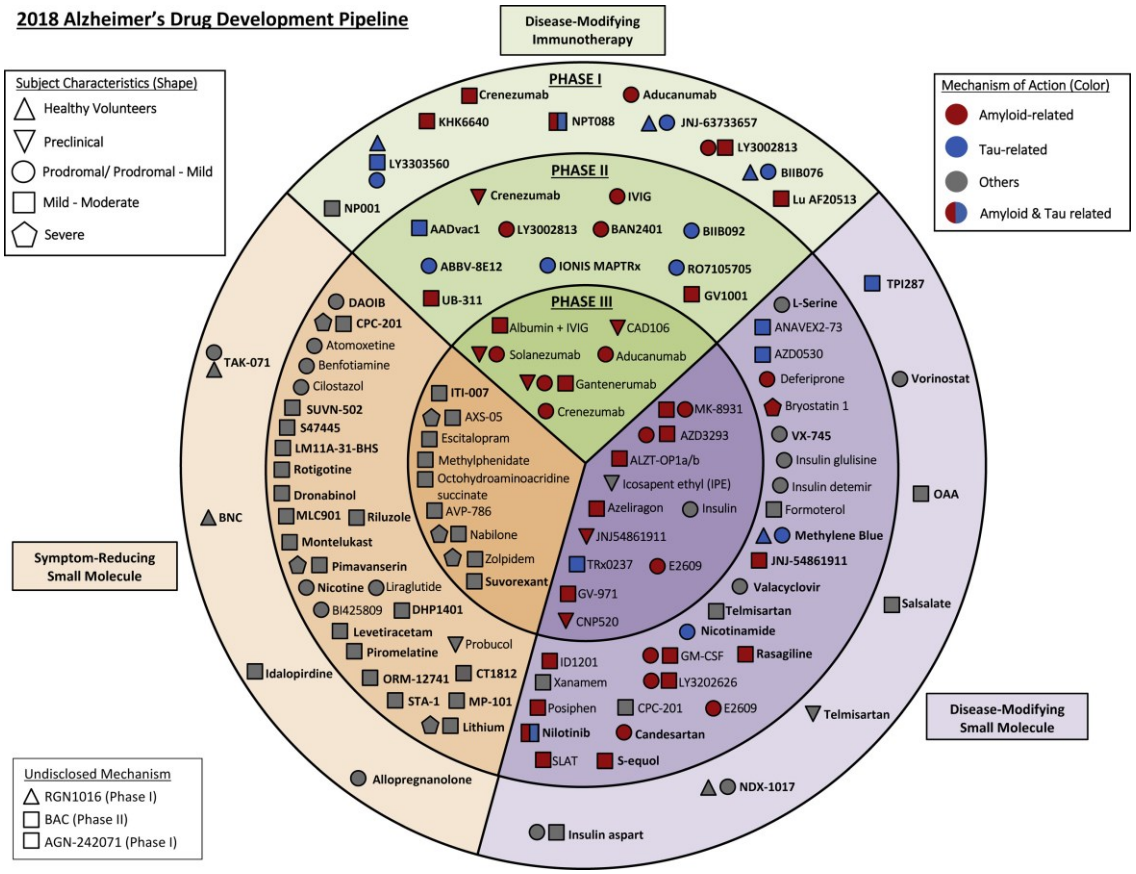

Figure 5. A summary of agents under clinical trials for the intervention in AD. The agents are classified according to mechanisms of action and clinical phases. Taken from Cummings et al., 2018 [73].

In all, the high prevalence of AD and its growing healthcare burden call for the development of preventative therapeutics or disease modifying treatments which can help us control the progression of the disease.

Amyloid-β protein

Biogenesis of amyloid-β protein and the amyloid cascade hypothesis

Amyloid-β proteins are a series of proteolytic products with 37-43 amino acid residues derived from the amyloid precursor protein [80]. APP is a widely expressed type I transmembrane protein with a long extracellular glycosylated N-terminus, a membrane-crossing domain and a short cytoplasmic C-terminus [81]. The APP protein has several isoforms with different length ranging from 695 to 770 amino acids [82]. APP695 is the most abundant isoform in the central nervous system and is mainly expressed by neurons [82]. It has been reported that APP and some of its proteolytic products play important roles in regulating synaptic functions and neural plasticity [83, 84]. They might also take part in modulating neurogenesis and cellular stress responses [85, 86]. The function of APP proteolytic products depends largely on how APP is processed in neurons. In the non-amyloidogenic

pathway (Fig. 6A), APP proteins that are anchored on the cell surface will be cleaved by the α-secretase disintegrin and metalloproteinase domain-containing protein 10 (ADAM10), which is also mainly located at the cell surface [87, 88]. The cleavage releases soluble APPα (sAPPα) fragments to the extracellular space. While the remaining C-terminal fragments (CTF-α, also known as C83) will be processed by γ-secretase complex with successive ε- and γ- cleavages to generate APP intracellular domains (AICD) and p3 fragments [87]. The non-amyloidogenic processing does not produce Aβ proteins because the first cleavage by ADAM10 occurs within the Aβ region. The activation of the non-amyloidogenic pathway via enhancing α-secretase activities is thought to be neuroprotective not only because of the reduced formation of Aβ species, but also due to the generation of sAPPα, which is beneficial to synaptic functions and can promote the neurite growth [89]. The amyloidogenic pathway (Fig. 6B) starts with the internalization of APP to endosomes, wherein APP proteins will be cleaved by β-secretases 1 or 2 (BACE1 or BACE2, respectively) [82]. The first cleavage results in the formation of soluble APPβ (sAPPβ) and a short C-terminal fragment (CTF-β, or C99) [90]. CTF-β fragments are further processed by γ-secretase complexes with successive proteolytic cleavages at multiple sites to generate AICD and various Aβ isoforms (Fig. 7) [90]. The major products of the amyloidogenic pathway are Aβ40 and Aβ42, which also comprise the main components of amyloid plaques in vivo [91, 92]. In vivo, Aβ may also undergo several posttranslational modifications or truncations and generate a plethora of proteins with different properties. Although Aβ40 is the dominant product of the amyloidogenic processing of APP, Aβ42 has been found to be more toxic and prone to form aggregates than Aβ40 in cellular and animal studies. Besides, an elevation in the amount of Aβ42 in the brain has been reported in familial AD patients [93], suggesting the pivotal role of Aβ42 in the progression of AD.

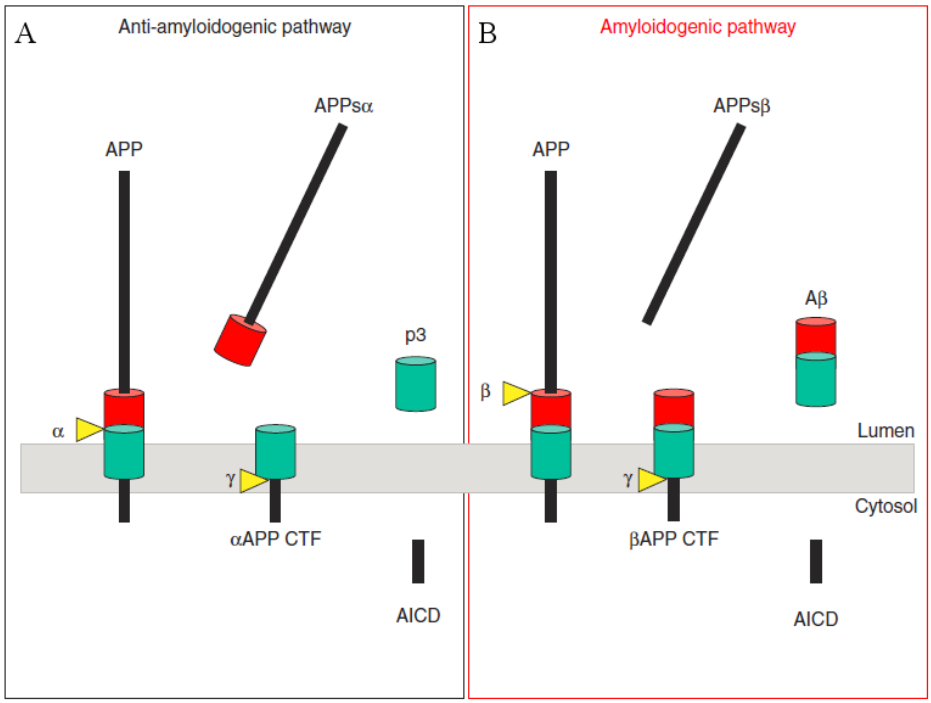

Figure 6. Two proteolytic pathways of APP processing. In the non-amyloidogenic pathway (A), APP is cleaved by α-secretase and will not generate Aβ species. While in the amyloidogenic pathway (B),

APP is sequentially processed by β- and γ- secretases to produce various Aβ species. Taken from Haass et al., 2012 [81].

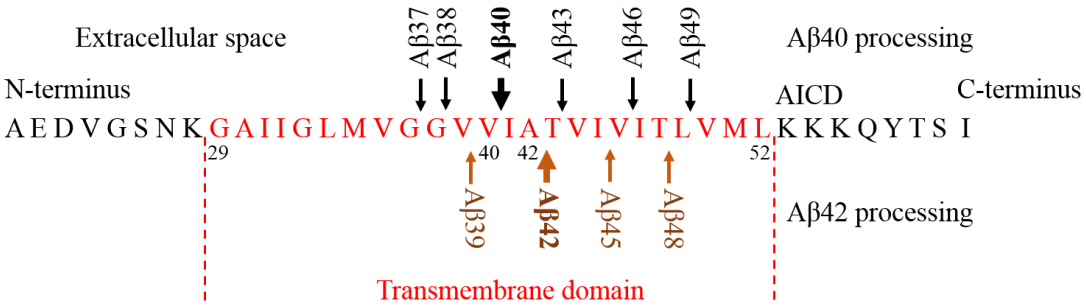

Figure 7. Cleavage sites of γ-secretase within the transmembrane domain of APP protein. Modified from Haass et al., 2012 [81].

Aβ has long been speculated as the major cause of Alzheimer's disease until recent evidence from Aβ-targeted immunotherapies showing that elimination of Aβ plaques in the brain has no clinical effect on the cognition of AD patients. There is also a temporal lag of about 10 years between brain Aβ depositions and clinical syndromes of AD, according to some clinical studies [43]. However, the amyloid cascade hypothesis still plays a fundamental role in the field of AD research (Fig. 8) [94]. According to the hypothesis, the imbalance between the generation and the clearance of Aβ in the CNS increases the content of Aβ proteins in the brain [95-97]. The accumulation of Aβ initiates the formation of neurotoxic oligomers, further triggering extensive neuronal damages such as synaptic dysfunction, calcium dyshomeostasis, oxidative stress and neuroinflammation [98, 99]. Currently it has been recognized that soluble Aβ oligomers are the most neurotoxic species in the brain [98]. The aberrant neuronal function might disturb intracellular signaling pathways and alter activities of protein kinases and phosphatases, leading to the hyperphosphorylation of tau proteins and later the formation of neurofibrillary tangles and neuronal degenerations [100]. Toxic Aβ species may also deposit along cerebral blood vessels, impairing cerebrovascular structures and functions [101]. The cerebral amyloid angiopathy (CAA) is extremely detrimental to the overall brain function as it breaks the integrity of the blood-brain barrier [102]. The persistence of all these pathologies will irreversibly contribute to hippocampal and cortical atrophy and significant cognitive decline [103, 104]. In addition to the challenges arisen from clinical trials of anti-Aβ immunotherapies that a reduction in brain Aβ burden has no clinical effect, the correlation between Aβ plaque burden and cognitive function is also less well-defined compared with that of tauopathies [105, 106]. Besides, some individuals with significant brain Aβ deposits do not have dementia related phenotypes [106]. Nevertheless, the central role of Aβ aggregation in the pathogenesis of AD indicates that it might be critical for the early diagnosis and intervention of Alzheimer's disease.

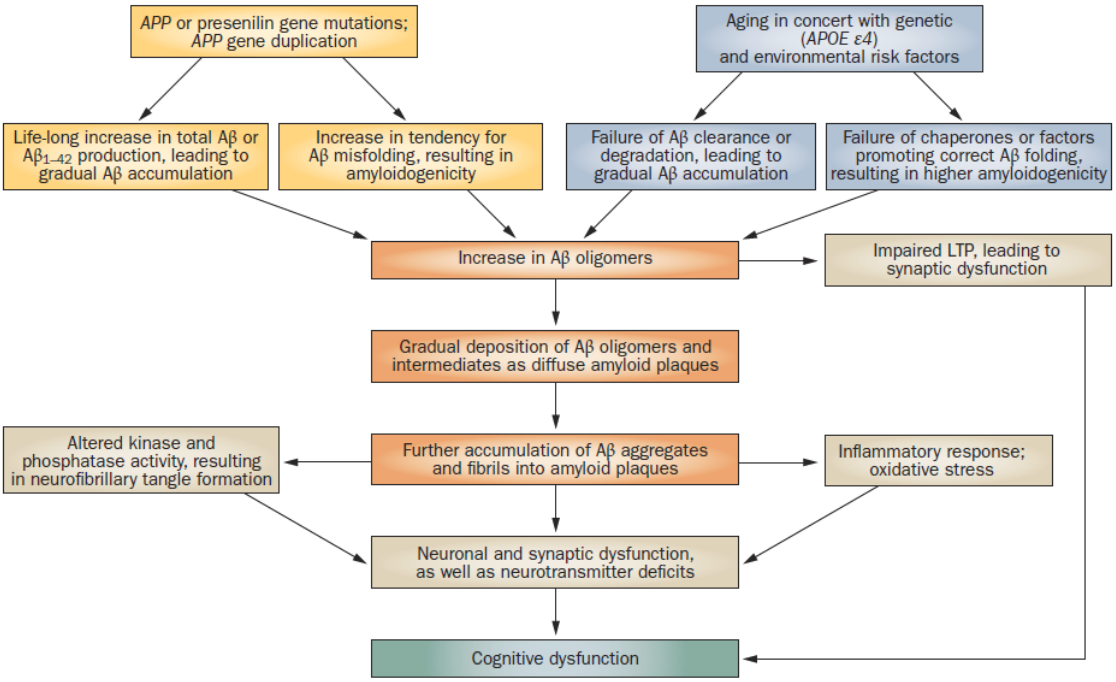

Figure 8. The amyloid cascade hypothesis of AD. The dyshomeostasis in the metabolism of Aβ leads to an accumulation of Aβ species in the central nervous system. In both familial and sporadic AD, soluble Aβ will aggregate into oligomers and fibrillary structures, which will cause a number of pathological changes in CNS. Soluble oligomers are highly toxic to neurons and will impair synaptic function, neurotransmission and intracellular signaling. Fibrillary structures of Aβ will deposit in brain parenchymal and form amyloid plaques. Taken from Blennow et al., 2010 [107].

Misfolding and aggregation of Aβ proteins

The formation of toxic Aβ species is believed to be a pivotal trigger for other pathological changes in the brain of AD patients [108]. These species also act as clinical biomarkers and targets in drug research and development of AD. How do Aβ monomers fold and self-assemble into oligomers and fibrils in the brain? Aβ belongs to the family of intrinsically disordered proteins (IDPs) [109]. The conformation of Aβ monomer depends largely on environmental conditions [110, 111]. In the present study we will mainly discuss the structure of Aβ42 species in aqueous environment. The theoretical isoelectric point (pI) of Aβ42 is slightly acidic (5.31), meaning that the protein will be negatively charged under physiological condition at pH 7.4 [112]. The monomeric units of Aβ42 usually adopt random coil structures in aqueous solutions [113]. It consists of a disordered N-terminus covering the first 10 amino acids, a core hydrophobic region from position 12 to position 28, and a hydrophobic C-terminus [114]. The last 10 residues at the C-terminus and the area from Lys16 to Phe20 have the greatest hydrophobicity while the N-terminal residues are relatively hydrophilic [115]. The hydrophobic regions of Aβ are prone to form intra- or inter-molecular β-sheet structures, which are essential for the aggregation of Aβ proteins under aqueous conditions (Fig. 9) [116, 117]. Information obtained by nuclear magnetic resonance (NMR) experiments suggested that amino acids within residues Val24 and Gly29 in Aβ42 are able to form a β-turn structure, maintained by an intramolecular salt bridge between Asp23 and Lys28 [118]. The propensity of Aβ42 to form cross β-conformations facilitates the generation of elongated Aβ aggregates [119]. The aggregation process

of Aβ42 has been extensively studied due to its critical role in the pathogenesis of AD, and more generally, in understanding protein misfolding.

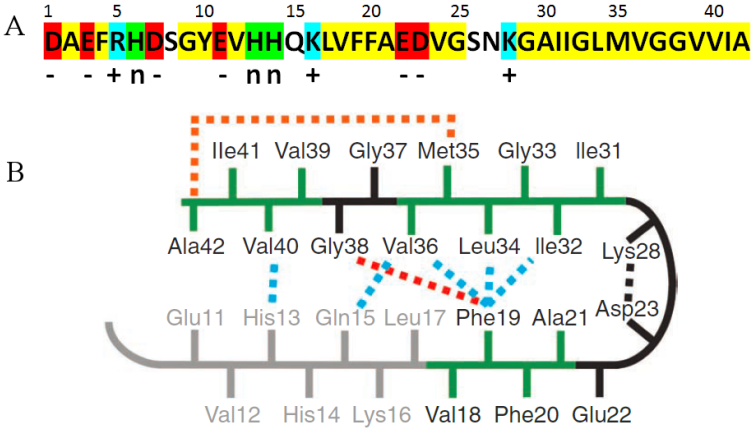

Figure 9. Sequence of Aβ42 (A) and the proposed conformation of an Aβ42 monomer within amyloid fibrils (B). Hydrophobic residues are marked in yellow. Positively charged residues, negative charged residues or those with pK values close to neutral pH are presented in blue (+), red (-) and green (n), respectively (A). Reproduced from Meisl et al., 2017 [120]. It is generally believed that residues 1-17 (grey) of Aβ42 are unstructured while residues 18-42 will form a β-turn-β-fold conformation via hydrophobic interactions (green) and a salt bridge between Asp23 and Lys28 (black dashed line). Side chain interactions (blue dashed line) are also observed within monomers. Molecular contacts between Phe19 and Gly38 (red dashed line) and between Ala42 and Met35 (orange dashed line) are also reported. Taken from Ahmed et al., 2010 [121].

Although the molecular mechanism underlying the fibrillation of Aβ is not fully resolved, the major microscopic events have been recognized (Fig. 10). The self-aggregation of Aβ proteins is accompanied by the conformational change of Aβ monomers in aqueous environment [122, 123]. The hydrophobicity of the C-termini drives Aβ monomers to assemble into oligomers ranging from a dimer (~9 kDa) to a few hundred kDa [124]. Upon oligomerization the conformation of Aβ protein will transform from random coil to β-strand/turn/β-strand structure, as evident by MD simulations, CD spectroscopy and NMR studies [125]. These intermediate species are soluble, varying in shapes, and act as nuclei for further aggregation. The formation of small oligomers starting from Aβ monomers is termed as primary nucleation [126]. Soluble Aβ monomers stack to the surface of oligomers via hydrogen bonds (H-bonds) and hydrophobic interactions, leading to the formation of elongated protofilaments and protofibrils [127, 128]. Aβ proteins within these pre-fibrillar structures adopt in-register parallel β-sheet structures [129, 130]. Some protofilaments may also wrap in pairs to form helical structures [119]. Mature Aβ fibrils derive from the lateral assembly of protofilaments composed of the addition of Aβ monomers to already formed fibrillar oligomers. The fibrillation of Aβ proteins will reach a steady state, as the concentration of Aβ monomers drops to a low level [126, 131]. The presence of elongated fibrils provides extra surfaces for Aβ monomers in solution, which may further initiate the oligomerization of Aβ. This process is referred to as fibril-catalyzed secondary nucleation and has drawn growing attention due to its importance in the generation of toxic Aβ oligomers [132]. Mature amyloid fibrils may undergo the fragmentation process in conditions such as mechanical agitation. The formation of short fragmented Aβ species is thought to

enhance the cytotoxicity of Aβ [133]. Besides, it promotes the proliferation of fibrillary structures by offering more fibril ends and surfaces for the attachment of Aβ monomers [134, 135]. The kinetics of Aβ self-aggregation is commonly monitored via measuring the fluorescence emission of Thioflavin T (ThT), a fluorescent dye specific for amyloid fibrils (Fig. 11). ThT is able to bind to the β-sheet surface along the side chain channels of the fibrils [136]. The binding of ThT stabilizes the rotation of its central C-C bond and dramatically increases the fluorescence emission. The binding also leads to significant red shifts in the excitation maximum (from 385 nm to 450 nm) and the emission maximum (from 445 nm to 482 nm) of ThT [112, 137]. A characteristic aggregation kinetic for Aβ aggregation in the ThT assay includes a step with very low fluorescence known as the lag phase, a steeply increasing phase termed as the growth phase, and a final plateau phase [138]. The different phases correspond to different dominant microscopic events during the aggregation process and can be well reflected by changes in the ThT fluorescence.

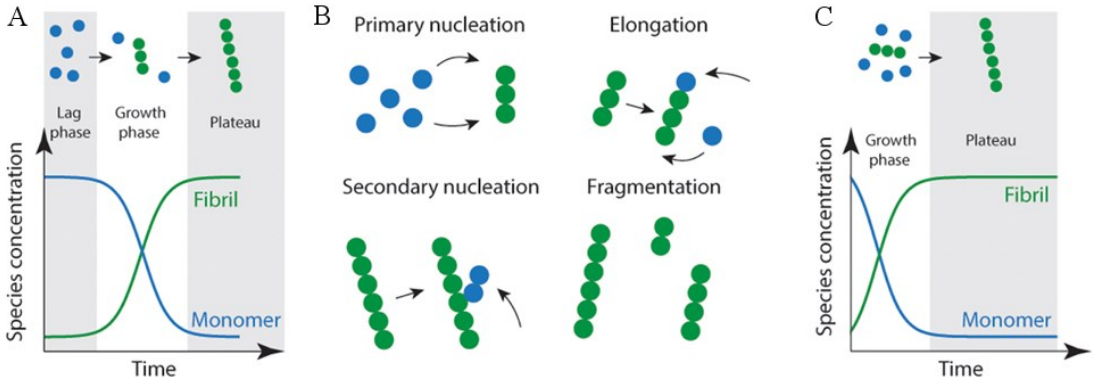

Figure 10. Self-aggregation of Aβ and the fibril formation process. The aggregation of Aβ includes three phases (A). In the lag phase, Aβ monomers are the dominant species and will form nuclei via primary or secondary nucleation (as shown in B). During the growth phase, in which the elongation process takes place, the concentration of monomers depletes rapidly. Finally, the concentration of Aβ fibrils and monomers reach steady states. Mature fibrils may disassemble into Aβ fragments. The presence of short fragments is able to accelerate the self-aggregation of Aβ by shortening the lag phase (C). Taken from Zeineddine et al., 2015 [139].

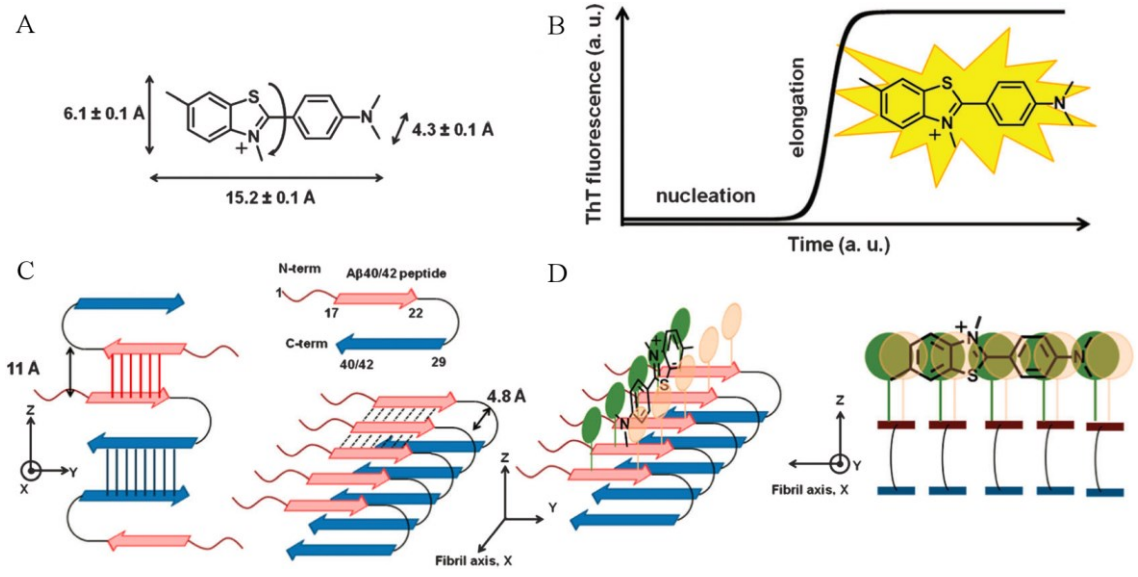

Figure 11. Thioflavin T (ThT) and its application in monitoring the fibrillation of Aβ. A scheme of Thioflavin T with dimensions and the rotation of C-C bond (A). It is commonly used to detect the fibrillation of Aβ since the fluorescence emission of ThT is significantly enhanced when bound to amyloid fibrils with cross-β-sheet structures (B). β-sheet interactions among Aβ proteins are mediated by side chain interactions (left, C) and hydrogen bond interaction (right, C). ThT binds to the surface of amyloid fibrils (D). Hydrophobic amino acid residues along the side chains of the fibril axis are marked in Green and orange circles. Taken from Noël et al., 2013 [138].

Morphologies and structures of Aβ fibrils

The structures of Aβ fibrils are challenging to characterize because of the heterogeneity and polymorphism of these species. Morphologies of Aβ fibrils are mostly determined through atomic force microscopy (AFM) or electron microscopy (EM) imaging. It has been shown that mature Aβ fibrils in general have a length of over 1 μm, while the lateral width of Aβ fibrils rarely exceeds 25 nm [140]. Aβ fibrils often display twisted structures and show crossover patterns under TEM inspection (Fig. 12) [140]. Kirschner et al. revealed that mature Aβ fibrils have cross-β structures in which the individual β-strands are oriented perpendicular to the fibril axis [141]. A more detailed study about the 3D structure of Aβ fibrils using NMR methods demonstrated that residues 18-26 and residues 31-42 of Aβ42 monomers form two intermolecular β-sheet structures in the fibril, respectively [142]. These parallel cross-β structures are stabilized by intramolecular hydrophobic interactions and the salt bridge, as abovementioned [142]. Later on, several atomic structures of Aβ42 fibrils have been resolved by electron cryo-microscopy (cryo-EM). Schmidt et al. observed in their fibrillary structures that Aβ42 dimers in the same layer had the same conformation and packed with each other in a face to face pattern. The β-strands formed by hydrophobic C-termini are responsible for the inter-molecular interaction [143]. A high resolution structure of a disease relevant Aβ42 fibril has been published in 2017 (Fig. 13). By combining cryo-EM and NMR, Gremer et al. were able to resolve the backbone of all the 42 amino acids and all the side chains in their fibrillar structures. The 4.0-angstrom (Å) structure has an "*LS*" shaped topology composed of two intertwined protofilaments [144]. The discovery of the structural information on Aβ42 fibrils will undoubtedly aid to understand mechanisms of the abnormal aggregation of Aβ.

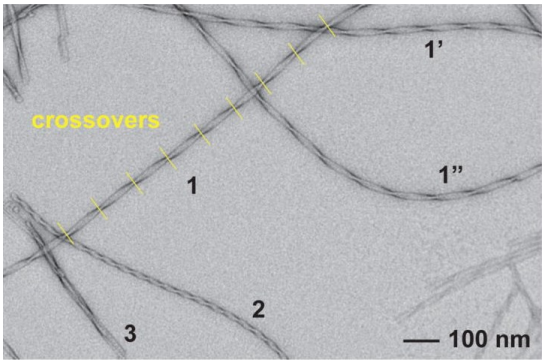

Figure 12. Morphologies of Aβ40 fibrils obtained using negative TEM imaging. The polymorphism of fibrils can be observed by comparing the structure of fibrils 1, 2 and 3. Fibrils 1′ and 1′′ show different bending patterns. Taken from Fändrich et al., 2011 [140].

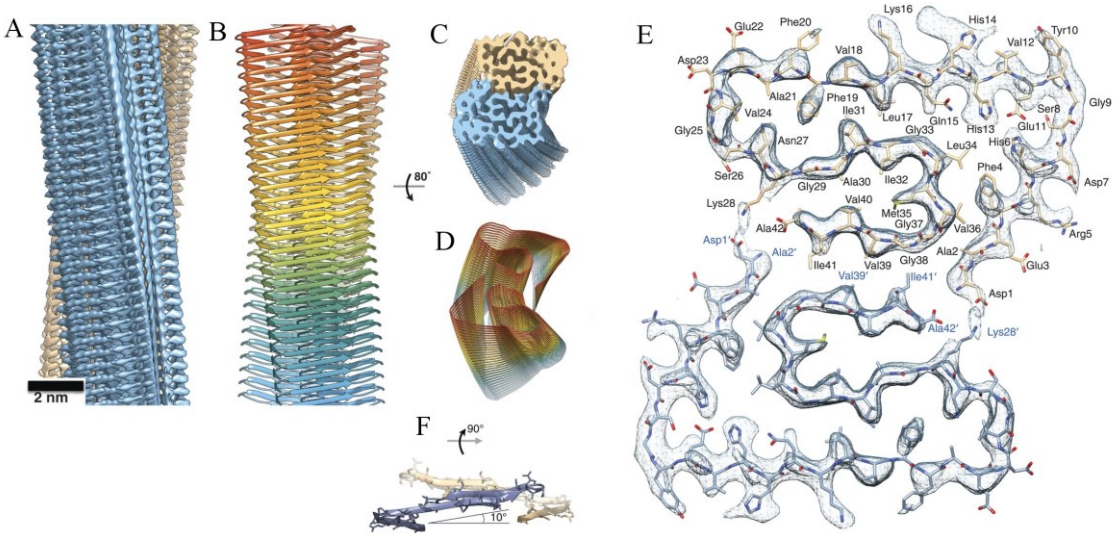

Figure 13. Structure of Aβ42 fibrils determined using cryo-EM and solid state NMR. 3D reconstruction of Aβ42 fibrils comprised of two protofilaments showing parallel cross-β structures (A and B). A tilted view of EM density map and backbone model (C and D). Atomic view of two Aβ42 monomers from protofilaments with all amino acid residues assigned (E) and a side view of two Aβ42 monomers showing the orientation of these units. Modified from Gremer et al., 2017 [144].

Hydrodynamics of Aβ assemblies

The heterogeneity in sizes and morphologies of Aβ assemblies (Fig. 14) observed in vivo and in vitro correlates with the diversity and complexity of Aβ related neuropathologies in animal and clinical studies. It has been recognized that soluble Aβ oligomers are more cytotoxic than insoluble fibrillar Aβ assemblies [99]. Therefore it is important to decipher the size information of different Aβ species and to clarify the size dependency of the neurotoxicity of Aβ species [145]. The sizes of Aβ species are generally characterized by microscopic imaging, size exclusion chromatography (SEC), scattering techniques and analytical ultracentrifugation (AUC). Bitan et al. reported in their study a hydrodynamic radius (R_H) of 1-2 nm for Aβ40 monomers detected by SEC in combination with dynamic light scattering (DLS) [146]. Zhang-Haagen et al. calculated the radii of gyration (R_g) for Aβ40 and Aβ42 in 1, 1, 1, 3, 3, 3-hexafluoro-2-propanol-D2 (dHFIP) by applying small angle neutron scattering (SANS). The R_g values are 1.0 ± 0.1 nm for Aβ40 and 1.6 ± 0.1 nm for Aβ42, respectively [147]. These calculated values are consistent with R_H value of 0.9 ± 0.05 nm determined by fluorescence correlation spectroscopy (FCS) [148]. The soluble Aβ assemblies cover various species ranging from < 10 kDa (e.g. Aβ dimers) to > 100 kDa (such as annular protofibrils) [149]. These soluble Aβ oligomers are particularly interesting because of their biological relevance. Aβ derived diffusible ligands (ADDLs) and Aβ*56 are two of the best known oligomeric entities that have been identified to mediate neuronal damages in vivo [150, 151]. Structural analysis from X-ray crystallography suggested that Aβ monomers within soluble Aβ oligomers adopt folded β-hairpin structures [152]. The dimensions of these oligomers are 1-3 nm in height and 5-10 nm in width or length, implying relatively compact shapes [153]. Bitan et al. investigated the size distribution of Aβ42 oligomers treated with photo-induced cross-linking of unmodified proteins (PICUP). They proposed that the oligomerization of Aβ42 begins with the rapid formation of pentamer/hexamer

units, which then will aggregate into large oligomers and protofibrils [146]. Wolff et al. corroborated this finding with AUC and SANS experiments showing that the smallest detectable oligomeric species in aqueous solutions are Aβ pentamers/hexamers. These pentamers/hexamers are characterized by a sedimentation coefficient of 2.56 S and R_g between 2 and 4 nm [154]. The structure of Aβ oligomers and their consequent toxicity have made Aβ oligomers a very important drug target for disease diagnosis and prevention.

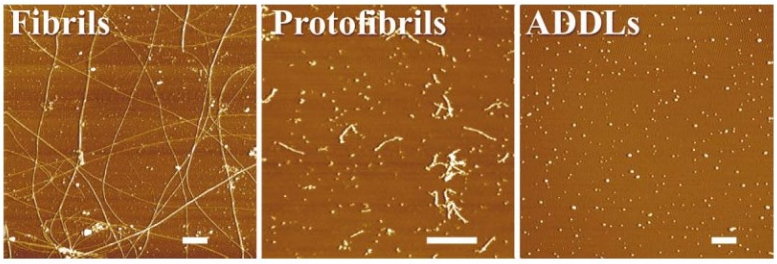

Figure 14. Different Aβ42 assemblies imaged by atomic force microscopy imaging (AFM). The formation of amyloid fibrils consists of multiple steps, including the generation of oligomers (such as ADDLs), protofilaments and protofibrils. Scale bar: 200 nm. Taken from Klein et al., 2001[155].

Zinc ions in the aggregation of Aβ protein

A great number of physiological factors can interact with Aβ proteins and modulate its self-aggregation process. Metal ions like iron (Fe^{3+}/Fe^{2+}), zinc (Zn^{2+}) and copper (Cu^{2+}) and other trace elements are widely distributed in vivo and play fundamental roles in regulating physiological functions [156]. Endogenous Zn^{2+} is necessary for the proper functioning of glutamatergic synapses that are abundant in cerebral cortex and the limbic system [157]. The homeostasis of Zn^{2+} is therefore essential for the neurotransmission and synaptic activities. It has been found that Aβ plaques in the brain of Alzheimer's patients contain high amounts of zinc and copper ions [158]. The local concentration of Zn^{2+} within Aβ plaques can reach 1 mM, much higher than the physiological concentration of Zn^{2+} in the brain [158, 159], suggesting the dyshomeostasis of Zn^{2+} in the central nervous system of AD. The N-terminus of Aβ monomer has been identified as the major binding area for metal ions [160]. In detail, the Asp1, His6, His13 and His14 residues of Aβ42 play major roles in coordinating metal ions like Zn^{2+} and Cu^{2+} [160]. Amino acids at position 2, 3, 7 and 11 (Ala2, Glu3, Asp7 and Glu11) were also believed to participate in metal binding [160]. Two different binding modes have been proposed in the case of Aβ42-Zn^{2+} interaction. In the first binding mode, Zn^{2+} coordinates with the imidazole rings of the three Histidine residues. The amine group at position 1 (Asp1) or the carboxylate group at position 11 (Glu11) might also be involved in the coordination process [161]. However, a recent study reported a different binding mode (Fig. 15), in which Zn^{2+} interacts with two His residues (His6, His13 or His14) and the carboxylate groups from Glu11, and Asp1 or Glu3 or Asp7 [162]. Both binding modes result in the formation of tetrahedral complexes. The dissociation constant of Aβ42-Zn^{2+} complexes are assessed to be within 1 μM and 20 μM, depending on experimental conditions [160]. Despite the moderate binding affinity, Zn^{2+} could significantly influence the self-association of Aβ42, therefore leading to different biological outcomes. Evidence from stopped-flow spectroscopy suggests a rapid interaction between Zn^{2+} and

Aβ proteins on a millisecond time scale [163, 164]. The impact of Zn^{2+} on the aggregation of Aβ42 is dependent on the applied stoichiometry. The presence of superstoichiometric Zn^{2+} promotes the generation of non-fibrillar, amorphous aggregates with reduced neurotoxicities [165, 166]. However, it has also been reported that Zn^{2+} ions promote the generation of small spherical Aβ oligomers that are harmful to neurons [167]. These Zn^{2+} coupled Aβ oligomers are rich in β-sheets and cross-β structures. Abelein et al. demonstrated that substoichiometric Zn^{2+} slows down the fibrillation of Aβ40 via modulating the fibril ends and disturbing the elongation process [168]. The effects of Zn^{2+} on the structures of Aβ proteins are diverse. Some molecular simulation experiments showed that Zn^{2+} ions stabilize β-hairpin structures, a common motif within Aβ oligomers, and facilitate the formation of non-fibrillar oligomers [169]. NMR studies revealed at atomic level that the coordination of Zn^{2+} to Aβ40 increases the rigidity of its N-terminus and induces the formation of a turn-like conformation at residues Val24-Lys28 [170]. The mobility of the originally rigid C-terminus is elevated simultaneously in the presence of Zn^{2+} binding. These conformational changes make Aβ monomers more susceptible to form amorphous aggregates, compared with Zn^{2+} free Aβ monomers [170, 171]. The interaction between Zn^{2+} and Aβ oligomers or fibrils is also of interest as these two species are more relevant to disease pathologies than Aβ monomers. Miller et al. demonstrated that Zn^{2+} coordination to Aβ42 oligomers lowers the solvation energy for large Aβ42 assemblies and increases the aggregation propensity. Besides, Zn^{2+} coordination favors the formation of less structured assemblies, leading to the generation of polymorphic aggregates [172]. Although massive research has been accumulated in the field of Zn^{2+}-Aβ interaction, it is still disputable how physiological Zn^{2+} ions influence the aggregation process of Aβ.

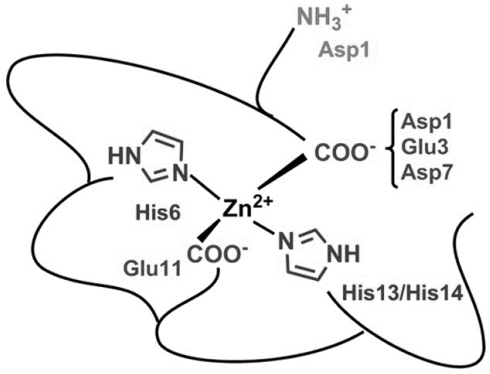

Figure 15. Proposed Zn^{2+} binding sites in Aβ (pH 7.4). Zn^{2+} forms a tetrahedral complex with Aβ by interacting with His residues and carboxylate groups. Modified from Alies et al., 2016 [162].

Drug developments targeting Aβ

Given the crucial role of Aβ in the pathogenesis of AD, numerous studies have been carried out to ameliorate Aβ pathologies, in an attempt to slow down the progression of AD. Aβ pathology-targeted therapies can be divided into three categories, according to the respective mechanisms. The first category includes agents that can promote the elimination of Aβ species in the brain. Mawuenyega et al. compared the production and clearance rates of Aβ40 and Aβ42 in the CNS of AD patients and healthy controls by metabolic labeling. They observed that the clearance of Aβ species in AD patients is significantly impaired [97]. Antigen-antibody complex formation can boost the elimination of

target proteins in vivo and therefore has been utilized to reduce brain Aβ burdens [173]. Both active and passive immunotherapies have been applied to eliminate Aβ species in the brain [174]. In active immunotherapies, vaccines containing Aβ42 or other Aβ fragments are administered together with immune-stimulating adjuvants. AN-1792, the first active anti-Aβ vaccine, was developed in 2000. It uses full length Aβ42 as the antigen and QS21 as the adjuvant [175]. However, about 6% of the vaccinated AD patients had aseptic meningoencephalitis [176]. The clinical trial was then terminated for safety reasons. Other vaccines, including CAD106 and ACC-001 which consist of Aβ1-6 as antigens, are under clinical trials [177, 178]. The overall concerns for active immunotherapies focus on potential side effects related to the complex immune response. Passive immunotherapy is based on the activity and specificity of exogenously administered anti-Aβ antibodies [179]. A series of anti-Aβ antibodies have been designed to recognize different epitopes of Aβ42, or different forms of Aβ aggregates, and some of them have been proceeded to phase III clinical trials. The latest phase III study on solanezumab led by Eli Lilly & Co., a humanized IgG1 monoclonal antibody targeting the Aβ16-24, did not show any significant effect on the cognitive dysfunction in patients with mild AD compared with the placebo [180]. A phase 1b study on aducanumab, a human IgG1 monoclonal antibody reacting with soluble Aβ oligomers and insoluble fibrils, showed promising effects on both reducing brain Aβ burdens and slowing down the cognitive decline in patients with prodromal or mild AD [181]. Other antibodies developed to direct against Aβ species include bapineuzumab, gantenerumab and crenezumab. Gantenerumab and crenezumab are still being tested in some preventative trials in subjects with AD-inducing mutations [72, 182].

The second category includes mostly small molecules that can regulate the generation of Aβ proteins. The pivotal role of β- and γ- secretases in the amyloidogenic processing of APP has made both enzymes important targets in the development of novel inhibitors of Aβ production [183]. However, molecules showing inhibitory effects on β- or γ- secretases should be taken with caution because of the wide involvement of these two enzymes in regulating other physiological processes. For example, β-secretase has been reported to take part in the metabolism of neuregulin 1 (NRG1) which is responsible for the myelination of neurons [184]. More complex and broader functions have been documented in studies on γ-secretase. Notch protein, for example, is a substrate of γ-secretase and determines cell fates and cell signal communications in development [185, 186]. Semagacestat was the first non-selective γ-secretase inhibitor that was tested in clinical trials [187]. The phase III clinical trial was terminated prior to the designated ending point for significant side effects and the lack of clinical effects. Adverse events such as loss of weight, skin cancers and infections and hematological disorders have been reported in patients following semagacestat treatment [188]. Some selective inhibitors and γ-secretase modulators have been designed to avoid influencing Notch proteolysis [189]. Nevertheless, the clinical studies of these Notch-sparing inhibitors are also not promising, with respect to the safety and therapeutic effects. So far only a limited number of β-secretase inhibitors have been investigated in clinical trials. MK-8931 (verubecestat) has a good tolerability among healthy volunteers and AD patients in phase I studies. Besides, it also reduces the content of CSF Aβ in a dose-dependent manner [190]. Unfortunately, the latest clinical trial revealed that verubecestat did not influence the cognitive function of patients with mild to moderate AD, and was associated with increased adverse effects [191].

The third category contains compounds that can modulate the self-aggregation of Aβ proteins. The rationale behind these compounds is that by shifting the self-aggregation process of Aβ toward non-toxic, off-pathway aggregates, neuronal damages induced by toxic species might be avoided [192, 193]. Numerous small molecules have been demonstrated to possess the property to interfere with the self-aggregation and lead to the generation of non-toxic species. Polyphenols are widely examined because of their good accessibilities and multifaceted effects [194]. Curcumin and epigallocatechin gallate (EGCG) are common ingredients in daily diets. In vitro evidence suggests that these polyphenolic compounds bind directly to various Aβ species, suppressing the formation of ordered fibrils and other toxic intermediates [195, 196]. The anti-amyloidogenic effects of these compounds were also supported by animal studies showing that AD animal models receiving treatments indeed have decreased Aβ pathologies and elevated cognitive functions [197]. Some peptides or peptidomimetics have also been developed to modulate the fibril formation of Aβ. The advantages of peptide-based compounds over small molecules are their high selectivity and possibility of rational design. For instance, Chen et al. developed a series of cyclic decapeptides with strong affinities towards Aβ monomers. These peptides stabilize monomeric Aβ proteins via interacting with the N-terminus and thus block the accumulation of toxic oligomers. The side effects of these cyclic peptides, such as the hemolysis, could be bypassed through chemical modifications [198]. Hoyer et al. found that $Z_{A\beta3}$ stabilizes a β-hairpin conformation of Aβ40 and inhibits its further aggregation [199]. Richman and co-workers reported that CP-2, a six-residue cyclic D,L-α-peptide, disrupts the oligomerization of Aβ40 by stabilizing small oligomeric Aβ40 species (1-3 mers) in parallel β-sheet conformation [200].

D-enantiomeric peptides are promising drug candidates

Although peptides have a variety of features favoring their clinical application, there are still some limitations. One of the linimations of peptidic compounds is their susceptibility to proteolysis. The proteolytic stability of peptide-based drugs is particularly important when they are administered orally. Utilizing D-enantiomeric peptides (D-peptides) is one of the mostly used and promising methods to overcome the in vivo proteolysis. The first D-peptide that is able to bind to Aβ species in an AD mouse model was selected via mirror image phage display in 2003 [201]. Wiesehan and coworkers identified D3 (Fig. 16), an all-D-enantiomeric twelve-residue peptide, as a novel agent against Aβ pathology [201]. This peptide contains five arginine residues and has a theoretical pI of 12.6. D3 not only suppresses the aggregation of Aβ proteins in a concentration dependent manner, but also eliminates toxic oligomers [202]. D3 also shows promising effects in animal studies. The administration of D3 in APP/PS1 mouse models significantly decreased brain Aβ loads without causing neuroinflammation. Meanwhile, D3 helps to mitigate Aβ related inflammatory responses by reducing reactive microglia and astrocytes in the brain [203-205]. The permeability of D-peptides through the blood brain barrier (BBB) was confirmed by in vitro and in vivo studies [204, 206, 207]. The stability of D3 and its derivatives in conditions mimicking the digestive system has been determined by reversed-phase high-performance liquid chromatography (RP-HPLC). The results show that the D-enantiomeric form of peptides have far higher stability in gastric and intestinal fluids, as well as in liver microsomes, than the corresponding L-enantiomers [208]. In addition to its perfect bioavailability, behavioral tests showed that oral treatment of D3 significantly promotes the cognitive

performance of AD mouse model [205, 209]. Researchers demonstrated that the protective effects of D3 come not only from its elimination of toxic Aβ species, but also from its inhibition on neuroinflammation. These findings suggest that D3 have multifaceted effects on AD pathologies.

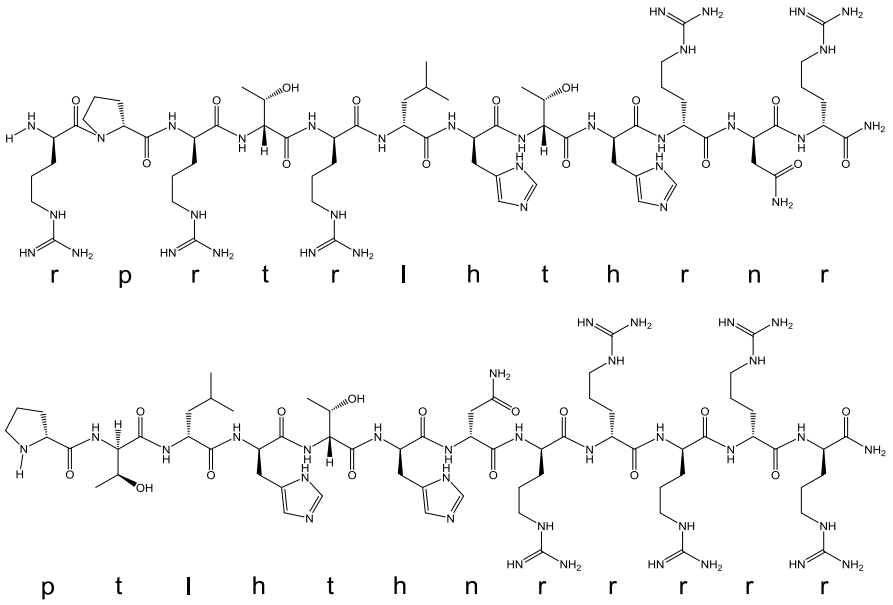

Figure 16. Lewis structures of D*-enantiomeric peptides D3 (up) and RD2 (down). The C-termini are amidated for both peptides.*

The selection of D3 was carried out via mirror image phage display from a peptide library. D-enantiomeric Aβ42 (D-Aβ42) at 2 nM was used as a target and repeated biopanning was applied to reinforce the screening process [210]. The working concentration of D-Aβ42 was extremely low so that most of the Aβ42 molecules could stay as monomers to enable the interaction with potential binding partners. However, it is still elusive whether D3 interacts with monomeric Aβ42 since no direct information about the binding can be deciphered from the phage display screening. The first and foremost evidence showing a direct binding of D3 to monomeric Aβ42 was demonstrated by surface plasmon resonance (SPR). Different forms of Aβ species were immobilized on sensor chips and running buffer carrying various concentrations of analytes flew through the sensor chip during the experiment. D3 preferentially bind to Aβ42 monomers and oligomers in comparison with Aβ40 species and Aβ42 fibrils [211]. A more detailed characterization of the binding affinities of D3 and its analogs to Aβ42 was performed by Ziehm and co-workers. The dissociation constant (K_D) of the interaction between C-terminally amidated D3 and Aβ42 was 3.8 ± 0.6 μM as determined by SPR experiments, implying a strong binding between these two molecules [212]. However, there is still no clear image about the complex formation between D-peptides and Aβ species, especially monomers. In silico studies showed that the interaction is mediated by electrostatic attraction between oppositely charged amino acid residues on D3 and Aβ42, respectively. Asp7, Glu11, Glu22, and Asp23 from Aβ42 were identified as potential binding sites for D3 as they had the lowest interaction energies as revealed in MD simulations [213]. The contribution of charge effect to the interaction between D3 and Aβ was further corroborated by SPR measurements comparing the binding of amidated and non-amidated D3 peptides to Aβ42. An increase in positive charges from +5 to +6 dramatically enhanced the binding affinities (15 ± 1.5 μM for non-amidated D3, 3.8 ± 0.6

μM for amidated D3) [212]. Interestingly, RD2, an optimized derivative of D3 with the same amino acids and charges but different sequence (Fig. 16), was also found to strongly interact with Aβ42. The K_D value determined by SPR experiments was 3.6 ± 0.7 μM for RD2 and Aβ42 [214]. The interaction between D-peptides and Aβ monomers is crucial for understanding the in vitro and in vivo mechanisms of action of D-peptides on Aβ aggregation.

It has been demonstrated that D-peptides are effective in eliminating toxic Aβ oligomers, the main species responsible for Aβ aggregation related neuropathologies [98]. The interference of D-peptides on the size distribution of Aβ aggregates could be quantitatively determined via a combination of density gradient centrifugation (DGC) and analytical RP-HPLC, which is termed as quantitative determination of interference with Aβ aggregate size distribution (QIAD) [202, 214]. In this assessment, pre-incubated Aβ42 samples were treated with different concentrations of D-peptides for a certain period of time. The mixtures were subjected to DGC with iodixanol density gradients to fractionate species with different sizes. All fractions were harvested and analyzed by RP-HPLC to quantify the amount of Aβ42 proteins in each fraction. In the presence of D3 or RD2, the fraction corresponding to 7 S Aβ42 oligomers were remarkably decreased, while fractions representing high molecular weight Aβ42 species had increased amounts of Aβ42 proteins, indicating a shift in the size distribution of Aβ species toward large, non-toxic species [202]. This measurement also demonstrated that RD2 is more efficient than D3 in eliminating toxic Aβ42 oligomers [214]. In addition to promoting the elimination of toxic oligomers, RD2 can also inhibit the fibril formation of Aβ42 in a concentration dependent manner as shown in ThT assays [214]. Similarly, Aβ42 aggregates formed in the presence of superstoichiometric D3 were also non-fibrillar, amorphous structures [209]. In vivo, RD2 successfully reversed cognitive dysfunction and reduced the brain Aβ pathology in old-aged AD mouse models. The content of Aβ oligomers in brains of RD2 treated AD mice was significantly decreased compared with the mice with placebo treatment [215].

To summarize, two D-peptides, D3 and RD2, have been found to bind to monomeric Aβ42 strongly and eliminate toxic Aβ oligomers efficiently. In vivo experiments showed that both D-peptides are capable of rescuring the cognitive function of AD mouse models without inducing adverse effects. D3 and RD2 share similarities on interacting with Aβ species and decelerating the neurodegeneration, but they might have distinctive mechanisms of action. These D-peptides are promising disease-modifying agents for AD related pathologies.

Analytical ultracentrifugation

Theoretical background

Centrifugation is a broadly used technique to separate particles according to their sizes and shapes. In the field of biology, the sedimentation of a macromolecule in solution is determined not only by the hydrodynamic and thermodynamic properties of the molecule, but also by solvent conditions [216]. One of the most significant progress in the field of centrifugation was made by Svedberg and his colleagues about one century ago for their work on analytical ultracentrifugation [216].

The sedimentation of a particle in a solvent under a gravitational field is determined by three forces (Fig. 17).

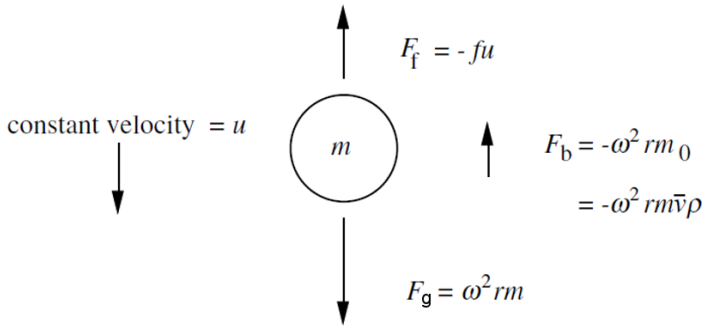

Figure 17. The forces involved in the sedimentation of a particle in solution during the centrifugation.

The first force is the gravitational force (F_g) which is proportional to the mass, distance from the center of rotation, and the acceleration of the rotor.

$$F_g = m\omega^2 r = \frac{M}{N}\omega^2 r \qquad \text{eq.1}$$

In the equation, the mass of a single particle m (in g) can be replaced by the molar weight of the particle M (in g/mol) divided by the Avogadro's number N. The acceleration during the spinning is determined by the radial position of the molecule (r) and the angular velocity (ω, in rad/s). This is the driving force which makes the particle sediment along the radius.

There is also a buoyant force (F_b), which according to Archimedes' principle is determined by the weight of the solvent (m_0) displaced by the molecule.

$$F_b = -m_0\omega^2 r \qquad \text{eq.2}$$

where m_0 can be expressed as:

$$m_0 = m\bar{v}\rho = \frac{M}{N}\bar{v}\rho \qquad \text{eq.3}$$

Here, $\bar{v}$ represents the partial specific volume (g/cm^3) of the particle and ρ is the density (g/cm^3) of the solvent.

When the particle starts to move along the radius in a solvent, it will experience the frictional force (F_f) that is proportional to its velocity u:

$$F_f = -fu \qquad \text{eq.4}$$

where f is the frictional coefficient of the particle, depending on its shape and size, and the viscosity of the solvent.

The buoyance and the frictional force act against the gravitational force during the sedimentation. All three forces will reach balance within microseconds during the sedimentation process:

$$F_g + F_b + F_f = 0 \qquad \text{eq.5}$$

$$\frac{M}{N}\omega^2 r - \frac{M}{N}\bar{v}\rho\omega^2 r - fu = 0 \qquad \text{eq.6}$$

After rearranging the terms and parameters, we have the following equation:

$$\frac{M(1-\bar{v}\rho)}{Nf} = \frac{u}{\omega^2 r} \equiv s \qquad \text{eq.7}$$

The equation, known as Svedberg equation, describes the sedimentation coefficient (s) of a particle in solvent during the centrifugation process. This value is dependent on experimental conditions, e.g. temperature, buffer composition, and solute concentration. The sedimentation coefficient has dimensions of seconds and is expressed in Svedberg unit (S). 1 S is equal to 1×10^{-13} s.

The sedimentation of the solute may create concentration gradient along the centrifuge cell, leading to the accumulation of particles at the bottom. Particles at the bottom may diffuse back to the low concentration area. The sedimentation and back diffusion act oppositely during the centrifugation process [217]. The whole process can be described by appropriate models to evaluate the size distribution of a sample.

Analytical ultracentrifuge and detectors

The centrifuge is specifically designed to enable the recording of radial concentration gradients created by the sedimentation of particles at high speed centrifugation. Nowadays AUC has been developed to meet the demand of high quality output as well as easy handling. Rotors and cells are important parts for a centrifuge (Fig. 18). The maximum speed of AUC is 60,000 rpm (~290,000 g) and this requires the rotor as well as cells to be able to withstand such high centrifugal forces. The centrifuge is also implemented with a temperature control system and vacuum pump(s).

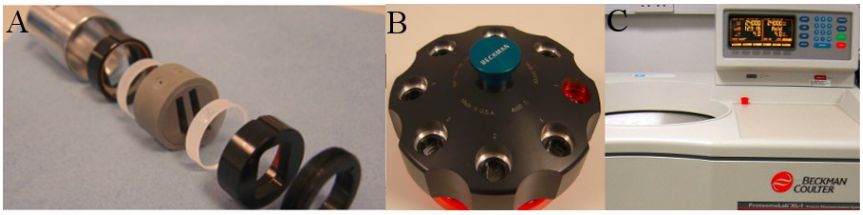

Figure 18. AUC cells and the 8-hole rotor. An overview of a 12-mm double-sector aluminum cell (A). The 8-hole rotor (B) and an analytical ultracentrifuge (C). Modified from https://www.ncl.ac.uk/nuppa/services/analytical-ultracentrifugation/#overview [218].

There are three detection systems available on the market for the detection of the sedimentation process. The first system is the Rayleigh interference optics, which measures the concentration gradient of a sample based on the change in refractive indices [219]. This detection system is used for samples that are not suitable for absorbance measurements. The second detection system, which is probably the most common method in this field, is the absorbance optical system (Fig. 19A). This system uses a high intensity xenon flash lamp as the light source, allowing the measurement at wavelength between 190 and 800 nm. The detection wavelength can be selected according to the absorbance of the sample and the light will be transmitted to samples via a monochromator. The light intensity of all samples at different radial position can be recorded with the help of a movable slit assembly and the time information of the reference magnet at the bottom of the sample chamber. The

absolute sample concentration at a certain radial position can be accurately determined based on the Beer-Lambert law. Generally, the absorbance of the sample at a chosen wavelength should not exceed 1.2 OD in an AUC measurement. Absorbance optics has higher sensitivity and reproducibility than interference optics, especially in measuring dilute samples [219]. The third detection system utilizes fluorescence to monitor the movement of fluorescent labeled particles in solution (Fig. 19B). The detection system has a fixed-wavelength laser source at 488 nm, and is equipped with a dichroic mirror and a cut-off filter which collects emission lights within 505 nm and 565 nm. The fluorescence signals at various radial positions are measured at different time points, enabling the acquisition of sedimentation profiles [220].

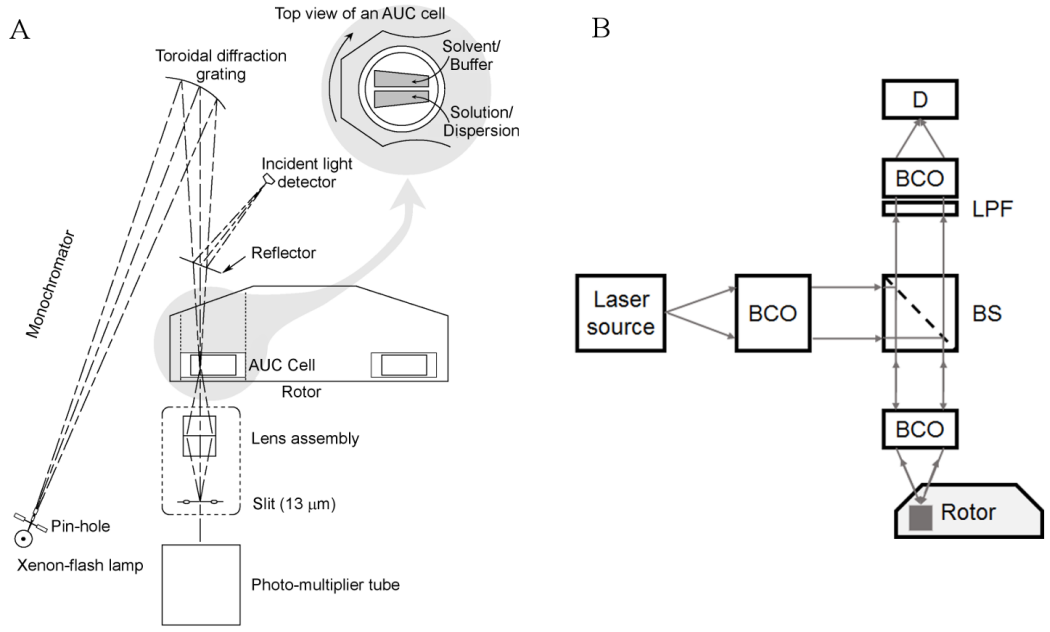

Figure 19. Schematics of the absorbance detection system (A) and the fluorescence detection system (FDS) (B) for analytical ultracentrifugation. BCO, beam collimating assembly; BS, beam splitting unit; LPF, long pass filter; D, detector. Modified from Ralston, 1993 and Kingsbury et al., 2011 [219, 220].

Sedimentation velocity and sedimentation equilibrium experiments

Two types of experiments can be performed with analytical ultracentrifuge, namely the sedimentation velocity (SV) experiment and the sedimentation equilibrium (SE) experiment.

Sedimentation velocity measurement is a precise and absolute method to determine the size distribution of a sample in liquid environment [221]. Samples are subjected to a sufficiently high angular speed to speed up the sedimentation process. The depletion of the solute generates concentration gradient along the radial position, forming sedimentation boundaries (Fig. 20). The movement of the boundary over time contains the information about sedimentation coefficients of particles of interest [222].

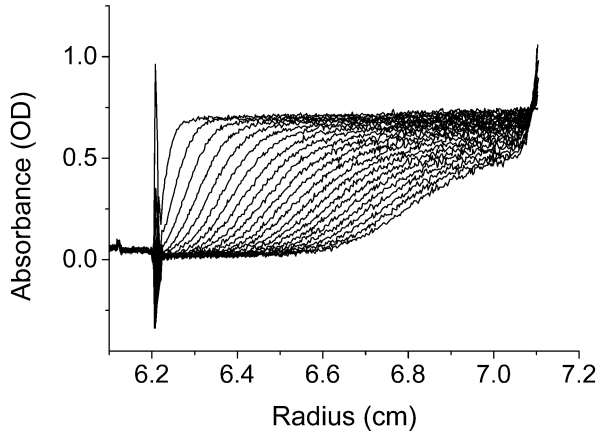

Figure 20. Boundary profiles recorded in a sedimentation velocity experiment. Bovine serum albumin (BSA) was centrifuged at 40,000 rpm, 20 °C. Data was acquired using the absorbance detection system. The sharp spikes on the left and right sides of the profile are the meniscus and bottom, respectively. Sedimentation of particles in solution leads to a gradual depletion of solute from the meniscus, forming sedimentation boundaries. The broadening of the boundary during centrifugation is caused by the diffusion effect.

It should be noted that sedimentation is not the only process during a centrifugation. One could notice the spreading of boundaries during the centrifugation process, which is caused by diffusion [223]. The determination of the sedimentation coefficient is based on evaluating the movement of the sedimentation boundaries. The velocity of the boundary can be described by the following function, assuming that the boundary is sharp:

$$u = dr_b/dt \qquad \text{eq.8}$$

where u refers to the rate of movement of the midpoint of the boundary r_b .

Thus,

$$\mathrm{s} \equiv \frac{u}{\omega^2 r} = \frac{dr_b/dt}{\omega^2 r} \qquad \text{eq.9}$$

This is equal to:

$$\ln\left(\frac{r_b}{r_m}\right) = s\omega^2 r \qquad \text{eq.10}$$

where r_m is the radial position of the meniscus.

The most critical step of a SV experiment is to determine the movement of sedimentation boundaries accurately. In order to quantify the contribution of diffusion to the shape of sedimentation boundaries, the diffusion coefficient, D, has been introduced.

$$D = \frac{RT}{Nf} \qquad \text{eq.11}$$

where R is the gas constant, and T is the absolute temperature. f is the fictional coefficient, and is largely dependent on the size and shape of a particle. It can be described by the Stokes's law:

$$f = 6\pi\eta R_s \qquad \text{eq.12}$$

As can be seen from this equation, f is proportional to the viscosity η of the medium, and the Stokes radius R_s of the particle. The frictional coefficient increases when the particle is getting asymmetrical [224]. The ratio between a measured f and the calculated f_0 based on the molecular weight and specific volume by assuming a smooth spherical shape is termed as frictional ratio f/f_0. The frictional ratio is always above 1. Globular particles usually have f/f_0 at around 1.2. The more elongated and asymmetrical the particle, the higher the f/f_0 will be [217].

Lamm developed an equation (the Lamm equation) to describe sedimentation and diffusion of the solute in a sedimentation velocity measurement [225, 226].

$$\left(\frac{\delta C}{\delta t}\right)_r = -\frac{1}{r}\left\{\frac{\delta}{\delta r}\left[s\omega^2 r^2 - Dr\left(\frac{\delta C}{\delta r}\right)_t\right]\right\} \qquad \text{eq.13}$$

The equation describes how the sedimentation boundaries evolve during the centrifugation process. It also serves as the mathematical basis for evaluating the sedimentation of particles with relatively small *s*-values. The fitting reports *s*-values of the solute under a certain experimental condition ($s_{T,b}$). These values are usually standardized to the *s*-values in pure water at 20 ℃, namely $s_{20,w}$, according to the following equation:

$$s_{20,w} = \frac{(1-\bar{v}\rho)_{20,w}}{(1-\bar{v}\rho)_{T,b}}\frac{\eta_{T,b}}{\eta_{20,w}}s_{T,b} \qquad \text{eq.14}$$

One should be careful when using this model, since it is only valid for dilute samples that are stable within the duration of sedimentation. SV analysis is a powerful method for the determination of the size and shape information of non-interacting species in solution. Besides, SV has also been applied to study self-associating systems and protein-ligand complexation with careful experimental designs [227, 228].

In addition to the continuous distribution Lamm equation analysis, a least-squares direct boundary modeling, ls-g*(*s*), has been developed to analyze non-diffusing particles. The detailed mathematics of this model can be found in Schuck and co-workers' study [229].

The second type of analysis is the sedimentation equilibrium (SE) measurement. Instead of centrifuging samples at a high speed to favor the sedimentation, SE analysis is done at a relatively low speed to obtain an equilibrium between the sedimentation and the back diffusion of the solute [230]. There is no movement of the boundary when the equilibrium is reached (Fig. 21). The molar mass of a solute can be calculated by analyzing the concentration gradient:

$$\frac{d\ln C}{d(r^2)} = \frac{M(1-\bar{v}\rho)\omega^2}{2RT} \qquad \text{eq.15}$$

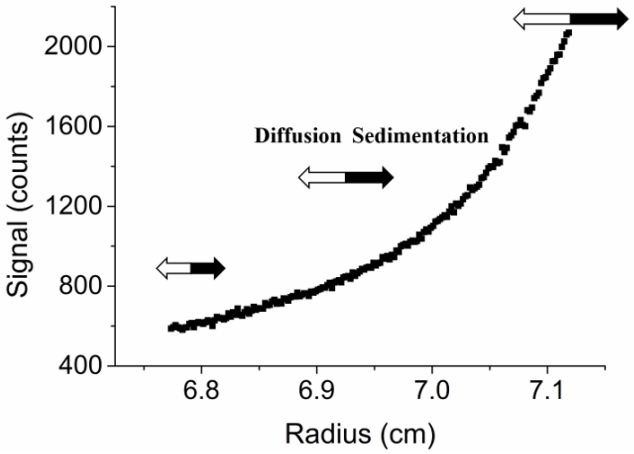

Figure 21. The equilibrium profile in a sedimentation equilibrium experiment using FDS. The concentration of the solute along the radial position increases due to sedimentation (indicated in black arrow). The diffusion of solute due to the concentration gradient counteracts the sedimentation (indicated in open arrow). The concentration distribution is exponential when the sedimentation and diffusion are at equilibrium.

The SE measurement is robust in studying the molecular weights of macromolecules. It can be applied to a wide range of molecular sizes. This method does not require the presence of reference molecules but takes time to establish equilibrium states during the centrifugation [231]. In addition, SE measurements are also applied to evaluate the interaction between two macromolecules, e.g., SE experiments with different loading concentrations at several speeds can be performed to determine the thermodynamic parameters of a protein-ligand interaction system [232].

Currently there are several software packages available for data evaluation. The most commonly used programs include Sedfit [233] developed by Peter Schuck et al, and Ultrascan [234] developed Borries Demeler. The software contains almost all models/algorithms and functions needed for analyzing the sedimentation profiles.

Microscale thermophoresis

Experimental setup

Thermophoresis, also known as Ludwig-Soret effect, was first described by Carl Ludwig in 1856. It describes the directed movement of molecules in response to a thermal gradient. Braun and co-workers quantified for the first time the thermal diffusion of DNA molecules to a temperature gradient in aqueous solution in 2002, which then inspired the development of new techniques to study macromolecular thermophoresis [235]. Later on, Microscale thermophoresis (MST) was introduced by the company NanoTemper Technologies to monitor and quantify the thermophoretic behavior of fluorescent molecules in microscopic temperature gradients.

The instrument (Fig. 22A and B) is composed of optics which can excite fluorescent molecules and collect corresponding emission signals of fluorescent samples within μm area. Currently several types of filter combinations for different fluorophores are available on market [236]. The instrument

uses an infrared (IR) laser with a wavelength of 1480 nm to generate microscopic temperature gradient. The IR laser is focused on a diameter of about 50 µm and creates a temperature difference ΔT of 2~6 °C [236]. All samples are held within a series of capillaries below the IR laser. Molecules move in to or out of the center of the heating zone under IR laser exposure, leading to changes in the concentration of fluorescent molecules at the focus area (Fig. 22C). The fluorescence optics detects the concentration gradient by measuring the change in the fluorescence emission of the focus area. This method employs the advantage of fluorescence labels, requiring sub-nanomolar concentrations of the analyte while maintaining the sensitivity of the measurement [237]. The accessibility of low concentrations of analytes makes the accurate determination of high affinity interactions possible. Up to 16 samples can be measured in a single experiment. In principle, a fixed amount of the fluorescently labeled molecule is titrated with the unlabeled binding partner covering several orders of magnitude of concentrations above and below the dissociation constant. Sometimes buffer additives like BSA or Tween-20 could be used to tackle the surface adsorption of fluorescent molecules, if necessary [236]. MST has been applied to study protein-ligand interactions in biological liquids like blood serum or cell lysates.

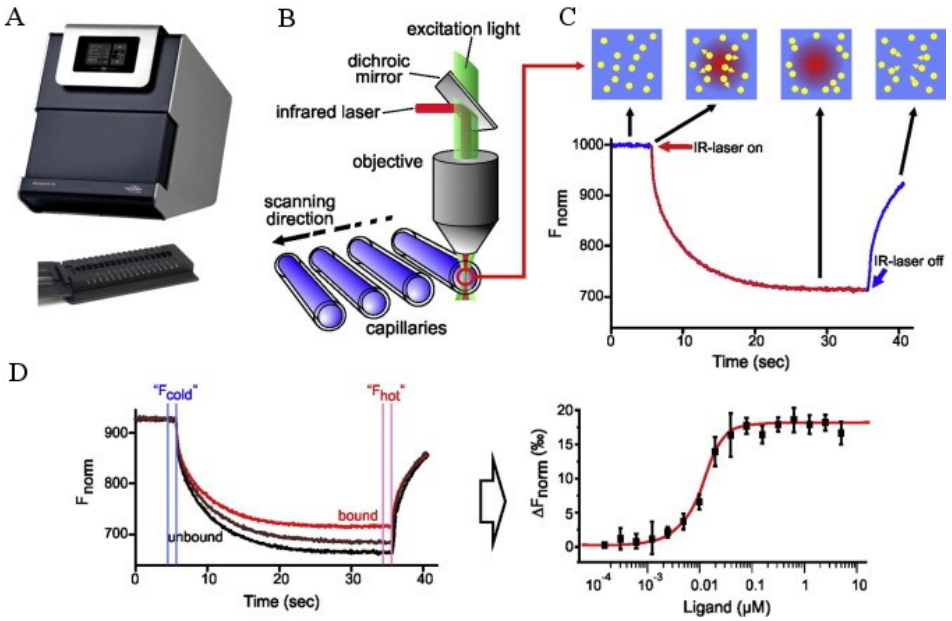

Figure 22. Experimental setup for MST measurements and the data analysis. An MST instrument developed by NanoTemper Technologies with a sample tray which can hold 16 capillaries (A). Fluorescence optics for MST instruments (B). Samples within capillaries are illuminated using excitation light at specific wavelengths and are heated via an infrared laser at the same focus zone. The changes in fluorescence due to local temperature gradient will be recorded with the same objective. Typical fluorescence signals for a MST measurement (C). Particles are evenly distribution during the initial phase without IR laser. Upon heating particles will move out of the heating zone, causing a decrease in fluorescence signals at the same area. Finally, the IR laser will be switched off and particles will return back to the focus area because of mass diffusion. In a binding experiment, target molecule is titrated with different concentrations of the binding partner and time traces of unbound and bound states will be recorded (D). The thermophoresis is expressed by the change in normalized fluorescence (ΔF_{norm}) between cold phase (F_{cold}) and hot phase (F_{hot}). The dissociation constant of the interaction can be determined via fitting the ΔF_{norm}-ligand concentration plot. Taken from Jerabek-Willemsen et al., 2014 [238].

A typical MST experiment includes three phases composed of a set of microscopic events. The first phase is the measurement of the baseline fluorescence of all samples when there is no IR laser illumination. Molecules should be homogeneously distributed in the capillary and this phase lasts about 5 s, depending on the experimental setup. The IR laser will then be ignited to produce local heating. The sudden heating within the first second causes a temperature jump (T-jump), which induces a rapid change in fluorophore properties due to fast temperature changes. Upon the activation of the IR laser, molecules start to move within the capillary. The thermophoretic movement depends on the size, charge, conformation or hydration shell of the molecules [239]. The interaction between two molecules will alter at least one of these parameters and will lead to a different thermophoretic behavior [240]. The IR laser will keep working for 30 s so that the thermophoresis can reach a steady state. It will subsequently be shut down and molecules begin to move back to the focus point, known as "back diffusion" driven by the mass diffusion. The whole time traces for all samples are recorded and analyzed to characterize the binding event (Fig. 22D).

Theoretical background

The thermophoresis can be described as a molecular flow driven by a temperature gradient:

$$j = -cD_T \Delta T \qquad \text{eq.16}$$

In this function, j represents the molecular flow, c is the concentration of a molecule, D_T refers to the thermal diffusion coefficient, and T is the temperature.

However, there is also the mass diffusion that opposes the thermophoresis:

$$j = -D\Delta c \qquad \text{eq.17}$$

where D is the diffusion coefficient.

The concentration change induced by the thermal gradient can be expressed by the Soret coefficient:

$$S_T = \frac{D_T}{D} \qquad \text{eq.18}$$

The Soret coefficient may be positive or negative depending on the movement of molecule under temperature gradient (to the hot area or to the cold area) [241].

The concentration change when the system reaches steady state can be given by:

$$\frac{c_{hot}}{c_{cold}} = \exp(-S_T \Delta T) \qquad \text{eq.19}$$

In this equation, c_{hot} and c_{cold} stand for the concentrations in the hot area and cold area, respectively.

A more detailed description of the Soret coefficient can be expressed by the following equation [242]:

$$S_T = \frac{A}{k_B T}\left[-\Delta s_{hyd}(T) + \frac{\beta \sigma_{eff}^2}{4\varepsilon\varepsilon_{0T}} \times \lambda_{DH}\right] \qquad \text{eq.20}$$

where A defines the area of molecular surface, k_B is the Boltzmann constant, and T is the temperature of the system. Δs_{hyd} is the hydration shell effect, σ_{eff} is the effective charge of the

molecule in solution, ε is the dielectric constant, λ_{DH} represents the Debye-Hückel screening length, and β is the temperature derivative of ε. This equation provides us with an overview on what factors may influence the thermophoresis.

The quantification of MST data is relatively straightforward. The normalized fluorescence F_{norm}, which is defined by the following equation, is used for data analysis:

$$F_{norm} = \frac{F_{hot}}{F_{cold}} \quad \text{eq.21}$$

where F_{hot} means the fluorescence in the hot phase, and F_{cold} stands for the fluorescence in the cold phase.

As the titration takes place, the fraction of bound (FB) analytes increases, resulting in a change in the normalized fluorescence F_{norm}.

$$F_{norm} = (1 - FB)F_{norm\ unbound} + (FB)F_{norm\ bound} \quad \text{eq.22}$$

The fluorescence of the sample is determined by two factors. First, the concentration of the fluorescent molecules within the focus point; second, the fluorescence change induced by the temperature. Thus the F_{norm} can further be expressed by:

$$F_{norm} = \exp(-S_T \Delta T) + \frac{\delta F}{\delta T} T \approx 1 + (\frac{\delta F}{\delta T} - S_T)T \quad \text{eq.23}$$

where $\frac{\delta F}{\delta T}$ in the equation denotes the temperature dependence of the fluorophore.

MST data can be analyzed by two different models which are incorporated into the software. The first model is the Langmuir model dealing with the 1:1 binding reaction.

$$A + B \rightleftharpoons AB$$

A and B are binding partners and AB is the heterocomplex. The dissociation constant can be defined by:

$$K_D = \frac{[A]_{free}[B]_{free}}{[AB]} \quad \text{eq.24}$$

It is usually hard to determine the free concentrations of the binding partners, however this can be deduced from the loading concentrations.

$$[A] = [A]_{free} + [AB]$$

$$[B] = [B]_{free} + [AB]$$

Thus,

$$K_D = \frac{([A]-[AB])([B]-[AB])}{[AB]} \quad \text{eq.25}$$

Assuming that A is the ligand, and B is the target molecule with fluorescent tag, the fraction of the bound FB can be expressed by the following equation:

$$FB = \frac{[AB]}{[B]} = \frac{[A]+[B]+K_D-\sqrt{([A]+[B]+K_D)^2-4[AB]}}{2[B]} \quad \text{eq.26}$$

The FB is now a function of $[A]$, $[B]$ and K_D. And K_D is the single parameter which will be fitted.

In case the Langmuir model is not appropriate to describe the obtained data, a more complex model is available for data analysis. The Hill model is used to evaluate cooperative binding and gives us the EC_{50} value as well as the Hill coefficient n.

$$A + nB \rightleftharpoons AB_n$$

In the cooperative binding reaction, the FB is given by:

$$FB = \frac{1}{(1+EC_{50}/[B])} \quad \text{eq.27}$$

MST is an immobilization-free method with high sensitivity and low sample consumption. The application of fluorescently labeled Aβ42 at nanomolar concentrations in the MST measurement can significantly slow down the self-aggregation of Aβ42, which can facilitate the study on the interaction between Aβ42 monomers and ligands.

Brief introductions on CD and AFM

Circular dichroism

Circular dichroism spectroscopy is a popular technique to determine structural properties of a biological sample in its liquid state. The technique utilizes the so-called circularly polarized light generated by special prisms or filters. The plane polarized light can be viewed as a combination of two circularly polarized lights with identical magnitudes [243], one of the circularly polarized lights rotating clockwise (right handed, R), while the other light rotating counter-clockwise (left handed, L). A molecule may have different absorbance toward the right handed and left handed circularly polarized lights, which is termed as circular dichroism [244]. Only optically active or chiral molecules have this property. The structural characteristics of a molecule will display corresponding spectral bands in CD spectroscopy, which can be used to deduce the structural information of the molecule of interest [245]. The most common application of CD spectroscopy is to determine the secondary structure of biomolecules like proteins. The absorption of a protein at wavelength below 240 nm originates mainly from the peptide bond [246]. Different secondary structures exhibit different but characteristic spectral properties in the CD measurement (Fig. 23).

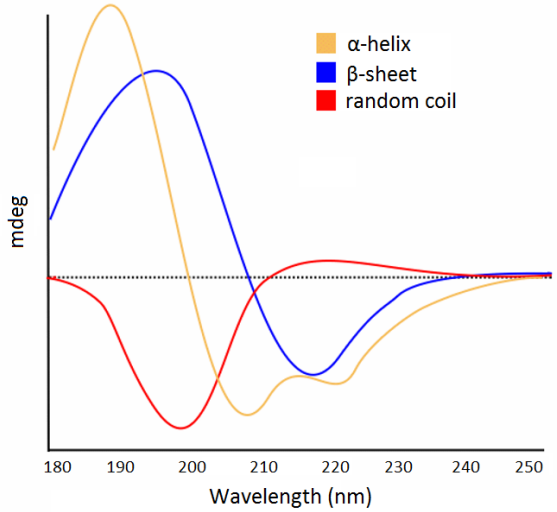

Figure 23. CD spectra for different secondary structure elements present in protein samples. Modified from http://www.proteinchemist.com/cd/cdspec.html [247].

In addition to determine the secondary structure of a protein in its native state, CD is also applied to monitor protein unfolding and aggregation processes. It offers us a dynamic view on how the secondary structure of the target protein changes during the folding and unfolding processes or in the presence of binding partners [248]. There are a number of algorithms available for the deconvolution of CD spectra based on reference datasets to evaluate the secondary structure compositions (fractions of helices, β-strand, β-turn and unordered structures) [249]. This can help us quantitatively analyze in detail, for instance, how protein-ligand interaction influences the secondary structural changes.

Atomic force microscopy

The advances in scanning probe microscopy (SPM) have provided us with the possibility to study the morphology of macromolecules at nanometer levels. Atomic force microscopy is probably one of the most widely used SPM techniques in the field of imaging amyloid structures. Initially developed by Binnig et al. in 1986, AFM utilizes a sharp tip (radius 1-20 nm) mounted on a cantilever to detect changes in the forces following the interaction between the tip and biological sample (Fig. 24) [250].

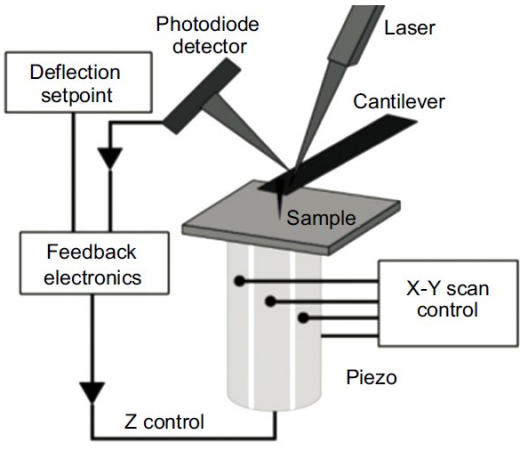

Atomic force microscope

Figure 24. Schematic of the atomic force microscopy. Taken from Ruggeri et al., 2016 [251].

During the measurement, the deflection of the cantilever caused by the interaction with the sample surface can be monitored by changes in the position of the reflected laser beam on a photodiode detector. Therefore the topography of a sample can be obtained based on processing the signals from the feedback electronics.

The force responsible for the interaction between the tip and a biological sample is generally the electromagnetic force (Fig. 25). While there are also other types of forces mediating the interaction, such as the van der Waals force or electrostatic force [251].

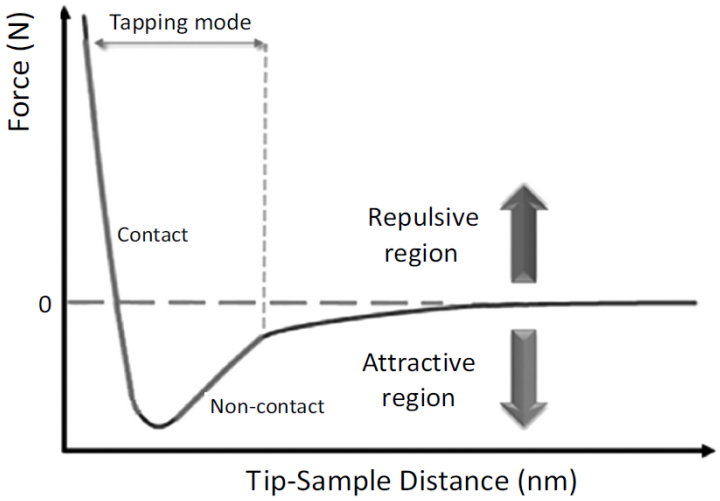

Figure 25. The force involved in the tip-sample interaction and its relationship with the distance during an AFM measurement. Taken from Ruggeri et al., 2016 [251].

In addition to study the end product of Aβ fibrillation, the intermediate species during the aggregation process, such as oligomers and protofibrils, are also identifiable using AFM imaging (Fig. 14). Mastrangelo et al. observed in their study that low molecular weight Aβ42 oligomers are relatively compact and have ordered structures. These species show constant height at 1-3 nm [252] and the lengths (or width) lie within 5 to 10 nm. Protofibrils are usually ribbon shaped with heights approximate to 1.5 nm and the width at 6 nm to 8 nm. The average length of protofibrils (>40 nm) is much longer than that of Aβ42 oligomers [252, 253]. The height of Aβ42 fibrils varies depending on detailed microscopic structures [253]. Smooth fibrils have a height of about 5 nm, while the heights of nodular fibrils are about 11 nm at the center of nodules and about 5 nm at the internodal points [253]. The morphological information obtained from AFM imaging is usually complemented by conventional ThT assays such that the aggregation of amyloid proteins can be characterized comprehensively.

Aim of the present work

The aggregation of Aβ proteins in the brain is an important hallmark of Alzheimer's disease. The early occurrence of Aβ aggregation related pathologies also highlights the significance of deciphering factors that may influence the aggregation process of Aβ and developing strategies that can modulate Aβ aggregation. Among all forms of Aβ species, toxic assemblies such as soluble oligomers have been found to be the most detrimental species to the brain. The present study focused on investigating the interaction between Aβ proteins and several ligands. In particular, the interaction between Aβ42 and D-enantiomeric peptides will be elaborated. We are interested in answering the following questions: 1) how Zinc ions (Zn^{2+}) influence the aggregation of Aβ42 at stoichiometric concentration; 2) whether and how two D-enantiomeric peptides, namely D3 and RD2, interact with Aβ proteins, and how does the interaction affect the fibril formation of Aβ42; 3) Do these D-enantiomeric peptides form complexes with Aβ monomers. The thesis contains four chapters that describe the characterization of the interaction between each binding partner and Aβ proteins.

In Chapter I, the effect of Zinc ions (Zn^{2+}) on the aggregation of Aβ42 was re-examined using analytical ultracentrifugation and other techniques. The accumulation of Zn^{2+} in Aβ plaques has long been documented and investigated, while the influence of Zn^{2+} on the aggregation process of Aβ42 remains controversial. We studied how stoichiometric Zn^{2+} alters the fibrillation of Aβ42 by analyzing size distributions of samples in the presence or absence of equimolar Zn^{2+} at different incubation time points. In combination with ThT assays, CD spectroscopy and AFM, we collected and interpreted kinetic and hydrodynamic information about the interaction between Zn^{2+} and Aβ.

Chapter II deals with the interaction between the all-D-enantiomeric peptide D3 and Aβ42. D3 has been demonstrated to be beneficial to the cognitive ability of AD mouse models by removing toxic Aβ oligomers, while the detailed mechanism of actions are still elusive. The affinity between D3 and Aβ42 was re-evaluated using microscale thermophoresis. The complex formation between D3 and Aβ42 monomers was analyzed via analytical ultracentrifugation equipped with a fluorescence detection system and molecular dynamics simulation. The effect of substoichiometric D3 on the aggregation and structural conversion of Aβ42 was explored using ThT assay, CD measurements and AFM imaging. By determining the size and shape of the complexes we aim to elucidate the early events underlying the interaction between D3 and Aβ42.

In Chapter III, the optimized D-peptide RD2 was investigated. RD2 has been shown to be very effective in restoring the cognitive function of transgenic AD mouse models by eliminating toxic Aβ assemblies. We carried out biophysical characterizations to determine whether RD2 interacts with Aβ42 monomers and how the interaction influences the overall aggregation process of Aβ42. In addition, we sought to compare the difference between D3 and RD2 regarding their mechanisms of actions based on our results.

Chapter IV serves as a methodological validation of the application of analytical ultracentrifugation (AUC) and microscale thermophoresis (MST) in the study of highly flexible and aggregation-prone Aβ42 monomers and ligands. In this chapter, three monoclonal antibodies against Aβ (6E10, 4G8 and 12F4) were chosen as binding partners. We determined the size and shape information of Aβ42-

antibody complexes using fluorescence based AUC. The binding affinities were evaluated based on the sedimentation coefficient distribution analysis and microscale thermophoresis. The binding parameters were compared with reported values from other techniques. The successful characterization of the interaction of a well-established system via these methods will substantiate the whole study.

Chapter I
Revisiting the effect of Zn^{2+} on the aggregation of Aβ42

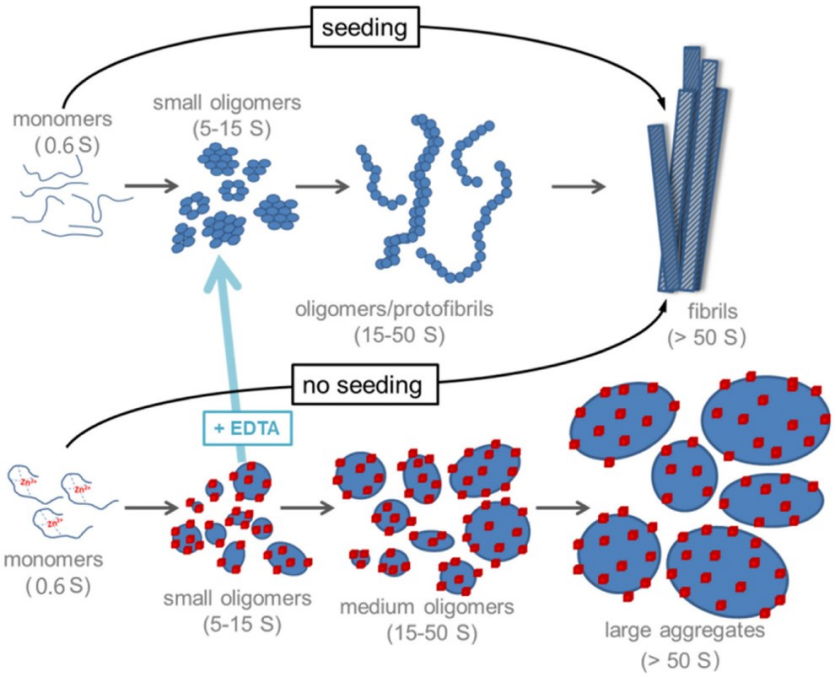

Abstract

The abnormal aggregation of amyloid β (Aβ) peptides in the brain has been recognized as a central event in Alzheimer's disease (AD). Divalent metal ions such as Zn^{2+} have been shown to be closely involved in modulating Aβ self-association. Although the link between Zn^{2+} dyshomeostasis and brain Aβ deposition has been established, the effect of Zn^{2+} on the aggregation of Aβ is still incompletely clarified. By combining analytical ultracentrifugation (AUC), circular dichroism (CD) spectroscopy, thioflavin T (ThT) assay and atomic force microscopy (AFM) imaging, we analyzed the impact of stoichiometric Zn^{2+} on the aggregation process of Aβ42, the main toxic isoform of Aβ species in the brain. Aβ42 aggregates found in the presence of Zn^{2+} were smaller in size, non-fibrillary and showed less β-sheet structures than aggregates formed in absence of Zn^{2+}. AUC showed that Zn^{2+} was capable of retaining monomeric Aβ42 in solution. Zn^{2+} chelation by EDTA totally reversed the inhibitory effect of Zn^{2+} on Aβ42 fibrillation. Our results provide further evidence that Zn^{2+} shifts the self-association of Aβ42 toward a non-fibrillary pathway by interfering with the aggregation process at multiple levels.

This chapter was adapted from the following publication:

Zhang T, Pauly T, Nagel-Steger L. Stoichiometric Zn^{2+} interferes with the self-association of Aβ42: Insights from size distribution analysis. *Int J Biol Macromol*. 2018 Jul 1; 113:631-639. DOI: 10.1016/j.ijbiomac.2018.02.123. The graph was taken from figure 6 of the abovementioned publication.

Introduction

Alzheimer's disease (AD) is a devastating neurodegenerative disease which is clinically characterized by progressive and irreversible decline in cognitive abilities among the elderly [9]. Currently there are approximately 40 million people suffering from AD and the number of patients keeps rising [9]. Although extensive research is being performed in the field of AD, important issues regarding the underlying pathomechanisms are still not understood.

The major neuropathological changes of AD include abnormal accumulation of amyloid β (Aβ) proteins in the brain parenchyma and the formation of neurofibrillary tangles in neurons [254]. The amyloidogenic processing of amyloid precursor protein (APP) leads to the generation of Aβ species. Aβ42 and Aβ40 are two predominant products during this process [81]. The self-association of Aβ into oligomers and fibrils has been demonstrated to be a key event in disease progression [255]. Dysregulation of Aβ metabolism happens in the early stage of AD and might act as an upstream factor of other neuropathological changes, such as tau hyperphosphorylation, synaptic toxicity and oxidative stress [256, 257]. The central role of Aβ in the pathogenesis of AD highlights the importance of clarifying the mechanisms by which Aβ peptides aggregate in physiological environment. Zn^{2+} belongs to the transition metal family and is the second most abundant trace element in human body [258]. Zn^{2+} plays multiple roles in regulating protein structures and functions, as well as in maintaining synaptic transmission [259]. Evidence from both in vivo and in vitro studies has established a close connection between Zn^{2+} dyshomeostasis and Aβ deposition [260]. Zn^{2+} was found to accumulate at Aβ plaques up to 1 mM, nevertheless, the concentration of free Zn^{2+} in the brain is largely dependent on synaptic activity [261]. The amount of free Zn^{2+} in synaptic cleft will rise from several nanomolar to around 300 μM during neurotransmitter release [262]. The temporal and spatial distribution patterns of Zn^{2+} are related to the aberrant accumulation and the synaptic toxicity of Aβ species in the synaptic cleft [263].

Despite substantial evidence that Zn^{2+} dysregulation is associated with Aβ deposition, the interaction between Aβ peptides and Zn^{2+} is not fully understood [160]. Current evidence obtained from NMR and spectroscopic experiments proposed that the N-terminal part of Aβ contains metal ion binding sites and is responsible for complexing metal ions like Zn^{2+} and Cu^{2+} [162, 170, 264]. For example, it has been reported that residues at position 1 (Asp), 3 (Glu), 7 (Asp), 11 (Glu), and three His residues (position 6, 13, 14) are involved in the interaction between Aβ and Zn^{2+} [162]. While earlier studies reported one high affinity binding site with K_d of 160 nM in combination with two lower affinity binding sites with K_D in the range of 5 μM [265], later work confirms a 1:1 stoichiometry with K_D values in the range of 1 μM to 20 μM, depending on the experimental setup [160, 266]. Tõugu *et al.* determined an even higher K_d of 60 μM for Zn^{2+} binding specifically to monomeric Aβ40 [267]. The binding affinity of Aβ to Zn^{2+} is much lower in comparison to Cu^{2+}, which yields a K_D value of ~10^{-10} M for the interaction with Aβ [160]. Regardless of the moderate binding affinity, it is commonly agreed that Zn^{2+} is capable of forming a tetrahedral complex with Aβ peptide at 1:1 stoichiometry [162, 264]. The impact of Zn^{2+} on the aggregation process of Aβ remains controversial. Some studies found that Zn^{2+} treatment led to the formation of off-pathway, amorphous aggregates that were non-toxic to neurons [165, 268], while other research showed that Zn^{2+} promoted the generation of toxic

oligomers and stabilized these harmful Aβ species [164, 167, 269]. In addition, a recent study discovered that Zn^{2+} undergoes rapid exchange between different Aβ entities, suggesting that even trace amounts of Zn^{2+} could have a profound influence on Aβ assembly [270]. Apart from the current knowledge, one of the remaining questions of Aβ-Zn^{2+} interaction is: what is the composition and the size distribution of Aβ aggregates formed over time in the presence of Zn^{2+}?

The present study aimed to investigate the effect of Zn^{2+} on the self-association of Aβ42 through combining complementary approaches. In detail, the impact of Zn^{2+} on the structural transition, fibrillation and morphology of Aβ42 were characterized. In particular, sedimentation velocity analysis was performed to better clarify size distributions of various Aβ species formed in the absence or presence of Zn^{2+}. We also sought to elucidate potential mechanisms underlying Aβ-Zn^{2+} interaction on the basis of the presented data.

Materials and Methods

Chemicals and peptides

Synthetic human Aβ42 (Catalog No. H-1368) was purchased from Bachem (Weil am Rhein, Germany). Peptides were predissolved in 1, 1, 1, 3, 3, 3-Hexafluoro-2-propanol (HFIP) and divided into aliquots. All aliquots were further lyophilized and stored at -80 °C before use. 10 mM sodium phosphate buffer or MOPS buffer (both at pH 7.4) was prepared to dissolve Aβ42 aliquots. Zinc chloride ($ZnCl_2$) and EDTA disodium salt were commercially available and were used as Zn^{2+} source and chelator, respectively. To prepare stock solutions they were dissolved in distilled water at 1 mM final concentrations.

Circular dichroism spectroscopy

The secondary structures of Aβ samples were monitored by far-UV CD spectroscopy (Jasco J-815, Tokyo, Japan). Aβ42 aliquots were dissolved either in sodium phosphate buffer (10 mM, pH 7.4), or in sodium phosphate buffer with 40 μM $ZnCl_2$, or in sodium phosphate buffer with 40 μM $ZnCl_2$ and 40 μM EDTA, respectively. The final concentration of Aβ42 was 40 μM. Samples were incubated at 20 °C during the whole measurement. CD spectra for each sample were recorded between 190 nm and 260 nm at 0 h, 8 h, 24 h, 48 h, 72 h and 120 h (or 122 h), using a 1 mm path-length cuvette with a volume of 200 μl. Scans were carried out at a data pitch of 0.2 nm and a speed of 50 nm/min. Final spectra were averaged on the basis of 10 consecutive scans and the buffer spectra were subtracted accordingly. To evaluate the transition kinetics of secondary structures, the mean residual ellipticity (MRE) values at 198 nm, which are used to characterize protein secondary structures[245], were plotted against the incubation time. According to the reported solubility of zinc phosphate in aqueous solutions [271], 40 μM Zn^{2+} can be assumed soluble in 10 mM sodium phosphate buffer.

Turbidity measurement

The turbidity of all samples was determined by measuring the absorbance at 405 nm using a UV-Vis spectrophotometer (Jasco V-650, Tokyo, Japan). Briefly, sample solutions containing 40 μM Aβ42 alone, 40 μM Aβ42 plus equimolar Zn^{2+} and 40 μM Aβ42 with equimolar Zn^{2+} and EDTA were

incubated at 20 °C for 120 hours. The absorbance values of all samples at 405 nm were obtained by recording the spectra between 200 nm and 500 nm at 0 h, 8 h, 24 h, 48 h, 72 h and 120 h, respectively. At each time point sample solutions were shortly pipetted up and down for mixing before 80 µl solution was withdrawn and loaded into a 1 cm cuvette. The turbidity values were plotted against the incubation time to monitor changes of solution properties over time. All samples were prepared in duplicate.

Preparation of seeds

Seeds are fragments obtained from mature fibrils, which upon addition to solutions of the monomeric precursor cause shortening of the lag time. This effect is typically determined in a thioflavin T assay. Aβ42 seeds formed either in the absence or presence of Zn^{2+} were prepared as previously described [272], with minor modifications. In brief, 40 µM Aβ42 was incubated with or without the presence of equimolar Zn^{2+} at 20 °C in sodium phosphate buffer (10 mM, pH 7.4) for 96 h. Samples were then sonicated in an ice cooled ultrasonic water bath for 1 h.

Thioflavin T assay

The 1 mM thioflavin T (ThT) stock solution was prepared in distilled water and filtered before use. For samples without seed treatment, 40 µM Aβ42 with or without equimolar Zn^{2+} or EDTA were incubated in sodium phosphate buffer (10 mM, pH 7.4) at 20 °C. For samples treated with seeds, 5 µl of either Zn^{2+}-free or Zn^{2+}-containing Aβ42 seeds (hereafter referred to as Aβ42 seeds and Aβ42-Zn seeds, respectively) were added into 40 µM Aβ42 solutions with or without equimolar Zn^{2+} to achieve a final seed concentration of 1 µM, given in monomer equivalents. The working concentration of ThT in all samples was 5 µM. All samples were then pipetted into a 96-well microplate (Nunc, Darmstadt, Germany), with 200 µl solution in each well. The fluorescence was measured with a microplate reader (Infinite M200, Tecan, Männedorf, Switzerland) every 30 min. The excitation and emission wavelengths for the measurement were 445 nm and 485 nm, respectively. All samples were prepared in duplicate.

Analytical ultracentrifugation

Sedimentation velocity centrifugation experiments were performed using a Beckman Optima XL-A centrifuge (Beckman-Coulter, Brea, CA, USA) equipped with an absorbance detection system and an eight-hole rotor. 40 µM Aβ42 samples were incubated in the absence or presence of equimolar Zn^{2+} either in sodium phosphate buffer or MOPS buffer (10 mM, pH 7.4) at 20 °C for 0 h, 24 h and 72 h, respectively. Additionally, 40 µM Aβ42 treated with 4 µM Zn^{2+} (0.1 equimolar) in MOPS buffer was analyzed under the same experimental set-up. The low ionic strength conditions were chosen in order to constrain the Aβ42 aggregation. Potential side effects under sedimentation conditions, i.e. primary charge effects, which would lead to reduced *s*-values, could not be observed. Samples (400 µl) were filled into 12-mm aluminum cells with quartz glass windows. All measurements were conducted at 20 °C. The centrifugation speeds and detection wavelengths for each experiment are specified in Table 1. To better characterize samples incubated for 72 hours, which contained a rather broad size distribution of Aβ aggregates, we performed two runs of centrifugation with the same samples beginning at a low speed suitable for the detection of large aggregates, followed by the second run at elevated speed for the smaller aggregates. Note that all

samples were placed in still for about 1.5 h prior to the second run, to equilibrate the temperature. The software package Sedfit (Version 15.01b) was used to evaluate all datasets [233]. More specifically, continuous distribution ($c(s)$) Lamm equation model was applied to analyze data collected at 0 h, 24 h and 72 h (2nd run) [273]. Since aggregates analyzed at the low speed in the first run were large enough to justify neglecting the effect of diffusional broadening on the boundary shape, the ls-g*(s) method was applied to evaluate data acquired from the first round of centrifugation at 72 h [229]. Fitting parameters (Table S1), including the partial specific volume of Aβ42, buffer density and viscosity at 20 °C, were calculated with Sednterp (Version 20130813BETA). The graphical output was created using GUSSI (Version 1.2.1) [274] and all reported s-values were corrected to $s_{20,w}$-values (sedimentation coefficients in water at 20 °C).

Table 1. Experimental conditions for sedimentation velocity analysis in the present study, all measurements were performed at 20 °C.

Aβ sample	Speed information		Wavelength (nm)
	revolutions per minute (rpm)	relative centrifugal force (×g)	
0 h	50,000	201,600	230
24 h	35,000	98,784	230
72 h [a]	15,000	18,144	230
72 h [b]	40,000	129,024	210

[a] first run performed at low speed for the detection of large aggregates.

[b] second run performed after remixing of sample cells at high speed to resolve the smaller species.

Atomic force microscopy

Atomic force microscopy imaging was carried out by using a JPK AFM microscope (JPK Instruments AG, Berlin, Germany) in AC mode. Samples of 40 μM Aβ42 with or without equimolar Zn^{2+} treatment were incubated in sodium phosphate buffer (10 mM, pH 7.4) at 20 °C for 72 hours. Samples were then centrifuged at 16,000×g at 20 °C for 30 min in order to enrich the aggregates at the bottom of the tube. Then 50 μl sample from the bottom part of the tube were collected and pipetted onto freshly cleaved mica surface. After 30 min of incubation samples on mica were rinsed with distilled water for three times and were subsequently dried with nitrogen gas. The imaging was conducted in air using silicon cantilevers (OMCL AC160 TS, Olympus) with a nominal tip diameter of 7 nm at a line rate of 0.5 Hz with tip velocity 2.39 μm/s. All images were processed with JPKSPM data processing software (JPK Instruments AG, Berlin, Germany). ImageJ implemented with ridge detection plugin was applied to evaluate the length of particles in both samples [275]. Final histograms showing the size distributions were generated by OriginPro (version 9.0, OriginLab Cooperation, MA, US).

Results

The influence of stoichiometric Zn^{2+} on the evolution of aggregate size distributions of Aβ42 was studied. All experiments were performed in 10 mM sodium phosphate buffer, except for the AUC measurements, in which 10 mM MOPS buffer was also tested additionally. Sodium phosphate was chosen because of its high transparency in the far UV range. The amount of 40 μM Zn^{2+} is assessed to be soluble in 10 mM sodium phosphate buffer [271] and would not influence the measurement.

Zn^{2+} treatment accelerated the structural transition of Aβ42, but resulted in decreased β-sheet structure content

During amyloid formation Aβ proteins accumulate β-sheet structures which finally leads to the transformation into a cross-β-sheet architecture [276]. Therefore, the measurement of β-sheet content of a protein sample over time is one option for monitoring the progress of amyloid formation. To investigate the effect of Zn^{2+} on the structural transition of Aβ42, the secondary structures of peptides at different time points were measured using CD spectroscopy. The conversion kinetics was described by plotting MRE values obtained at 198 nm, which is characteristic for disordered conformation, against the incubation time. Zn^{2+}-free Aβ42 samples transformed gradually from random coil to β-sheet structure (Fig. 26A), showing a typical transition pattern of Aβ peptides in aqueous solution [277, 278]. The inflection point of the transition is located between 40 and 50 hours for 40 μM Aβ42 under our solvent conditions at 20 °C. The CD spectrum of Zn^{2+}-free Aβ42 sample remained stable after 72 hours for at least additional 48 hours of incubation. As shown in Fig. 26B, the ellipticity at 198 nm for Zn^{2+}-containing Aβ42 sample at 0 h decreased by about 40 %, as compared to Zn^{2+}-free sample. In addition to this, we found that the secondary structure of Zn^{2+}-containing samples reached an equilibrium state after 24 h. The final MRE value at 217 nm of peptides treated with Zn^{2+} was only about 42 % of that obtained in Zn^{2+}-free samples, suggesting a much lower content of β-sheet structures in solution. The decrease in the ellipticity in Zn^{2+}-containing samples was not caused by Zn^{2+} induced precipitation of Aβ42 peptides, as evidenced by six-fold lower turbidity values of the Zn^{2+}-containing sample compared to the Zn^{2+}-free sample (Fig. S1). Next, it was tested whether Zn^{2+} chelation by EDTA could block the effect of Zn^{2+} on the conformational transition of Aβ42. 40 μM EDTA was introduced into Zn^{2+}-containing samples either directly at the beginning or delayed after 23 hours of incubation. The spectra and the transition kinetics (Fig. 26C, D and Fig. 27) demonstrated that EDTA completely restored the aggregation process, further confirming the influence of Zn^{2+} on the structural transformation of Aβ42. CD analysis revealed that Zn^{2+} accelerated the structural transition of Aβ42 while limited the formation of β-sheet structures, and that this conformational influence can be reversed by Zn^{2+} chelation.

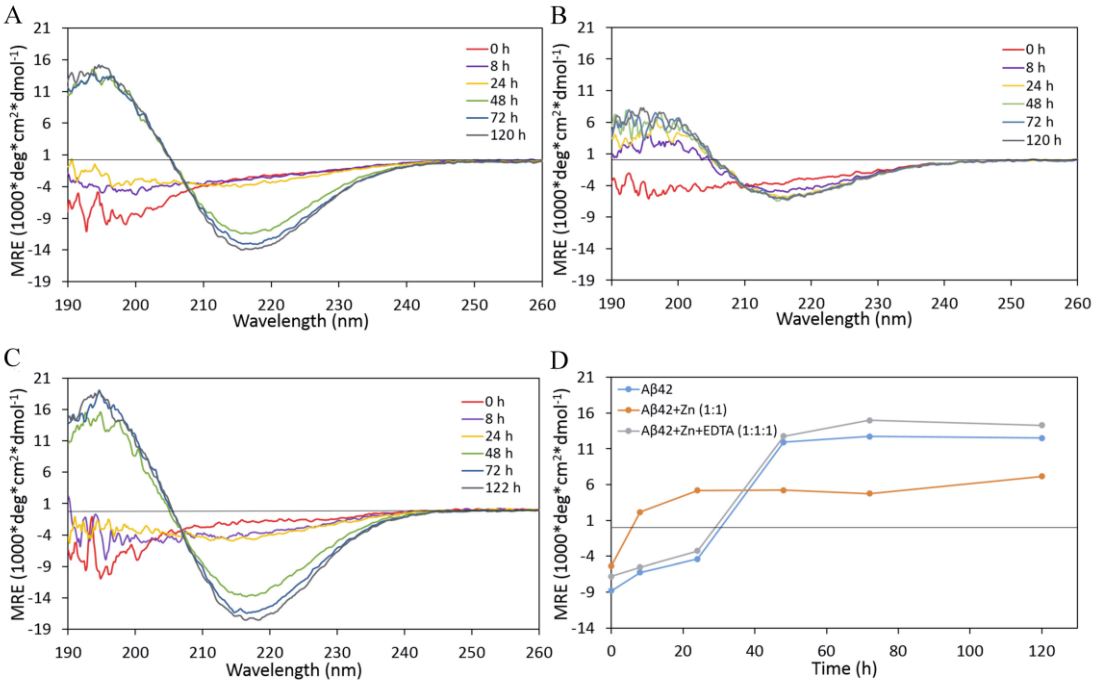

Figure 26. Zn^{2+} treatment accelerated the structural transition of Aβ42 while resulted in less β-sheet structures. CD spectra of 40 μM Aβ42 alone (A), 40 μM Aβ42 with equimolar Zn^{2+} (B) and 40 μM Aβ42 co-incubated with equimolar Zn^{2+} and EDTA (C), showing the structural conversion of Aβ42 under different treatments over time. EDTA was added from the beginning of the incubation. The transition kinetics of all three samples presented as MRE values obtained at 198 nm over time are shown in D. Measurements were performed in 10 mM sodium phosphate buffer at 20 °C.

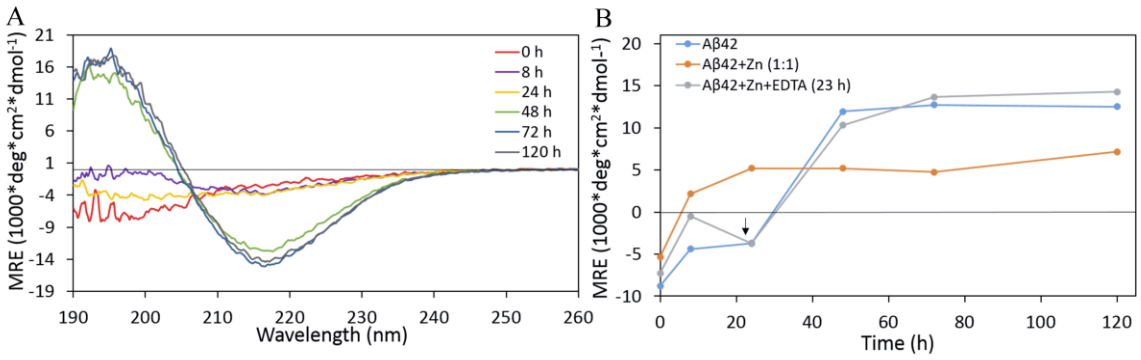

Figure 27. Addition of EDTA in Zn^{2+}-containing Aβ42 sample after 23 hours of incubation can restore the structural transition. CD spectra of Zn^{2+}-containing Aβ42 sample with 40 μM EDTA addition at 23 h was shown in A. The transition kinetics is expressed by plotting the MRE values at 198 nm versus the incubation time (B). The black arrow indicates the addition of 40 μM EDTA.

The presence of Zn^{2+} suppressed Aβ42 fibrillization by interfering with the aggregation process

Aβ peptides adopting β-sheet structures are considered to be building blocks for amyloid fibrils that are capable of enhancing the fluorescence emission of thioflavin T (ThT) upon binding [136]. This property of ThT has been broadly utilized to analyze amyloid fibril formation. It is generally accepted that the self-association of Aβ42 from unordered structures to fibrils includes a lag phase, a rapid growth phase and the final plateau phase, and the overall fibrillation process can be tracked by

measuring the ThT fluorescence [126]. As displayed in Fig. 28, 40 μM Aβ42 without Zn^{2+} treatment displayed sigmoidal-like aggregation kinetics and the fluorescence reached a plateau after 24 hours, indicating the accumulation of Aβ fibrils in solution. However, Aβ42 incubated with equimolar Zn^{2+} exhibited a different aggregation kinetics that was featured by a loss of lag phase and low final fluorescence intensity, indicating that peptides might aggregate rapidly but the further formation of amyloid fibrils was inhibited in the presence of Zn^{2+}. This is in agreement with the reduced amount of β-sheet structure. Again, the addition of 40 μM EDTA to Zn^{2+}-containing samples was sufficient to neutralize the effect of Zn^{2+} as visible from the regained sigmoidal shape of the aggregation kinetics of Aβ42.

To address how Zn^{2+} influences the aggregation process, we performed seeded aggregation kinetics analysis comparing seeds prepared from either pre-incubated Aβ42 or Aβ42 with Zn^{2+}. As shown in Fig. 28, Aβ42 samples incubated with 1 μM Aβ42 seeds had no lag phase anymore and the ThT fluorescence rapidly reached the plateau value, indicating that the prepared Aβ42 seeds were indeed capable of accelerating amyloid formation. However, addition of 1 μM Aβ42 seeds to 40 μM Aβ42 containing Zn^{2+} reached a much lower plateau fluorescence value as compared to either Aβ42 alone or Aβ42 containing 1 μM Aβ42 seeds, suggesting that Zn^{2+} effectively canceled the susceptibility of Aβ42 towards seeding. Interestingly, materials prepared after the same protocol from pre-incubated equimolar Aβ42 and Zn^{2+} mixtures appeared to be incompetent in seeding the amyloid formation, as the ThT kinetics of samples treated with Aβ42-Zn seeds were comparable to those of the seed-free counterparts. Results from the ThT assay led us to conclude that stoichiometric Zn^{2+} not only influenced the lag phase, but also interfered with the elongation process.

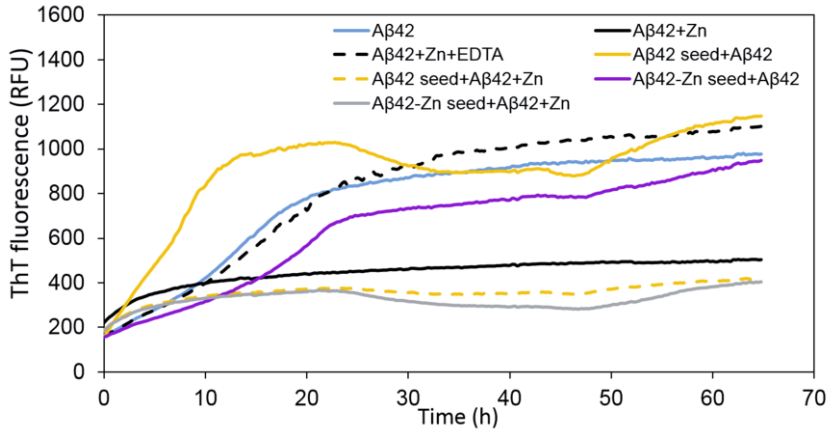

Figure 28. The presence of Zn^{2+} suppressed Aβ42 fibrillization by interfering with the aggregation process. ThT assay showing the representative kinetics of 40 μM Aβ42 under different treatments. 40 μM Aβ42 alone (light blue), 40 μM Aβ42 with 40 μM Zn^{2+} (solid black), 40 μM Aβ42 with 40 μM Zn^{2+} and equimolar EDTA (dashed black), 40 μM Aβ42 plus 1 μM Aβ42 seeds in the absence (solid yellow) or presence (dashed yellow) of 40 μM Zn^{2+}, 40 μM Aβ42 plus 1 μM Aβ42-Zn seeds in the absence (magenta) or presence (grey) of 40 μM Zn^{2+}. The final concentration of ThT in each sample was 5 μM. All samples were incubated in 10 mM sodium phosphate buffer (pH 7.4) at 20 °C and the measurement lasted for 65 h.

Characterization of size distributions of Aβ42 species by sedimentation velocity measurement

Sedimentation velocity analysis provides first-principle hydrodynamic information on the size distribution and the shape of molecules in solution [279, 280]. The sedimentation velocity of a molecular species is largely dependent on its buoyancy mass and shape [281]. The movement of different species in solution driven by centrifugal force is precisely reflected by changes in positions and shapes of the sedimentation boundaries [279]. The size distribution can thus be determined by fitting the recorded boundaries with a sum of solutions of the Lamm equation by appropriate algorithms [226, 229, 273]. In order to gain more insight into the compositions of Aβ aggregates in solution, we evaluated size distributions of 40 μM Aβ42 incubated with or without equimolar Zn^{2+} for 0 h, 24 h and 72 h, respectively. From ThT experiments it follows that these time points are located either before entering the rapid growth phase or after reaching the plateau phase, thus avoiding the phase of rapid size changes. At time point 0 h, two populations of species can be identified in both the Zn^{2+}-free and Zn^{2+}-containing samples (Fig. 29A). The most prominent species, represented by the highest peak of the $c(s)$ distribution with an average s-value of about 0.6 S in samples with and without Zn^{2+}, corresponded to the Aβ42 monomer. Further, Aβ42 oligomers could be detected in both samples with s-values between 5 S and 15 S, accounting for 15 % in the sample without Zn^{2+} and about 40 % in the sample with Zn^{2+}. The $c(s)$ distribution analysis suggested that there were more Aβ42 monomers in Zn^{2+}-free samples (74.5 % of total signal) than in Zn^{2+}-containing samples (54.4 % of total signal). After 24 hours of incubation at 20 °C, the size distributions in samples with and without Zn^{2+} shifted toward larger s-values (Fig. 29B), indicating the growth of aggregates. As can be seen from the bar chart (Fig. 30), aggregates within 15-50 S were the predominant species in both samples. The content of monomers in Aβ42 treated with Zn^{2+} was again much lower than that in the Zn^{2+}-free sample after 24 h incubation. Nevertheless, the weight averaged s-value for broadly distributed aggregates was larger for the broad distribution found between 10 S and 50 S in the Zn^{2+}-containing sample than that between 5 and 30 S in Zn^{2+}-free sample. At 72 h, to address the increasing heterogeneity of the size distribution of Aβ42 aggregates in solution, we performed two successive runs of ultracentrifugation with the same sample at different speeds. The first run was performed at 15,000 rpm (18,144×g) to monitor the larger aggregates and the second run at 40,000 rpm (129,024×g) to resolve the smaller aggregates. Data obtained at 15,000 rpm were analyzed by ls-g*(s) analysis on the assumption that the diffusion of target species is negligible during the SV experiment [282]. As shown in the bar chart (Fig. 30) and in the sedimentation profiles (Fig. S2); Aβ42 without Zn^{2+} treatment had a significant loss of total absorbance compared with the fresh sample and Zn^{2+}-containing sample, indicating the formation of high molecular weight aggregates which were fully sedimented during the acceleration phase. Aβ42 treated with Zn^{2+} showed a very broad and continuous distribution in the ls-g*(s) analysis (Fig. 29C). In contrast, in Zn^{2+}-free samples we saw two populations of species, with a major peak at around 20 S and a second broad peak over 80 S. In the second run of centrifugation at 40,000 rpm, a speed high enough to resolve the monomeric and small oligomeric species, the $c(s)$ analysis demonstrated the presence of a residual fraction of around 12 % small species (< 5 S, primarily monomers) in the Zn^{2+}-containing sample (Fig. 29D), whereas in Zn^{2+}-free samples the major peak appeared at about 19 S, and the amount of monomeric Aβ42 was too low to be accurately evaluated. Going through the overall size distributions, we found that the amount of oligomers between 5 S and 15 S decreased

gradually in Aβ42 sample treated with stoichiometric Zn^{2+}, while in Zn-free sample this group of species remained relatively constant at about 14 % of total signal. In addition to the sedimentation coefficient distribution, the *c*(*s*) analysis of SV data also provides a weight averaged frictional ratio (f/f_0) for the sedimenting species of a sample. This f/f_0 value represents the ratio of the frictional coefficient of a macromolecule in solution and the theoretical frictional coefficient under the assumption of a perfect spherical shape of the macromolecule. It is informative about the shape of molecules: values between 1 and 1.3 typically characterize globular species, while larger values indicate an elongated shape, like e.g. found for fibrillary structures. At 0 h and 24 h the f/f_0 values for the samples without Zn^{2+} (1.56 and 1.52, respectively) were higher than those values reported for the Aβ42 samples with Zn^{2+} (1.43 and 1.35, respectively), indicating the presence of elongated structures like protofibrils and fibrils in samples without Zn^{2+}. Those structures appear to be absent for Zn^{2+}-containing Aβ42. Similar results were observed in experiments utilizing MOPS buffer at 1:1 stoichiometry of Aβ42 to Zn^{2+} (Fig. S3, S4 and Tab. S2). To further understand the effect of Zn^{2+} on the aggregation behavior of Aβ42, we employed a set of AUC experiments with 0.1 equivalent Zn^{2+} in MOPS buffer. It can be seen from the bar chart (Fig. S5) that the most obvious difference in the size distributions occurred at 72 h. The Aβ42 alone showed large amount of aggregates over 50 S (>50 % of total signal) and trace amount of monomers. However, Aβ42 treated with 0.1 equimolar Zn^{2+} had fewer large aggregates but much more monomeric to hexameric species (~35 % of total signal) than samples without Zn^{2+} treatment. It should be noted here, that albeit it seems reasonable to assume a difference in the sedimentation behavior between free monomer and zinc-bound monomer the s-value resolution was not high enough to detect this. Sedimentation velocity analysis provided a dynamic view on the changes in size distributions and compositions of aggregates in Zn^{2+}-free and Zn^{2+}-containing Aβ42 samples at different time points. These results clearly supported that the presence of Zn^{2+} resulted in the generation of heterogeneous Aβ42 aggregates with broad size distributions, instead of forming distinct Aβ42 species and fibrils in Zn^{2+}-free samples.

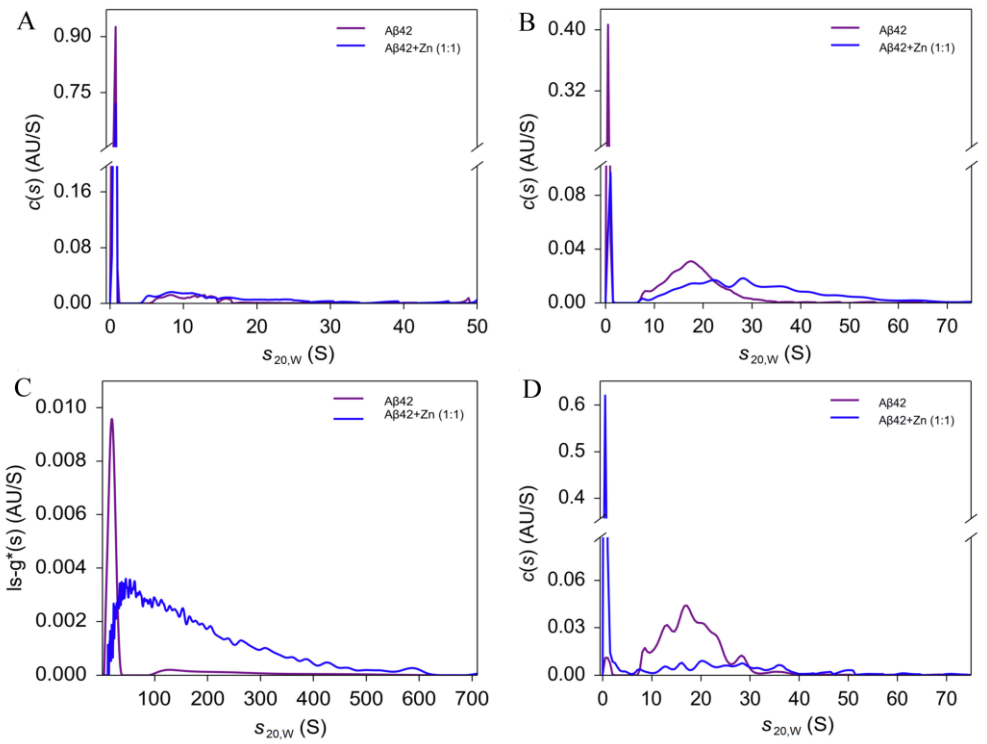

Figure 29. Characterization of size distributions of Aβ42 species by sedimentation velocity measurement. Size distributions of 40 μM Aβ42 incubated with or without 40 μM Zn^{2+} for 0 h (A), 24 h (B) and 72 h (C and D) were determined by sedimentation velocity analysis at 20 °C in sodium phosphate buffer. Note that C and D were obtained from the same samples centrifuged at two different speeds; 15,000 rpm in C and 50,000 rpm in D. Size distributions displayed in A, B and D were evaluated with continuous distribution c(s) Lamm equation model, while s-value distribution showing in C was derived from ls-g(s) distribution analysis.*

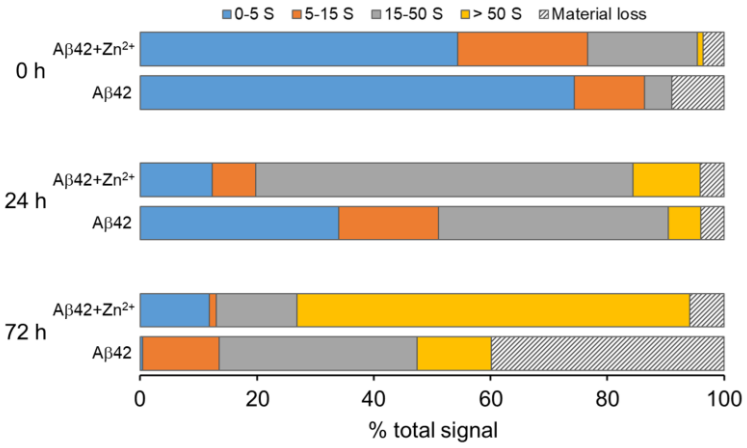

Figure 30. Bar chart summarizing SV results for Aβ42 treated with or without equimolar Zn^{2+} obtained in 10 mM sodium phosphate buffer at 20 °C. The changes in percentage of aggregates within predefined s-value ranges over time are presented accordingly.

Equimolar Zn^{2+} treatment led to the generation of non-fibrillary Aβ aggregates

The morphologies of 40 μM Aβ42 incubated with or without equimolar Zn^{2+} for 72 hours were acquired by atomic force microscopy. As shown in Fig. 31, there was a considerable amount of well-

defined Aβ42 fibrils in Zn^{2+}-free sample. These fibrillary structures can explain the high fluorescence intensity of Aβ42 alone after 72 hours of incubation in the ThT assay, as well as the loss of absorbance recorded in the ultracentrifugation. The size analysis (Fig. S6A) showed that more than 50 % of the aggregates in Zn^{2+}-free sample had lengths larger than 500 nm. However, Aβ42 treated with equimolar Zn^{2+} exhibited different morphologies. No fibrils were found in Zn^{2+}-containing samples. Instead, we observed mainly spherical aggregates. Size analysis (Fig. S6B) of the particle sizes revealed that ~60 % of the represented aggregates in Zn^{2+}-containing sample had a length between 200 and 400 nm. Estimated *s*-values for particles of this size lie between 200 and 750 S, also depending on the assumed axial ratio of oblate ellipsoids. The *s*-values correspond to about 5,600 to 23,000 monomeric units. Since the rather low measured height of about 1 nm is most probably an artefact of the immobilization and drying procedure during sample preparation, we considered in our calculations also less flattened particles. The amount as well as the *s*-value range is in line with the results from SV analysis (Fig. 29C and Fig. 30). Hence, the AFM imaging corroborated our finding that Zn^{2+} treatment suppressed Aβ42 fibrillation by promoting the generation of non-fibrillary aggregates.

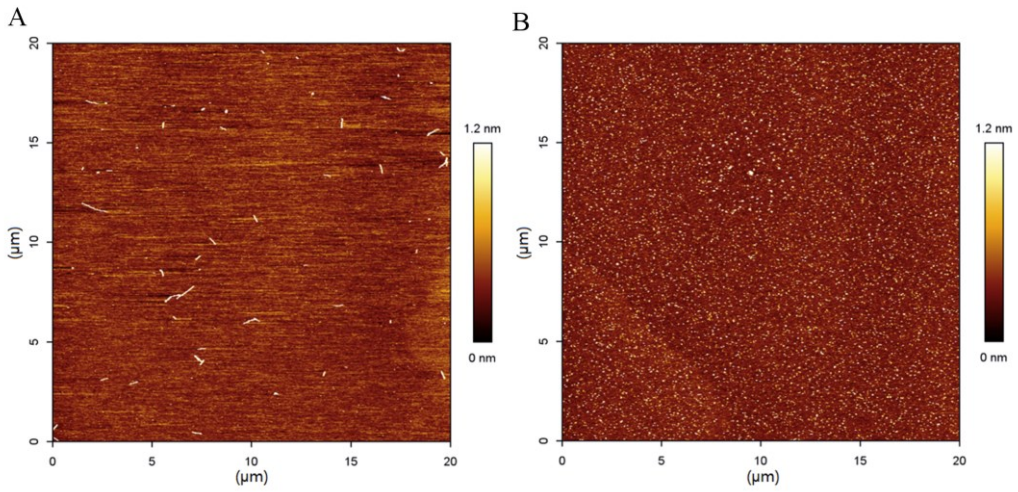

Figure 31. Equimolar Zn^{2+} treatment led to the generation of small, non-fibrillar Aβ aggregates. Morphologies of 40 µM Aβ42 incubated in the absence (A) or presence (B) of 40 µM Zn^{2+} for 72 h in sodium phosphate buffer were acquired by atomic force microscopy imaging. The morphologies were measured in AC mode at room temperature.

Discussion

Although Zn^{2+} dyshomeostasis has been proven to be closely involved in Aβ pathology, the influence of Zn^{2+} on the self-association of Aβ is not fully understood. So far the reports on how Zn^{2+} affects the aggregation process of Aβ are still controversial. In the present study, we investigated the effect of Zn^{2+} on the aggregation of Aβ42 by evaluating the structural conversion, fibril formation, particle size distributions and morphologies of Aβ42 in the absence or presence of stoichiometric Zn^{2+} over time. By CD measurements the structural conversion of Aβ42 treated with or without Zn^{2+} was recorded over time. Aβ42 pretreated with HFIP is well monomerized and adopt random coil

conformation upon being dissolved in an aqueous environment [283]. However, highly flexible Aβ42 monomers in aqueous solutions will gradually transform to β-sheet-rich structures and serve as building blocks for self-association [284]. The structural transition is considered to be the initial step for Aβ aggregation. Aβ peptides with β-sheet structures will be stacked by intermolecular hydrogen bonds and hydrophobic interactions and finally form protofilaments and fibrils [114, 285]. The CD spectra of 40 μM Aβ42 alone in 10 mM sodium phosphate buffer showed a structural conversion over time from mainly random coil conformation to β-sheet structures between 24 h and 48 h-time point. In contrast, the presence of Zn^{2+} alters the secondary structures of Aβ42 rapidly and profoundly. The CD spectrum of Aβ42 with Zn^{2+} recorded at the first time point is similar to the one taken for the Aβ42 sample without Zn^{2+} at 8 h. After 8 hours of incubation the ellipticity at 198 nm for the Zn^{2+}-containing sample becomes positive, indicating an increase in the formation of ordered structures. Nevertheless, its final MRE value at 198 nm at 120 h is only half of the value obtained in Zn^{2+}-free sample. This reduction in ellipticity in Zn^{2+}-containing samples could be either attributed to a loss of Aβ42 due to precipitation or to Zn^{2+} induced conformational changes. Based on our study we conclude that the difference in the CD spectra between Zn^{2+}-free and Zn^{2+}-containing samples indicates most probably that the binding of Zn^{2+} to Aβ42 peptide rapidly promoted its structural conversion. This is well supported by both computational studies and NMR experiments, showing that Zn^{2+} binding led to an increase of turn structures in the N-terminal region of Aβ and the formation of a relatively ordered structure [113, 169]. By applying stopped-flow fluorescence spectroscopy, Guo *et al.* demonstrated that Zn^{2+} interacts with Aβ42 within 1 ms and alters the conformation of Aβ42 immediately [286]. It is also reported that Zn^{2+} coordination reduced the abundance of helical structures at the hydrophobic core and the region from Lys28 to Val36 of Aβ [113, 287-289]. This will increase the exposure of the hydrophobic region of Aβ42 and thereby promote aggregation [287, 290]. The introduction of EDTA to chelate Zn^{2+} either at the beginning or in the middle of co-incubation not only recovered the CD signal but also restored the structural transition kinetics. Some studies demonstrated that addition of EDTA is ineffective in resuming Aβ fibril formation in the ThT assay [270]. The discrepancy could be due to the different time points of EDTA addition. Matheou *et al.* added EDTA into solutions after 250 hours of incubation [270], whereas we added EDTA at the beginning or after 23 hours of incubation. It is possible that Zn^{2+} within Aβ aggregates might not be readily accessible to EDTA after prolonged incubation.

A dual effect of Zn^{2+} on the ThT kinetics of Aβ has been observed. The fluorescence of ThT is known to be strongly enhanced in the presence of β-sheet-rich amyloid structures [136]. Aβ42 peptides treated with equimolar Zn^{2+} aggregated faster than Zn^{2+}-free Aβ42 in the beginning as we cannot see the lag phase anymore. Zn^{2+} may accelerate the aggregation of Aβ42 through several mechanisms. Aβ42 in physiological pH environment is charged about −3, whereas Zn^{2+} is positively charged. The binding of Zn^{2+} to Aβ42 will decrease the overall charge of the complex, thus leading to a decreased electrostatic repulsion of singular Aβ entities in solution [160]. Additionally, the reduced negative charge of Aβ42 complexed with Zn^{2+} could also influence the ThT binding, because ThT is positively charged. Another factor involved in the self-association of Aβ is the hydrophobicity of the peptide. Evidence from molecular dynamic simulations tells that Zn^{2+} coordination will alter the secondary structure of Aβ peptide and lead to the exposure of its hydrophobic regions [287, 291]. Both effects will contribute to an increase in the self-association rate, thus shortening the lag phase. Although the

initial aggregation has been sped up, Aβ42 treated with Zn^{2+} seems to form much less ThT positive fibrils than the Zn^{2+}-free sample. This means the presence of Zn^{2+} is able to restrain Aβ fibrillization. The seeding experiment could provide some information on how Zn^{2+} reduced Aβ fibril formation. It is generally accepted that during the elongation phase Aβ monomers rich in β-sheet structures will attach to fibril ends and add up to the preformed fibrils [292]. The presence of preformed seeds will accelerate the aggregation of Aβ peptides by providing elongation competent structures directly from the start of incubation on [126]. Notably, in our study we found that Aβ seeds, proven effective in combination with monomeric Aβ42, were incapable of enhancing amyloid formation in the presence of 40 μM Zn^{2+}. Additionally, the Aβ-Zn seeds were incompetent to shorten the lag phase of freshly prepared Aβ42. We propose that there may be two effects which Zn^{2+} could exert on the elongation phase. First, Zn^{2+} coordination may influence the rigidity of Aβ monomers and disrupt the formation of a salt bridge between Asp23 and Lys28, as reported from NMR studies and molecular dynamics simulation [170, 293, 294]. The disruption of the salt bridge while introducing altered structural constrains by the coordinative binding of stoichiometric Zn^{2+} may create elongation incompetent monomers [294, 295]. Second, Zn^{2+} may also bind to fibril ends and modulate the local environment which is necessary for peptide folding. The interaction between Zn^{2+} and Aβ fibril ends does not require a high amount of Zn^{2+} to be present, as the number of fibril ends is limited. AUC data for samples with 0.1 equimolar Zn^{2+} could substantiate this hypothesis. Zn^{2+} may thus interrupt the aggregation of Aβ42 by either changing the conformation of Aβ monomers or by modifying the structures of fibril ends. Abelein *et al.* found that substoichiometric Zn^{2+} can significantly retard Aβ fibril formation by reducing the elongation rate [168], while we observed that stoichiometric Zn^{2+} could also suppress the elongation process. Note that the aggregation of Aβ42 sample treated with 1 μM Aβ42-Zn seeds was slightly delayed, which supports the assumption that Aβ seeds formed in the presence of Zn^{2+} have different structures from Zn^{2+}-free Aβ aggregates.

The size and morphologies of Aβ aggregates with or without Zn^{2+} treatment were determined by SV analysis and AFM imaging, respectively. The *s*-values for the monomeric Aβ42 (~0.6 S) are in agreement with our previous report [296]. Interestingly, the freshly prepared samples with and without Zn^{2+} treatment already showed some difference concerning their size distributions. A higher amount of species within 5 and 50 S in Zn^{2+}-containing samples than in Zn^{2+}-free samples confirmed that Zn^{2+} treatment accelerates the aggregation of Aβ42 peptides strongly, as has been shown in the ThT assay. Although the *s*-values of aggregates formed in the presence of Zn^{2+} continue to increase over time, we did not observe a significant loss of initial absorbance in these samples. This contrasts with Noy *et al.* reporting that stoichiometric Zn^{2+} immediately led to absorbance reduction in Aβ40 samples in the AUC measurement [164]. However, our measurements of Zn^{2+}-free Aβ42 samples at 72 hours were consistent with the absorbance reduction shown in Noy *et al.*'s research [164]. Based on the AFM imaging at 72 hours we concluded that the missing absorbance signal in Zn^{2+}-free samples might be caused by sedimentation of Aβ42 fibrils or fibrillar networks during the acceleration phase. AUC analysis at 72 h revealed a dramatic difference in the size distributions between Zn^{2+}-containing and Zn^{2+}-free Aβ42 samples, particularly in the content of species below 5 S (primarily Aβ42 monomers). This might also indicate an inhibitory effect of Zn^{2+} on the elongation process at both substoichiometric and stoichiometric concentrations. The MOPS samples

displayed similar size distributions in the AUC analysis to samples in sodium phosphate buffer at 1:1 Aβ42-Zn^{2+} stoichiometry, suggesting that the impact of stoichiometric Zn^{2+} is independent of the buffer.

Conclusion

By using a combination of complementary methods we showed that the presence of equimolar Zn^{2+} influences the self-association of Aβ42 by accelerating the production of non-fibrillar aggregates with a broad size distribution. We propose that this effect may be mediated by Zn^{2+} induced conformational changes in Aβ42 peptides and a disruption of both the lag phase and the elongation phase. Our study underpins the significant role of Zn^{2+} in pathological Aβ aggregation as a stabilizing ligand of specific size classes of aggregates. In the presence of Zn^{2+} the fraction of small species ranging from monomer to hexamer is larger than in samples without Zn^{2+}. In addition, the capability of AUC in resolving low molecular mass particles makes it an ideal complementary approach for the study of these heterogeneous samples.

Supporting information

Table S1. Parameters for the analysis of sedimentation velocity data.

Partial specific volume ($\bar{v}$, cm^3/g) [a]	Aβ42	0.7377
Molecular mass (g/mol)	Aβ42	4514.1
Density (ρ, g/cm^3) [b]	10 mM sodium phosphate	0.9996
	10 mM MOPS	0.9990
Viscosity (η, poise) [b]	10 mM sodium phosphate	0.01005
	10 mM MOPS	0.01010

[a] The partial specific volume of Aβ42 has been calculated based on the amino acid composition according to ref as implemented in Sednterp.

[b] Buffer densities and viscosities were taken from tabulated values available in Sednterp.

All parameters shown are valid for 20 °C.

Table S2. Weight averaged frictional ratio (f/f_0) [a] for Aβ42 samples in the absence or presence of equimolar Zn^{2+}.

Incubation time (h)	10 mM sodium phosphate		10 mM MOPS	
	Aβ42	Aβ42+Zn^{2+}	Aβ42	Aβ42+Zn^{2+}
0	1.56	1.52	1.47	1.41
24	1.43	1.35	1.52	1.24
72 [b]	1.33	1.38	1.09	1.31

[a] values were determined by continuous distribution *c*(*s*) analysis.

[b] run at 40,000 rpm.

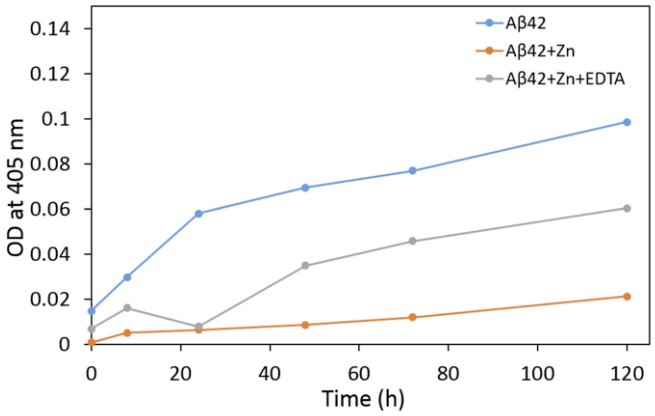

Figure S1. Turbidity assay of Aβ42 peptides in the presence or absence of stoichiometric Zn^{2+}. Turbidity was measured as pseudo absorption at 405 nm for 40 μM Aβ42 alone (blue), 40 μM Aβ42 with equimolar Zn^{2+} (orange) and 40 μM Aβ42 with equimolar Zn^{2+} and EDTA (grey). Samples were prepared in duplicate and the averaged values were shown.

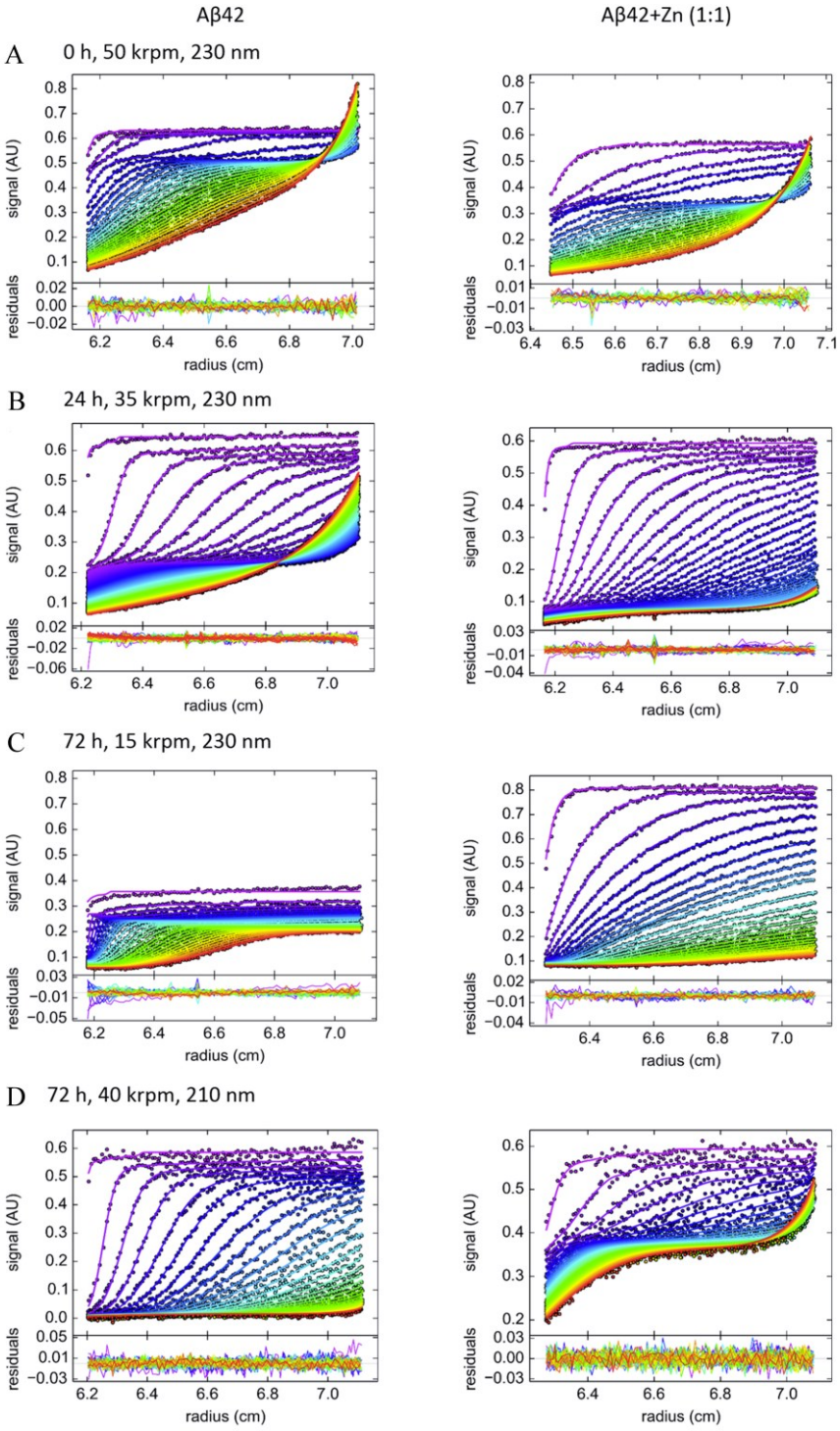

Figure S2. Sedimentation velocity profiles of 40 μM Aβ42 incubated with or without equimolar Zn^{2+} over time. The profiles were recorded at 0 h (A), 24 h (B) and 72 h (C and D), respectively. The dots in each graph represent corresponding data points detected by the optical detector, and the fitting outputs generated by pre-selected models are shown in color curves. Plots of residuals of the fitting are included at the bottom of each profile. The detection speeds and wavelengths are also specified accordingly. For clarity only a reduced number of scans as well as data points are shown.

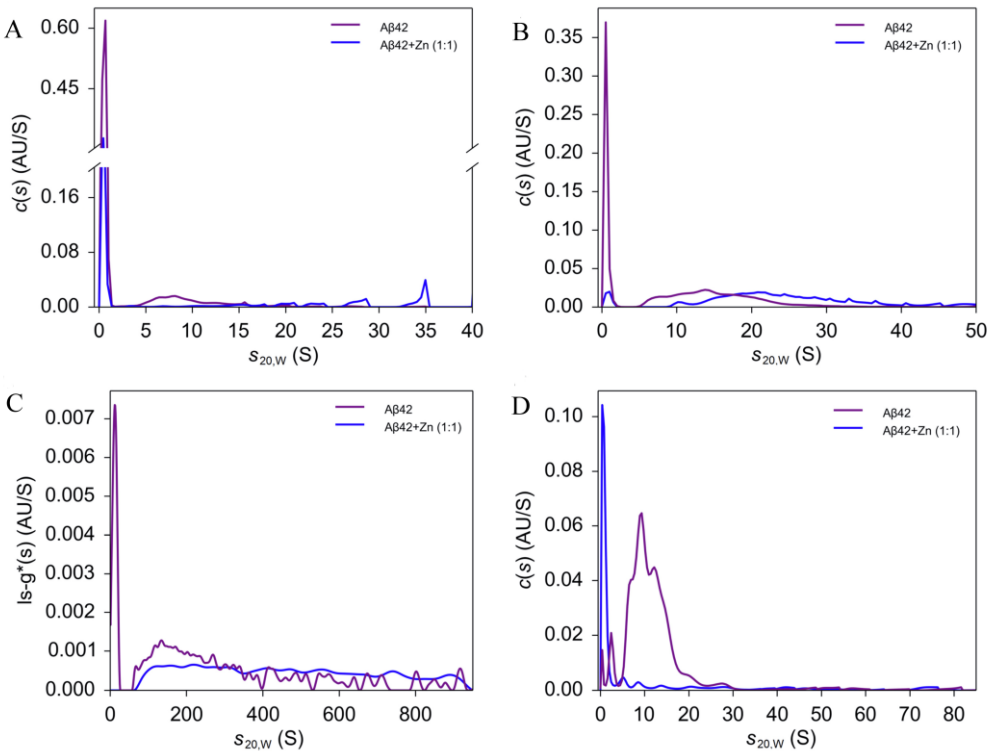

Figure S3. Size distributions of Aβ42 species in the absence or presence of stoichiometric Zn^{2+} in 10 mM MOPS buffer. 40 μM Aβ42 was incubated with or without equimolar Zn^{2+} for 0 h (A), 24 h (B) and 72 h (C and D) at 20 ℃. Samples were centrifuged at the same speed as their counterparts in sodium phosphate buffer. Data sets were analyzed with continuous distribution c(s) Lamm equation model (A, B and D) or ls-g(s) model (C). The sedimentation coefficients were standardized to the s-values in water at 20 ℃ ($s_{20,w}$).*

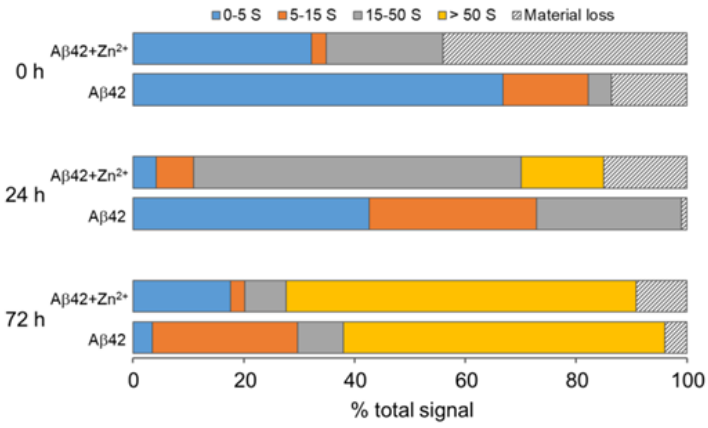

Figure S4. Bar chart of s-value distributions obtained by SV measurements for either Aβ42 alone or with equimolar Zn^{2+} in MOPS buffer, pH 7.4 for three different incubation times: 0 h, 24 h, 72 h.

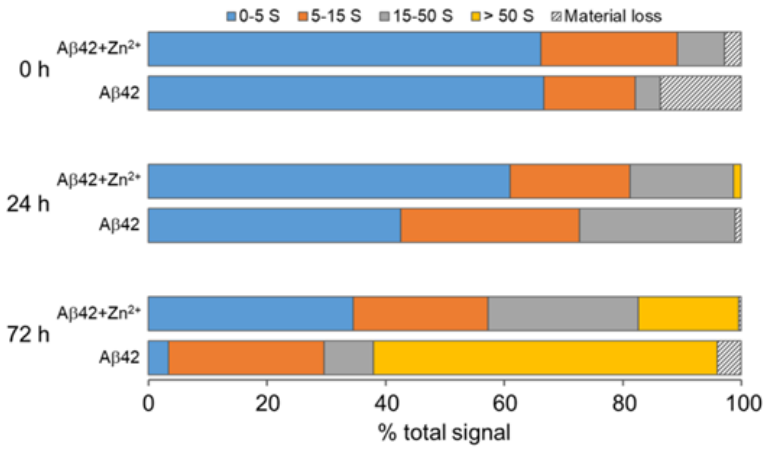

Figure S5. Bar chart of s-value distributions obtained by SV measurements for either Aβ42 alone or with 0.1 equivalents of Zn^{2+} in MOPS buffer, pH 7.4 for three different incubation times: 0 h, 24 h, 72 h.

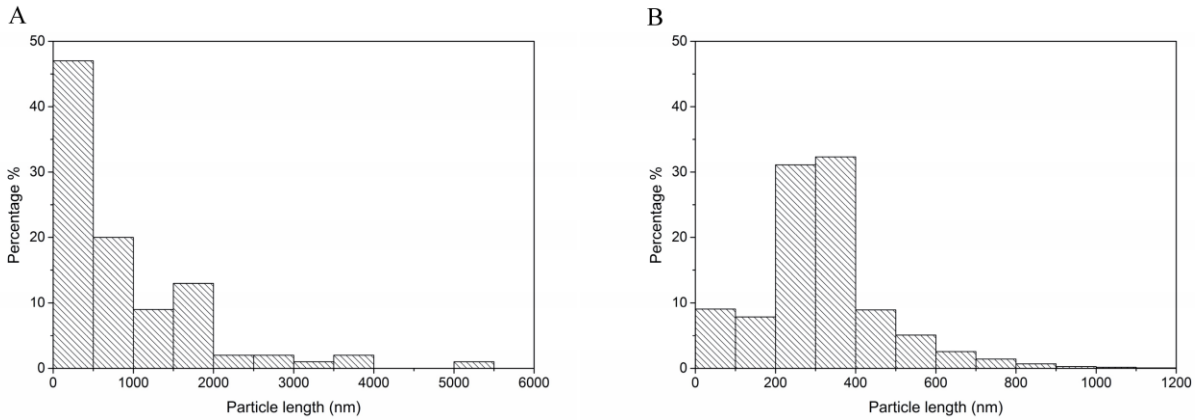

Figure S6. Particle size analysis of 40 µM Aβ42 samples in the absence (A) or presence (B) of 40 µM Zn^{2+} after 72 h of incubation at 20 °C in 10 mM sodium phosphate buffer (pH 7.4). Particles on an area of 400 μm^2 were counted and analyzed. The size analysis corresponds to the morphologies shown in Fig. 30.

Chapter II
Characterization of the interaction between D-enantiomeric peptide D3 and Aβ42

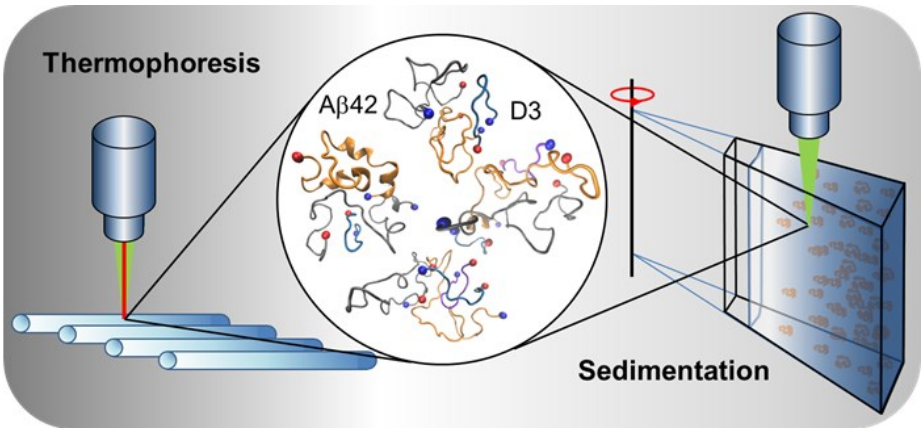

Abstract

Amyloid-β peptide (Aβ) is an intrinsically disordered protein (IDP) associated with Alzheimer's disease. The structural flexibility and aggregation propensity of Aβ pose major challenges for elucidating the interaction between Aβ monomers and ligands. All-D-peptides consisting solely of D-enantiomeric amino acid residues are interesting drug candidates that combine high binding specificity with high metabolic stability. Here we characterized the interaction between the 12-residue all-D-peptide D3 and Aβ42 monomers, and how the interaction influences Aβ42 aggregation. We demonstrate for the first time that D3 binds to Aβ42 monomers with submicromolar affinities. These two highly unstructured molecules are able to form complexes with 1:1 and other stoichiometries. Further, D3 at substoichiometric concentrations effectively slows down the β-sheet formation and Aβ42 fibrillation by modulating the nucleation process. The study provides new insights into the molecular mechanism of how D3 affects Aβ assemblies and contributes to our knowledge on the interaction between two IDPs.

This chapter was adapted from the publication:

Tao Zhang, Jennifer Loschwitz, Birgit Strodel, Luitgard Nagel-Steger, Dieter Willbold. Interference with amyloid-β nucleation by transient ligand interaction. *Molecules. 24(11), 2129; doi: 10.3390/molecules24112129. (Cover story)*

Introduction

Intrinsically disordered proteins (IDPs) are a group of proteins which lack stable secondary and tertiary structures [297]. The structural flexibility of these proteins is often relevant for their functional roles in various biological activities [298]. In addition to physiological functions, IDPs are also implicated in protein misfolding diseases, in which the misfolding and abnormal aggregation of one or more IDPs are considered to be crucial early events in disease pathogenesis [109]. Amyloid-β peptide (Aβ) is one of the key molecules in the pathogenesis of Alzheimer's disease (AD) [299]. Aβ is composed of 39 to 43 amino acid residues and cleaved from the amyloid precursor protein (APP) [80, 300]. Aβ monomers in aqueous environments have been recognized as IDPs due to their overall random coil structures [301]. However, Aβ monomers are able to form ordered conformations upon self-assembling into toxic oligomers, which are the most relevant species for disease development and progression [98], as well as into fibrillar structures [144]. The central role of Aβ in the pathogenesis of AD has raised a lot of interest in identifying physiological or non-physiological molecules that can modulate the aggregation process of Aβ and antagonize toxic Aβ oligomers.

Based on the rationale that stabilization of Aβ in its monomeric IDP conformation should efficiently inhibit the aggregation of Aβ, and even destabilize and ultimately eliminate already existing toxic Aβ assemblies, we carried out a mirror image phage display selection, and obtained "D3", a peptide consisting of 12 D-enantiomeric amino acid residues [201, 302]. D-enantiomeric peptides comprise a promising substance class for the development of therapeutic agents because of their high potency and low proteolytic susceptibility [303]. The arginine-rich D3 peptide lacks well-defined structural features, and can thus be described as a small IDP. D3 demonstrated its beneficial effects in targeting Aβ species in vitro and in AD transgenic mouse models [212], as well as its stability [208, 210], while the detailed mechanism of action underlying the interaction between the highly flexible D3 and Aβ monomers remained elusive. Specific high-affinity interactions between intrinsically disordered proteins are something, which has not been expected until very recently [304]. The inherent flexibility of the binding partners, and the dynamic nature of the interaction, contradict the existence of a well-defined 1:1 complex structure, as one would expect in the case of a typical receptor-ligand-complex, which is principally accessible to high-resolution structural biology methods. This excludes the existence of a well-defined three-dimensional structure of 'the' complex that would be amenable to routine high resolution structure determination methods. The strong aggregation propensity of Aβ poses additional challenges to distinguish ligand binding from self-association. Due to the structural diversity and opposite charges of D3 and Aβ monomers, we reasoned that the interaction between these two molecules is not a standard ligand-receptor interaction. Instead, it might resemble a specific high affinity interaction between two small IDPs, characterized by a variable stoichiometry.

To characterize the interaction between D3 and Aβ42 monomers, which is essential for understanding the mechanism of the action of D-peptides on Aβ pathology, we applied solution-based fluorescence approaches to investigate the binding and complex formation between D3 and monomeric Aβ42 at concentrations as low as possible to avoid confounding aggregation-related artifacts, wherever feasible. Experimental data on the interaction from fluorescence-based analytical

ultracentrifugation (AUC-FDS) and microscale thermophoresis (MST) was supported by molecular dynamics (MD) simulations. Furthermore, the influence of D3 on the aggregation of Aβ42 was studied at clearly substoichiometric ratios by employing a thioflavin T (ThT) assay, circular dichroism (CD) spectroscopy and atomic force microscopy (AFM). By combining various experimental techniques and MD simulations, we set out to clarify the interaction between unstructured D3 and Aβ42 monomers. The findings will not only deepen our knowledge on the mechanism of action of D3, but also shed some light on the formation of IDP-IDP complexes in general.

Results

Characterization of the dissociation constant of Aβ42 and D3 interaction

The dissociation constant of Aβ42 and D3 interaction was evaluated using the solution-based MST. This method has been developed on the basis of the Soret effect (or thermophoresis), which describes the directed movement of particles in response to a temperature gradient in a fluid [236, 237]. Particles with different sizes, structures or charges may exhibit different thermophoretic behaviors [240]. In this context we examined the thermophoresis of unbound and bound molecules through titrating D3 to fluorescein isothiocyanate (FITC)-Aβ42, or vice versa. The fluorophore alone that had been incubated with different concentrations of D3 did not show any thermophoretic response in any control experiments, implicating no direct interaction between D3 and fluorescein (Fig. S7). A 1:1 binding model was applied to fit all of the data, resulting in reasonable fits, as judged from root-mean-square deviation (RMSD) values and residuals. As evident from Fig. 32A, D3 binds to FITC-Aβ42 with a K_D of 270 [240,310] nM (68.3% confidence interval). The positive thermophoretic response of FITC-Aβ42 and D3 samples suggests that the bound state had higher depletion compared with the unbound state. To study how ionic strength may impact the binding, we measured the K_D in a buffer with reduced ionic strength. As indicated in Fig. 33, the binding between FITC-Aβ42 and D3 was enhanced about threefold in a low ionic strength buffer, with a K_D of 88 [82,99] nM.

Another set of experiments, using 40 nM FITC-D3 and various concentrations of unlabeled Aβ42, was performed to verify the dissociation constant (Fig. 32B). The determined K_D for FITC-D3 and Aβ42 was 600 [400,870] nM. This value is about twice of that one derived from the experiments with FITC-Aβ42 and D3 under the same conditions. However, considering the much smaller thermophoretic response in FITC-D3 samples than those in FITC-Aβ42 samples, the deviation between the two K_D values is generally within the range of precision. Due to the low concentrations of analytes in MST, the monomer binding should be the dominant reaction in solution. Therefore, MST data demonstrated that there is a strong interaction between flexible D3 and aggregation-prone Aβ42 monomers at nanomolar affinities, and that electrostatic effects play a role in the interaction.

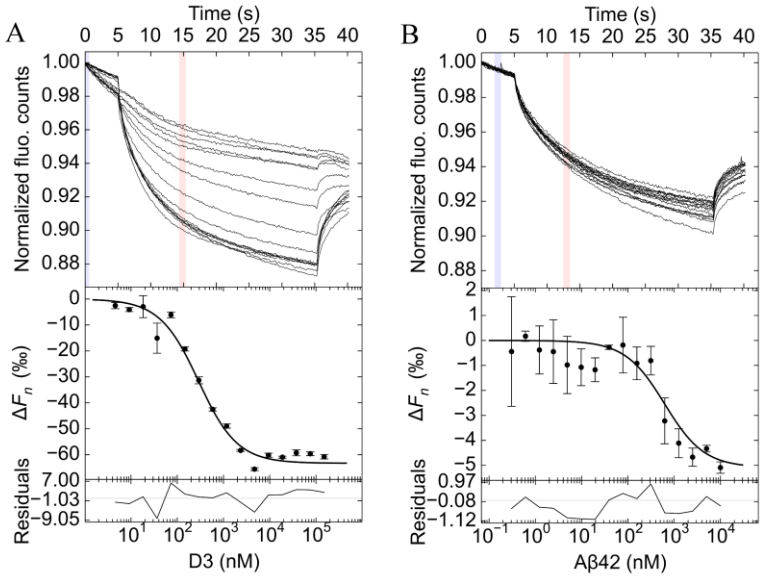

Figure 32. Microscale thermophoresis analyses to determine the dissociation constant of Aβ42 and D3 interaction. Experiments with D3 and 40 nM FITC-Aβ42 (A) and the reciprocal approach with Aβ42 and 40 nM FITC-D3 (B) were conducted at 22 °C. Samples were prepared in 20 mM sodium phosphate, 50 mM NaCl (pH 7.4). To minimize unspecific surface adsorption, 0.01% (v/v) Tween 20 (Tw20) in A and 0.0004% (w/v) polyethylenimine (PEI) in B were used. Representative time traces from one measurement are shown. ΔF_n *was calculated according to the reference zone (light blue) and the analysis zone (light red). Data was analysed using the 1:1 binding model implemented in PALMIST software with 68.3% confidence interval. Residuals of the fitting are included at the bottom of each graph. Samples were prepared in triplicate.*

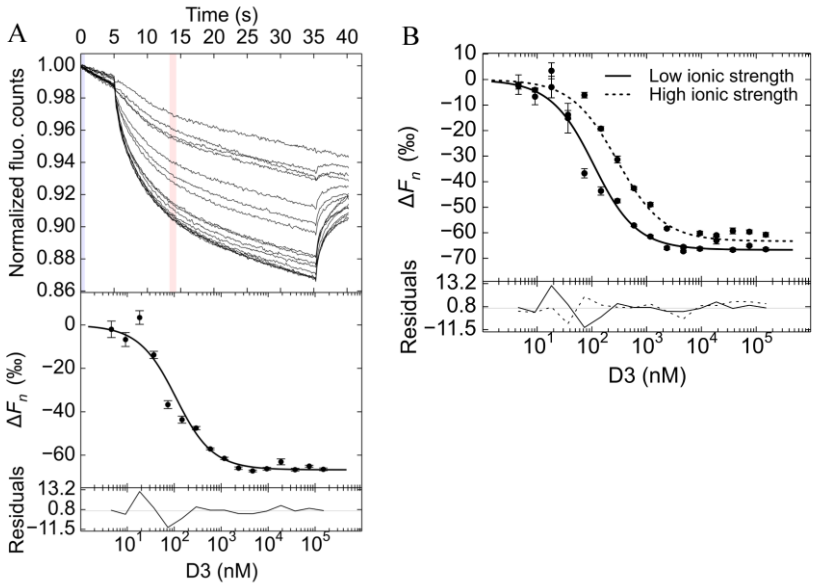

Figure 33. Microscale thermophoresis analysis to evaluate the dissociation constant between Aβ42 and D3 in 5 mM sodium phosphate, 50 mM NaCl (pH 7.4) in the presence of 0.01% (v/v) Tw20. 40 nM FITC-Aβ42 was incubated with different concentrations of D3 at 22 °C. The time traces from one measurement was shown in A, together with the reference zone (light blue) and analysis zone (light red). ΔF_n *was calculated based on the time traces and the binding plot was fitted using 1:1 binding model in PALMIST software. The binding curves obtained from low ionic buffer (solid curve) and high ionic buffer (dotted curve) are displayed in B.*

AUC analysis of Aβ42 and D3 mixtures

To investigate the complexation between Aβ42 and D3, we performed sedimentation velocity measurements in an analytical ultracentrifuge using a fluorescence detection system. Aside from the high sensitivity, the advantage of the fluorescence detection system is the selectivity of detection, since unlabeled analytes are invisible [220, 305, 306]. The high sensitivity enables the measurement at analyte concentrations close to the determined dissociation constants in the nanomolar range. Among the two possible setups, experiments with FITC-D3 and unlabeled Aβ42 should possess a higher sensitivity for detection of a 1:1 complex than the reversed experiments, because the size difference between D3 and D3-Aβ42 is larger than that between Aβ42 and Aβ42-D3. The sedimentation coefficient ($s_{20,w}$) for FITC-D3 was determined as 0.54 ± 0.02 S (Fig. 34A). D3 itself does not form any self-assemblies or aggregates (see magenta curve in Fig. 34A). The sedimentation velocity measurement confirmed that D3 stays monomeric in solution, since no other sedimenting species could be detected.

At concentrations close to the dissociation constant, the addition of unlabeled Aβ42 to FITC-D3 should result in the appearance of a new sedimenting species, indicating either the sedimentation of hetero-complexes, or the sedimentation of a reaction boundary as found for rapid reactions [307, 308]. Ideally, the total signal would stay constant irrespective of the added amount of unlabeled binding partner. Nevertheless, in the presence of excessive amounts of Aβ42, a significant fluorescence signal loss for FITC-D3 samples was noticed already during the FDS calibration process at 3000 rpm (726 *g*) (Fig. S8). Corresponding to this, we observed from the *c*(*s*) analysis that the area under curve for the monomeric species around 0.5 S also showed an Aβ42-concentration-dependent reduction. We hypothesize that the observed signal loss is a consequence of the sedimentation of large aggregate species, which resulted from the further growth of small Aβ42-D3 complexes during the thermal equilibration process (~2 h at 3000 rpm during optics calibration). This could be supported by turbidity assays, showing that the addition of D3 to Aβ42 samples promotes the rapid formation of co-precipitates in a concentration-dependent manner (Fig. S9). It can be seen from *c*(*s*) distributions for FITC-D3 and Aβ42 mixtures (Fig. 34A) that the $s_{20,w}$ of the main peak shifted from 0.5 S in FITC-D3 alone to 0.71 ± 0.04 S in samples with a 50-fold excess of Aβ42. This sedimentation coefficient cannot be interpreted as FITC-D3 monomer, since the monomer can only reach a theoretical maximum of 0.7 S under the assumptions of a perfect sphere and no hydration, according to its molecular mass and partial specific volume. Because D3 does not oligomerize by itself, it was concluded that D3 forms a 1:1 complex with the Aβ42 monomer. Additionally, we observed a small fraction of FITC-D3 sedimenting at *s*-values between 1 and 3 S (shown in the insert of Fig. 34A), indicating low amounts of larger complexes. The averaged $s_{20,w}$ for the new species, by integrating the peak between 1 and 2 S, is 1.45 ± 0.08 S, according to *c*(*s*) analyses from five independent experiments, suggesting the presence of complexes with higher stoichiometries. Although the detected amount of the newly formed species was rather low, we were able to observe an increase in the weight average $s_{20,w}$ for FITC-D3 samples along with Aβ42 addition (Fig. S10A). The AUC analyses on FITC-Aβ42 and D3 exhibited similar *c*(*s*) distribution patterns to those from FITC-D3 and Aβ42 (Fig. 34B). The FITC-Aβ42 monomer has an $s_{20,w}$ of 0.77 ± 0.02 S and comprises more than 95% of the total signal of the sample solution. The monomeric nature of the

sample persists throughout the measurement, permitting the study of any Aβ42 monomer-D3 interactions. As mentioned, the FITC-Aβ42 monomer has an $s_{20,w}$ of 0.77 ± 0.02 S, which impedes the observation of the 1:1 complex of D3 and FITC-Aβ42, which can be expected to be very close to 0.71 S. Incubating D3 with FITC-Aβ42 led to the formation of a new species at 1.54 ± 0.11 S in a D3 concentration-dependent manner. Besides, the weight average $s_{20,w}$ of FITC-Aβ42 and D3 mixtures increased gradually with an increasing D3 concentration (Fig. S10B). Since the $c(s)$ distribution of Aβ42 alone did not show any peak between 1 and 2 S [154], the new species are most likely hetero-complexes of FITC-Aβ42 and D3 at stoichiometries higher than 1:1, rather than Aβ42 homo-oligomers. Both sets of AUC experiments, using FITC-D3 and Aβ42, as well as FITC-Aβ42 and D3, clearly validate the interaction between Aβ42 monomers and D3. The results revealed for the first time the complex formation between highly flexible and aggregation-prone Aβ42 monomers and unstructured D3 peptides at variable stoichiometries.

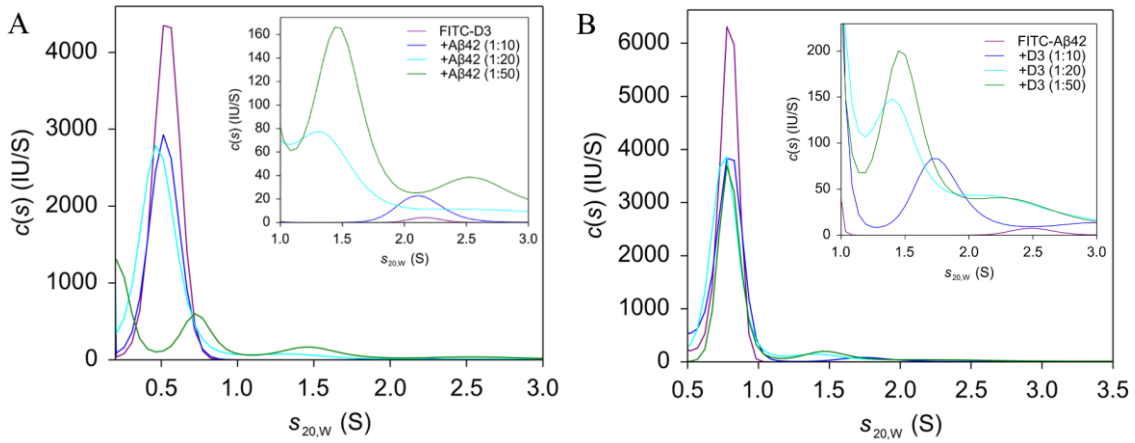

Figure 34. Sedimentation velocity analyses of 0.2 µM FITC-D3 incubated with different concentrations of Aβ42 (A) and 0.33 µM FITC-Aβ42 incubated with different concentrations of D3 (B) using AUC-FDS. FITC-D3 samples were prepared in 20 mM sodium phosphate, 50 mM NaCl (pH 7.4), 0.0004% (w/v) PEI. FITC-Aβ42 samples were prepared in 55 mM Tris, 50 mM NaCl (pH 7.4), 0.01% Tw20. Note that PEI and Tw20 were used to overcome the unspecific surface adsorption. Samples were centrifuged at 60,000 rpm (289,000 g) for 15 h and were analysed with the c(s) model to determine sedimentation coefficient distributions. Inserts show the enlargement of the size distribution between 1 and 3 S. All s-values were standardized to $s_{20,w}$.

Complex formation studied by molecular dynamics simulation

We performed MD simulations to gain further insights into the complexation between Aβ42 and D3. The different complexes formed between twenty Aβ42 and five D3 molecules during the simulation were used to derive theoretical sedimentation coefficients for different stoichiometries focusing on four stoichiometries, namely 1:1, 1:2, 2:1 and 2:2 (D3:Aβ42) which had *s*-values close to the experimentally observed values (Fig. 35A and S11). The 1:1 and 1:2 complexes were calculated to have $s_{20,w}$ at around 1 S, while the 2:1 and 2:2 complexes were calculated to have values at 1.3 to 1.4 S. We also calculated *s*-values for larger complexes observed in the initial implicit solvent simulations, and calculated an $s_{20,w}$ of 1.6 to 1.7 S for 1:3, ~1.7 S for 2:3 and ~1.9 S for 1:4 stoichiometries (D3:Aβ42). The calculated *s*-value for 1:1 complex in MD simulations corroborated

AUC results that D3 forms 1:1 complexes with Aβ42, while the new species observed at ~1.45 S in AUC measurements with FITC-D3 and high excess of Aβ42 results most likely from complexes with higher stoichiometries (for instance, 1:2 D3:Aβ42). In turn, the new species observed at ~1.54 S in AUC measurements with FITC-Aβ42 and high excess of D3 is most likely to be the 2:1 or 3:1 (D3:Aβ42) complex.

The lack of a fixed stoichiometry in the complexation between D3 and Aβ42 led us to think whether the interaction induces significant structural changes in disordered Aβ42 monomers or not. We then analyzed the secondary structure of Aβ42 in all four complexes obtained in the simulation. Aβ42 monomers remained predominantly unstructured with less than 10% β-structures in all complexes (Fig. 35B); this indicates that the interaction between D3 and Aβ42 monomers is rather flexible and dynamic.

Results from MD simulations are in line with fluorescence AUC measurements and implicate that the interaction between D3 and Aβ42 monomers is analogous to the dynamic interaction between two IDPs.

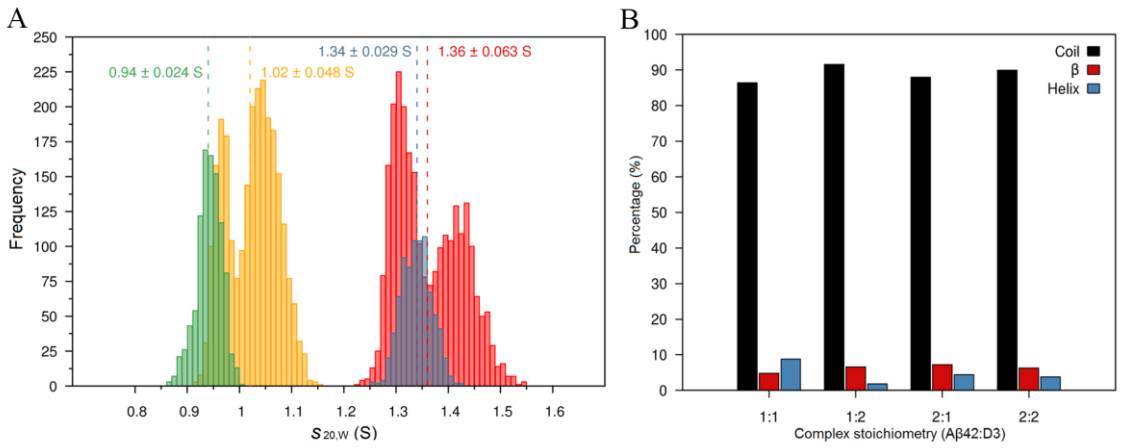

Figure 35. Sedimentation coefficient ($s_{20,w}$) distribution of D3 and Aβ42 monomer complexes (A) and calculation of the secondary structure of Aβ42 monomers in these complexes (B) based on MD simulations. The average $s_{20,w}$ with standard deviations for the 1:1 (green), 2:1 (yellow), 1:2 (blue) and 2:2 (red) D3:Aβ42 complexes are given for each complex above the corresponding histograms. Random coil, turns and bends are denoted as coil structures, β-sheets and β-bridges as β-structures, α-, 3_{10}- and π-helices as helix structures.

D3 retards the fibrillation of Aβ42 at substoichiometric concentrations

The aggregation kinetics of Aβ42 as observed in the ThT assay generally displays a sigmoidal pattern characterized by three phases: The lag phase, the rapid growth phase and the plateau phase [126, 135, 292]. In the primary nucleation, which is the limiting event during lag phase, Aβ monomers associate and form aggregates (primary nuclei) without the involvement of already formed assemblies [126]. During rapid growth or elongation Aβ monomers are added to the ends of already formed aggregates (such as nuclei), leading to fibrillar structures. Additionally, once formed fibrillar structures provide surfaces at which monomers can be catalyzed to form nuclei. This process is called secondary nucleation [309]. Finally, a plateau is reached due to the consumption of free monomers

[126, 310]. At high concentrations of D3 the fibril formation as monitored by ThT can be largely suppressed (data not shown). However, here we used only 0.1 fold D3 concentration to render the measurements comparable to the CD measurements. As shown in Fig. 36A and Table 2, Aβ42 alone displayed a sigmoidal fibrillation kinetics and an earlier onset of rapid growth than Aβ42 incubated with D3. The $t_{1/2}$ and t_{lag} of Aβ42 alone were determined to be 30.0 ± 0.7 h and 17.3 ± 1.6 h, respectively, according to the fitting (Fig. S12). Addition of 0.1 equimolar D3 slowed down the fibril formation of Aβ42 significantly, as $t_{1/2}$ and t_{lag} were prolonged to 79.3 ± 2.3 h and 67.6 ± 3.8 h, respectively. We also noticed that the growth phase seemed to be unaffected, as both samples had similar slopes. All samples reached comparable plateau fluorescence signals after 120 h of incubation irrespective of the addition of D3. Thus, D3 effectively elongates the lag phase of Aβ42 aggregation, very similar to what was described for bexarotene [311]. To figure out whether or not the interaction between D3 and Aβ42 was affected by the buffer system, we performed ThT measurements in Tris-HCl buffer with the same ionic strength as the phosphate buffer. A comparable ThT kinetics was observed in both buffers (Fig. S12 and Table S4), suggesting that the retardation effect of D3 on Aβ42 aggregation is not very dependent upon the buffer system. The difference in the ThT kinetics of Aβ42 with or without D3 hints that samples might have different aggregate compositions. We therefore performed AUC experiments on equivalent samples incubated for 24 h. At 24 h, Aβ42 alone should have ThT positive species, while Aβ42 plus D3 should still be in the lag phase. Samples of Aβ42 alone contained a fraction of large aggregates, which were sedimented to the cell bottom during the acceleration process of AUC (Fig. S13), these presumably being products of the elongation phase. In contrast, Aβ42 samples with D3 had no such large aggregates, but a significantly higher amount of monomers (~0.7 S) than Aβ42 alone (Fig. S14). The dramatic difference in the size distribution of Aβ42 with or without D3 suggests that D3 is able to interfere with the very early stage of Aβ aggregation, which is the nucleation process, by retaining Aβ monomers and delaying the growth and amplification of Aβ nuclei.

To further investigate how D3 may interfere with the aggregation process of Aβ42, we performed seeding experiments. In these experiments, the introduction of fibril fragments generated by sonication into Aβ monomer solutions offers surfaces and/or fibril ends for the attachment of monomeric species, leading to an immediate growth of fibrillar structures [139, 312]. The presence of Aβ42 seeds significantly accelerated the aggregation of Aβ42 by canceling the lag phase, as evident from ThT kinetics (Fig. 36B). In particular, the addition of 5% seeds in Aβ42 samples immediately initiated the rapid ThT fluorescence increase of Aβ42 aggregation. The inhibitory effect of D3 on the fibrillation was also visible in Aβ42 samples incubated with seeds. Aβ42 samples with both D3 and 1% seeds had a longer lag phase than Aβ42 without D3 (Fig. 36B). Although D3 at 0.1 fold was not able to restore the sigmoidal aggregation kinetic of Aβ42 in the presence of 5% seeds, we could still observe a retardation of the elongation process in samples with D3 treatment, by comparing the slopes of the ThT kinetics with those of Aβ42 samples incubated solely with 5% seeds (Fig. 36B), suggesting that substoichiometric D3 could interfere with the elongation of Aβ42 fibrils. ThT kinetics indicated that D3 may also interact with aggregated Aβ42 species (such as oligomers and fibrillar structures).

Table 2 Half completion time ($t_{1/2}$), slope (k) and lag time (t_{lag}) for fibrillation kinetics of 20 μM Aβ42 incubated with or without 2 μM D3.[a]

Sample	$t_{1/2}$ (h)	k	t_{lag} (h)
Aβ42	30.0 ± 0.7	0.15 ± 0.01	17.3 ± 1.6
Aβ42+D3	79.3 ± 2.3	0.18 ± 0.07	67.6 ± 3.8

[a] Data was obtained by fitting an empirical equation to ThT kinetics using AmyloFit [313].

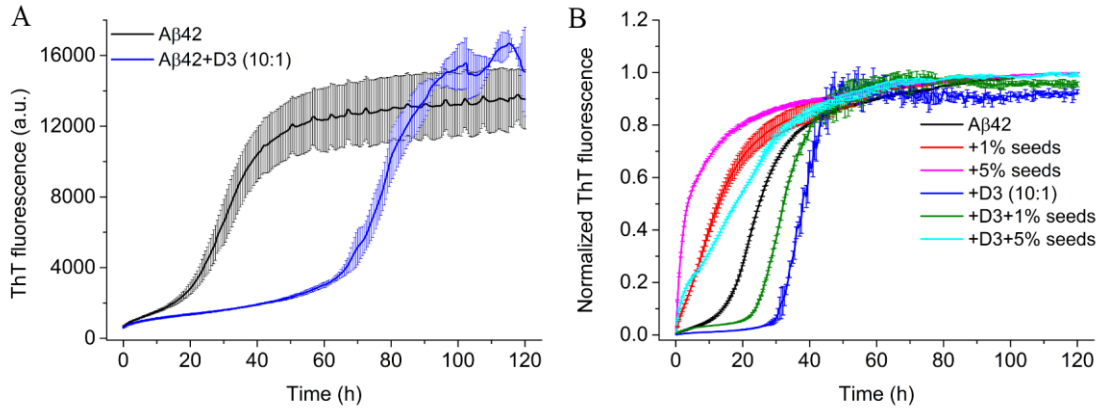

Figure 36. ThT assays showing fibrillation kinetics of 20 μM Aβ42 and 20 μM Aβ42, with 2 μM D3 in (A), and of 10 μM seeded Aβ42 (1% or 5% seeds), incubated without or with 0.1 fold D3 in (B). Color usage is explained in the figure. Samples were incubated in 20 mM sodium phosphate, 50 mM NaCl (pH 7.4) at 20 °C. ThT data is averaged based on samples prepared in triplicate.

D3 slows down the secondary structure conversion of Aβ42 at substoichiometric concentrations

The fibrillation of Aβ42 is accompanied by a structural transformation of Aβ42 monomer from random coil to β-sheet structures. D3 itself does not have stable secondary structure elements and is disordered in solution (Fig. S15). The addition of low amounts of D3 did not contribute detectably to the overall spectra of Aβ42 samples so that the structural conversion of Aβ42 was observable without requiring correction for the D3 signal. As shown in Fig. 37A, Aβ42 alone adopted mainly random coil structure at the beginning and converted to β-sheet conformation during the incubation at 20 °C. The transition kinetics of Aβ42 alone based on incubation time-dependent ellipticities at 217 nm and 198 nm exhibited sigmoidal patterns for both wavelengths (Fig. 37C, D). However, Aβ42 treated with D3 alone had markedly different transition kinetics, as can been seen from Fig. 37B and C, D. The overall transition kinetics of 40 μM Aβ42 was significantly delayed in the presence of 4 μM D3. The ellipticity at 217 nm for Aβ42 sample with D3 was about 72% of that for Aβ42 alone at 120 h, pointing to decreased β-sheet structures in samples with D3. Dichroweb deconvolution of CD spectra to evaluate secondary structure components of samples incubated with or without D3 demonstrated similar trends (Fig. 37E, F). There was a gradual loss of unordered conformations accompanied by accumulations of β-strand structures in all samples. Nevertheless, free Aβ42 sample had faster conversion rates than Aβ42 samples containing 0.1 fold D3. The fractions of β-strand structures in Aβ42 samples without D3 addition were also higher than those in

samples incubated with D3 at most of the time points. Even, if 4 μM D3 was added into 40 μM Aβ42 after a preincubation period of 33 h (Fig. S16), it still visibly delayed the structural transformation of Aβ42. The results from CD measurements are in agreement with those obtained from ThT assays in demonstrating that substoichiometric D3 decelerates the fibril formation process of Aβ42 via retarding the secondary structure conversion. The data also offers experimental evidence to corroborate MD simulations that D3 favors a less structured state of Aβ42.

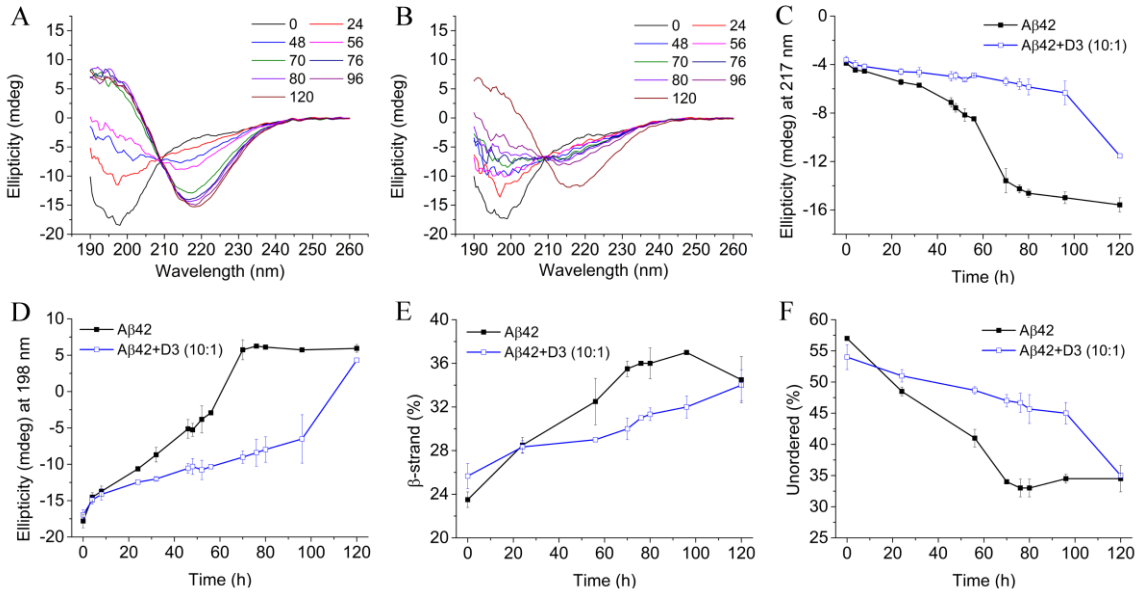

Figure 37. Circular dichroism (CD) measurements and spectrum deconvolution analyses. 40 μM Aβ42 was incubated with (A) or without (B) 4 μM D3 in 20 mM sodium phosphate, 50 mM NaF (pH 7.4) at 20 °C. CD spectra were recorded at indicated time points between 0 and 120 h of incubation. Transition kinetics are shown by plotting ellipticities at 217 nm (C) and 198 nm (D) against the incubation time. Changes in fractions of β-strand (E) and unordered structures (F) over the incubation time were obtained using the CDSSTR algorithm and reference dataset 7 in Dichroweb. All samples were prepared in triplicate.

Morphologies of Aβ42 samples in the presence of substoichiometric D3

AFM imaging was conducted to detect morphologies of Aβ42 samples incubated with or without D3 for 48 h and 120 h. According to ThT assays and CD measurements, Aβ42 alone should have a considerable amount of fibrillary structures after incubating for 48 h. This was confirmed by AFM imaging, which showed rod-like fibrillar structures in Aβ42 alone at 48 h, as displayed in Fig. 38A. The typical height for single fibrils was around 5 nm. Some protofibrils and oligomers (~2 nm in height) were also visible in Aβ42 alone after 48 h of incubation. However, Aβ42 incubated with 0.1 eq. D3 had no fibrils but some amorphous aggregates with heights varying from 10 nm to 20 nm (Fig. 38B). Small species with similar dimensions to protofibrils and oligomers in Aβ42 alone were also present. After 120 h of incubation, most of the materials transformed to amyloid fibrils in free Aβ42 samples, as shown in Fig. 38C. These fibrils did not differ much to Aβ42 fibrils found at 48 h with respect to the height, but became more elongated, which agrees well with Arimon et al.'s findings [253]. Substoichiometric D3 did not stop the fibril formation as we could see rod-like fibrils in Aβ42 incubated with D3 at 120 h (Fig. 38D). Surprisingly, amorphous aggregates also grew to

larger size than those at 48 h. AFM imaging provided additional evidence that D3 affects the aggregation process of Aβ42 at substoichiometric levels.

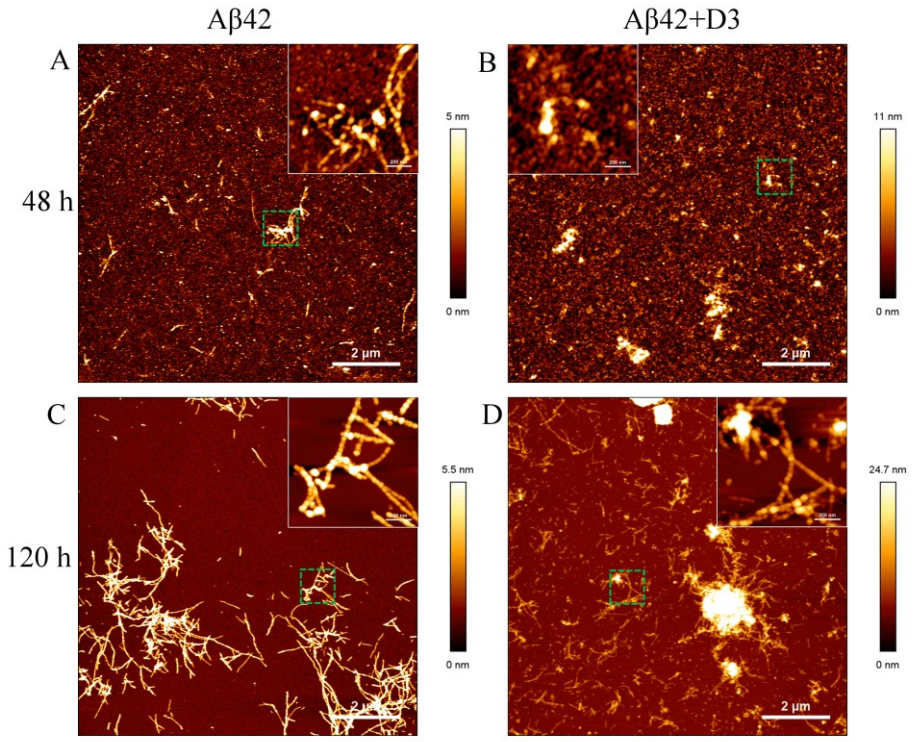

Figure 38. Atomic force microscopy (AFM) imaging to study morphologies of 40 µM Aβ42 in the absence (A and C) or presence (B and D) of 4 µM D3 in 20 mM sodium phosphate, 50 mM NaCl (pH 7.4) at 20 °C after 48 h and 120 h of incubation. The imaging was carried out at room temperature in air, using AC mode. Inserts show amplifications of areas marked with green squares. The scale bars are 2 µm and 200 nm, respectively.

Discussion

The present study reports how two IDPs, the all-D-enantiomeric peptide D3 and Aβ42 monomers interact, and how the interaction may influence the fibrillation of Aβ42. We chose solution-based methods in combination with fluorescence-based detection in order to minimize the required concentrations of analytes as well as surface-related effects. The binding affinity between D3 and Aβ42 was evaluated using MST in both possible setups. Smooth capillary scans, as well as the reproducibility of the determined dissociation constant in successive rounds of measurements, indicated the absence of irreversible aggregation. A simple 1:1 binding model was sufficient for fitting the data from both setups. Other more complex models did not significantly improve the fit. The K_D for D3 and Aβ42 at about 400 nM is about 10-fold smaller than that reported in our previous SPR studies (~4 µM) [212, 214]. Possibly, the fixation of N-terminally biotinylated Aβ42 monomers onto sensor chips via biotin–streptavidin coupling rendered the interaction between D3 and Aβ42 monomers less efficient than that found for both components free in solution [212]. Lowering the ionic strength in MST measurements decreased the K_D, pointing to the involvement of electrostatic interactions between the positively-charged D3 and the negatively-charged Aβ42. Ionic strength may

affect protein-protein interactions in many ways, e.g., a reduction in the salt concentration may cause a decrease in the screening effect of salt-ions near the protein surface [314], thus enhancing the electrostatic attraction between oppositely-charged proteins, and increasing the binding affinity. This effect is confirmed by Borgia et al. who found that reducing the ionic strength strongly promotes the complex formation between two IDPs carrying opposite charges [304]. Our findings agree well with a study on a decapeptide containing three L-Arg residues, in that reducing the ionic strength of the buffer strengthens the interaction between ligands and Aβ40 monomers [315]. This feature of D3 and Aβ42 interaction also coincides well with the interaction between two typical IDPs, in which the electrostatic effect usually has an important contribution [316, 317].

AUC analyses from both FITC-Aβ42 and FITC-D3 samples demonstrated that binding between D3 and Aβ42 leads to the formation of new species sedimenting faster than the corresponding monomer, which represent most of the probably small hetero-complexes. Albeit a 1:1 hetero-complex could only be clearly detected in FITC-D3 samples treated with Aβ, an equivalent new species is most probably also present in the case of FITC-Aβ42 with D3, but its expected *s*-value cannot be distinguished from the *s*-value of free FITC-Aβ42. In the case of a small change in mass upon complex formation, 5 kDa (FITC-Aβ42) versus 6.6 kDa (FITC-Aβ42+D3), unfavorable conditions like an extended shape upon complex formation, or high dissociation rates, can cause the complex to sediment at reduced speed, resulting in a sedimentation coefficient of the 1:1 complex indistinguishable from that of the free monomer. Nevertheless, the increase in weight average *s*-values in both groups of samples confirmed the complexation between D3 and Aβ42 monomers. It is evident from AUC analyses on individual proteins that monomers are the dominant species in Aβ42 or D3 samples at the nanomolar concentrations used in the study. Therefore, the monomer interaction is the major event under the hereby applied experimental conditions. Similar findings were also reported by Cox et al., showing that small heat shock proteins can transiently interact with α-synuclein monomers and prevent its aggregation [318]. Through MD simulations, we have identified four possible complexes of D3 and Aβ42 within the *s*-value range of AUC experiments. The higher stoichiometry complexes may therefore evolve from the further interaction between 1:1 complexes and additional D3 or Aβ42 molecules in solution. Indeed, the reduction in the amount of monomeric species in both AUC setups points to the fact that D3 or Aβ42 monomers have been consumed in the presence of their binding partners.

The initial step of Aβ42 fibril growth is the formation of nuclei which serve as seeds for the further growth of amyloid fibrils. By complementing ThT kinetics with AUC experiments, we were able to monitor the complete composition of Aβ samples including ThT negative species, such as monomers and small oligomers. The much higher content of Aβ42 monomers and small oligomers in samples with substoichiometric D3 than in samples without D3 explains the much slower aggregation and structural transformation kinetics of D3-containing samples. It seems that interacting with D3 impedes the formation of any Aβ oligomers required for seeding the fibrillation. The outcome of D3 affecting the aggregation kinetics of Aβ42 is similar to results obtained by Assarsson et al., showing that the small hydrophilic proteins, calbindin D_{9k}, and single-chain monellin, retard the fibril formation process of Aβ40 in a net charge-dependent manner. They found that proteins with positive or low negative net charges are particularly effective in slowing down the fibrillation [319]. Interestingly, we also observed in seeding experiments that substoichiometric amounts of D3 retard

the fibril formation of Aβ42 efficiently, even in the presence of a relatively high amount of seeds. AUC and MST measurements demonstrated that D3 directly interacts with Aβ42 monomers. Sequestration of monomers by 0.1 fold D3 would decrease the available Aβ42 concentration by 10%. Although aggregation is concentration dependent, a difference in ThT kinetics for 18 μM versus 20 μM Aβ42 was not detectable (data not shown). Therefore the formation of the stable 1:1 complex alone is insufficient to explain the diverse effects of D3 on the fibrillation of Aβ42 at substoichiometric concentrations. Given the highly flexible nature of small D3-Aβ42 monomer complexes revealed by MD simulations, which is very similar to what has been reported for the transient interaction for the chaperonin GroEL and Aβ42 monomer [320], the simplest explanation may be that the D3 forms transient complexes with Aβ monomers, rendering them fibrillation-incompetent and interfering with the nucleation process. This would allow D3-mediated stabilization of Aβ monomers and inhibition of amyloid growth even at substoichiometric concentrations.

Intriguingly, the seeding ThT kinetics showed that both the lag phase and the growth phase of fibril formation can be affected by D3. A possible explanation could be that D3 binding the seeds renders those seedings incompetent. Although one might argue that retarding the elongation of Aβ42, particularly by interacting with fibril ends, might lead to an increase in the generation of toxic oligomers catalyzed by secondary nucleation [309], we have shown in animal studies that D-peptides actually reduced the amount of toxic oligomers in the central nervous system and conferred protective effects [214]. It can be seen from the ThT kinetics of Aβ42 incubated with both D3 and seeds that the aggregation process of Aβ42 displayed a biphasic pattern in these samples, i.e., samples showed an initial increase in ThT fluorescence to a first plateau, followed by a second rapid increase in ThT fluorescence.

The biphasic aggregation kinetics has been observed for Aβ at relatively high protein concentrations [321, 322], and is likely due to the formation of metastable globular oligomers and curvilinear fibrils in the first phase, which act as off-pathway inhibitors of Aβ fibrillation [323]. A possible explanation might be that D3 can not only bind to Aβ42 monomers and preserve their disordered conformations, but also transiently interacts with Aβ42 subunits in Aβ42 assemblies, such as oligomers and fibrillar structures. The presence of D3 may redirect Aβ42 seeds to off-pathway species, thus canceling their seeding capabilities. These mechanisms play a role in a D3-mediated deceleration of Aβ fibrillation, and could complement the interaction of D3 with Aβ monomers.

ThT assays are corroborated by CD measurements, showing that D3 is effective in retarding the secondary structure conversion of Aβ42 to β-sheet structures. The transformation of unordered Aβ42 monomers to β-sheet rich structures is critical to the fibrillation, since they function as building blocks for amyloid fibrils [324]. The result is consistent with a previous MD analysis showing that D3 disrupts the formation of β-sheet structures in Aβ42 by binding adjacently to the N-terminal half of Aβ42, where the central hydrophobic core is located [213]. In fact, the content of β-sheet structures in Aβ42 and D3 complexes (~5%) is much lower than that observed for the Aβ42 dimer (~15%) in previous simulations in the same force field [325]. The rather unordered structure of Aβ42 monomers in complex with D3 makes them incapable of participating in Aβ nuclei growth and amplification processes encompassing the accumulation of a certain amount of ordered structures [121, 326, 327]. The experimental data, together with MD simulations, also reveal that when bound to D3, Aβ42 maintains unordered structures similar to those in free solution. To our knowledge, this is the first

experimental evidence that D3 directly influences the structural conversion of Aβ42 at substoichiometric concentrations, most probably by transiently forming complexes with Aβ monomers and small assemblies. The morphologies obtained using AFM reflects exactly what we have concluded from ThT and CD measurements, that the growth of fibrillary structures is greatly delayed in the presence of D3. The amorphous Aβ42 aggregates formed in the presence of substoichiometric D3 implicate that the complexation between D3 and Aβ42 triggers further aggregation to form large co-precipitates, at least under the unphysiologically high Aβ concentrations. Previous studies revealed that these amorphous co-precipitates are non-toxic species in cell culture assays [209]. We have, however, never observed the formation of large amorphous precipitates under physiological conditions, where the concentration of Aβ is at the low nanomolar level. This result is consistent with previous findings that D3 reduces Aβ oligomer-mediated toxicity, and therefore has beneficial effects on cognition in vivo [209, 212].

Conclusion

Mechanistic insights into the mode of action of the compound D3 could be gained by strongly reducing the reactant concentrations. Submicromolar concentrations of Aβ42, which are close to the previously determined critical concentration for aggregation of 90 nM [328] as well as substoichiometric concentrations of D3 were applied in order to suppress the formation of precipitates. We conclude from our results that D3 is able to interact with Aβ42 monomers with submicromolar affinity, leading to the formation of complexes at 1:1 as well as other stoichiometries. The complexes are highly disordered and lack defined conformations. The addition of 0.1 fold D3 significantly slows down the fibrillation of Aβ42 by retaining Aβ in unstructured monomeric conformation and thus by interfering with nuclei formation. Besides, D3 also slowed down the elongation of fibrillar structures by canceling the catalytic ability of Aβ seeds. Our study demonstrates the versatile role of D3 in modulating the fibrillation of Aβ42 through modulating multiple events. The substoichiometric and diverse effects of D3 envision the promising application of its mode of action for the development of interventions in Alzheimer's disease but also in other protein misfolding based pathologies.

Supporting information

Materials and methods

Chemicals and reagents

Fluorescein isothiocyanate (FITC) labeled Aβ42 protein (product No. M-2585.1000) was purchased from Bachem (Weil am Rhein, Germany). The conjugation was made via one additional β-Alanine (β-Ala) at the N-terminus of Aβ42 sequence (FITC-β-Ala-Aβ42, hereinafter referred to as FITC-Aβ42). The purity of the product is 88.2%, according to the manufacturer. Unlabeled Aβ42 protein (product No. H-1368.1000) was also obtained from Bachem with a purity of 95.2%, as determined by HPLC. Aβ42 products (1 mg) were first dissolved in 100% 1, 1, 1, 3, 3, 3-hexafluoro-2-propanol (HFIP) overnight to monomerize the materials. The solutions were then divided into aliquots and were lyophilized to evaporate HFIP. Proteins were stored at -80 °C until use. C-terminally amidated D3 (H-rprtrlhthrnr-NH2) was available from peptides & elephants (Hennigsdorf, Germany) as lyophilized powder with >95% purity. The fluorescently labeled D3 from the same manufacturer was prepared via conjugating 5(6)-carboxyfluorescein with an additional L-lysine (Lys) residue at the C-terminus of D3. The purity for the product was determined to be 98% in HPLC tests. The stock solutions of D3 were prepared with H_2O, and were diluted to working concentrations with either 20 mM sodium phosphate, 50 mM NaCl (pH 7.4) or 55 mM Tris-HCl, 50 mM NaCl (pH 7.4), depending on the experiment. Tween-20 (Tw20, 0.01%, v/v) and polyethylenimine solution (PEI, branched, average Mw ~1300, 0.0004%, w/v) were used to attenuate surface adsorption of FITC-Aβ42 and FITC-D3 in fluorescence based measurements in the present study, respectively.

A 1 mM stock solution of thioflavin T (ThT) was prepared in H_2O and sterile-filtered before use to remove any particles that may influence the aggregation of Aβ42.

Microscale thermophoresis

The dissociation constant of Aβ42 and D3 interaction was characterized by microscale thermophoresis. In detail, FITC-Aβ42 was dissolved in 20 mM sodium phosphate, 50 mM NaCl (pH 7.4), 0.01% (v/v) Tw20 to obtain 80 nM stock solutions. 300 μM D3 was prepared in the same buffer. FITC-Aβ42 was then titrated with D3 solutions in 1:1 serial dilution steps to prepare 16 samples, in which the concentration of FITC-Aβ42 was kept constant at 40 nM, and the starting concentration of D3 was 150 μM. Samples were loaded into standard capillaries and the thermophoresis was detected using a Monolith NT.115 (NanoTemper Technologies GmbH, Munich, Germany). The experiment was performed with 40% LED power and 60% MST power. In order to understand how ionic strength influences the interaction between Aβ42 and D3, MST measurement was repeated in 5 mM sodium phosphate, 50 mM NaCl (pH 7.4), 0.01% (v/v) Tw20 under the same conditions. For experiments with FITC-D3 and Aβ42, 80 nM FITC-D3 was mixed with different concentrations of Aβ42 in 20 mM sodium phosphate, 50 mM NaCl (pH 7.4), 0.0004% (w/v) PEI to prepare a concentration series with Aβ42 concentration starting at 10 μM. The final concentration of FITC-D3 in each sample was set to 40 nM. The LED power and MST power were adjusted to 30% and 60%, respectively. The on and off time for the IR laser was set to 30 s and 5 s. Since the working concentration of labeled molecules was rather low in this measurement, any signal loss due to surface

adsorption might bias the data acquisition. Therefore trace amounts of Tw20 and PEI were used as additives in solution to minimize the unspecific surface adsorption of FITC-Aβ42 and FITC-D3 in capillaries, respectively. All measurements were conducted at 22 °C and samples were prepared in triplicate.

In order to exclude that a direct interaction between D3 and the fluorophore contributes to the observed signals control experiments with fluorescein alone titrated with D3 at the same concentrations as applied for FITC-Aβ42 were performed.

The data was evaluated with PALMIST software to obtain the dissociation constants [329]. Changes in the normalized fluorescence (ΔF_n) with concentrations of the titrant were quantified and fitted with 1:1 binding model available in the software using 68.3% confidence interval. The graphic outputs were created using GUSSI (version 1.2.1) [274].

Analytical ultracentrifugation

Sedimentation velocity analysis was conducted to evaluate size distributions of Aβ42 and D3 mixtures. All measurements were performed using an XL-A analytical ultracentrifuge (Beckman coulter, Brea, CA, USA). For the determination of complex formation between D3 and Aβ42, a fluorescence detection system (Aviv Biomedical Inc., Lakewood, NJ, USA) was used. FITC-D3 at 0.2 μM was incubated with different concentrations of Aβ42 to prepare mixtures at molar ratios of 1:10, 1:20 and 1:50 (D3:Aβ42). All samples were prepared in 20 mM sodium phosphate, 50 mM NaCl (pH 7.4) containing 0.0004% PEI (w/v). Samples were then loaded into 3-mm double-sector titanium cells (Nanolytics, Potsdam, Germany), with each sector containing 100 μl sample. The detection system uses an excitation laser at 488 nm and an emission cut-off filter at 505 nm to collect fluorescence signals. The amplification factor was adjusted to the same value for all samples for comparability. To complement, 0.33 μM FITC-Aβ42 was incubated with or without various concentrations of D3 in 55 mM Tris-HCl, 50 mM NaCl (pH 7.4), 0.01% Tw20, and samples were analyzed under the identical condition to AUC measurements on FITC-D3 samples. Data was acquired at 20 nm radial resolution. After thorough thermal equilibration the centrifugation was carried out at 60,000 rpm (289,000 *g*) at 20 °C for 15 h. Carrier proteins, such as albumin and kappa casein, are usually recommended to minimize unspecific surface adsorption for fluorescence based AUC [330]. They are not suitable here, since both proteins are found to interact with Aβ42 [331-333]. Therefore, either PEI or Tw20 was included to suppress the surface adsorption of labeled molecules during the sedimentation.

An additional absorbance based AUC was performed to check the size distribution of 20 μM Aβ42 treated with or without 2 μM D3 for 24 h. In brief, 380 μl samples were loaded into 12-mm double-sector aluminum cells and were thermally equilibrated prior to the final centrifugation. The centrifugation was performed at 45,000 rpm, 20 °C for 15.5 h. Sedimentation profiles were recorded at 210 nm, with a radial resolution of 20 μm.

All sedimentation profiles were subjected to the software package Sedfit (version 15.01b) for data evaluation. The data was analyzed with the continuous distribution *c*(*s*) Lamm equation model to obtain the sedimentation coefficient distributions [273]. Fitting parameters (Table S3) including the

buffer density and viscosity were determined using Sednterp (version 20130813BETA). Partial specific volumes for labeled and unlabeled Aβ42 proteins and D3 were calculated according to Sednterp and Durchschlag et al. [334, 335]. Final graphs were generated using GUSSI (version 1.2.1) [274] and sedimentation coefficients were standardized to *s*-values in pure water at 20 °C ($s_{20,w}$).

Molecular dynamics (MD) simulation and data analysis

Simulation setup

To obtain complexes formed by Aβ42 and D3, we performed five independent MD simulations of twenty Aβ42 proteins and five D3 molecules in implicit solvent. The peptides were randomly placed in a simulation box with edge lengths of 41 nm × 33 nm × 38 nm and simulated for 100 to 325 ns using the parallel processing MD software Gromacs 4.5.5 [336]. The five simulations were initiated with different initial velocity distributions but all corresponding to a temperature of 310 K. The OPLS/AA force field[337, 338] was used to describe all peptides and a Generalized Born model with a hydrophobic solvent accessible surface area term (GBSA) [339] represented the aqueous environment. The dynamics was integrated with a leap-frog stochastic dynamics algorithm and periodic boundary conditions were applied. Hydrogen atoms were treated as virtual interaction sites, permitting an integration time step of 4 fs while maintaining energy conservation [340]. The temperature was kept at 310 K using velocity rescaling with a stochastic term algorithm [341] and a time constant for coupling of 2 ps. The electrostatic interactions were treated with a cut-off method with a value of 1.2 nm, and the van der Waals interactions were also cut at 1.2 nm. Snapshots were saved every 20 ps during each of the five MD simulations, from which all Aβ42-D3 complexes with stoichiometries of 1:1, 1:2, 2:1, and 2:2 were extracted from simulations and clustered using the method of Daura and coworkers with a cut-off of 0.2 nm [342]. For each stoichiometry, the five most populated conformations were selected as starting structures for the subsequent MD simulations with explicit solvent.

The explicit solvent MD simulations were performed with Gromacs 2018 [343], using the OPLS/AA force field [337, 338] and TIP3P water model [344]. Each of the 4×5 complexes (i.e., 5 conformations for each of the 4 stoichiometries considered) was placed in a dodecahedron box containing 3000-5000 water molecules, and the resulting model system neutralized by adding the needed amount of Na^+ or Cl^- ions. Before starting the production MD simulations, the energy of the systems was minimized until a maximal force of 100 kJ mol^{-1} nm^{-1} was reached with the steepest descent method. For further equilibration, MD simulations with restraints with a force constant of 1,000 kJ mol^{-1} nm^{-2} on the heavy atoms of the peptides were performed for 50 ps under isothermal-isobaric (NPT) conditions with a temperature of 310 K and a pressure of 1 bar, using a velocity rescaling thermostat to regulate the temperature and a Berendsen barostat for pressure control [345]. Another 20 ns of equilibration without restraints followed, before the production MD runs of 500 ns were executed. These simulations were also run under NPT conditions, but using an isotropic Parrinello-Rahman barostat for pressure control [346]. In all of these MD simulations, the electrostatic interactions were calculated via the particle mesh-Ewald method [347, 348] in connection with periodic boundary conditions. The cutoff values for the van der Waals and short-range Coulombic interactions were set at 1.0 nm. The LINCS algorithm was used to constrain all bond lengths [349] and the hydrogen atoms

were treated as virtual interaction sites, allowing to apply an integration time step of 4 fs while maintaining energy conservation [340]. Snapshots were saved every 20 ps in each of the twenty 500 ns MD simulations.

Prediction of the sedimentation coefficient

For determining the sedimentation coefficients of the simulated complexes, we first combined all snapshots collected during the 5 × 500 ns per stoichiometry and then clustered them using the Daura algorithm[342] with a cut-off of 0.2 nm. For all resulting clusters, the sedimentation coefficient was calculated for the representative cluster conformation using the program HydroPro10 [350]. The partial specific volume was estimated by dividing the total volume of the Aβ42:D3 complex in question by the molecular weight of that complex employing the 3V Volume Calculator for the volume and Visual Molecular Dynamics (VMD) for the molecular weight.[351, 352] For each Aβ42:D3 stoichiometry the mean sedimentation coefficient along with the standard deviation was determined by averaging over all clusters obtained for the 1:1, 1:2, 2:1 and 2:2 stoichiometry, respectively.

Secondary structure

The influence of complexation with D3 on the secondary structure of Aβ42 was characterized using the DSSP (Define Secondary Structure of Proteins) algorithm with default settings [353]. This method defines the secondary structures on the basis of energy calculations of H-bridges in the protein backbone. The average secondary structure of Aβ42 per complex stoichiometry was determined, where β-sheet and β-bridge were treated as β-structures, α-helix and 3_{10}-helix regarded as helix structures, and random coil, bends and turns collectively considered as coil structures.

ThT assay

Aβ42 at 20 μM was incubated with or without 2 μM D3 in 20 mM sodium phosphate, 50 mM NaCl (pH 7.4). In parallel, 20 μM Aβ42 containing 2 μM D3 was prepared in 55 mM Tris-HCl, 50 mM NaCl (pH 7.4) retaining the ionic strength of the phosphate buffer to determine whether the effect of D3 depends on buffers. ThT was added at a final concentration of 5 μM in all samples. The final volume of each sample was 200 μl. Samples were prepared on ice and were pipetted into a 96-well plate afterwards. The plate was sealed with a microplate sealing film. All measurements were conducted at 20 °C with a microplate reader (Infinite M200, Tecan, Männedorf, Switzerland). The fluorescence was recorded at an excitation wavelength (λ_{ex}) of 445 nm and an emission wavelength (λ_{em}) of 485 nm every 30 min for 120 h. D3 alone does not induce ThT fluorescence. All samples were prepared in triplicate.

The ThT data was then subjected to the online server AmyloFit [313] with a customized sigmoidal equation (eq. 28) to determine the lag time t_{lag}, and the half completion time of the aggregation process $t_{1/2}$, according to previous studies [354, 355].

$$I_t = k_0 t + A/(1 + \exp(-k(t - t_{1/2}))) \qquad \text{eq.28}$$

Where k_0 represents the slope of the baseline, A is the amplitude, k denotes the apparent elongation rate constant. The lag time t_{lag} can be derived from the intercept between the time axis and the tangent with slope k from the midpoint of the fitted sigmoidal curve, which is given by the following equation (eq.29):

$$t_{lag} = t_{1/2} - 2/k \qquad \text{eq.29}$$

Seeding experiment

Aβ42 seeds were prepared from fibrils according to Ehrnhoefer et al. [272]. Aβ42 was first dissolved in 20 mM sodium phosphate, 50 mM NaCl (pH 7.4) to prepare a 40 μM sample solution. The sample was then incubated quiescently at room temperature for 120 h. Finally, Aβ42 sample was treated for 45 min in a cold ultrasonic bath.

Samples for ThT kinetics were prepared by introducing D3 and (or) Aβ42 seeds into freshly dissolved Aβ42 in 20 mM sodium phosphate, 50 mM NaCl (pH 7.4). The concentration of Aβ42 monomer in all samples was 10 μM, and all samples contained 5 μM ThT. The concentrations of Aβ42 seeds were set to either 1% or 5% (v/v) (corresponding to 0.1 or 0.5 μM, respectively, based on monomer concentration) and the final concentration of D3 was 1 μM. A sample of 10 μM Aβ42 without seeds, but with 1 μM D3 was used as a control. Samples were pipetted to a 96-well plate, with each well containing 200 μl samples. The plate was then covered with a sealing film. ThT fluorescence of all samples was recorded using the same device and parameters as described above for ThT assays. All samples were prepared in duplicate. Final data was normalized and averaged based on the repetitions.

Circular dichroism spectroscopy

Circular dichroism spectroscopy was applied to detect how D3 affects the secondary structure transition of Aβ42 under current experimental condition. Aβ42 aliquots were dissolved in 20 mM sodium phosphate, 50 mM NaF (pH 7.4) to obtain a working concentration of 40 μM. NaF was used to substitute NaCl in this measurement to maintain the ionic strength of the buffer, so as to avoid the strong absorbance of NaCl in the far-UV area. For samples with D-peptide treatment, D3 was introduced into Aβ42 solutions to get a final concentration of 4 μM, equivalent to a molar ratio of 10:1 (Aβ42:D3). Besides, Aβ42 samples with D3 addition at 33 h were also included to test whether D3 is potent in pre-incubated Aβ42 samples. All samples were prepared on ice before being transferred to 1 mm path length quartz cuvettes. The final volume of each sample was 200 μl. CD spectra were recorded from 260 nm to 190 nm using a J-815 spectropolarimeter (Jasco, Tokyo, Japan). All measurements were carried out with a step size of 0.5 nm and a bandwidth of 2 nm. The scanning speed was set to 100 nm/min and 10 scans were accumulated for each sample. Ellipticities at 198 nm and 217 nm were plotted against the incubation time to monitor the transition kinetics of Aβ42 samples in the absence or presence of D3. Samples were maintained at 20 °C within the measurement duration of 120 h and were prepared in triplicate. CD spectra for all samples were deconvoluted using the online server Dichroweb [356, 357] by applying the CDSSTR algorithm [358] and reference dataset Set 7 [359].

Turbidity assay

Turbidity measurements were conducted by measuring the absorbance of the sample at 405 nm [360] to check whether D3 induces the formation of large Aβ42 aggregates in the time scale of the thermal equilibration in AUC experiments. Samples were prepared by dissolving Aβ42 aliquots in 20 mM sodium phosphate, 50 mM NaCl (pH 7.4) and adding D3 stock solution (2 mM). The final concentration of Aβ42 was set to 40 μM in all samples and the molar ratios between Aβ42 and D3 were 10:1, 2:1, 1:1 and 1:2, respectively. Samples containing 40 μM Aβ42 alone were included as a control. The turbidity assay was carried out by measuring the spectra of all samples from 450 nm to 210 nm in a 1 cm quartz cuvette using a V-650 UV-Vis spectrophotometer (Jasco, Tokyo, Japan). The measurements were performed directly after preparing all samples and repeated after 2 h of incubation at ambient temperature. All samples were subjected to a 15 min centrifugation at 726 *g* (equivalent to the speed during the calibration in AUC experiments) afterwards and the supernatants were collected to measure the spectra again.

Atomic force microscopy

Atomic force microscopy imaging was performed to characterize morphologies of Aβ42 samples in the presence or absence of D3. In brief, 40 μM Aβ42 was incubated with or without 4 μM D3 in 20 mM sodium phosphate, 50 mM NaCl (pH 7.4) at 20 °C. At 48 h and 120 h, 10 μl samples were pipetted onto freshly cleaved mica and were further incubated at room temperature for 30 min. Mica with deposited samples were rinsed with ultrapure water for three times and finally dried with nitrogen gas. AFM imaging was carried out in air at room temperature, using silicon cantilevers (OMCL AC160 TS, Olympus, Tokyo, Japan) and a JPK NanoWizard 3 microscope (JPK Instruments AG, Berlin, Germany) in AC mode. The nominal tip diameter of the cantilever was 7 nm. AFM height images at 10×10 μm² and 1×1 μm² (both with a resolution of 1024×1024 pixel) for all samples were taken with a line rate of 1 Hz and respective scanning speeds of 22.55 μm/s and 2.48 μm/s. Data was processed with JPK NanoWizard SPM data processing software.

Table S3. Parameters used for evaluating sedimentation velocity data at 20 °C.

Partial specific volume $\bar{\mathbf{v}}$ (cm^3/g) [a]	FITC-Aβ42	0.732
	FITC-D3	0.667
Molecular mass (g/mol)	FITC-Aβ42	4974.6
	FITC-D3	2000
Buffer viscosity (P) [b]	20 mM sodium phosphate, 50 mM NaCl	0.01015
	55 mM Tris-HCl, 50 mM NaCl	0.01024
	H_2O	0.01002
Buffer density (g/cm^3) [b]	20 mM sodium phosphate, 50 mM NaCl	1.003
	55 mM Tris-HCl, 50 mM NaCl	1.002
	H_2O	0.9982

[a] Partial specific volumes of FITC-Aβ42 and FITC-D3 were calculated based on the amino acid composition and the formulated values for organic compounds documented by Durchschlag et al. [334].

[b] Buffer density and viscosity were calculated using Sednterp (version 20130813BETA).

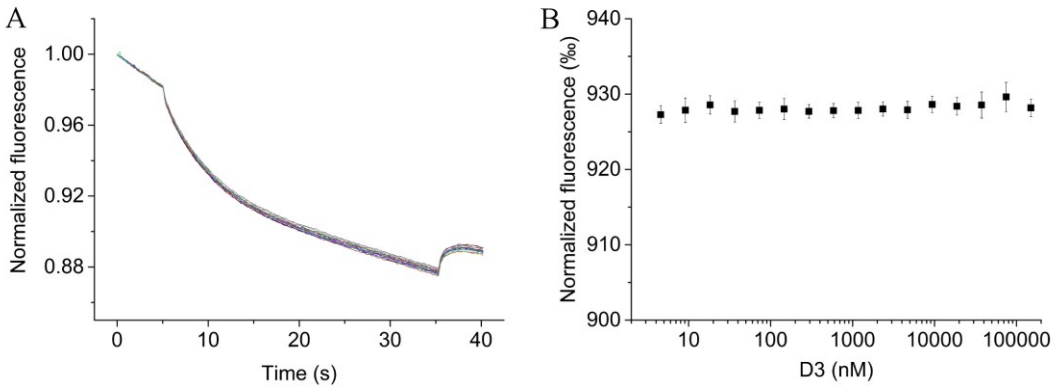

Figure S7. The fluorescein does not interact with D3. 40 nM fluorescein was titrated with different concentrations of D3 in 20 mM sodium phosphate, 50 mM NaCl (pH 7.4) at 22 °C. The time traces from one measurement was shown in A. The corresponding thermophoresis was shown in B. Samples were prepared in triplicate. The data was normalized and averaged.

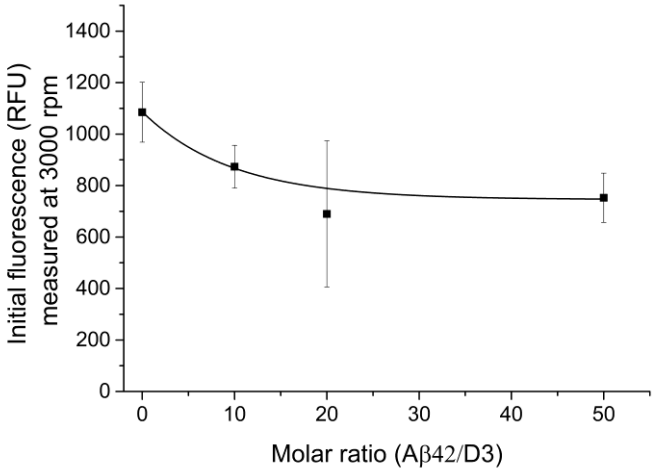

Figure S8. Initial fluorescence signals of 0.2 μM FITC-D3 incubated with different concentrations of freshly prepared Aβ42 in 20 mM sodium phosphate, 50 mM NaCl, 0.0004% (w/v) PEI. 100 μl samples were loaded into 3-mm double-sector titanium cells and were incubated for 2 h prior to the centrifugation for thermal equilibration. Fluorescence signals were recorded using the fluorescence detection system while the centrifuge was spinning at 3000 rpm (726 g). Data was averaged based on five independent experiments.

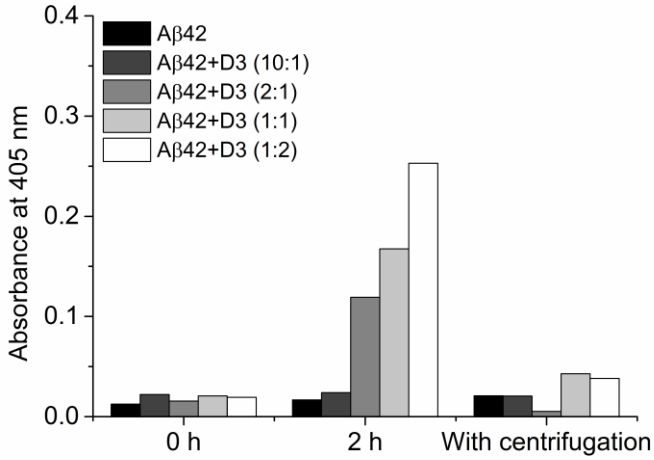

Figure S9. Turbidity measurements of Aβ42 in the absence of presence of D3. 40 μM Aβ42 was incubated with 4, 20, 40 and 80 μM D3 in 20 mM sodium phosphate, 50 mM NaCl, 0.01% Tw20 (pH 7.4) at ambient temperature. The turbidity expressed by the absorbance at 405 nm was determined by scanning the spectrum of the sample using a UV-Vis spectrophotometer. The centrifugation after 2 h of incubation was performed using a benchtop centrifuge at 726 g for 15 min.

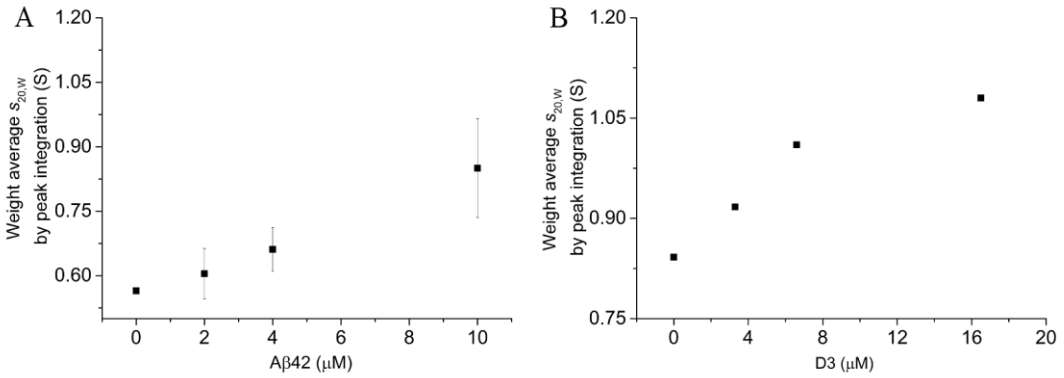

Figure S10. Weight average $s_{20,w}$ of FITC-D3 incubated with Aβ42 (A) and FITC-Aβ42 incubated with D3 (B) based on the peak integration of s-value distributions obtained from c(s) analyses shown in Figure 34 in the main text.

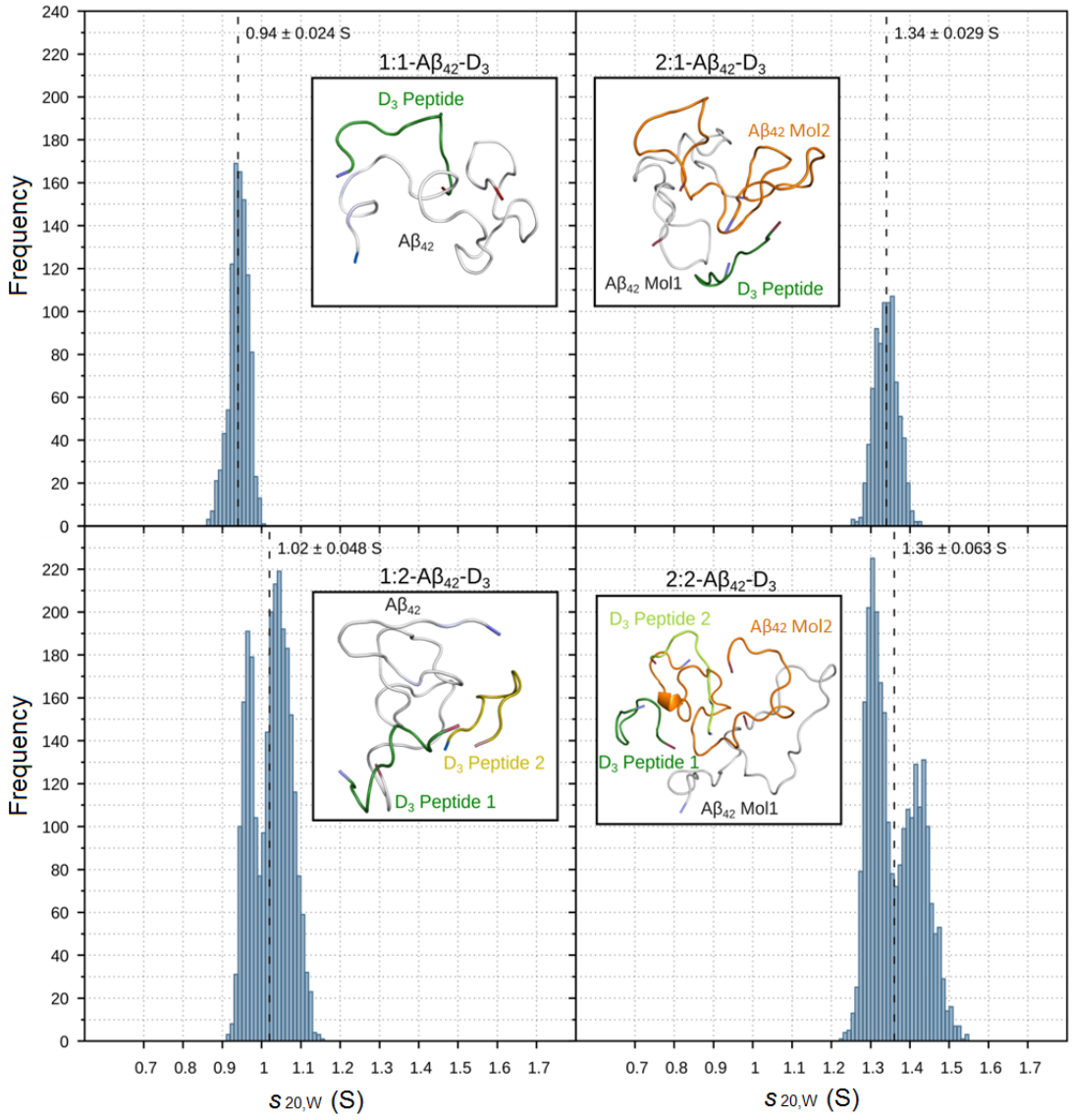

Figure S11. Histograms of the $s_{20,w}$ values for the simulated Aβ42-D3 complexes. The representative conformation taken from the most populated cluster of each complex stoichiometry is shown as an insert. The average $s_{20,w}$ value with standard deviation is given for each stoichiometry.

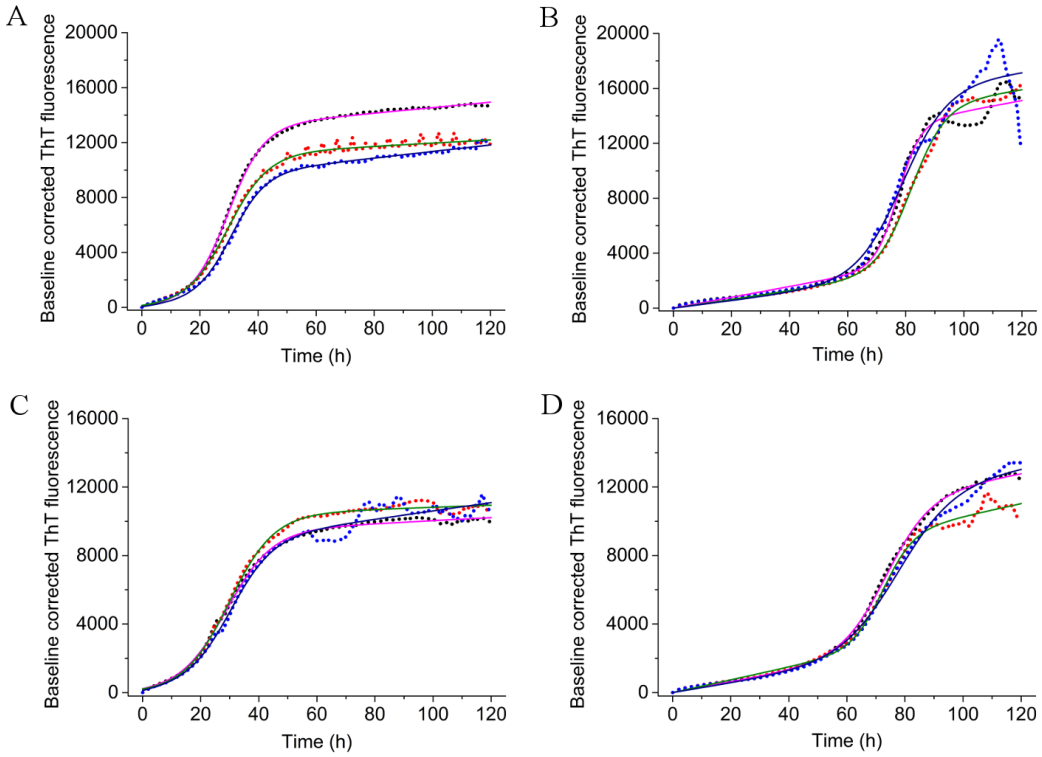

Figure S12. AmyloFit analyses of ThT kinetics for Aβ42 in the absence or presence of 0.1 fold D3 in different buffers. 40 μM Aβ42 was incubated without (A and C) or with (B and D) 4 μM D3 either in 20 mM sodium phosphate, 50 mM NaCl (A and B) or 55 mM Tris-HCl, 50 mM NaCl (C and D) at pH 7.4, 20 °C for 120 h. All kinetics were subjected to AmyloFit using the equation 28 in the main text to obtain t_{lag} and $t_{1/2}$. Fluorescence signals were corrected to the baseline. The raw data and the fitted data were expressed in dotted and solid lines, respectively. All samples were prepared in triplicate.

Table S4. AmyloFit analyses of ThT kinetics of Aβ42 at 20 μM incubated with or without 0.1 fold D3 in sodium phosphate buffer or Tris-HCl buffer at 20 °C. [a]

Sample	Buffer	$t_{1/2}$ (h)	k	t_{lag} (h)
Aβ42	sodium phosphate	30.0 ± 0.7	0.15 ± 0.01	17.3 ± 1.6
Aβ42	Tris-HCl	29.7 ± 0.8	0.13 ± 0.01	14.5 ± 1.4
+D3 (10:1)	sodium phosphate	79.3 ± 2.3	0.18 ± 0.07	67.6 ± 3.8
+D3 (10:1)	Tris-HCl	74.5 ± 2.8	0.14 ± 0.04	59.3 ± 2.2

[a] Data was obtained by fitting the kinetics with equations [354, 355] shown in the materials and methods section using the online webserver AmyloFit [313].

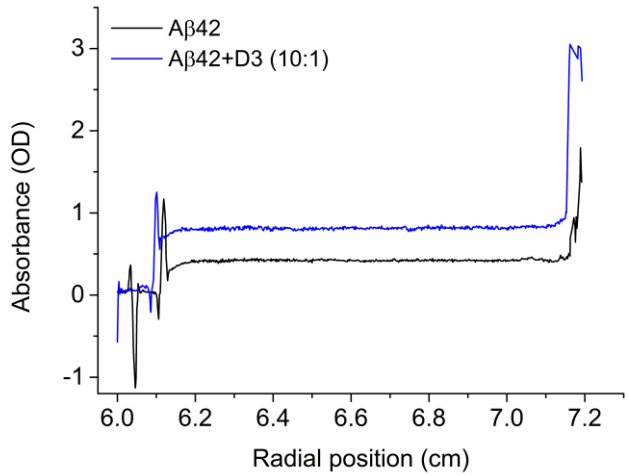

Figure S13. The first scan of the sedimentation profiles of 20 μM Aβ42 incubated without or with 2 μM D3 measured at 210 nm, 45,000 rpm by the absorbance based AUC.

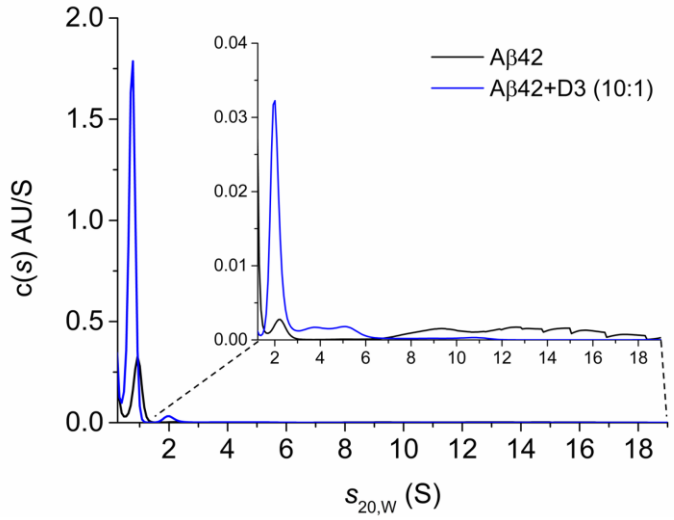

Figure S14. Sedimentation velocity analysis of Aβ42 incubated with or without 0.1 fold D3 for 24 h. Aβ42 at 20 μM was incubated without or with 2 μM D3 in 20 mM sodium phosphate, 50 mM NaCl (pH 7.4) at 20 °C for 24 h. Samples were analyzed in an AUC with absorbance detection at 45,000 rpm for 15.5 h and sedimentation profiles were evaluated using c(s) analysis to obtain $s_{20,w}$ values. The insert shows the distribution between 1.25 and 19 S.

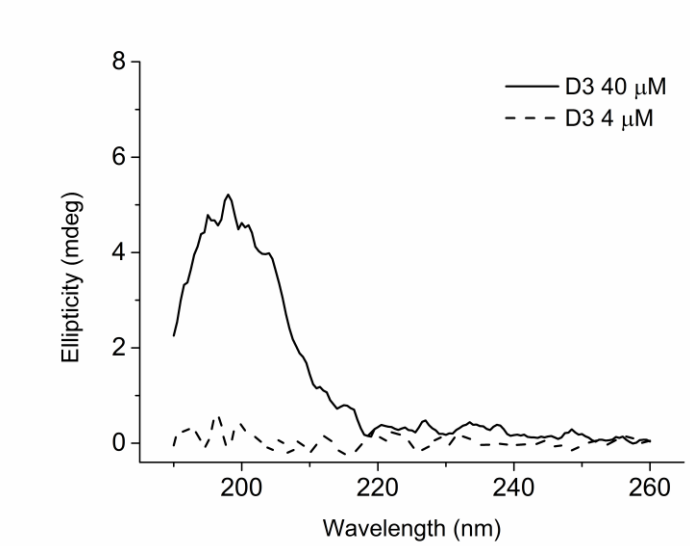

Figure S15. CD spectra of 4 μM (dashed) and 40 μM (solid) D3 in 20 mM sodium phosphate, 50 mM NaF (pH 7.4).

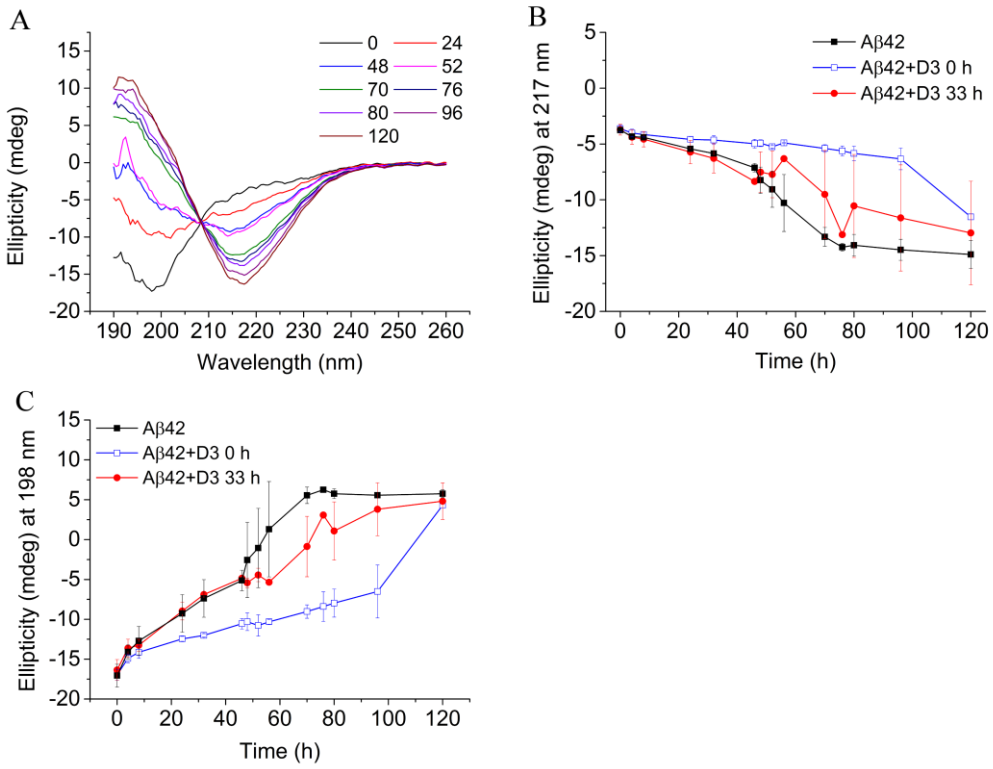

Figure S16. CD analyses showing the effect of delayed addition of 0.1 fold D3 on the secondary structure transition of Aβ42. 4 μM D3 was added after 40 μM Aβ42 was incubated for 33 h in 20 mM sodium phosphate, 50 mM NaF (pH 7.4) at 20 °C. The CD spectra at selected time points (h) are shown in A. The conversion kinetics of Aβ42 with D3 addition at 33 h by plotting ellipticities at 217 nm (B) or 198 nm (C) against the incubation time were compared with those of Aβ42 alone and Aβ42 with D3 addition at 0 h. Data was averaged based on triplicate.

Chapter III

Characterization of the interaction between D-enantiomeric peptide RD2 and Aβ42

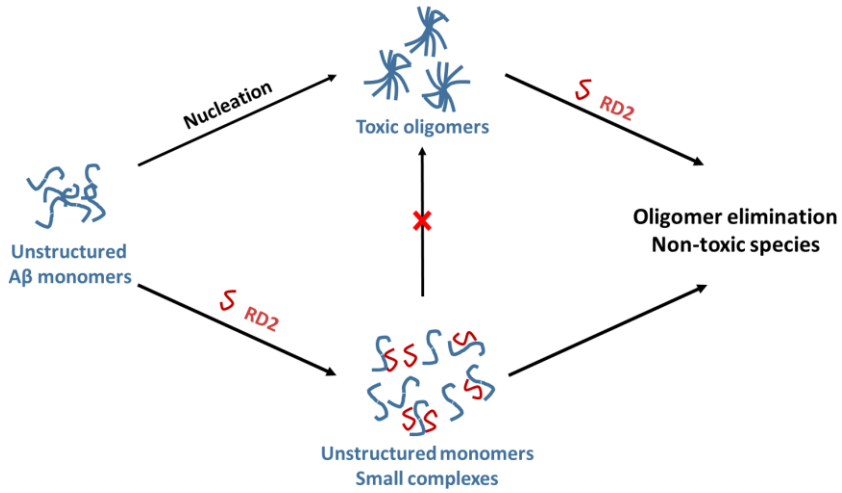

Abstract

The aggregation of amyloid β (Aβ) into oligomers and fibrillary structures are critical for the pathogenesis of Alzheimer's disease (AD). Recently research effort has focused on developing novel agents that can preferentially suppress Aβ oligomer mediated toxicities, for example, by directly targeting these toxic assemblies. The compound RD2 has been developed and optimized for Aβ42 monomer binding and stabilization in its native intrinsically disordered conformation. It has been demonstrated to improve and even reverse the cognition and behavioral deficits in AD mouse models, while the detailed mechanism of action is not fully clarified. Here we explored the interaction between RD2 and Aβ42 monomers, and its consequences for the fibrillation of Aβ42. RD2 binds to Aβ42 monomers with submicromolar affinities, according to the microscale thermophoresis. The binding results in the complex formation between RD2 and Aβ42 monomers at 1:1 and other stoichiometries, as revealed by analytical ultracentrifugation. At substoichiometric levels, RD2 slows down the secondary structure conversion of Aβ42 and significantly delays the fibril formation. Our research provides experimental evidence in supporting that RD2 eliminates toxic Aβ assemblies by stabilizing unstructured Aβ monomers. The study further supports the promising application of RD2 in counteracting Aβ aggregation related pathologies.

This chapter was adapted from the manuscript:

Tao Zhang, Luitgard Nagel-Steger, Dieter Willbold. Towards the mode of action of the clinical stage all-D-enantiomeric peptide RD2 on Aβ42 aggregation. *Manuscript to be submitted.*

Introduction

Alzheimer's disease (AD) is a progressive neurodegenerative disorder leading to cognitive and behavioral impairment in the elderly. The aggregation of amyloid β (Aβ) leads to the generation of oligomeric assemblies and fibrils [361]. Although amyloid plaques are mainly composed of fibrillar structures, increasing evidence proves that Aβ oligomers are the most toxic species in vivo and are highly relevant to Aβ aggregation related pathologies [135, 362, 363]. Therefore, inhibiting the formation of Aβ oligomers or by removing existing toxic oligomers could be a promising strategy for disease intervention. Aβ monomers are intrinsically disordered in aqueous solution, while it has been shown that monomeric units are partially folded within the toxic oligomers [98]. It is of high value to develop compounds that can stabilize Aβ monomers in the native unstructured conformation to attain the inhibition of oligomer formation and even the dissociation of already formed toxic assemblies.

Based on the abovementioned rationale, we developed a series of peptides consisting solely of D-enantiomeric amino acids. The lead compound D3, which was selected using mirror image phage display, has the ability to inhibit amyloid fibril formation and directly eliminate Aβ oligomers [201, 202, 209, 212]. Following the optimization we then obtained RD2, an all-D-enantiomeric peptide, for Aβ oligomer elimination. Our previous studies have demonstrated that RD2 efficiently reduces the content of Aβ oligomers both in vitro and in the brain of AD mouse models [214]. RD2 is not only able to enhance the cognition and learning ability of AD mouse models [214], but also reverse cognitive deficits in transgenic mice with full-blown pathologies [215]. Besides, RD2 has excellent bioavailability and proteolytic stability according to our previous research [364, 365]. Although it has been well established that RD2 possesses Aβ oligomer elimination efficacy, the underlying mechanism is not fully understood. In particular, whether the RD2 peptides interact with unstructured Aβ monomers remains to be investigated. Since RD2 is also disordered and positively charged in aqueous solution, we speculate that the interaction between RD2 and Aβ monomer might be similar to the interaction between two intrinsically disordered proteins carrying opposite charges, as has been described recently by Borgia et al. [304].

In order to study the interaction between RD2 peptides and Aβ42 monomers, we applied solution based analytical ultracentrifugation (AUC) and microscale thermophoresis (MST) to determine the binding and possible complex formation between these two molecules. These fluorescence approaches require nanomolar concentrations of analytes and therefore are helpful to minimize the self-aggregation of Aβ42, The binding event between RD2 and Aβ42 monomers could be reliably detected. Further, to study the influence of RD2-Aβ42 interaction on the aggregation process of Aβ42, we employed Thioflavin T (ThT) assays, circular dichroism (CD) spectroscopy and atomic force microscopy (AFM) imaging. Substoichiometric concentrations of RD2 were tested in the present study. We aim to illustrate the connection between RD2-Aβ42 monomer interaction and the effect of RD2 on the elimination of toxic Aβ oligomers.

Materials and methods

Chemicals and reagents

Fluorescein isothiocyanate (FITC) labeled and unlabeled Aβ42 were purchased from Bachem (Weil am Rhein, Germany). The labeling was prepared by linking the fluorophore to the N-terminus of Aβ42 via an additional β-alanine. The purities for FITC labeled Aβ42 (FITC-Aβ42) and free Aβ42 were 88.2% and 95.2%, respectively. RD2 peptides were synthesized by peptides & elephants (Hennigsdorf, Germany) as lyophilized powder with >95% purity. 1, 1, 1, 3, 3, 3-hexafluoro-2-propanol (HFIP), Thioflavin T, Tween-20 (Tw20) and other chemicals are commercially available from Sigma-Aldrich (Munich, Germany). Aβ42 products (1 mg) were incubated in HFIP overnight at room temperature and were divided into small aliquots. HFIP was then removed and Aβ42 proteins were stored at -80 °C before use. RD2 stock solution was prepared in distilled H_2O. Working solutions were prepared using 20 mM sodium phosphate, 50 mM NaCl (pH 7.4), unless otherwise specified.

Microscale thermophoresis

Microscale thermophoresis (MST) was performed to determine the dissociation constant of RD2 and Aβ42 interaction. This method is based on the Soret effect describing the directed migration of macromolecules under a temperature gradient [236, 239]. The movement is monitored by recording changes in fluorescence signals of dye labeled molecules incubated with different concentrations of the binding partner [237]. FITC-Aβ42 was dissolved in either 20 mM sodium phosphate, 50 mM NaCl (pH 7.4) or 5 mM sodium phosphate, 50 mM NaCl (pH 7.4) in the presence of 0.01% (v/v) Tw20 to get a stock concentration of 80 nM. RD2 was prepared in the same buffer to obtain two-fold serial dilutions ranging from 300 µM to 9.16 nM. Final samples were prepared by mixing equal volumes of FITC-Aβ42 and the serial dilutions of RD2 so that the final concentration of FITC-Aβ42 was 40 nM, and the concentration range of RD2 was from 150 µM to 4.58 nM. MST measurements were carried out at 22 °C using a Monolith NT.115 instrument (NanoTemper Technologies, Munich, Germany) with 40% LED power and 60% MST power. The on and off time of the infrared (IR) laser were set to 30 s and 5 s, respectively. Samples were prepared in triplicate. Control experiments by incubating free dye (fluorescein) with RD2 at the same concentration range were also included to confirm the interaction between RD2 and Aβ42. Binding curves were generated by quantifying changes in the normalized fluorescence (ΔF_n) as a function of the concentration of the titrant. The data was analyzed by PALMIST using a 1:1 binding model [329]. The confidence interval of the fitting was set to 68.3%. Graphic output was generated by GUSSI (version 1.2.1) [274].

Sedimentation velocity analysis

Size distributions of Aβ42 in the presence or absence of RD2 were investigated by utilizing analytical ultracentrifugation equipped with a fluorescence detection system (AUC-FDS). The system uses an excitation laser at 488 nm and an emission cut-off filter at 505 nm to monitor the sedimentation process of fluorescent molecules. 0.33 µM FITC-Aβ42 was mixed with various concentrations of RD2 in 20 mM sodium phosphate, 50 mM NaCl (pH 7.4) to prepare samples with molar ratios of 1:1, 1:10 and 1:20 (FITC-Aβ42:RD2). 100 µl sample were then loaded into 3-mm double-sector

titanium cells (Nanolytics, Potsdam, Germany). FITC-Aβ42 alone was included as a control. In parallel, 0.33 μM FITC-Aβ42 incubated with excessive concentrations of RD2 in 55 mM Tris-HCl, 50 mM NaCl (pH 7.4) were also centrifuged at the same speed and temperature to examine the size distribution. Both buffer contained 0.01% (v/v) Tw20 to overcome unspecific surface adsorption. All samples were incubated within cells for about 2 h for temperature equilibration and vacuum. The spinning began with a calibration process at 3000 rpm, and then accelerated to 60,000 rpm (289,000 g) for final centrifugation at 20 °C for 15 h. The sedimentation profile was recorded with a radial resolution of 20 nm.

To determine how RD2 may influence the aggregation of Aβ42, an absorbance based sedimentation velocity measurement was performed. Aβ42 at 20 μM was incubated with or without 2 μM RD2 in 20 mM sodium phosphate, 50 mM NaCl (pH 7.4) at 20 °C for 24 h. Samples (380 μl) were then loaded into 12-mm double-sector aluminum cells and were centrifuged at 45,000 rpm, 20 °C for 15.5 h. Sedimentation profiles were recorded at 210 nm, with a step size of 20 μm.

All measurements were carried out using a Beckman Optima XL-A ultracentrifuge (Beckman-Coulter, Brea, CA, USA). Experimental data was evaluated with the software package Sedfit (version 15.01b) and the continuous distribution *c*(*s*) Lamm equation model to obtain the sedimentation coefficient (*s*-value) distribution [273]. Buffer density and viscosity (Table S5) were calculated using Sednterp (version 20130813BETA). Partial specific volume ($\bar{v}$) was determined according to Sednterp and Durchschlag et al. [334]. The final graphs were created by GUSSI (version 1.2.1) [274].

Thioflavin T assay

Thioflavin T assay was conducted to assess the aggregation kinetics of Aβ42 in the presence or absence of RD2 peptide. In brief, Aβ42 aliquots were dissolved in 20 mM sodium phosphate, 50 mM NaCl (pH 7.4). RD2 was introduced into Aβ42 solutions to obtain samples containing 1 μM or 2 μM D-peptide. ThT was added into all samples to get a final concentration of 5 μM. Sample solutions were then transferred to a 96-well microplate, with each well containing 200 μl solution. The fluorescence was recorded using a microplate reader (Tecan, Männedorf, Switzerland) with an excitation wavelength (λ_{ex}) of 445 nm and an emission wavelength (λ_{em}) of 485 nm every 30 min for 120 h. The temperature was kept constant at 20 °C. Samples were prepared with repetitions. The kinetics of Aβ42 fibrillation was evaluated using AmyloFit [313] with a customized equation (eq.28) as previously mentioned [354, 355].

$$I_t = k_0 t + A/(1 + \exp(-k(t - t_{1/2}))) \quad \text{eq.28}$$

Where k_0 refers to the slope of the baseline. A is the amplitude. k represents the apparent elongation rate. $t_{1/2}$ is the half completion time of the aggregation process. The lag phase (t_{lag}), which is given by the intercept between the time axis and the tangent with slope k from the midpoint of the fitted curve, can be derived from the following equation (eq.29) [355].

$$t_{lag} = t_{1/2} - 2/k \quad \text{eq.29}$$

Seeding experiment

To prepare Aβ42 seeds from the fibrils, Aβ42 was first dissolved in 20 mM sodium phosphate, 50 mM NaCl (pH 7.4) to prepare 40 μM sample solution. The sample was then incubated quiescently at room temperature for 120 h. Finally, Aβ42 sample was sonicated for 45 min in a cold water bath [272].

Samples for ThT kinetics were prepared by introducing RD2 and (or) Aβ42 seeds into freshly dissolved Aβ42 in 20 mM sodium phosphate, 50 mM NaCl (pH 7.4). The concentration of Aβ42 monomer in all samples was 10 μM, and all samples contained 5 μM ThT. The concentrations of Aβ42 seeds were set to 1% or 5% (0.1 or 0.5 μM corresponding to monomer concentration) and the final concentrations of RD2 were 1 μM. 10 μM Aβ42 without seeds and RD2 was used as a control. Samples were pipetted to a 96-well plate, with each well containing 200 μl samples. The plate was then covered with a sealing film. ThT fluorescence of all samples was recorded using the same device and parameters as described for ThT assays. All samples were prepared in duplicate. Final data was normalized and averaged based on the repetitions.

Circular dichroism spectroscopy

The secondary structure conversion of Aβ42 incubated with or without RD2 was characterized using circular dichroism (CD) spectroscopy. 40 μM Aβ42 in the absence or presence of 4 μM RD2 was prepared in 20 mM sodium phosphate, 50 mM NaF (pH 7.4). 200 μl sample was then loaded into a 1 mm quartz cuvette and was maintained at 20 °C. CD spectra were recorded using a J-815 spectropolarimeter (Jasco, Tokyo, Japan) from 260 nm to 190 nm, with a step size of 0.5 nm and a bandwidth of 2 nm. The scanning speed was 100 nm/min. 10 scans were accumulated for the same sample at each time point, up to 120 h of incubation. In a separate experiment with delayed RD2 addition, tiny volume of RD2 stock was introduced into 40 μM Aβ42 which was pre-incubated for 33 h to get a final RD2 concentration at 4 μM. Ellipticities at 217 nm and 198 nm were plotted against the incubation time to detect the conversion kinetics. The deconvolution of CD spectra was performed with the online software Dichroweb [357] and the CDSSTR algorithm [359] using reference dataset Set 7 [366]. The fractions of unordered structure and β-strand were determined for Aβ42 samples with or without RD2 treatment. Samples were prepared in triplicate.

Atomic force microscopy imaging

The influence of RD2 on the aggregation of Aβ42 was also examined by atomic force microscopy to determine morphologies of Aβ aggregates at different incubation time points. 40 μM Aβ42 was incubated with or without 4 μM RD2 in 20 mM sodium phosphate, 50 mM NaCl (pH 7.4) at 20 °C for 120 h. Solutions were sampled at 48 h and 120 h and pipetted onto freshly prepared mica for incubation at room temperature. The mica was then rinsed with distilled water and dried with nitrogen gas. AFM imaging was performed using silicon cantilevers (OMCL AC160 TS, Olympus, Tokyo, Japan) and JPK NanoWizard 3 microscope (JPK Instruments AG, Berlin, Germany) in AC mode. The nominal diameter of the cantilever was 7 nm. AFM height images of all samples were taken with a line rate of 1 Hz at room temperature in air. Data was processed with the JPKSPM data processing software from the same manufacturer.

Turbidity assay

Aβ42 aliquots were first dissolved in 20 mM sodium phosphate, 50 mM NaCl (pH 7.4) and mixed with RD2 stock (3.125 mM) to prepare working solutions. The final concentration of Aβ42 was set to 40 μM in all samples and the molar ratios between Aβ42 and RD2 were 10:1, 2:1, 1:1 and 1:2, respectively. Samples containing 40 μM Aβ42 alone were included as a control. The turbidity assay was carried out using a V-650 UV-Vis spectrophotometer (Jasco, Tokyo, Japan) by measuring the spectra of all samples from 450 nm to 210 nm in a 1 cm quartz cuvette. The measurement was performed directly after preparing all samples and was repeated after 2 h of incubation at ambient temperature. All samples were subjected to a 15 min centrifugation at 726 g (equivalent to the speed during the calibration in AUC experiments) afterwards and the supernatants were collected to measure the spectra again. The turbidity was quantified using the absorbance of the sample at 405 nm.

Results and discussion

RD2 interacts with Aβ42 with a high affinity

The dissociation constant between RD2 and Aβ42 monomer was measured by microscale thermophoresis. It has been shown that the critical aggregation concentration of Aβ42 is about 90 nM [328]. FITC-Aβ42 was applied at a low nanomolar concentration (40 nM) to minimize the self-aggregation of Aβ42 protein. The binding between RD2 and Aβ42 monomer should be the main event under the current condition. The influence of ionic strength on the interaction was also examined via comparing the K_D values in buffers with different ionic strength. As shown in the fluorescence time traces and plots in Fig. 39, the K_D for RD2 and FITC-Aβ42 in 5 mM sodium phosphate, 50 mM NaCl (pH 7.4) (low ionic strength buffer) was determined to be 130 [80, 190] nM by quantifying the thermophoresis. The K_D value increased to 330 [290, 380] nM when the ionic strength was elevated in 20 mM sodium phosphate, 50 mM NaCl (pH 7.4) (high ionic strength buffer). However, both values are much lower than the reported K_D (3.6 ± 0.7 μM) in SPR measurements. We excluded the possibility that RD2 directly influenced the property of the fluorophore as the control experiment did not show any difference with respect to the thermophoresis and bleaching in fluorescein samples incubated with different concentrations of RD2 (Fig. S17). It should be mentioned that the thermophoretic response of all samples was constant over the measurement and can be measured repeatedly, also indicating the absence of unwanted aggregation. The increase in the binding affinity of RD2 to Aβ42 monomer by reducing the ionic strength of the buffer may suggest that the interaction between these two molecules is partly mediated by charge effects. This is consistent with our previous study on the lead compound D3 showing that increasing the ionic strength of the buffer weakened the interaction between D3 and Aβ42 [367]. Similar finding on the interaction between a decapeptide containing three L-Arg residues and Aβ40 was also reported [315]. Borgia et al. recently demonstrated that oppositely charged proteins histone H1 and prothymosin-α form complexes with picomolar affinity and that the binding is strongly influenced by the ionic strength [304]. The screening of net charges of the protein by solvent ions is weakened when the ionic strength of the buffer is reduced, thus leading to enhanced electrostatic interaction of oppositely

charged molecules [314]. The binding affinity determined in SPR experiments was much lower than those measured in MST experiments. This discrepancy might be due to different experimental setups applied to quantify the K_D. N-terminally biotinylated Aβ42 was immobilized onto sensor chips through biotin-streptavidin coupling in previous SPR experiments. This may somehow influence the conformational flexibility of Aβ42 monomers and hinder the accessibility of RD2 to all the binding sites of Aβ42, making the interaction less efficient than that occurs in solution bases MST measurements.

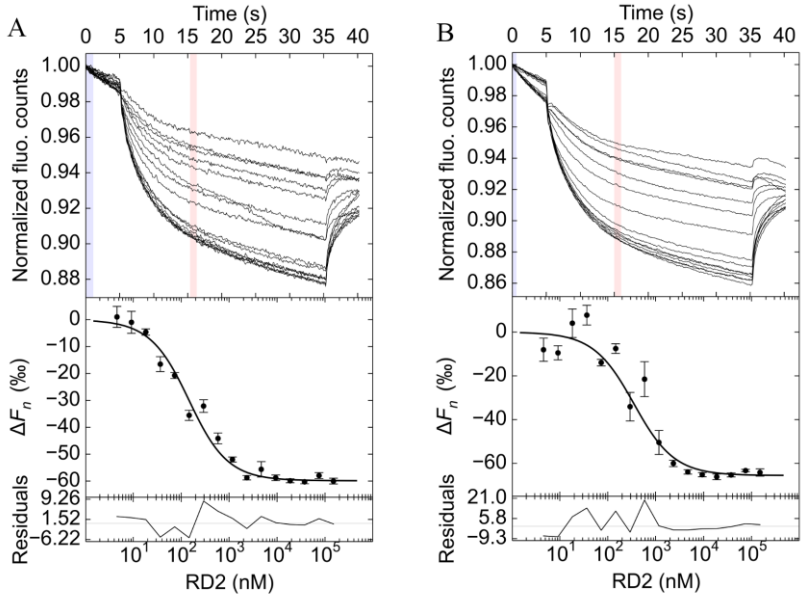

Figure 39. Determination of the dissociation constant for Aβ42 and RD2 interaction using microscale thermophoresis. 40 nM FITC-Aβ42 was incubated with different concentrations of RD2 in 5 mM sodium phosphate, 50 mM NaCl (A), or 20 mM sodium phosphate, 50 mM NaCl (B) in the presence of 0.01% Tw20 at pH 7.4, 22 °C. Binding curves were generated by quantifying the change in the normalized fluorescence (ΔF_n) according to the reference zone (light blue) and the analysis zone (light red). The 1:1 binding model was applied to evaluate dissociation constants using the software PALMIST. Time traces from one measurement are displayed on the top panel of each graph. Data points and fitting curves are presented on the bottom panel. Samples were prepared in triplicate.

Complex formation between Aβ42 and RD2 in sedimentation velocity analysis

We applied analytical ultracentrifugation equipped with a fluorescence detection system to evaluate size distributions of Aβ42 in the presence of different concentrations of RD2. The application of fluorescently labeled Aβ42 enabled us to use relatively low concentration of materials for sedimentation velocity analysis, which could help to reduce the self-aggregation of Aβ42 in aqueous solutions. As displayed in Fig. 40, the sedimentation coefficient of FITC-Aβ42 alone was determined to be 0.76 S in the *c*(*s*) analysis, corresponding to the monomeric unit. No further species above 1 S was found in free FITC-Aβ42 samples. The dominant monomeric species in solution offers the opportunity to identify the possible complex formation between RD2 and Aβ42 monomers. The presence of RD2 peptide affected the size distribution by reducing the abundance of the major peak at around 0.75 S. We could see a slight decrease in the area under curve for this species depending on RD2 concentrations. Besides, new species within 1 and 3 S could be observed in FITC-Aβ42

samples containing 3.3 and 6.6 µM RD2 (corresponding to 1:10 and 1:20 molar ratios, respectively). The averaged *s*-value for this new species by integrating the peak was 1.85 S. However, the fraction of the newly appeared species was low in both samples. MST results have revealed that RD2 binds strongly to Aβ42 monomers, while in AUC measurements we did not observe high abundance of the 1:1 complex. Considering our previous findings on D3, it is possible that in this experimental setup, we were not able to distinguish the 1:1 complex from FITC-Aβ42 monomer due to the similar *s*-values between these two species. The 1.85 S species was therefore complexes with higher than 1:1 stoichiometry. Similar size distributions were found in FITC-Aβ42 and RD2 samples incubated in Tris-HCl buffer (Fig. S18). The decrease in the amount of FITC-Aβ42 monomers suggested that monomers have been consumed in the presence of RD2 by forming small complexes and probably large co-precipitates. The weight average sedimentation coefficient for all samples was also determined. As shown in Fig. S19, there is a gradual increase in the average $s_{20,w}$ depending on the concentration of RD2. This further suggested that RD2 peptides indeed interact with Aβ42 monomers and lead to the formation of heterocomplexes. The weight averaged frictional ratios (f/f_0) of the sample at 1:20 (Aβ42:RD2) molar ratio was 1.25 in the *c*(*s*) analysis, while the typical f/f_0 for Aβ42 monomer is around 1.5 in our measurements. The f/f_0 is closely linked to the shape of a molecule. The higher the f/f_0 , the less symmetrical the molecule is. Globular proteins have a f/f_0 within 1.2 and 1.3 [368]. The decrease in the frictional ratio in the presence of RD2 might suggest the existence of compact globular structures in FITC-Aβ42 samples incubated with RD2, further pointing to the presence of heterocomplexes formed by RD2 and Aβ42 monomer. It has been reported, for example, that chaperones could transiently interact with aggregation prone protein such as Aβ42 or α-synuclein and prevent the aggregation [318, 320]. Cox et al. also utilized AUC to detect the interaction between αB-c_{core} and α-synuclein monomer. They observed a small shift in peak position in mixtures but no detectable stable complexes between αB-c_{core} and α-synuclein monomer [318]. It is obvious from AUC measurements that there is no highly populated and stable hetercomplexes observable between RD2 and Aβ42 monomer. Instead, we could see a small fraction of complexes with various stoichiometries. This may indicate that the interaction between RD2 and Aβ42 monomer is not a typical ligand-receptor interaction with well-defined conformation and stoichiometry, but is analogous to the transient interaction between IDP and the binding partner.

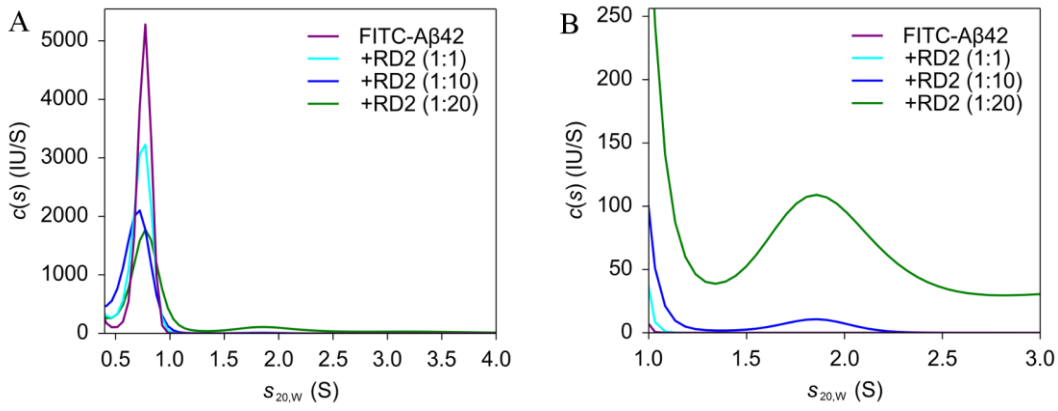

Figure 40. Sedimentation coefficient distributions of FITC-Aβ42 incubated with or without RD2 determined by sedimentation velocity analysis. 0.33 µM FITC-Aβ42 was incubated with different concentrations of RD2 in 20 mM sodium, 50 mM NaCl, pH 7.4 at 20 °C. 0.01% (v/v) Tw20 was used

as an additive in all solutions. Freshly prepared samples were centrifuged at 60,000 rpm at 20 °C for 15 h. Data was analyzed using continuous distribution c(s) Lamm equation model to determine the sedimentation coefficient distribution. Apparent s-values were normalized to s-values in pure water at 20 °C ($s_{20,w}$). An amplification of the distribution within 1 and 3 S is shown in (B).

RD2 slows down the fibrillation of Aβ42 at substoichiometric concentrations

Due to the fact that high molar ratios of RD2 lead to the rapid precipitation of Aβ42 in experiments that require micromolar concentrations of proteins (as shown in the turbidity assay in Fig. S20), we decided to reduce the concentration of RD2 to substoichiometric level in the ThT assay so as to minimize the influence of co-precipitation on ThT kinetics. Besides, we applied an empirical equation to quantitatively analyze the ThT kinetics. As shown in Fig. 41 and Table 3 (fitting curves in Fig. S21), we observed a sigmoidal kinetics for Aβ42 alone with $t_{1/2}$ and t_{lag} at 25.7 ± 0.2 h and 12.9 ± 0.2 h, respectively. However, the half completion time and lag phase of Aβ42 were remarkably prolonged in the presence of substoichiometric RD2 peptide. $t_{1/2}$ for Aβ42 samples containing 1 μM and 2 μM RD2 were 97.9 ± 2.3 h and 116.5 ± 2.1 h, respectively. Correspondingly, t_{lag} also increased to 93.6 ± 0.5 h and 109.1 ± 1.4 h, for Aβ42 incubated with 1 μM and 2 μM RD2. In addition to an increase in the lag phase in Aβ42 samples incubated with substoichiometric RD2, we noticed that ThT fluorescence signals at 120 h were also different among samples with different treatments. 1 μM RD2 did not significantly reduce the plateau ThT fluorescence of Aβ42 after 120 h of incubation, while Aβ42 containing 2 μM RD2 only reached about 74% of the plateau ThT signals of Aβ42 alone, implicating less pronounced fibril formation compared with Aβ42 alone after 120 h of incubation. Our results are consistent with a previous study showing that RD2 was able to inhibit the fibril formation of Aβ42 in a dose dependent manner [214]. Surprisingly, the slope of the rapid growth phase (the apparent elongation rate) of Aβ42 samples appeared to be different from Aβ42 treated with RD2, according to the fit (Table 3).

We then performed seeding experiments to investigate whether RD2 is still effective in the presence of Aβ42 seeds. As shown in the ThT kinetics (Fig. S22), the higher the concentration of seeds, the faster the fibrillation of Aβ42 will be. 5% seeds completely abolished the lag phase of Aβ42. RD2 at 0.1 fold, however, was able to counteract the seeding ability of Aβ42 seeds. Aβ42 incubated with 0.1 fold RD2 and 1% seeds still had a longer lag phase than free Aβ42 sample (Fig. S22), indicating that the seeding effect was completely canceled. In Aβ42 sample containing 5% seeds, although RD2 was not able to fully block the seeding ability, the elongation process of Aβ42 was decelerated, as evident from the slope of ThT kinetics. Results from the seeding experiments agree well with previous findings [214] and substantiate again that RD2 is also capable of reducing the catalytic ability of preformed Aβ assemblies.

The prolonged lag phase of Aβ42 in the presence of RD2 suggests that the initial process of Aβ42 fibrillation has been affected [312]. A previous study on the interaction between charged hydrophilic proteins and Aβ40 reported similar findings to our study that proteins with high positive charges strongly increase the lag time of Aβ40 fibrillation [319]. One possible explanation for the increased lag time is that the nucleation step (monomers associate into oligomers) [126] of Aβ42 is altered in the presence of RD2. Since RD2 is not likely to form stable complexes with Aβ42 monomers, but

only transiently interact with them, sequestering 10% of Aβ42 monomer is not able to explain such a strong effect. Alternatively, RD2 directly interacts with Aβ42 oligomers present in the lag phase and makes these small assemblies incapable of taking part in the further growth and proliferation. In seeding kinetics we observed that substoichiometric RD2 also affected the elongation process, probably by clustering Aβ42 seeds. The biphasic kinetics of Aβ42 with 5% seeds and 0.1 fold RD2 implies the formation of off-pathway species like small globular oligomers or curvilinear fibrils, as has been described previously [323]. MST experiments revealed that RD2 is able to interact with Aβ42 monomers. In addition, our previous study using the QIAD assay demonstrated that RD2 also eliminates toxic Aβ42 oligomers [202]. Together with seeding experiments, the data substantiates that both Aβ42 monomers and oligomers are involved in RD2 induced retardation of Aβ42 fibrillation. We therefore propose that both mechanisms are involved in the strong inhibitory effect of substoichiometric RD2 on fibril formation of Aβ42, and that interfering with the seeding capability of small Aβ42 assemblies might play a major role when Aβ protein concentration is relatively high. The kinetics assays demonstrated the RD2 has diverse effects on the fibrillation of Aβ42 by influencing the nucleation process and eliminating Aβ seeds.

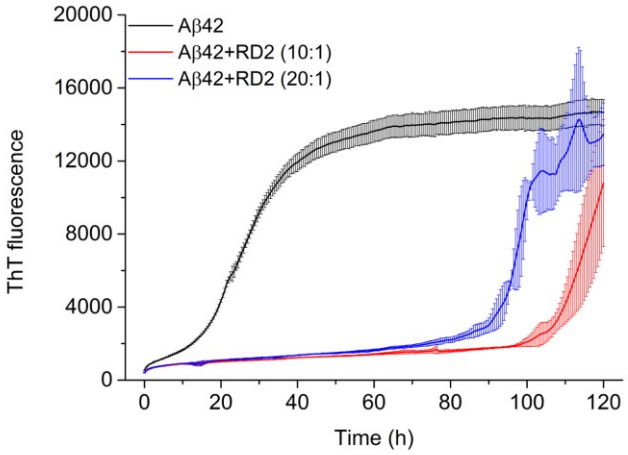

Figure 41. ThT kinetics of Aβ42 incubated with or without substoichiometric RD2. 20 μM Aβ42 alone (black), 20 μM Aβ42 with 1 μM RD2 (blue) and 20 μM Aβ42 with 2 μM RD2 (red) were incubated in 20 mM sodium phosphate, 50 mM NaCl (pH 7.4) at 20 °C. ThT fluorescence was recorded for 120 h to monitor the aggregation process. All samples are prepared with repetitions.

Table 3. Determination of $t_{1/2}$, k and t_{lag} for ThT kinetics of 20 μM Aβ42 in the absence or presence of RD2.[a]

Sample	$t_{1/2}$ (h)	k	t_{lag} (h)
Aβ42	25.7 ± 0.2	0.16	12.9 ± 0.2
Aβ42+RD2 (20:1)	97.9 ± 2.3	0.59 ± 0.38	93.6 ± 0.5
Aβ42+RD2 (10:1)	116.5 ± 2.1	0.27 ± 0.03	109.1 ± 1.4

[a] Measurements were conducted in 20 mM sodium phosphate, 50 mM NaCl (pH 7.4) at 20 °C. All ThT curves were fitted with eq.28 using the webserver AmyloFit.

RD2 delays the secondary structural conversion of Aβ42 at substoichiometric concentrations

The influence of RD2 on the secondary structural conversion of Aβ42 was evaluated in parallel using circular dichroism spectroscopy. Monomeric Aβ42 proteins are mainly unordered in aqueous environment [115], while the aggregation of Aβ42 into oligomers and fibrillary structures experiences a conversion of unordered structure to loosely packed strands and finally, parallel in-register β-sheet structures [121]. The secondary structure of RD2 was first determined to be unordered, as shown in Fig. S23. The contribution of 4 μM RD2 to the overall spectrum of Aβ42 is quite small. According to Fig. 42, the structural transition of 40 μM Aβ42 alone in sodium phosphate buffer displayed a sigmoidal pattern, showing a conversion from mainly random coil structures to β-sheet rich structures over the incubation time. The presence of 4 μM RD2 (molar ratio 10:1 Aβ42:RD2) significantly retards the formation of β-sheet structures. The structural conversion rate of Aβ42 was strongly decelerated when incubated with substoichiometric RD2 peptide. Aβ42 sample plus RD2 had much lower ellipticity at 217 nm after 120 h of incubation, suggesting a reduced content of β-sheet structures of Aβ42 at that time point. Deconvolution of CD spectra exhibited consistent trends that samples with RD2 had slower conversion rates than those without RD2 (Fig. 43). The unordered structures were more preserved in Aβ42 samples incubated with RD2 than free Aβ42 samples. RD2 addition after Aβ42 samples were incubated for 33 h did not significantly change the structural conversion of Aβ42, as shown in Fig. S24. ThT probes the formation of cross-β architectures of amyloid fibrils [136]. The decreased ThT fluorescence signals in Aβ42 samples with 0.1 fold RD2 at 120 h is therefore in accordance with the reduced formation of β-sheet structures in Aβ42 incubated with 0.1 fold RD2 in CD experiments. Both measurements confirmed that RD2 is able to delay the fibrillation of Aβ42 by retarding the secondary structural conversion. Our experimental evidence also corroborated previous MD simulation data that RD2 efficiently disrupts the formation of β-sheet structures and promotes the generation of coil structures probably by interacting with the fibril cores of Aβ42 oligomers [369]. Additionally, it appears that the presence of substoichiometric RD2 retain Aβ42 in unstructured conformations by the transient interaction, which could also explain the delayed ThT aggregation kinetics in Aβ42 samples with substoichiometric RD2.

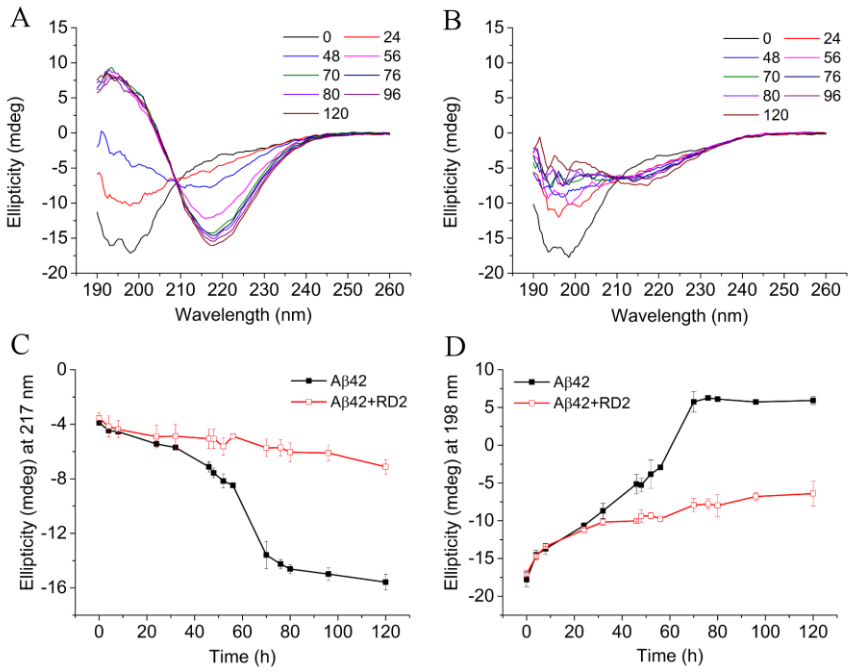

Figure 42. The secondary structure transition of Aβ42 in the absence or presence of substoichiometric RD2. CD spectra of 40 μM Aβ42 alone (A) and 40 μM Aβ42 incubated with 4 μM RD2 (B) were recorded from 260 nm to 190 nm in 20 mM sodium phosphate, 50 mM NaF at 20 °C, for 120 h. Spectra at selected time points (h) are shown. Ellipticity values at 217 nm (C) and 198 nm (D) are plotted against the incubation time to evaluate the transition kinetics. All samples were prepared in triplicate.

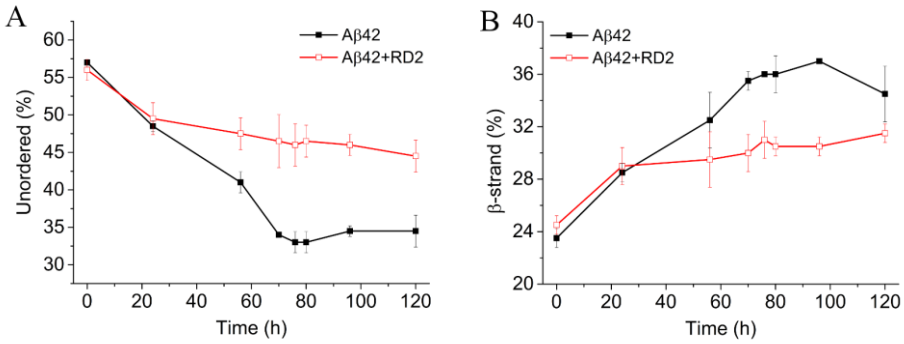

Figure 43. Deconvolution of CD spectra of 40 μM Aβ42 alone and 40 μM Aβ42 incubated with 4 μM RD2 in 20 mM sodium phosphate, 50 mM NaF (pH 7.4) to determine changes in fractions of unordered structures (A) and β-strand (B). CD spectra were analyzed using the online webserver Dichroweb with the method CDSSTR and reference dateset 7. The factions of unordered structure and β-strand are plotted against the incubation time. Samples were prepared in triplicate.

RD2 remodels the aggregation of Aβ42 by stabilizing Aβ monomers

ThT kinetics and CD measurements demonstrated that substoichiometric RD2 could efficiently delay the fibrillation of Aβ42 by prolonging the lag phase. We sought to confirm this by determining the size distribution of Aβ42 samples at the same concentration as those used in CD and ThT measurements. This permitted the simultaneous determination of both the consumption of Aβ42 monomers and the presence of oligomeric species in the absence or presence of 0.1 fold RD2. The

contribution of RD2 to the overall signals was very low so that only the sedimentation of Aβ42 species was reported and analyzed. After 24 h of incubation, the sample of Aβ42 alone should have oligomers and fibrillar structures, while Aβ42 with RD2 was still within the lag phase according to the ThT kinetics (Fig. 41). In AUC, we first observed that Aβ42 alone had a lower absorbance than the sample with RD2, likely due to the rapid sedimentation of large fibrillar structures in Aβ42 alone. Aβ42 alone showed a major species with an average $s_{20,w}$ at 0.9 S, a low-populated species at 2.1 S and a broad distribution above 6 S (Fig. 44). In Aβ42 with 0.1 fold RD2, we observed a high fraction of the species at ~0.75 S, which can be assigned to Aβ42 monomers. There were also low amounts of species at about 2 S and 4 S, however, species above 6 S were not visible in Aβ42 incubated with RD2. In particular, peak integration of the major species reported that the area under curve of the 0.75 S species in Aβ42 with RD2 was three-time higher than that of the 0.9 S species in Aβ42 alone, suggesting that Aβ42 monomers were more preserved in the presence of substoichiometric RD2 than those without D-peptide. A comparison of overall distributions points to the fact that the size distribution of Aβ42 has been shifted toward small *s*-values in the presence of 0.1 fold D-peptide, further corroborating a strong retardation effect of RD2 on Aβ42 aggregation by stabilizing monomers and decelerating the nucleation process. This also correlates well with the CD deconvolution that RD2 containing samples have a higher amount of unordered structure than Aβ42 alone, as Aβ42 monomers are mainly unordered in solution. It has been recognized that a range of oligomeric Aβ species are the main culprit of AD pathologies [370, 371]. For example, our previous study identified a group of Aβ42 oligomers at ~7 S with high neurotoxicity [202]. The modulation of RD2 on the aggregation of Aβ42 by preserving Aβ42 monomers and reducing the content of small oligomers might therefore confer a protective effect against cytotoxic Aβ oligomers.

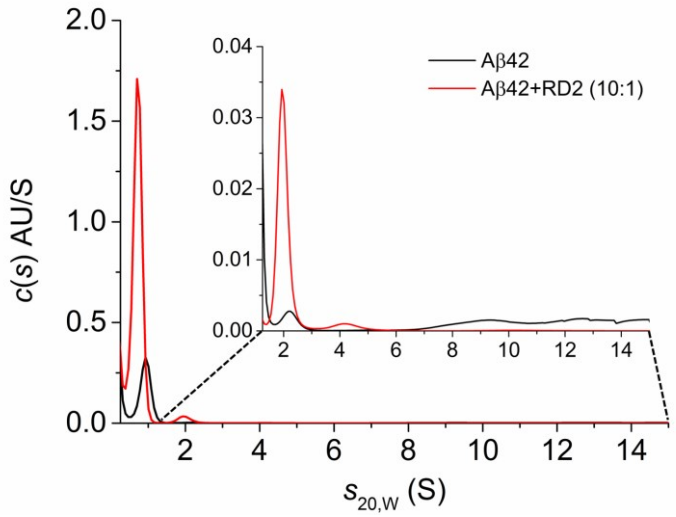

Figure 44. Sedimentation velocity analysis of Aβ42 in the absence or presence of substoichiometric RD2. Aβ42 at 20 μM was incubated with or without 0.1 fold RD2 in 20 mM sodium phosphate, 50 mM NaCl (pH 7.4) at 20 °C for 24 h. All samples were then centrifuged at 45,000 rpm, 20 °C for 15.5 h. Data was analyzed using the c(s) model implemented in Sedfit to obtain the sedimentation coefficient distribution. The amplification of the distribution between 1.25 and 15 S is shown in the insert. $s_{20,w}$ *is reported.*

Morphologies of Aβ42 species in the absence or presence of RD2

Morphologies of Aβ42 samples in the absence or presence of RD2 after 48 h and 120 h of incubation were detected using atomic force microscopy imaging to explore how RD2 affects the aggregation of Aβ42 over time. It should be noted that the imaging was carried out using micromolar concentrations of Aβ, several orders of magnitude higher than the physiological Aβ concentration as well as those used in MST and AUC analyses. As can be seen in Fig. 45A, Aβ42 alone already displayed fibrillary structures after 48 h of incubation, confirming ThT and CD results that Aβ42 alone has the highest aggregation rate under current experimental condition. Besides, we also observed the presence of oligomers and protofibrils with around 2 nm in height, similar to reported values [252]. Most of Aβ42 materials formed amyloid fibrils after 120 h of incubation, as evident from Fig. 45C. The height of Aβ42 fibrils was 5~8 nm according to the height measurement. Aβ42 incubated with RD2 peptide had different morphologies at 48 h, as displayed in Fig. 45B. The dominant species in RD2-containing sample were amorphous aggregates with heights varying from 10 to 15 nm. In addition to oligomers and protofibrils, we could also observe fibrillary structures with similar height to those found in Aβ42 alone. After 120 h of incubation, the main structures in Aβ42 with RD2 were also amyloid fibrils (Fig. 45D). However, there still remained amorphous aggregates and compact oligomers on mica surface. AFM experiments were in line with ThT and CD results that RD2 is effective in slowing down the fibril formation of Aβ42 at substoichiometric levels. The presence of amorphous aggregates in Aβ42 incubated with RD2 may be induced by the complexation between RD2 and Aβ42 species. It has been demonstrated that RD2 is capable of precipitating Aβ42 oligomers by forming large co-precipitates in density gradient centrifugation [214]. The interaction between RD2 and Aβ42 blocks the formation of ordered β-sheet structures and leads to the generation of amorphous aggregates with reduced neurotoxicity. Aileen Funke and co-workers reported in an early study that D3, the lead compound of RD2, shifted the fibril formation toward off-pathway, non-toxic amorphous co-precipitates at a high stoichiometry [209], whereas our findings implicate that D-peptide is also effective in modulating Aβ42 fibril formation when applied at substoichiometric concentrations. Together with ThT and CD measurements, we demonstrated that substoichiometric RD2 significantly retards the fibril formation of Aβ42.

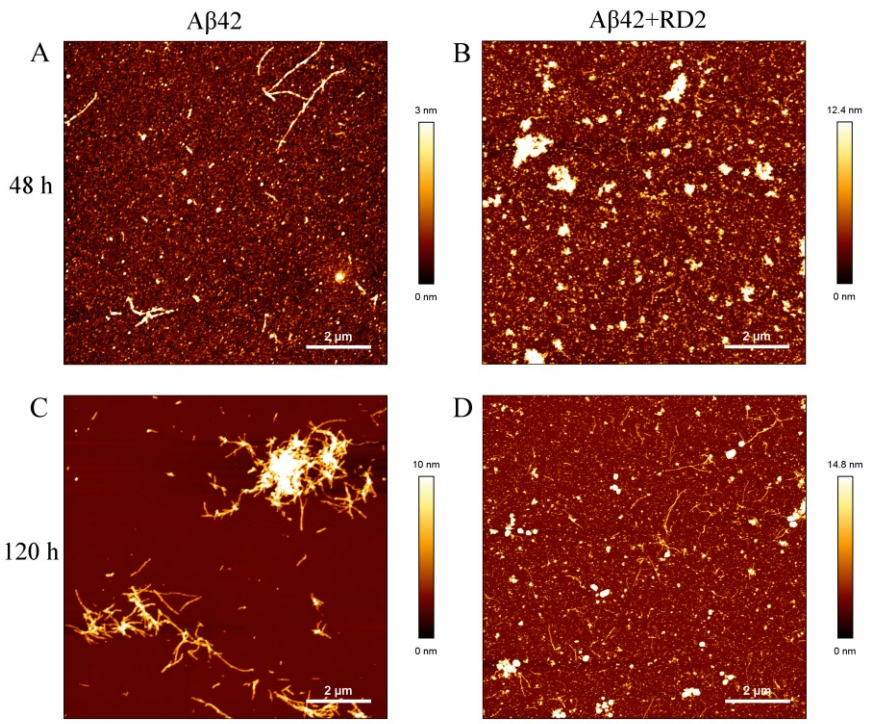

Figure 45. Morphologies of Aβ42 in the absence or presence of RD2 acquired by atomic force microscopy. 40 µM Aβ42 was incubated without (A and C) or with (B and D) 4 µM RD2 in 20 mM sodium phosphate, 50 mM NaCl (pH 7.4) at 20 °C. The imaging was performed at 48 h and 120 h using AC mode. Scale bars (2 µM) are shown inside each graph.

Conclusion

The interaction between the all-D-enantiomeric peptide RD2 and Aβ42 was characterized at multiple concentration levels using different biophysical methods. By using the solution based microscale thermophoresis and fluorescently labeled molecules, we demonstrated that RD2 is able to bind to Aβ42 monomers with submicromolar affinities, and that electrostatic interaction might contribute to the binding between these two molecules. The high affinity binding leads to the complex formation of Aβ42 monomer and RD2 at 1:1 and higher stoichiometries. At substoichiometric concentration, RD2 is able to retain Aβ42 monomers in the unstructured conformation and therefore interfere with the nucleation of Aβ. This effect of RD2 leads to significant delays in the secondary structure conversion and the fibrillation of Aβ. Besides, our study provides additional evidence to support the capability of RD2 in removing the catalytic activity of Aβ seeds. Our study demonstrates the versatile role of RD2 in modulating the fibrillation of Aβ42 by interfering with Aβ nucleation via interacting with monomers and eliminating oligomers, and provides complementary evidence at molecular levels to explain the mechanisms of action of RD2 on Aβ aggregation related pathologies.

Supporting information

Table S5. Buffer viscosities and densities at 20 °C.

Buffer viscosity (P) [a]	20 mM sodium phosphate, 50 mM NaCl	0.01015
	55 mM Tris-HCl, 50 mM NaCl	0.01024
	H_2O	0.01002
Buffer density (g/cm^3) [a]	20 mM sodium phosphate, 50 mM NaCl	1.003
	55 mM Tris-HCl, 50 mM NaCl	1.002
	H_2O	0.9982

[a] Values were calculated using the software Sednterp (Version 20130813 BETA).

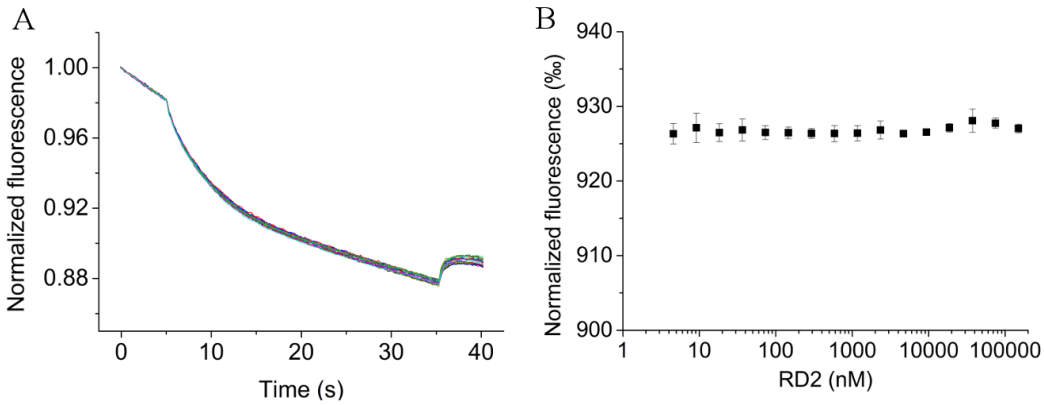

Figure S17. Microscale thermophoresis analysis of fluorescein in the presence of various concentrations of RD2. 40 nM fluorescein was titrated with RD2 in 20 mM sodium phosphate, 50 mM NaCl, 0.01% Tw20 (pH 7.4) at 22 °C. Time traces from one measurement are shown in (A). The quantification of thermophoresis based on the time traces are displayed in (B). Experiments were performed in triplicate.

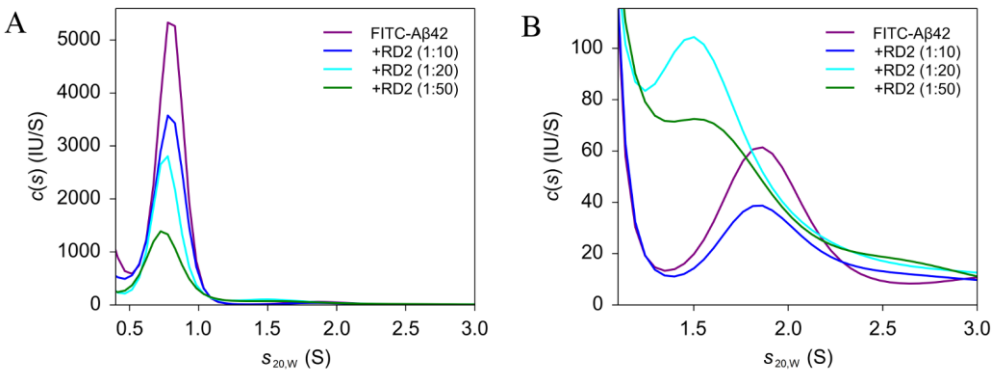

Figure S18. Sedimentation coefficient distribution analysis of 0.33 μM FITC-Aβ42 incubated with different concentrations of RD2 in 55 mM Tris-HCl, 50 mM NaCl (pH 7.4) in the presence of 0.01% Tw20 (v/v) at 20 °C (A). All samples were centrifuged at 60,000 rpm for 15 h. Sedimentation profiles were analyzed using the continuous distribution c(s) Lamm equation model. s-values were standardized to the s-value in pure water at 20 °C ($s_{20,w}$). The amplification of the size distribution within 1 and 3 S is displayed in (B).

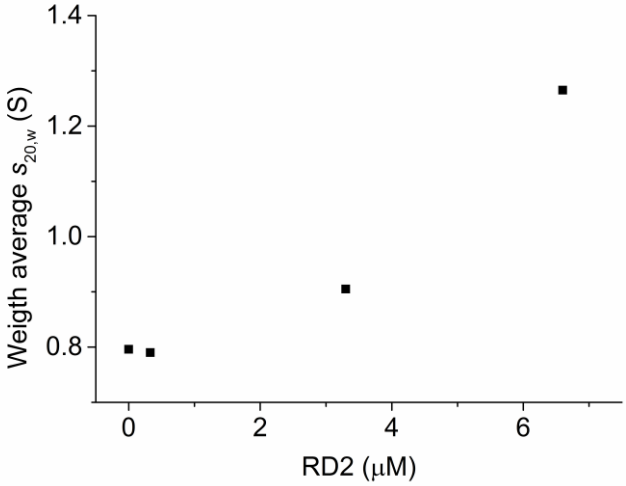

Figure S19. The weight average $s_{20,w}$ of FITC-Aβ42 samples incubated with different concentrations of RD2 as determined by peak integration of the size distribution in c(s) analyses shown in Figure 41 in the main text.

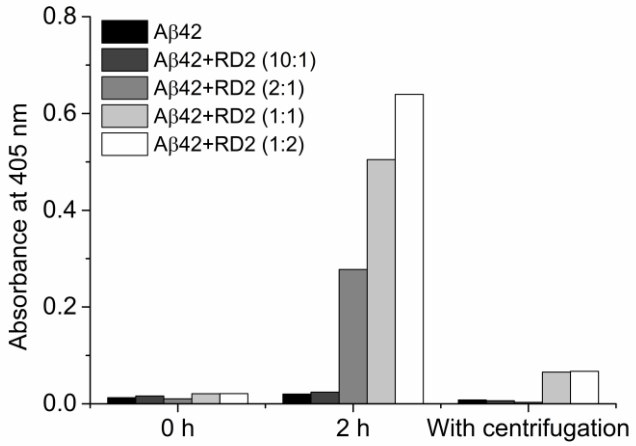

Figure S20. Turbidity assay of Aβ42 in the absence or presence of RD2. 40 μM Aβ42 was incubated with different concentrations of RD2 (molar ratios 10:1, 2:1, 1:1 and 1:2, Aβ42:RD2) in 20 mM sodium phosphate, 50 mM NaCl, 0.01% (v/v) Tw20 (pH 7.4) at ambient temperature. The turbidity was measured using the absorbance at 405 nm at 0 h, 2 h of incubation. Afterwards all samples were centrifuged at 726 g for 15 min and the turbidity was measure again for the supernatants.

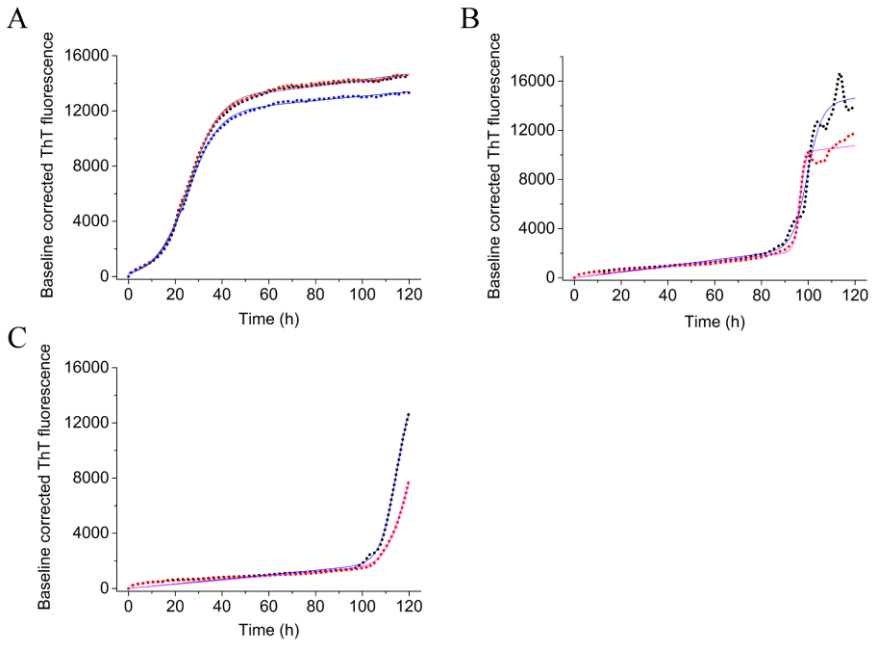

Figure S21. AmyloFit analysis of the ThT kinetics for Aβ42 in the absence or presence of RD2. 20 μM Aβ42 proteins alone (A), 20 μM Aβ42 proteins with 1 μM RD2 (B) and 20 μM Aβ42 proteins with 2 μM RD2 (C) were incubated in 20 mM sodium phosphate, 50 mM NaCl (pH 7.4) at 20 °C for 120 h. All kinetics were fitted using the webserver AmyloFit with the customized equation (eq.28). Raw data and fitted data are presented in short dotted and solid curves, respectively. Samples were prepared with repetitions.

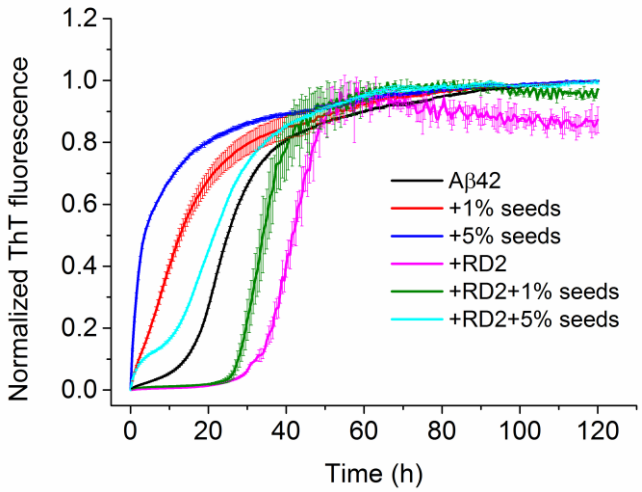

Figure S22. Seeding kinetics of Aβ42 in the absence or presence of 0.1 fold RD2. 10 μM Aβ42 was incubated with or without 1 μM RD2 in the presence of different concentrations of Aβ42 seeds in 20 mM sodium phosphate, 50 mM NaCl (pH 7.4) at 20 °C. The data was averaged and normalized based on duplicate.

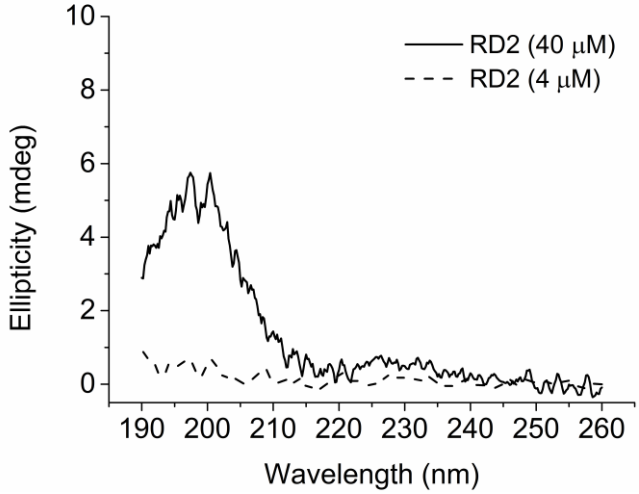

Figure S23. CD spectra of RD2 at different concentrations. RD2 samples at 40 μM and 4μM were prepared in 20 mM sodium phosphate, 50 mM NaF (pH 7.4) and were subjected to CD measurements.

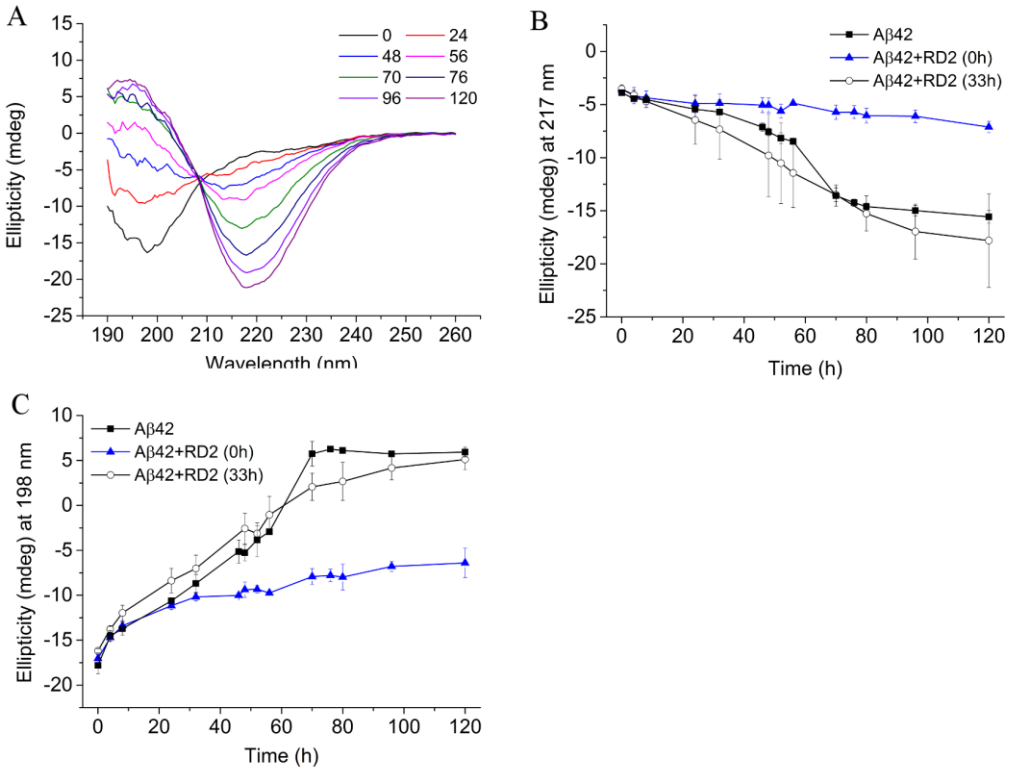

Figure S24. CD analysis of delayed addition of 0.1 fold RD2 into Aβ42 samples preincubated for 33 h in 20 mM sodium phosphate, 50 mM NaF (pH 7.4) at 20 °C. (A) CD spectra were obtained using the same experimental condition as measurements shown in Figure 41. Transition kinetics by plotting ellipticity values at 217 nm (B) and 198 nm (C) against the incubation time are displayed and compared with kinetics for 40 μM Aβ42 alone and 40 μM Aβ42 with RD2 incubation from the beginning (corresponding to the data in Figure 42).

Chapter IV
Characterization of the interaction between Aβ42 and anti-Aβ antibodies

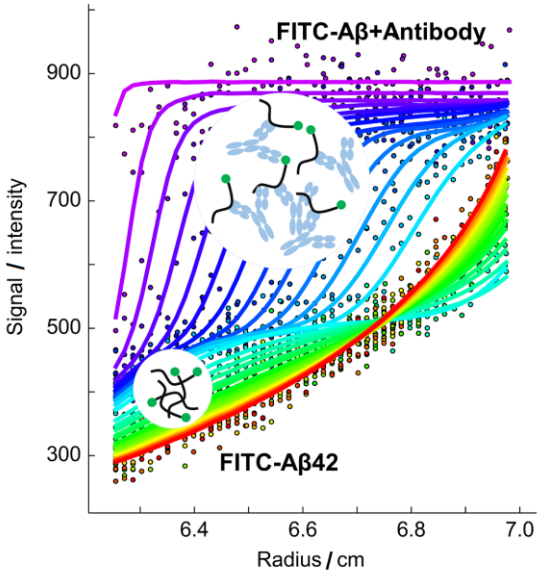

Abstract

Amyloid β-peptides (Aβ) play a major role in the pathogenesis of Alzheimer's disease. Therefore, numerous monoclonal antibodies against Aβ have been developed for basic and clinical research. The present study applied fluorescence based analytical ultracentrifugation and microscale thermophoresis to characterize the interaction between Aβ42 monomers and three popular, commercially available antibodies, namely 6E10, 4G8 and 12F4. Both methods allowed us to analyze the interactions at low nanomolar concentrations of analytes close to their dissociation constants (K_D) as required for the study of high affinity interactions. Furthermore, the low concentrations minimized the unwanted self-aggregation of Aβ. Our study demonstrates that all three antibodies bind to Aβ42 monomers with comparable affinities in the low nanomolar range. K_D values for Aβ42 binding to 6E10 and 4G8 are in good agreement with formerly reported values from SPR studies, while the K_D for 12F4 binding to Aβ42 monomer is reported for the first time.

This chapter was adapted from the manuscript:

Tao Zhang, Luitgard Nagel-Steger, Dieter Willbold. Solution based determination of dissociation constants for Aβ42 binding to antibodies. *Accepted for publication in ChemistryOpen*.

Introduction

The aggregation of amyloid β-peptides (Aβ) into toxic oligomeric assemblies and fibrillar structures has been suggested to play an important role in the pathogenesis of Alzheimer's disease (AD) [372]. Aβ is the proteolytic product of the amyloid precursor protein. It is the main component of amyloid deposits in brains of Alzheimer's patients [98]. A multitude of strategies has been developed to characterize and counteract Aβ pathologies in vivo, in an attempt to achieve early diagnosis and intervention of AD. Antibodies directed against Aβ are important tools for the characterization of Aβ species and have been proposed for the treatment of Aβ related pathologies. For example, monoclonal anti-Aβ antibodies are widely applied in enzyme-linked immunosorbent assay (ELISA), western blot or immunohistochemistry to determine Aβ proteins in cerebrospinal fluid, blood or tissue samples [373]. Several antibodies have been and are being tested in different stages of clinical trials to evaluate their efficacies on the cognitive performance of AD patients [179]. These antibodies recognize different epitopes of Aβ and some of them are claimed to be able to discriminate between different aggregation states of Aβ. For instance, Bapineuzumab targets the N-terminus (aa1-5) of Aβ and recognizes almost all kinds of Aβ species, including monomers, oligomers and fibrillar structures [374]. Solanezumab binds specifically to the central region of Aβ (aa16-23) responsible for the self-aggregation process and recognizes soluble Aβ species but not Aβ fibrils or amyloid plaques [375]. In addition to these antibodies for disease intervention, a number of anti-Aβ antibodies are broadly used as tools for basic research purposes. Considering the extensive and promising use of anti-Aβ antibodies in the field of AD research, it is necessary to quantitatively characterize the properties of antibodies recognizing different epitopes under near-physiological conditions to facilitate the application of these agents.

In vitro characterization of the interaction between Aβ and anti-Aβ antibodies is usually carried out using ELISA, surface plasmon resonance (SPR) or isothermal titration calorimetry (ITC), through which the binding affinities, kinetics or thermodynamics can be obtained [373, 376-379]. X-ray crystallography has also been utilized to determine the high resolution structure of Aβ in complex with antibodies, albeit most studies chose Aβ fragments (N-terminus or the mid-region) or used Fab fragments for crystallization [380-384]. Since Aβ is highly flexible and prone to form aggregates already at low micromolar concentrations in aqueous solution, it is rather complicated to quantify the binding between antibodies and specific Aβ species, particularly the monomer, as a variety of Aβ species with different sizes and conformations may be present in solution. The impact of Aβ aggregation on the characterization might get pronounced in experiments requiring micromolar concentration of Aβ, such as ITC, putting aside the fact that for a reliable determination of binding constant the titrated concentrations should cover also the range of K_D. In SPR or ELISA measurements one of the analytes has to be immobilized on the surface of a sensor chip or a plate. In the case of surface immobilized Aβ species, one might encounter surface induced conformational changes, crowding effects or changes in the epitope accessibility [385]. In the complementary set-up, where the antibody is immobilized, the self-aggregation of Aβ at high concentrations is still inevitable. Besides, the mass transport limitation in SPR might also need to be critically considered when dealing with high-affinity bindings [386]. One strategy to overcome these difficulties is to use fluorescently labeled molecules with solution based techniques so as to reduce the concentration of

Aβ and antibodies to low nanomolar levels, so that the self-aggregation of Aβ will be significantly suppressed. Besides, it is also beneficial to the reliable determination of dissociation constants in the low nanomolar range. This could be helpful for the characterization of the interaction between Aβ monomers and anti-Aβ antibodies.

Analytical ultracentrifugation (AUC) is a solution based absolute method which has been widely used in characterizing macromolecules and protein-protein interactions. The development of the fluorescence based detection system permits the measurement of protein samples at picomolar to low nanomolar concentrations [306, 387, 388]. This high sensitivity in combination with a large dynamic range enables the study of high affinity interactions as found for antibody-antigen binding [389]. In contrast to AUC, microscale thermophoresis (MST) is a recently developed method based on the migration of macromolecules in response to thermal gradients [237]. This approach exploits the deviating thermophoretic behavior of a labeled molecule in the presence of different concentrations of its binding partner. By combining these two fluorescence based assays, we studied the interaction between fluorescein labeled Aβ42 (FITC-Aβ42) and three mAbs directed against Aβ (6E10, 4G8 and 12F4) to determine the antigen-antibody complex formation and binding affinities. Their epitopes of Aβ42 cover the N-terminus for 6E10, the C-terminus for 12F4, as well as the central hydrophobic core region for 4G8.

Materials and methods

Materials

Fluorescein isothiocyanate-β-Alanine labeled Aβ42 (FITC-Aβ42) were purchased from Bachem (Weil am Rhein, Germany). The labeling was prepared by conjugating the fluorophore FITC to the amine group of the additional β-Alanine at the N-terminus of Aβ42. The purity of FITC-Aβ42 product was 88.8%, according to the HPLC determination of the manufacturer. The molecular mass of the labeled molecule is 4974.4 Da, as determined by electrospray ionization mass spectrometry (ESI-MS). The HPLC and MS results provided by the manufacturer can be found in the supporting information (Fig. S25 and S26). Purified antibodies 6E10, 4G8 and 12F4 were obtained from BioLegend (San Diego, CA, UAS). All antibodies are mouse derived monoclonal antibodies and are reactive to human Aβ proteins with different epitopes (Table 4). 1, 1, 1, 3, 3, 3-hexafluoro-2-propanol (HFIP) other chemicals are commercially available from Sigma-Aldrich (Munich, Germany). Aβ42 products (1 mg) were incubated in HFIP overnight at room temperature and were divided into small aliquots. HFIP was then removed and Aβ42 proteins were stored at -80 °C before use. All samples were prepared in 20 mM sodium phosphate, 50 mM NaCl at pH 7.4, with the addition of 0.005% (v/v) Tween 20.

Table 4. Epitopes of the antibodies in Aβ42 and the concentration of stock solutions.[a]

	6E10	4G8	12F4
Epitope	residues 3-8 (EFRHDS)	residues 18-22 (VFFAE)	residues 37-42 (GGVVIA)
Stock (mg/ml)	1	1	0.5

[a] According to the information from the manufacturer.

Sedimentation velocity analytical ultracentrifugation analysis

Sedimentation velocity (SV) analysis of the fluorescent samples was performed using a Beckman Optima XL-A centrifuge (Beckman-Coulter, Brea, CA, USA) equipped with an 8-hole rotor and a fluorescence detection system (Aviv, Lakewood, NJ, USA). FITC-Aβ42 stock was mixed with antibody stock solutions to prepare samples with 40 nM FITC-Aβ42 and different concentrations of the antibody in 20 mM sodium phosphate, 50 mM NaCl (pH 7.4), 0.005% (v/v) Tween 20. Samples were then loaded into 3-mm double-sector titanium cells, with 100 µl per sample. Afterwards, all samples were thermally equilibrated to 20 °C in the centrifuge before the experiment. The centrifugation was carried out at 50,000 rpm (201,600 *g*) and 20 °C for 15 h. The detection system uses an excitation wavelength at 488 nm and an emission cut-off filter at 505 nm for data acquisition. The sedimentation profiles were analyzed using the software package Sedfit (version 15.01b) and the continuous distribution *c*(*s*) Lamm equation model to obtain the sedimentation coefficient (*s*-value) distribution [390]. Buffer density and viscosity (Table S6) were calculated using Sednterp (version 20130813BETA). The partial specific volume ($\bar{v}$) of was FITC-Aβ42 determined according to Sednterp and Durchschlag et al. [334]. For mixtures of Aβ42 and antibodies, a partial specific volume ($\bar{v}$) of 0.73 cm^3/g was used for the calculation of *s*-value. The final graphs of the sedimentation coefficient distribution were created by GUSSI (version 1.2.1) [274], with all *s*-values standardized to $s_{20,w}$. The isotherm of weight average $s_{20,w}$ as a function of the loading composition (s_w) for each antibody was created by integrating the distribution from 0.5 to 14 S in GUSSI [306]. The isotherms were further analyzed in Sedphat (version 10.58f) using the 'A + B ←→ AB Hetero-Association' model with a confidence interval of 68.3% to determine the K_D values [305]. The fitted binding plots were displayed via GUSSI [274].

The size distribution of the antibody alone was also evaluated via analytical ultracentrifugation with an absorbance detection system. In brief, the 6E10 antibody was prepared in 20 mM sodium phosphate, 50 mM NaCl (pH 7.4) to obtain a concentration of 1.2 µM. 380 µl antibody sample were then loaded into a 12-mm double-sector aluminum cell. After thermal equilibration samples were centrifuged at 40,000 rpm (129,024 *g*), 20 °C. The sedimentation was monitored using a detection wavelength at 230 nm and a step size of 20 µm. The density and viscosity of the buffer were calculated according to Sednterp (version 20130813BETA). The partial specific volume of the antibody was assumed to be 0.73 cm^3/g. The size distribution was determined using the continuous distribution *c*(*s*) Lamm equation model implemented in Sedfit [390].

Microscale thermophoresis

The binding between FITC-Aβ42 and antibodies was characterized using microscale thermophoresis to determine the dissociation constant (K_D). FITC-Aβ42 at 40 nM was titrated with different concentrations of antibody solutions in 20 mM sodium phosphate, 50 mM NaCl (pH 7.4), 0.005% (v/v) Tween 20. Samples were immediately transferred to standard capillaries (NanoTemper, Munich, Germany) and the thermophoresis was measured by a Monolith NT.115 system from the same manufacturer at room temperature (~ 23 °C). The excitation light of the LED was chosen according to the fluorophore of the labeled molecule. The LED power and the infrared (IR) laser power were set to 40% and 50%, respectively. The on- and off-phase of the IR laser were set to 30 S and 5 S,

respectively.The normalized fluorescence (F_{norm}) is plotted against the titrant concentrations to obtain the binding plots. K_D values for each antibody were reported based on the fitting of a 1:1 binding model via OriginPro (version 9.0.0).

A control MST experiment was performed by titrating 40 nM fluorescein with the same concentration of 6E10 as has been used in experiments on FITC-Aβ42. The measurement was conducted under the same condition.

Results and discussion

Complex formation between Aβ42 monomers and anti-Aβ antibodies

We have initially characterized the size distributions of Aβ42 and the individual antibody using sedimentation velocity measurements with different detection systems. Aβ42 monomer is an intrinsically disordered protein in aqueous solution. The $s_{20,w}$ of FITC-Aβ42 as measured by the fluorescence detection system is 0.81 ± 0.02 S and the weight-average frictional ratio (f/f_0) is 1.44 ± 0.1, suggesting a relatively elongated conformation [391]. It is also clear from the distribution that 40 nM FITC-Aβ42 did not form aggregates during the centrifugation process. The antibody 6E10 showed an $s_{20,w}$ of 7.2 S, additionally a small fraction, ~5% of an antibody dimer with $s_{20,w}$ of 11.7 S was detected by the absorbance based AUC measurement (Fig. S27). The oligomerization of antibodies is a well-known general property, which for example plays a critical role in determining the shelf life of commercially manufactured antibodies [392]. The weight-average frictional ratio (f/f_0) of 6E10 was 1.24, pointing to a globular shape of the antibody in solution.

In the presence of antibodies, FITC-Aβ42 formed complexes with the binding partner in a concentration dependent manner, as shown in Fig. 46. The amount of unbound FITC-Aβ42 (found at ~0.8 S) decreased with increasing amounts of added antibody, while the antigen-antibody complex at ~7 S (Table 5) accumulated gradually with the titration of antibodies to the FITC-Aβ42 solution. In addition, we also observed a minor population of species with larger *s*-values in almost all antibody-containing samples. We speculate that these species most likely contain complexes formed by FITC-Aβ42 and antibody dimers. The complex of FITC-Aβ42 and dimeric antibody should sediment with about 11 S, very close to the *s*-value of an antibody dimer alone. Regarding the main complex at ~7 S, it is evident that there is only one antibody molecule bound to FITC-Aβ42, however, we cannot distinguish between antibodies that have one and two Aβ42 molecules bound, as the increase in the added molecular mass (4 kDa) to the mAb (150 kDa) cannot be resolved in the *s*-value regime. During the analysis we also noticed that the weight-average frictional ratio (f/f_0) of Aβ42-antibody mixtures decreased from about 1.5 for FITC-Aβ42 alone to about 1.2 in FITC-Aβ42 saturated with antibodies, which also hints to the complexation between Aβ42 monomers and antibodies.

Table 5. Weight-average $s_{20,w}$ of the major complex formed by antibodies and FITC-Aβ42.[a]

	6E10	4G8	12F4
Weight-average $s_{20,w}$ (S)	6.8 ± 0.4	6.8 ± 0.4	6.9 ± 0.3

[a] Values were determined by peak integration of the $c(s)$ distribution from 4 to 10 S using GUSSI (version 1.2.1) and were expressed as mean ± S.D.

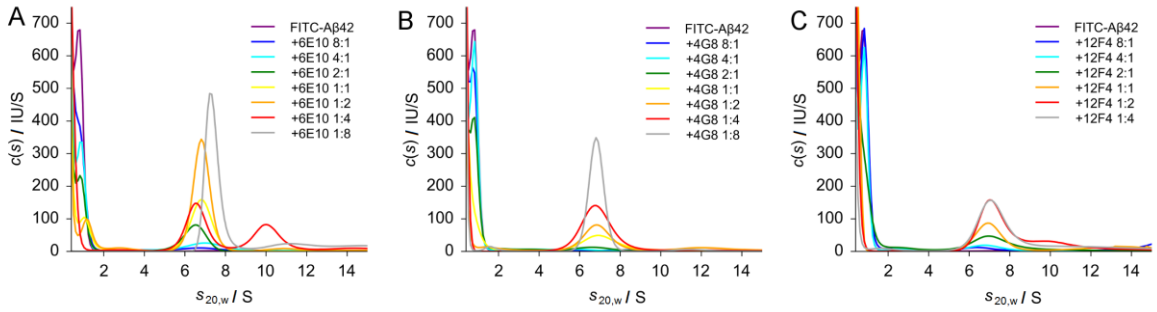

Figure 46. Sedimentation velocity analysis of FITC-Aβ42 in the presence of varying concentrations of three anti-Aβ antibodies. FITC-Aβ42 at 40 nM was titrated with 6E10 (A), 4G8 (B) and 12F4 (C) in 20 mM sodium phosphate, 50 mM NaCl (pH 7.4), 0.005% (v/v) Tween-20. All samples were centrifuged at 50,000 rpm (201,600 g) and 20 °C for 15 h. The sedimentation coefficient distribution was obtained using the continuous distribution c(s) Lamm equation model. The standardized $s_{20,w}$ for 20 °C and water as a solvent is reported.

Determining the dissociation constants between Aβ42 monomers and antibodies based on the size distributions

Next, we sought to determine the K_D values for each antibody based on the results from $c(s)$ analyses. Note that the fluorescence signals of all samples in AUC measurements were constant over the measurement and were rather similar to each other, suggesting the absence of quenching or losing materials in the experiment. The complex formation between FITC-Aβ42 and antibody will lead to a gradual increase in the weight average s-value of the sample. Based on the mass action law, the signal-weight average sedimentation coefficient (s_w) isotherm can be built in order to determine the binding affinity [306]. As can be seen from the fitting of the isotherms (Fig.47 and Table 6), all three antibodies form complexes with FITC-Aβ42 monomers with nanomolar affinities. The K_D determined for 6E10 and FITC-Aβ42 was 30.1 [13.2, 63.3] nM; the K_D values for 4G8 and 12F4 were 11.3 [1.0, 45.5] nM and 14.6 [4.7, 37.1] nM, respectively. The values obtained under 68.3% confidence interval are given in brackets.

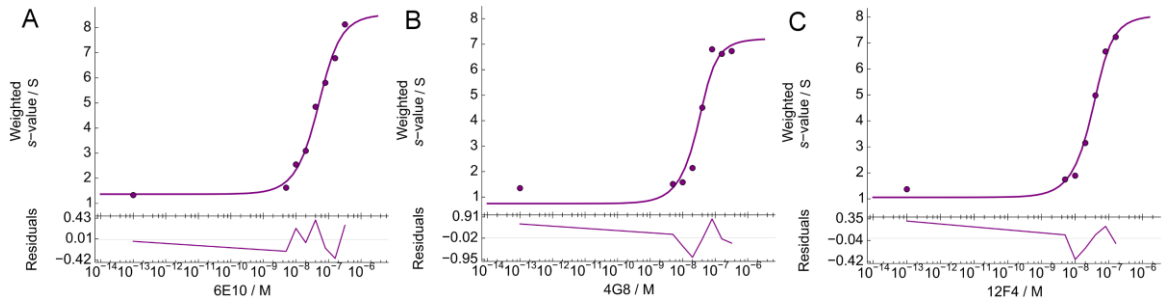

Figure 47. Binding isotherms of signal-weight average sedimentation coefficient (s_w) as a function of the logarithm of the loading concentration for 6E10 (A), 4G8 (B) and 12F4 (C). The isotherms were generated by integrating the distribution from 0.5 to 14 S according to the c(s) analysis and were fitted using the 'A + B ←→ AB Hetero-Association' model implemented in Sedphat (version 10.58f) to determine the dissociation constants. For data evaluation, a concentration of 1 × 10^{-13} M of the antibody was assigned to samples of FITC-Aβ42 alone.

Quantifying the dissociation constants using the microscale thermophoresis analysis

To further investigate the interaction between FITC-Aβ42 and the antibodies, we carried out MST measurements using the same concentrations of FITC-Aβ42 and solvent conditions as used for AUC experiments. The thermophoretic behavior of a given target molecule can be influenced by changes in its size, charge and solvation upon binding to another molecule [239]. The fluorophore fluorescein alone did not interact with the antibody, as demonstrated by the control experiment (Fig. S28), therefore any change in the thermophoresis could be attributed to the binding between Aβ42 monomers and the antibodies. The binding plots were analyzed via the simple 1:1 binding model despite the bivalent nature of the antibodies for two reasons. Firstly, using more complex models, for example the Hill model, could not improve the quality of the fit. Secondly, the titration of 40 nM Aβ42 with the indicated concentrations of mAb will saturate only a single binding site. As shown in Fig. 48 and Table 6, samples incubated with different antibodies exhibited different thermophoretic effects in MST measurements, although they are similar in size. The binding curve of FITC-Aβ42 and 6E10 revealed a K_D of 10.3 ± 4.6 nM. The descending trend of F_{norm} in the presence of 6E10 suggested that bound FITC-Aβ42 molecules moved out of the heated zone faster than free molecules, indicating an increase in the thermophoretic mobility of FITC-Aβ42-6E10 complexes [239]. The K_D for FITC-Aβ42 and 4G8 was determined to be 12.8 ± 4.6 nM. Interestingly, the binding plot of FITC-Aβ42 and 4G8 displayed a pattern opposite to that of FITC-Aβ42 and 6E10, meaning that complexes had lower thermophoretic mobility than free FITC-Aβ42 molecules [239]. 12F4 bound to FITC-Aβ42 with a K_D of 9.5 ± 5 nM. The binding of 12F4 to FITC-Aβ42 also led to a decrease in the thermophoretic mobility, but to a lesser degree than that induced by 4G8. The reason for the deviation in the thermophoretic behavior of three Aβ42-antibody complexes is not clear yet. The antibodies used in the study recognize different epitopes of Aβ42 monomer. One possibility is that different degrees of posttranslational modifications of the antibodies like glycosylation influence their thermophoretic behavior. According to literature 4G8 carries sialic acids on its surface, while 6E10 does not [393, 394]. Additionally, the binding of antibodies to different regions of Aβ42 might induce alterations in the hydration shell of the complex, subsequently leading to different thermophoresis effects [236].

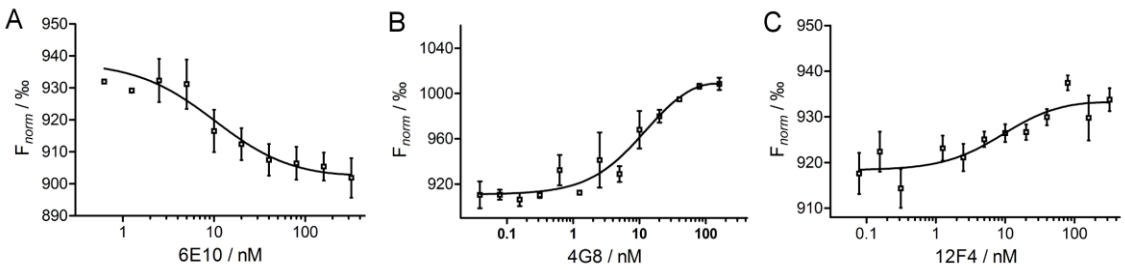

Figure 48. Microscale thermophoresis analysis of the interaction between FITC-Aβ42 and different antibodies. FITC-Aβ42 at 40 nM was titrated with different concentrations of antibodies in 20 mM sodium phosphate, 50 mM NaCl (pH 7.4), 0.005% (v/v) Tween-20 at ~ 23 °C. Binding plots of FITC-Aβ42 to 6E10 (A), 4G8 (B) and 12F4 (C) were fitted using the 1:1 binding model. Measurements were performed in triplicate.

Since the concentration of fluorescently labeled molecule is usually very low in fluorescence based measurements, it might be necessary to block the unspecific surface adsorption of the target molecule to maintain the input concentration. Therefore additives such as carrier proteins or detergents have been suggested for AUC or MST to deal with this problem [236, 306]. However, carrier proteins that are commonly used in fluorescence based AUC are not considered in the present study to avoid potential interference of these proteins with the interaction between antibodies and Aβ [395, 396]. Tween-20 (0.005%, v/v) was thus used as an alternative to overcome the surface adsorption of FITC-Aβ42 in both experiments. Comparing dissociation constants measured in the present study with reported values from literature (Table 6), we found that the determined dissociation constants for all tested antibodies are in general agreement with those from literature, regardless of the methodology. Additionally, the three antibodies have rather similar affinities toward Aβ42 monomers, irrespective of the recognized epitopes. In light of the bivalent nature of the IgG antibody, it has been suggested in previous SPR studies that a bivalent model might be necessary to properly fit the data, especially when Aβ is immobilized on sensor chips [377]. Nevertheless, the 1:1 binding model appears to be sufficient to fit the SPR data reasonably well in the case of Aβ binding to immobilized antibodies [373]. This indicates that the antibody might bind to Aβ monomers exclusively either with a single site or with both sites [377]. It should be mentioned that both AUC and MST report the information about the bound and unbound states of the labeled molecule. At a concentration lower than the critical aggregation concentration of about 90 nM [328], Aβ is unlikely to form aggregates within the time scale of both experiments, which definitely helps to reduce the incidence of multiple binding between Aβ oligomers and antibodies. The size distribution of all antibody-containing FITC-Aβ42 samples also revealed that complexes with only one antibody molecule were the dominant species in solution. Therefore, the simple 1:1 binding model also provided reasonable fitting results with good residuals in our study.

Table 6. A comparison of dissociation constants of the interaction between Aβ monomer and three antibodies.

K_D (nM)	6E10	4G8	12F4
AUC [a]	36.5 (30.6-43.4)	11.3 (1-45.5)	14.6 (4.7-37.1)
MST [b]	10.3 ± 4.6	12.8 ± 4.6	9.5 ± 5
SPR [c]	22.3	30.1	n/a

[a] Obtained based on fitting the isotherms of signal-weight average sedimentation coefficient (s_w) using the 'A + B ⟷ AB Hetero-Association' model and 68.3% confidence interval in Sedphat (version 10.58f).

[b] Obtained according to the 1:1 binding model.

[c] Obtained from SPR measurements in which Aβ40 monomers were injected over immobilized antibodies on the sensor chip and the 1:1 Langmuir binding model was used for data evaluation [373].

Conclusion

The combination of fluorescent labeling and solution based methods allows us to investigate the interaction between the aggregation-prone Aβ42 monomer and its binding partners in the concentration range of their dissociation constants. We obtained reliable binding parameters which are in good agreement with SPR studies on Aβ and antibodies. Besides, the dissociation constant between 12F4 and Aβ42 monomer was reported for the first time based on our measurements. The determined values may offer additional information for the application of these antibodies. AUC and MST are also capable of analyzing challenging samples such as tissue lysates, blood serum or other biological liquids [242, 397], which envisions the possible translation of the approach to physiological samples. However, solution based methods also have some limitations. For example, the fluorophore tag might have an impact on the interaction process by modifying the epitope or interacting directly with the binding partner. However, neither of the possibilities was evident in this study. Nevertheless, the rapid aggregation of Aβ oligomers in solution still renders it challenging to characterize the interaction between oligomeric species and antibodies via these solution based methods. Taken together, we demonstrate that AUC and MST can be useful on their own and are rigorous complements to surface based techniques for studying the interaction between Aβ species and various ligands.

Supporting information

Table S6. Parameters for the *c*(*s*) analysis of AUC sedimentation profiles at 20 °C.

FITC-Aβ42	Partial specific volume ($\bar{\nu}$) [a]	0.732 cm^3/g
	Molecular mass (MW)	4974.6 g/mol
20 mM sodium phosphate,	Density (ρ)	1.003 g/cm^3
50 mM NaCl	Viscosity (η)	0.010154 poise

[a] Determined based on the software Sednterp and Durchschlag et al.

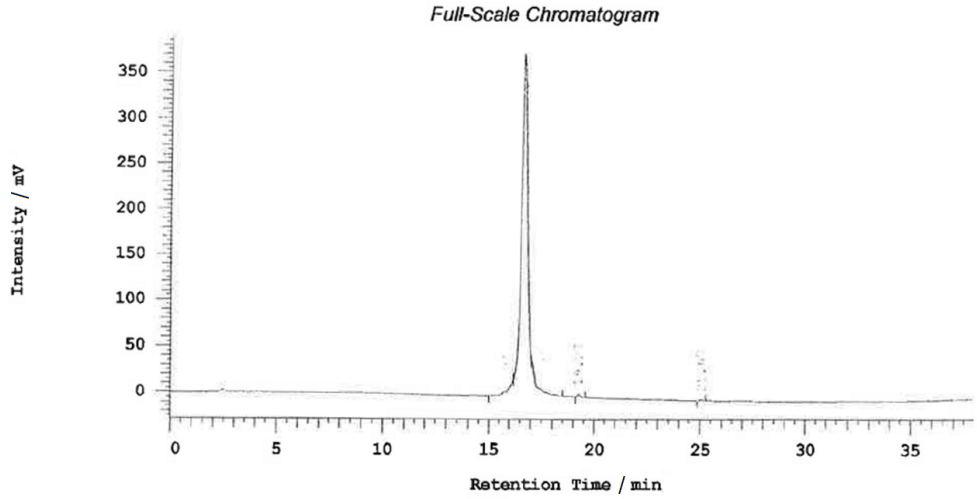

No.	RT	Area %	Area
1	15.63	3.164	269055
2	16.67	88.825	7554290
3	17.45	7.496	637529
4	19.27	0.422	35930
5	25.07	0.093	7904
		100.000	8504708

Figure S25. The HPLC chromatogram of the FITC-Aβ42 product from the manufacturer.

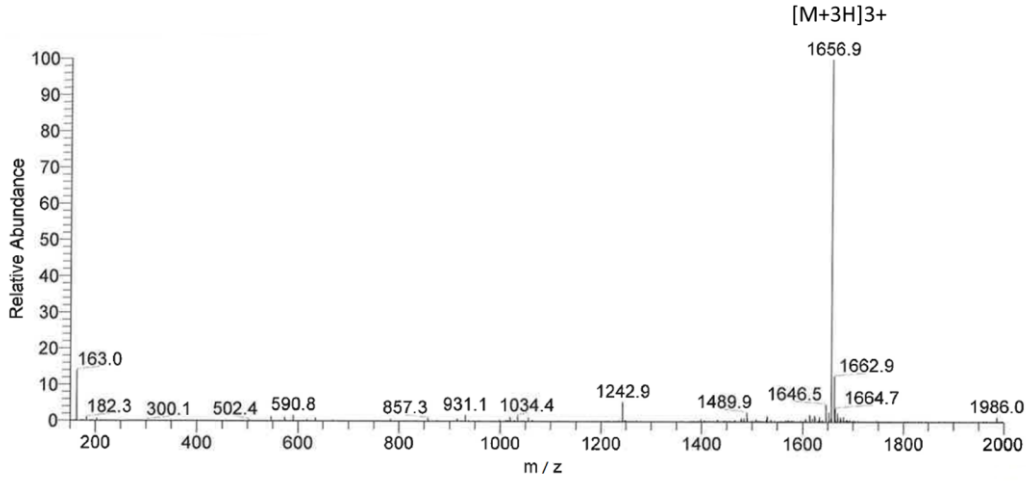

Figure S26. The electrospray ionization mass spectrometry (ESI-MS) result for the FITC-Aβ42 product from the manufacturer.

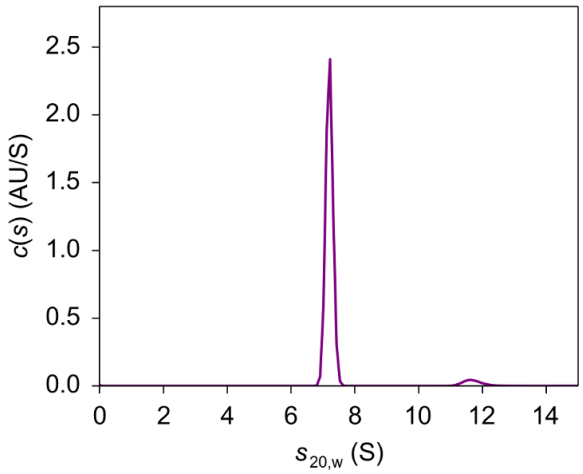

Figure S27. Sedimentation coefficient distribution of 6E10. The antibody sample was prepared in 20 mM sodium phosphate, 50 mM NaCl (pH 7.4) and was centrifuged at 40,000 rpm (129,024 g), 20 °C. $s_{20,w}$ was evaluated with the continuous distribution c(s) Lamm equation model. The major species at 7.2 S is the antibody monomer and accounts for ~95% of the total species, the species at ~11 S is most likely the antibody dimers.

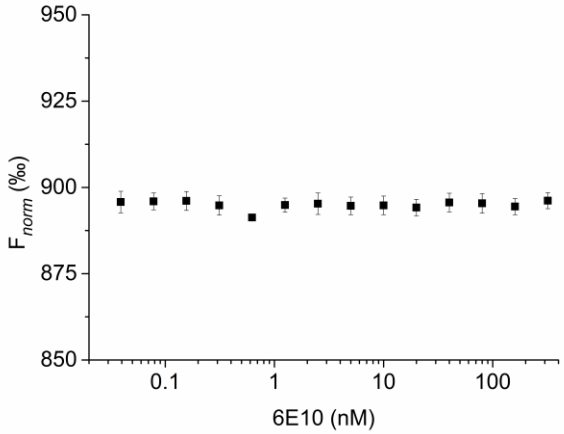

Figure S28. Microscale thermophoresis analysis of 40 nM fluorescein in the presence of different concentrations of 6E10. Samples were prepared in 20 mM sodium phosphate, 50 mM NaCl (pH 7.4) and were measured in triplicate.

General discussions

The misfolding and abnormal aggregation of Aβ have been under research, not only due to the critical role of Aβ aggregation in AD etiology, but also because of the importance of understanding the functioning of intrinsically disordered proteins in general. Aβ monomers are mainly unstructured in aqueous solution under physiological conditions. The rather flexible conformation of the protein therefore depends highly on the environment (solvent, ionic strength, pH and temperature) and the aggregation state (e.g. oligomers or fibrillar structures). The structural diversity of Aβ is linked to the solubility and the toxicity of various Aβ species. The N-terminal part of Aβ (D1-K16) is more hydrophilic than the rest of the protein and has a low propensity to form β-sheet structure. The central hydrophobic core (L17-A21), which plays an important role in the fibril formation of Aβ, tends to adopt β-strand conformations during the aggregation process. D23-K28 will form a turn structure via intramolecular salt-bridging [118]. The C-termini of Aβ proteins (starting from G29) are also hydrophobic in solution. It has been demonstrated in NMR studies that the C-terminus of Aβ42 is more rigid than that of Aβ40 [398]. The C-terminal area of Aβ has high probability of form β-sheet structures during the fibrillation. The N-terminus of Aβ, which is generally regarded as disordered both in free and aggregated forms, could regulate the aggregation rate and the stability of amyloid fibrils [399]. The overall conformational tendency of different regions of Aβ contributes to the final β-strand/turn/β-strand conformation of Aβ monomer within the fibrillary structures.

The aggregation of Aβ from monomeric units to oligomers and fibrils can be dissected into a number of microscopic events and is an essential target for disease diagnosis and intervention. Nowadays it is relatively clear that the aggregation of Aβ includes primary nucleation, elongation, secondary nucleation and fragmentation processes [139]. Each process has its own biophysical characteristics. In the primary nucleation Aβ monomers spontaneously assemble into small oligomers, or “nuclei”. During the elongation process, monomers add to existing nuclei to form protofilaments and fibrils. Secondary nucleation describes the formation of Aβ oligomers from monomers catalyzed by existing fibril surfaces [309]. The fragmentation by mechanical stresses gets more likely with increasing length of a fibril, which could generate more fibril ends as attachment sites for monomers. Each single process could be modulated to perturb the aggregation process of Aβ. For example, bexarotene suppresses the primary nucleation of Aβ and delays the formation of toxic species, thus maintaining the mobility of Caenorhabditis elegans model of Aβ mediated toxicity at a level similar to that of worms without Aβ expression [311]. Abelein et al. reported that Zn^{2+} interacts with Aβ42 fibril ends and interferes with the elongation process [168]. The fibril catalyzed secondary nucleation is thought to be the major pathway responsible for the generation of toxic oligomers [132]. Munke et al. designed several single-chain antibody fragments (scFvs) which can selectively inhibit the secondary nucleation process of Aβ42 and effectively reduce the production of neurotoxic oligomers [400].

The characterization of the interaction between ligands and different Aβ assemblies is often challenging due to the difficulty in obtaining homogenous Aβ species. The structural flexibility and high aggregation propensity of Aβ indeed make it hard to unveil how a certain binding partner interacts with Aβ species, especially for Aβ monomers. Very detailed crystal structures of complexes

formed by anti-Aβ antibodies and Aβ fragments have been published via using x-ray crystallography [380, 382], while it is still challenging for full-length Aβ monomers.

Dyshomeostasis of metal ions such as Zn^{2+} in the central nervous system is an important pathological change in AD patients. How Zn^{2+} interacts with Aβ and how the interaction influences the brain function might be a key point in understanding the exact role of Aβ aggregation in AD pathologies. In the first part of the thesis, we revisited the effect of Zn^{2+} on the fibrillation of Aβ via using analytical ultracentrifugation and other techniques. It seems that stoichiometric Zn^{2+} can rapidly induce conformational changes in Aβ by reducing the random coil structures. This rapid alteration in secondary structure correlates with a fast increase in ThT fluorescence in Aβ42 samples incubated with Zn^{2+} during the lag phase of Aβ42 alone. The partial neutralization of the net charge of Aβ42 molecules will also facilitate its self-association by reducing the electrostatic repulsion between different molecules. Corresponding to the accelerated aggregation in ThT assays and CD measurements, AUC analyses also showed that the amount of oligomers (5-15 S) was higher in Aβ42 incubated with Zn^{2+} than that in Zn^{2+} free Aβ42 samples. This observation was supported by a very similar study from Lee et al., showing that Zn^{2+} promotes the oligomerization of Aβ in a way different from the formation of ADDLs. The oligomers in the presence of Zn^{2+} had less β-sheet structures than those species formed in Aβ alone [401]. Although the aggregation of Aβ was directed to "off-pathway", we found that this effect could be reversed by the addition of EDTA. Interestingly, Aβ42-Zn^{2+} samples with the addition of EDTA at 23 h firstly showed a partial restoration of unordered conformation, and then a similar fibrillation process to Aβ42 alone. This may suggest that partially folded Aβ42 proteins are loosely accumulated with each other in the presence of Zn^{2+}. However, the effect of EDTA may also depend on the aggregation state of Aβ42. Matheou et al. introduced EDTA into Zn^{2+} containing Aβ42 samples after 250 h of incubation and discovered that EDTA was not able to resume the normal aggregation kinetics [270], probably indicating that after prolonged incubation, the off-pathway aggregates have different conformations or intermolecular interaction patterns to freshly formed off-pathway aggregates.

In the seeding experiments in which Zn^{2+} containing and Zn^{2+} free Aβ42 seeds were prepared and compared to assess their effects on Aβ42 aggregation kinetics, we observed interesting phenomena. First, Aβ42 seeds were unable to accelerate the fibrillation of Aβ42 in the presence of Zn^{2+}. Evidence from stopped-flow spectroscopy has proved that the interaction between Aβ42 and Zn^{2+} is rapid at millisecond time scale. The rapid interaction induces immediate conformational change in Aβ monomers and promotes its aggregation into non-fibrillar species [163, 164]. This may explain why Aβ42 seeds were not capable of enhancing the aggregation process in the presence of Zn^{2+}. Additionally, Zn^{2+} could also interact with the end of Aβ42 seeds and prevent monomers from stacking onto fibrillar assemblies, according to Abelein et al.'s research. Second, we also noticed that Aβ42 seeds prepared together with Zn^{2+} was inactive to speed up the aggregation process. We propose that this is a consequence of the non-fibrillary structures of Aβ42 seeds formed in the presence of Zn^{2+}. The elongation process happens due to the addition of Aβ monomers to the end of fibrillary structures by adopting β-sheet conformations. MD simulations demonstrated that Zn^{2+} binding does not influence the formation of β-sheet structures in C-terminal hydrophobic region of Aβ42. However, less ordered structures are also stabilized during the Zn^{2+} coordination, which

induces the formation of less uniformed assemblies [172]. The alteration in the structural property of Aβ seeds will for sure lead to different seeding capabilities.

How does Zn^{2+} influence the toxicity of Aβ42 aggregates? Sharma et al. showed that Zn^{2+} inhibits the fibrillation of Aβ42 and reduces the cytotoxicity of Aβ42 oligomers [165]. In contrast to this study, the recent research from Lee and coworkers demonstrated that "off-pathway" Aβ oligomers generated in the presence of Zn^{2+} are actually more toxic than ADDLs [401]. These aggregates not only impaired cell viability, but also damaged the long term potentiation (LTP) of hippocampal neurons and triggered microglia activation. The in vitro and ex vivo studies proved that the rapid interaction between Aβ42 and Zn^{2+} might play a role in Aβ aggregation related neuropathologies.

In addition to divalent metal ions, peptidic ligands have also been extensively studied for their efficacies and mechanisms in modulating the aggregation of Aβ. One example is the utilization of the central hydrophobic core (KLVFFA) of Aβ to interfere with the aggregation process of Aβ. It is generally accepted that this region binds to full length Aβ with high affinities and is critical for the interaction between Aβ molecules as well as the fibril formation [402]. Pallitto et al. designed several ligands by combining the central hydrophobic core with repeating lysine residues and discovered that these peptides increased the size and changed the morphologies of Aβ aggregates [403]. Peptidic ligands usually have high specificities and affinities for their targets, while the disadvantages of peptidic ligands include in vivo immunogenicity and susceptibility toward proteolysis. One promising strategy is to engineer peptidic ligands consisted of D-enantiomeric amino acids. Peptides composed solely of D-amino acids are a novel kind of drug candidates. They are highly resistant to proteolysis and are believed to be less immunogenic than their L-counterparts. D3 is the lead compound of a series of D-peptides with oligomer-eliminating activities and was selected by mirror image phage display using Aβ42 as a screening target [201, 210]. Previous in vivo studies have figured out that D3 improves the cognitive function of AD transgenic mice by converting toxic Aβ oligomers into non-toxic species [201, 209]. Further studies demonstrated that these 12-amino acid cationic peptides have good BBB permeability and in vivo stability, suggesting promising clinical applications [207, 208, 404]. RD2 is an optimized compound for toxic oligomer elimination. It has been demonstrated both in vitro and in vivo that RD2 has stronger efficacy than D3 in removing Aβ oligomers [214]. Furthermore, RD2 is especially potent in rescuring the cognition and behavioral ability of AD mouse models [215]. One of the interesting physical properties of these D-peptides is that they contain several D-arginine residues, meaning that they are usually positively charged in physiological conditions. CD experiments showed that the D-peptides are generally unstructured in aqueous solution. The high content of charge and conformational flexibity play important roles in the mechanism of action. Though the effects of D3 and RD2 on the elimination of toxic Aβ assemblies have been well-established using in vitro and in vivo assays. The detailed mechanism is not fully understood. Thus, it is of great value to study whether and how these arginine-rich D-peptides interact with intrinsically disordered Aβ monomers and further influence the aggregation process.

D3 and RD2 have the same amino acid compositions but different sequence. Interestingly, SPR experiments revealed that D3 and RD2 have rather similar binding affinities toward Aβ42 monomers, with K_D values at around 4 μM (Table 7). It has been shown that both D-peptides can mitigate Aβ

pathologies and rescue the cognitive impairment in AD mouse models. The mechanism of action of these D-peptides is based on the elimination of Aβ oligomers that are highly toxic to the central nervous system. The binding affinities were reevaluated using microscale thermophoresis. The fluorescence based method allowed us to reduce the concentration of Aβ42 to nanomolar range, so that the self-aggregation of Aβ42 could be suppressed. Moreover, the low analyte concentration is beneficial to the determination of high affinity bindings. We found that K_D values determined by MST were decreased by one order of magnitude for both D-peptides (Table 7). We wondered that the discrepancy in K_D values derived from different methods is likely due to different experimental setups. Aβ42 proteins were immobilized on sensor chips via biotin-streptavidin conjugation in SPR experiments. This may reduce the structural flexibility of unordered Aβ42 monomers, especially near the immobilization sites. However, both the protein and the binding partner are allowed to move freely in MST measurements. This could ensure the full access of D-peptides to all the potential binding sites of Aβ42. Free Aβ42 molecules could also maintain their conformational flexibility to facilitate the interaction. Indeed, evidence from SPR experiments using different Aβ fragments has shown that D3 can bind to multiple regions of Aβ42 with K_D values ranging from 14 to 85 μM [405]. The high affinity binding came from a combination of different binding events, known as the avidity effect [405]. Previous MD simulations discovered that the interaction between D-peptides and Aβ42 are mainly driven by electrostatic interactions. It is therefore natural to test the binding between D-peptides and Aβ42 under different ionic strength to check if this alters the K_D values. Ziehm et al. quantified the dependence of D3 and Aβ42 interaction on the concentration of sodium chloride using SPR technique and found that the binding was strongly weakened when the concentration of NaCl was increased to 300 mM [405]. In the present study, the K_D values of D-peptides and Aβ42 were decreased to around 100 nM when the ionic strength of the buffer was reduced from 99 mM to 61 mM in MST experiments. Our measurements corroborated the role of charge effects in the interaction between D-peptides and Aβ42. The mechanism by which reducing the ionic strength enhances the interaction between IDPs carrying opposite charges is not fully resolved. It is possible that under high ionic strength conditions solvent ions screen the charges on the protein surface and weaken the interaction [406]. In addition, similar to the SPR data, D3 and RD2 also have approximate affinities toward Aβ42 monomers according to MST measurements.

Table 7. Comparison of determined K_D values for Aβ42 and D-peptides based on different experimental approaches and conditions.

Experimental approach	Aβ42-D3	Aβ42-RD2
MST [a]	270 [240, 310] nM	330 [290, 380] nM
MST [b]	88 [82, 99] nM	130 [80, 190] nM
SPR [c]	4.0 ± 0.9 μM	3.6 ± 0.7 μM

[a] measurements were performed in 20 mM sodium phosphate, 50 mM NaCl (pH 7.4) by titrating D3 or RD2 to FITC-Aβ42 at 22 °C.

[b] measurements were conducted in 5 mM sodium phosphate, 50 mM NaCl (pH 7.4) by titrating D3 or RD2 to FITC-Aβ42 at 22 °C.

[c] SPR measurements were carried out at 25 °C by injecting D3 or RD2 diluted in 20 mM sodium phosphate, 50 mM NaCl (pH 7.4) to Aβ42 immobilized on sensor chips via biotin-streptavidin coupling [214].

The complex formation between D-peptides and Aβ42 monomers was investigated using fluorescence based analytical ultracentrifugation, supported by *s*-value estimation from the molecular dynamics simulation. In AUC measurements different labeling approaches were used to determine the size distributions of D-peptide and Aβ42 mixtures, in an attempt to discover the heterocomplexes. The first evidence on the formation of the 1:1 D3 and Aβ42 complex came from experiments using FITC-D3 and Aβ42, showing the shift in the *s*-value of the species at ~0.5 S (FITC-D3 monomer) toward 0.71 S when Aβ42 was present in high excess. Since D3 monomers are unlikely to self-associate into large species, and can hardly reach such a high *s*-value, the shift in *s*-value can only be attributed to the formation of the smallest Aβ42-D3 complexes. While in AUC measurements using FITC-Aβ42 and D-peptides, the overlap in the *s*-value of Aβ42 monomer and the 1:1 complex preludes the detectability of the smallest heterocomplex. Additionally, it is also evident from the *c*(*s*) analyses that Aβ42 monomers and D-peptides could form complexes at about 1.5 S and larger *s*-values, although the content of detected complexes is rather low. From the size distribution we also observed that there is an increase in the weigth average *s*-value in Aβ42 and D-peptide mixtures in all fluorescence AUC measurements, which obviously confirm the presence of species with increased *s*-value in these samples. The overall size distribution of the mixtures further confirmed that D-peptide and Aβ42 are able to form complexes at different stoichiometries. As supported by MD simulations, we observed complexation between D3 and Aβ42 at multiple stoichiometries. All the *s*-values for the simulated complexes are within the range of experimentally determined *s*-values. However, we were unable to determine the exact stoichiometries of all the complexes, because of the low amount of these species in AUC and the possible involvement of small complexes in the further formation of large co-precipates. The concentration dependent loss of fluorescence signals in the initial centrifugation process of AUC measurements could point to the formation of large co-precipates of D-peptide and Aβ42 during the incubation and initial centrifugation. We speculate that these high molecular weigth co-precipates sediment fast in the centrifugation and thus cannot be recorded by AUC. This was further substantiated by the turbidity assay performed using micromolar concentrations of Aβ42 and D-peptides. However it should be noted that the concentrations of Aβ used in the present work is still much higher than the physiological concentration of Aβ, the presence of co-precipates is mostly observable in vitro in the presence of high Aβ concentrations. The fluorescence labeling was conjugated to Aβ42 in AUC experiments with RD2. Besides FITC-Aβ42 monomers, the most populated species was observed at around 1.85 S. Since the size distributions of RD2 samples are rather similar to those of D3 samples, we believe that RD2 should also be able to form complexes with Aβ42 at multiple stoichiometries. Although AUC and MD simulations both demonstrate that D-peptides are capable of forming 1:1 and larger complexes with Aβ42 monomers, much work is needed to further characterize the

structural information as well as the exact stoichiometries of the complexes. The low population of D-peptide and Aβ complexes in AUC might suggest that the interaction is transient in nature.

The impact of hydrophilic charged proteins on the fibril formation of Aβ40 was already documented by Assarsson et al., reporting that single-chain monellin and calbindin D_{9k} retard Aβ40 fibrillation in a charge dependent manner. It has been demonstrated that the more positive charge the ligand has, the stronger the retardation effect will be [319]. D-peptides are also hydrophilic are highly charged in aqueous solution. The effect of D-peptide on the aggregation of Aβ42 was examined at substoichiometric levels to mitigate the rapid precipitation of materials in solution. The lag phase of Aβ42 aggregation was significantly delayed in the presence of substoichiometric levels of D3 or RD2, even when Aβ42 was incubated with 1% seeds. The rapid elongation process of Aβ42 fibrillation in the absence of seeds seems to be unaffected by D-peptides according to the ThT kinetics, while in Aβ42 samples with 5% seeds we noticed that D-peptides could slow down the elongation by comparing the slope of the aggregation kinetics. The retardation of the fibrillation was accompanied by a slow secondary structure transition of Aβ42 samples incubated with D3 or RD2 in CD measurements. Morphologies of Aβ aggregates from AFM imaging also agree well with different aggregation pathways of Aβ42 treated with or without D-peptides. Interestingly, the sedimentation velocity measurement showed that 0.1 fold RD2 could help to preserve Aβ42 monomers in solution, which correlates well with the retardation of Aβ42 fibrillation in the presence of D-peptides. How do D-peptides influence the fibrillation of Aβ42 at such a low stoichiometry? It is unlikely that D-peptides form stable complexes with Aβ monomers and reduce the effective concentration of Aβ monomers available for the fibrillation. In ThT and CD experiments which usually require micromolar Aβ42, sequestering 10% Aβ42 monomers is not sufficient to induce such a strong retardation in secondary structural transition and the fibrillation process. A possible explanation is that D-peptides may transiently interact with Aβ monomers and retain them in unstructured conformations that are not suitable for the self-association, as can be seen from CD measurenments and absorbance based AUC measurements. The high content of Aβ42 monomers in Aβ samples incubated with 0.1 fold D3 or RD2 for 24 h revealed that the formation of Aβ42 oligomers has been decelerated by D-peptide interaction. The stabilization of Aβ monomers therefore slows down the nucleation process and prolongs the lag phase. The presence of Aβ seeds could accelerate the fibrillation process by catalyzing secondary nucleation and initiating fibril elongation [311]. Although the elongation process is not significantly altered by D-peptides in Aβ samples without seeds, we found that D-peptides slowed down the elongation in Aβ samples containing high concentration of preformed seeds. Based on these findings, the second possible mechanism is that D-peptides interact with and cancel the catalytic ability of existing Aβ seeds, and prevent them from taking part in the further elongation process. For instance, D-peptides can cluster Aβ42 oligomers and small fibrillar structures (seeds) and form off-pathway species with them, therefore postponing the rapid elongation. Besides, our previous study already demonstrated that D-peptides are able to eliminate Aβ42 oligomers in pre-incubated Aβ samples by promoting the formation of large aggregates, as indicated in density gradient centrifugation analyses [212]. Combining the evidence from AUC and MST that D-peptides bind to Aβ42 monomers and seeding experiments showing that D-peptides also interact with Aβ42 assemblies, we propose that both mechanisms contribute to the retardation effect of substoichiometric D-peptides on Aβ fibrillation. Furthermore, we envision that

applying high molar ratios of D-peptides may exert stronger inhibitory effects on the aggregation of Aβ.

Up to now the detailed mechanisms of the interaction between D-peptides and Aβ42 are still not completely resolved. Most of the information about the binding sites came from SPR experiments and MD simulations. It seems that there is no well-defined binding site between D-peptides and Aβ42 monomers. Experimental analyses in the present work and our previous study suggest that electrostatic effect is important for the interaction between D3 and Aβ monomers [405]. Olubiyi et al. reported that the interaction between D3 and Aβ42 is mainly mediated by the electrostatic interaction between D-Arg residues on D3 and Glu and Asp residues on Aβ42. Our latest MD simulations also had consistent findings that hydrogen bonds and salt bridges between the oppositely charged amino acid residues play dominant roles in the interaction. Apart from hydrogen bonds and electrostatic interactions, we also identified π-cation interactions between D-Arg residues at C-termini of D3 peptides and Tyr10 or His13 of Aβ42, which can be anticipated from the property of Arg residues. These new interaction modes imply that D3 is more versatile than we expected in the interaction with Aβ42. Upon binding to D3, the conformation of Aβ42 will remain as random coil structures and the molecules seldom form β-sheet structures in these heterocomplexes. The mainly disordered conformation of Aβ42 in complex with D3 suggests the highly flexible nature of the interaction. The simulation data is in line with CD measurements showing that the presence of substoichiometric D3 or RD2 slows down the secondary structure transition of Aβ42. A detailed examination of the content of β-structures in MD simulations demonstrated that Aβ42-D-peptide complexes have much less β-structures than Aβ42 dimers [325]. The difference in the secondary structure between Aβ42-D-peptide complexes and Aβ42 oligomers (for example, Aβ42 dimers) could also result in different aggregation processes.

Due to the similarity in the amino acid composition of D3 and RD2, it is therefore very interesting to compare the difference between these two isoforms regarding their interaction with Aβ42. Previous SPR measurements demonstrated similar binding affinities of D3 and RD2 toward Aβ42. Besides, both D-peptides are effective in restoring the cognition and behavioral ability of AD mouse models in animal studies [209, 214]. In particular, RD2 has been demonstrated to significantly reduce the Aβ oligomer level in AD transgenic mouse models with full-blown pathologies and completely reverse the cognitive impairment [215]. In the present study, effects of D3 and RD2 on the aggregation of Aβ42 were mainly addressed at substoichiometric concentrations. The dissociation constants were also determined to be quite close for both D-peptides based on MST measurements. The complex formation as measured by fluorescence based AUC also displayed similar results that the content of monomeric Aβ42 was reduced in the presence of D-peptides, and that additional species accumulated in Aβ42 and D-peptide mixtures. The overall effects of D3 and RD2 on the aggregation of Aβ42 are rather similar. However, ThT kinetics, seeding experiments and CD measurements point out that RD2 seems to be more effective than D3 in retarding the secondary structure conversion and fibril formation of Aβ42. Turbidity measurements also substantiated a stronger effect of RD2 than D3 in promoting the generation of large co-precipates with Aβ42 at micromolar concentrations. The observed differences in these experiments suggest that RD2 might be more potent than D3 in recognizing and eliminating Aβ assemblies like oligomers. In MST

measurements we observed similar trends for D3 and RD2 that reducing the ionic strength of the buffer enhances the binding affinity, which indicates that the charge effect is also vital for the interaction between RD2 and Aβ. Nevertheless, alterations in side chains of D-peptides may differentially affect the binding pattern, thus leading to different outcomes.

The low loading concentration of fluorescent molecules in fluorescence based AUC and MST measurements permits the measurement at concentration ranges close to the dissociation constant of our system (Aβ42 and D-peptides). However, the surface adsorption of fluorescent molecules should be addressed appropriately. In the present study we used Tween-20 or PEI to tackle the unspecific attachment of Aβ42 or D-peptides to the surface. Commonly used surface blocking proteins such as BSA are not practical in our system. It is evident from the AUC measurement of FITC-Aβ42 alone that Tween-20 did not interact with Aβ42 since we could only identify FITC-Aβ42 monomers in the size distribution analysis. MST data further proved that Tween-20 had no impact on the interaction between Aβ42 and D-peptides. A cationic polymer, PEI, was used in AUC and MST experiments on FITC-D3. PEI is unlikely to interact with D3 due to the charge-charge repulsion. As shown in the size distribution analysis, FITC-D3 is able to form multiple complexes with Aβ42 monomers in solutions containing 0.0004% (w/v) PEI. Besides, MST measurements using FITC-D3 and Aβ42 reported approximate K_D value to that determined for FITC-Aβ42 and D3, suggesting that the interaction between Aβ42 and D-peptides is not significantly affected by the additives in solution.

In chapter IV, we applied fluorescence based sedimentation velocity and microscale thermophoresis to study the interaction between Aβ42 and three anti-Aβ antibodies recognizing different epitopes. One of the advantages of using fluorescence detection and matrix-free methods is that this allows us to carry out experiments in concentration ranges close to the dissociation constant of a system. In the present study, Aβ42 was used at a concentration lower than the reported critical oligomerization concentration, therefore the self-aggregation of Aβ42 could be well controlled to avoid the formation of Aβ42 oligomers. The binding parameters for Aβ42 monomers and antibodies can be determined reliably. All three antibodies, 6E10, 4G8 and 12F4, are able to form complexes with Aβ42 monomers with low-nanomolar affinities. The determined K_D values from AUC and MST agree well with those reported in SPR studies [373]. It is also interesting to discover that all three antibodies show similar affinities of binding to Aβ42 monomers to each other, although they have completely different Aβ epitopes. Although antibodies have two equivalent binding sites for Aβ42, the 1:1 binding model is sufficient to fit the data and the use of other more complex models such as the hill model did not significantly improve the quality of the fit. By using the well-established antigen-antibody system, we also validated that fluorescence based AUC and microscale thermophoresis can provide rigorous and reliable information for aggregation-prone and intrinsically disordered Aβ42 proteins and their binding partners. In addition, the approach of involving specific antibodies might be utilized as a competitive assay to identify, for example, the binding site between Aβ and the ligands.

Conclusions and perspectives

The present study addressed how a divalent metal ion (Zn^{2+}) and several ligands (D-peptides and anti-Aβ antibodies) interact with Aβ42 and further influence its aggregation process. Various biophysical methods have been applied to characterize the kinetics, morphologies and hydrodynamics of the interactions between different binding partners and Aβ42. Moreover, the complex formation between D-peptides and Aβ42 monomers, which is essential for understanding the mechanisms of action of D-peptides on Aβ aggregation, was elaborated.

In chapter I, we are able to present an overview about the evolution of Aβ42 aggregation with or without Zn^{2+} treatment by applying analytical ultracentrifugation and other techniques. AUC analyses demonstrated that Zn^{2+} promotes the formation of non-fibrillar species with broad size distributions. In particular, the presence of Zn^{2+} favors the formation of oligomeric aggregates, which might be responsible for Zn^{2+} related Aβ neurotoxicity. Chapter IV shows the successful application of fluorescence based AUC and microscale thermophoresis to investigate the interaction between anti-Aβ antibodies and Aβ42 monomers in the concentration range of their dissociation constants. The complexation and the binding parameters were characterized and quantified. In chapter II and III, we investigated how D-peptide D3 and RD2 interact with Aβ42 monomers and further influence its fibrillation process. We demonstrated that both D3 and RD2 are able to interact with Aβ42 monomers with nanomolar affinities. Electrostatic attraction has an important impact on the interaction. These D-peptides form complexes with Aβ42 monomers at 1:1 and higher stoichiometries. Aβ42 proteins remain mainly in unordered conformations when they are in complex with D-peptides, suggesting the highly flexible nature of the interaction between D-peptides and Aβ42 monomers. D3 and RD2 can efficiently retard the secondary structural conversion and fibrillation of Aβ42 at substoichiometric concentrations, by interacting with both Aβ42 monomers and Aβ42 assemblies. Our study confirms the diverse effect of D-peptides on modulating the aggregation pathway of Aβ42 by interacting with monomers and eliminating oligomers. Overall, these results provide molecular insights into how D-peptides might help to counteract the aggregation of Aβ in the central nervous system and confirm the promising potential of D-peptides as clinical agents against Aβ related pathologies.

The key findings of the work can be summarized as follows:

- Stoichiometric Zn^{2+} interacts rapidly with Aβ42 and promotes its aggregation by inducing the formation of aggregates with less β-sheet structures and heterogeneous in size, compared with Zn^{2+} free Aβ42 aggregates.
- D3 and RD2 are able to interact with Aβ42 monomers with nanomolar affinities, and electrostatic interactions play an important role in the complex formation.
- The high affinity interaction between D-peptides and Aβ42 monomers leads to complex formation at 1:1 and higher stoichiometries. Small complexes formed by D-peptides and Aβ42 monomers are highly disordered in conformation.
- D3 and RD2 slow down the secondary structure transition and the fibril formation of Aβ42 at substoichiometric concentrations, probably by interacting with not only Aβ42 monomers, but eliminating already existing Aβ assemblies like oligomers. The diverse effects of D-

peptides retard the growth and amplification of Aβ nuclei, and abolish the catalytic activity of Aβ seeds.

- RD2 affects the structural transition and fibril formation of Aβ42 in a similar way to D3, but shows stronger efficacies than D3 in prolonging the lag phase and inhibiting the secondary structure conversion of Aβ42.
- Sedimentation velocity centrifugation could be successfully applied to determine low-nanomolar affinities for three selected anti-Aβ antibodies for binding Aβ42 monomers free in solution. The K_D value for 12F4 and Aβ42 monomer is reported for the first time.

Some perspectives also arise from the current study, including:

- The kinetics and detailed mechanisms of the interaction between D-peptides and Aβ42 monomers remain to be studied, probably by NMR and/or single-molecule techniques.
- With regard to the mechanism of action, the question arises on how D-peptides affect individual microscopic events of the fibrillation of Aβ42 (such as nucleation and elongation processes) and whether this can be applied to Aβ40 and other Aβ mutants remain to be explored.
- Why is RD2 more effective than D3 in modulating the aggregation of Aβ?

Bibliography

1. He, W., D. Goodkind, and P. Kowal, *An Aging World: 2015*. 2016, U.S. Census Bureau, National Institute on Aging: Washington, DC. p. 175.
2. *Dementia*. 2017; Available from: http://www.who.int/en/news-room/fact-sheets/detail/dementia.
3. Livingston, G., et al., *Dementia prevention, intervention, and care.* Lancet, 2017. **390**(10113): p. 2673-2734.
4. Lane, C.A., J. Hardy, and J.M. Schott, *Alzheimer's disease.* Eur J Neurol, 2018. **25**(1): p. 59-70.
5. Reitz, C. and R. Mayeux, *Alzheimer disease: epidemiology, diagnostic criteria, risk factors and biomarkers.* Biochem Pharmacol, 2014. **88**(4): p. 640-51.
6. Maurer, K., S. Volk, and H. Gerbaldo, *Auguste D and Alzheimer's disease.* Lancet, 1997. **349**(9064): p. 1546-9.
7. Lage, J.M., *100 Years of Alzheimer's disease (1906-2006).* J Alzheimers Dis, 2006. **9**(3 Suppl): p. 15-26.
8. Cipriani, G., et al., *Alzheimer and his disease: a brief history.* Neurol Sci, 2011. **32**(2): p. 275-9.
9. Scheltens, P., et al., *Alzheimer's disease.* Lancet, 2016. **388**(10043): p. 505-17.
10. López, O.L. and S.T. DeKosky, *Clinical symptoms in Alzheimer's disease*, in *Handbook of Clinical Neurology*, C. Duyckaerts and I. Litvan, Editors. 2008, Elsevier. p. 10.
11. Hane, F.T., B.Y. Lee, and Z. Leonenko, *Recent Progress in Alzheimer's Disease Research, Part 1: Pathology.* J Alzheimers Dis, 2017. **57**(1): p. 1-28.
12. Mufson, E.J., et al., *Molecular and cellular pathophysiology of preclinical Alzheimer's disease.* Behav Brain Res, 2016. **311**: p. 54-69.
13. Cacace, R., K. Sleegers, and C. Van Broeckhoven, *Molecular genetics of early-onset Alzheimer's disease revisited.* Alzheimers Dement, 2016. **12**(6): p. 733-48.
14. Andrieu, S., et al., *Prevention of sporadic Alzheimer's disease: lessons learned from clinical trials and future directions.* Lancet Neurol, 2015. **14**(9): p. 926-944.
15. Cummings, J.L. and G. Cole, *Alzheimer disease.* JAMA, 2002. **287**(18): p. 2335-8.
16. Baumgart, M., et al., *Summary of the evidence on modifiable risk factors for cognitive decline and dementia: A population-based perspective.* Alzheimers Dement, 2015. **11**(6): p. 718-26.
17. Hickman, R.A., A. Faustin, and T. Wisniewski, *Alzheimer Disease and Its Growing Epidemic: Risk Factors, Biomarkers, and the Urgent Need for Therapeutics.* Neurol Clin, 2016. **34**(4): p. 941-953.
18. Hersi, M., et al., *Risk factors associated with the onset and progression of Alzheimer's disease: A systematic review of the evidence.* Neurotoxicology, 2017. **61**: p. 143-187.
19. Robinson, M., B.Y. Lee, and F.T. Hane, *Recent Progress in Alzheimer's Disease Research, Part 2: Genetics and Epidemiology.* J Alzheimers Dis, 2017. **57**(2): p. 317-330.
20. Zhao, N., et al., *Apolipoprotein E, Receptors, and Modulation of Alzheimer's Disease.* Biol Psychiatry, 2018. **83**(4): p. 347-357.
21. Liao, F., H. Yoon, and J. Kim, *Apolipoprotein E metabolism and functions in brain and its role in Alzheimer's disease.* Curr Opin Lipidol, 2017. **28**(1): p. 60-67.
22. Rebeck, G.W., et al., *Apolipoprotein E in sporadic Alzheimer's disease: allelic variation and receptor interactions.* Neuron, 1993. **11**(4): p. 575-80.
23. Farrer, L.A., et al., *Effects of age, sex, and ethnicity on the association between apolipoprotein E genotype and Alzheimer disease. A meta-analysis. APOE and Alzheimer Disease Meta Analysis Consortium.* JAMA, 1997. **278**(16): p. 1349-56.
24. Michaelson, D.M., *APOE epsilon4: the most prevalent yet understudied risk factor for Alzheimer's disease.* Alzheimers Dement, 2014. **10**(6): p. 861-8.

25. Corder, E.H., et al., *Gene dose of apolipoprotein E type 4 allele and the risk of Alzheimer's disease in late onset families.* Science, 1993. **261**(5123): p. 921-3.
26. Ulrich, J.D. and D.M. Holtzman, *TREM2 Function in Alzheimer's Disease and Neurodegeneration.* ACS Chem Neurosci, 2016. **7**(4): p. 420-7.
27. Ulrich, J.D., et al., *Elucidating the Role of TREM2 in Alzheimer's Disease.* Neuron, 2017. **94**(2): p. 237-248.
28. Wang, Y., et al., *TREM2-mediated early microglial response limits diffusion and toxicity of amyloid plaques.* J Exp Med, 2016. **213**(5): p. 667-75.
29. Wang, Y., et al., *TREM2 lipid sensing sustains the microglial response in an Alzheimer's disease model.* Cell, 2015. **160**(6): p. 1061-71.
30. Colonna, M. and Y. Wang, *TREM2 variants: new keys to decipher Alzheimer disease pathogenesis.* Nat Rev Neurosci, 2016. **17**(4): p. 201-7.
31. Guerreiro, R., J. Bras, and J. Hardy, *SnapShot: genetics of Alzheimer's disease.* Cell, 2013. **155**(4): p. 968-968 e1.
32. Crous-Bou, M., et al., *Alzheimer's disease prevention: from risk factors to early intervention.* Alzheimers Res Ther, 2017. **9**(1): p. 71.
33. Luchsinger, J.A., *Adiposity, hyperinsulinemia, diabetes and Alzheimer's disease: an epidemiological perspective.* Eur J Pharmacol, 2008. **585**(1): p. 119-29.
34. Campos-Pena, V., et al., *Metabolic Syndrome as a Risk Factor for Alzheimer's Disease: Is Abeta a Crucial Factor in Both Pathologies?* Antioxid Redox Signal, 2017. **26**(10): p. 542-560.
35. Flicker, L., *Modifiable lifestyle risk factors for Alzheimer's disease.* J Alzheimers Dis, 2010. **20**(3): p. 803-11.
36. Fratiglioni, L., S. Paillard-Borg, and B. Winblad, *An active and socially integrated lifestyle in late life might protect against dementia.* Lancet Neurol, 2004. **3**(6): p. 343-53.
37. Jack, C.R., Jr., et al., *Tracking pathophysiological processes in Alzheimer's disease: an updated hypothetical model of dynamic biomarkers.* Lancet Neurol, 2013. **12**(2): p. 207-16.
38. Sperling, R., E. Mormino, and K. Johnson, *The evolution of preclinical Alzheimer's disease: implications for prevention trials.* Neuron, 2014. **84**(3): p. 608-22.
39. Hernandez, P., et al., *Tau phosphorylation by cdk5 and Fyn in response to amyloid peptide Abeta (25-35): involvement of lipid rafts.* J Alzheimers Dis, 2009. **16**(1): p. 149-56.
40. Blurton-Jones, M. and F.M. Laferla, *Pathways by which Abeta facilitates tau pathology.* Curr Alzheimer Res, 2006. **3**(5): p. 437-48.
41. Gotz, J., et al., *Formation of neurofibrillary tangles in P301l tau transgenic mice induced by Abeta 42 fibrils.* Science, 2001. **293**(5534): p. 1491-5.
42. Polanco, J.C., et al., *Amyloid-beta and tau complexity - towards improved biomarkers and targeted therapies.* Nat Rev Neurol, 2018. **14**(1): p. 22-39.
43. Sperling, R.A., et al., *Toward defining the preclinical stages of Alzheimer's disease: recommendations from the National Institute on Aging-Alzheimer's Association workgroups on diagnostic guidelines for Alzheimer's disease.* Alzheimers Dement, 2011. **7**(3): p. 280-92.
44. Sperling, R.A., J. Karlawish, and K.A. Johnson, *Preclinical Alzheimer disease-the challenges ahead.* Nat Rev Neurol, 2013. **9**(1): p. 54-8.
45. Thompson, P.M., et al., *Dynamics of gray matter loss in Alzheimer's disease.* J Neurosci, 2003. **23**(3): p. 994-1005.
46. Jack, C.R., Jr., et al., *Brain atrophy rates predict subsequent clinical conversion in normal elderly and amnestic MCI.* Neurology, 2005. **65**(8): p. 1227-31.
47. Du, A.T., et al., *Magnetic resonance imaging of the entorhinal cortex and hippocampus in mild cognitive impairment and Alzheimer's disease.* J Neurol Neurosurg Psychiatry, 2001. **71**(4): p. 441-7.
48. Jack, C.R., Jr., et al., *NIA-AA Research Framework: Toward a biological definition of Alzheimer's disease.* Alzheimers Dement, 2018. **14**(4): p. 535-562.

49. Dubois, B., et al., *Revising the definition of Alzheimer's disease: a new lexicon.* Lancet Neurol, 2010. **9**(11): p. 1118-27.
50. Lanctot, K.L., et al., *Neuropsychiatric signs and symptoms of Alzheimer's disease: New treatment paradigms.* Alzheimers Dement (N Y), 2017. **3**(3): p. 440-449.
51. Mega, M.S., et al., *The spectrum of behavioral changes in Alzheimer's disease.* Neurology, 1996. **46**(1): p. 130-5.
52. Wang, X., et al., *Genetic determinants of disease progression in Alzheimer's disease.* J Alzheimers Dis, 2015. **43**(2): p. 649-55.
53. Nelson, L. and N. Tabet, *Slowing the progression of Alzheimer's disease; what works?* Ageing Res Rev, 2015. **23**(Pt B): p. 193-209.
54. Maresova, P., et al., *Socio-economic Aspects of Alzheimer's Disease.* Curr Alzheimer Res, 2015. **12**(9): p. 903-11.
55. McKhann, G., et al., *Clinical diagnosis of Alzheimer's disease: report of the NINCDS-ADRDA Work Group under the auspices of Department of Health and Human Services Task Force on Alzheimer's Disease.* Neurology, 1984. **34**(7): p. 939-44.
56. Loy, C.T., et al., *Genetics of dementia.* Lancet, 2014. **383**(9919): p. 828-40.
57. Karch, C.M., C. Cruchaga, and A.M. Goate, *Alzheimer's disease genetics: from the bench to the clinic.* Neuron, 2014. **83**(1): p. 11-26.
58. Hulbert, S. and H. Adeli, *EEG/MEG- and imaging-based diagnosis of Alzheimer's disease.* Rev Neurosci, 2013. **24**(6): p. 563-76.
59. Hane, F.T., et al., *Recent Progress in Alzheimer's Disease Research, Part 3: Diagnosis and Treatment.* J Alzheimers Dis, 2017. **57**(3): p. 645-665.
60. Love, S., *Neuropathological investigation of dementia: a guide for neurologists.* J Neurol Neurosurg Psychiatry, 2005. **76 Suppl 5**: p. v8-14.
61. Mielke, M.M., et al., *Effects of Food and Drug Administration-approved medications for Alzheimer's disease on clinical progression.* Alzheimers Dement, 2012. **8**(3): p. 180-7.
62. Galimberti, D. and E. Scarpini, *Old and new acetylcholinesterase inhibitors for Alzheimer's disease.* Expert Opin Investig Drugs, 2016. **25**(10): p. 1181-7.
63. Mufson, E.J., et al., *Cholinergic system during the progression of Alzheimer's disease: therapeutic implications.* Expert Rev Neurother, 2008. **8**(11): p. 1703-18.
64. Miyamoto, T., et al., *Phosphorylation of tau at Y18, but not tau-fyn binding, is required for tau to modulate NMDA receptor-dependent excitotoxicity in primary neuronal culture.* Mol Neurodegener, 2017. **12**(1): p. 41.
65. Johnson, J.W. and S.E. Kotermanski, *Mechanism of action of memantine.* Curr Opin Pharmacol, 2006. **6**(1): p. 61-7.
66. Chen, H.S. and S.A. Lipton, *The chemical biology of clinically tolerated NMDA receptor antagonists.* J Neurochem, 2006. **97**(6): p. 1611-26.
67. Howard, R., et al., *Donepezil and memantine for moderate-to-severe Alzheimer's disease.* N Engl J Med, 2012. **366**(10): p. 893-903.
68. Zemek, F., et al., *Outcomes of Alzheimer's disease therapy with acetylcholinesterase inhibitors and memantine.* Expert Opin Drug Saf, 2014. **13**(6): p. 759-74.
69. Cummings, J., T. Morstorf, and G. Lee, *Alzheimer's drug-development pipeline: 2016.* Alzheimers Dement (N Y), 2016. **2**(4): p. 222-232.
70. Francis, P.T., M.J. Ramirez, and M.K. Lai, *Neurochemical basis for symptomatic treatment of Alzheimer's disease.* Neuropharmacology, 2010. **59**(4-5): p. 221-9.
71. Citron, M., *Alzheimer's disease: strategies for disease modification.* Nat Rev Drug Discov, 2010. **9**(5): p. 387-98.
72. Godyn, J., et al., *Therapeutic strategies for Alzheimer's disease in clinical trials.* Pharmacol Rep, 2016. **68**(1): p. 127-38.
73. Cummings, J., et al., *Alzheimer's disease drug development pipeline: 2018.* Alzheimers Dement (N Y), 2018. **4**: p. 195-214.

74. Wisniewski, T. and F. Goni, *Immunotherapeutic approaches for Alzheimer's disease.* Neuron, 2015. **85**(6): p. 1162-76.
75. Pedersen, J.T. and E.M. Sigurdsson, *Tau immunotherapy for Alzheimer's disease.* Trends Mol Med, 2015. **21**(6): p. 394-402.
76. Deuschl, G., et al., *A randomized trial of deep-brain stimulation for Parkinson's disease.* N Engl J Med, 2006. **355**(9): p. 896-908.
77. Dostrovsky, J.O. and A.M. Lozano, *Mechanisms of deep brain stimulation.* Mov Disord, 2002. **17 Suppl 3**: p. S63-8.
78. Grossman, N., et al., *Noninvasive Deep Brain Stimulation via Temporally Interfering Electric Fields.* Cell, 2017. **169**(6): p. 1029-1041 e16.
79. Zhen, J., et al., *Gamma rhythm low field magnetic stimulation alleviates neuropathologic changes and rescues memory and cognitive impairments in a mouse model of Alzheimer's disease.* Alzheimers Dement (N Y), 2017. **3**(4): p. 487-497.
80. Chen, G.F., et al., *Amyloid beta: structure, biology and structure-based therapeutic development.* Acta Pharmacol Sin, 2017. **38**(9): p. 1205-1235.
81. Haass, C., et al., *Trafficking and proteolytic processing of APP.* Cold Spring Harb Perspect Med, 2012. **2**(5): p. a006270.
82. O'Brien, R.J. and P.C. Wong, *Amyloid precursor protein processing and Alzheimer's disease.* Annu Rev Neurosci, 2011. **34**: p. 185-204.
83. Nicolas, M. and B.A. Hassan, *Amyloid precursor protein and neural development.* Development, 2014. **141**(13): p. 2543-8.
84. van der Kant, R. and L.S. Goldstein, *Cellular functions of the amyloid precursor protein from development to dementia.* Dev Cell, 2015. **32**(4): p. 502-15.
85. Zhou, Z.D., et al., *The roles of amyloid precursor protein (APP) in neurogenesis: Implications to pathogenesis and therapy of Alzheimer disease.* Cell Adh Migr, 2011. **5**(4): p. 280-92.
86. White, A.R., et al., *The Alzheimer's disease amyloid precursor protein modulates copper-induced toxicity and oxidative stress in primary neuronal cultures.* J Neurosci, 1999. **19**(21): p. 9170-9.
87. Zheng, H. and E.H. Koo, *Biology and pathophysiology of the amyloid precursor protein.* Mol Neurodegener, 2011. **6**(1): p. 27.
88. Thinakaran, G. and E.H. Koo, *Amyloid precursor protein trafficking, processing, and function.* J Biol Chem, 2008. **283**(44): p. 29615-9.
89. Bandyopadhyay, S., et al., *Role of the APP non-amyloidogenic signaling pathway and targeting alpha-secretase as an alternative drug target for treatment of Alzheimer's disease.* Curr Med Chem, 2007. **14**(27): p. 2848-64.
90. Zhang, Y.W., et al., *APP processing in Alzheimer's disease.* Mol Brain, 2011. **4**: p. 3.
91. Tekirian, T.L., et al., *Carboxy terminal of beta-amyloid deposits in aged human, canine, and polar bear brains.* Neurobiol Aging, 1996. **17**(2): p. 249-57.
92. Dewachter, I., et al., *Aging increased amyloid peptide and caused amyloid plaques in brain of old APP/V717I transgenic mice by a different mechanism than mutant presenilin1.* J Neurosci, 2000. **20**(17): p. 6452-8.
93. Pauwels, K., et al., *Structural basis for increased toxicity of pathological abeta42:abeta40 ratios in Alzheimer disease.* J Biol Chem, 2012. **287**(8): p. 5650-60.
94. Karran, E. and B. De Strooper, *The amyloid cascade hypothesis: are we poised for success or failure?* J Neurochem, 2016. **139 Suppl 2**: p. 237-252.
95. Iwata, N., M. Higuchi, and T.C. Saido, *Metabolism of amyloid-beta peptide and Alzheimer's disease.* Pharmacol Ther, 2005. **108**(2): p. 129-48.
96. Saido, T.C. and N. Iwata, *Metabolism of amyloid beta peptide and pathogenesis of Alzheimer's disease. Towards presymptomatic diagnosis, prevention and therapy.* Neurosci Res, 2006. **54**(4): p. 235-53.

97. Mawuenyega, K.G., et al., *Decreased clearance of CNS beta-amyloid in Alzheimer's disease.* Science, 2010. **330**(6012): p. 1774.
98. Lee, S.J., et al., *Towards an understanding of amyloid-beta oligomers: characterization, toxicity mechanisms, and inhibitors.* Chem Soc Rev, 2017. **46**(2): p. 310-323.
99. Smith, L.M. and S.M. Strittmatter, *Binding Sites for Amyloid-beta Oligomers and Synaptic Toxicity.* Cold Spring Harb Perspect Med, 2017. **7**(5).
100. Viola, K.L. and W.L. Klein, *Amyloid beta oligomers in Alzheimer's disease pathogenesis, treatment, and diagnosis.* Acta Neuropathol, 2015. **129**(2): p. 183-206.
101. Thal, D.R., W.S. Griffin, and H. Braak, *Parenchymal and vascular Abeta-deposition and its effects on the degeneration of neurons and cognition in Alzheimer's disease.* J Cell Mol Med, 2008. **12**(5B): p. 1848-62.
102. Bell, R.D. and B.V. Zlokovic, *Neurovascular mechanisms and blood-brain barrier disorder in Alzheimer's disease.* Acta Neuropathol, 2009. **118**(1): p. 103-13.
103. Kalin, A.M., et al., *Subcortical Shape Changes, Hippocampal Atrophy and Cortical Thinning in Future Alzheimer's Disease Patients.* Front Aging Neurosci, 2017. **9**: p. 38.
104. Apostolova, L.G., et al., *Hippocampal atrophy and ventricular enlargement in normal aging, mild cognitive impairment (MCI), and Alzheimer Disease.* Alzheimer Dis Assoc Disord, 2012. **26**(1): p. 17-27.
105. Nelson, P.T., et al., *Correlation of Alzheimer disease neuropathologic changes with cognitive status: a review of the literature.* J Neuropathol Exp Neurol, 2012. **71**(5): p. 362-81.
106. Morris, G.P., I.A. Clark, and B. Vissel, *Inconsistencies and controversies surrounding the amyloid hypothesis of Alzheimer's disease.* Acta Neuropathol Commun, 2014. **2**: p. 135.
107. Blennow, K., et al., *Cerebrospinal fluid and plasma biomarkers in Alzheimer disease.* Nat Rev Neurol, 2010. **6**(3): p. 131-44.
108. Bloom, G.S., *Amyloid-beta and tau: the trigger and bullet in Alzheimer disease pathogenesis.* JAMA Neurol, 2014. **71**(4): p. 505-8.
109. Uversky, V.N., C.J. Oldfield, and A.K. Dunker, *Intrinsically disordered proteins in human diseases: introducing the D2 concept.* Annu Rev Biophys, 2008. **37**: p. 215-46.
110. Shanmugam, G. and P.L. Polavarapu, *Structure of A beta(25-35) peptide in different environments.* Biophys J, 2004. **87**(1): p. 622-30.
111. Barrow, C.J., et al., *Solution conformations and aggregational properties of synthetic amyloid beta-peptides of Alzheimer's disease. Analysis of circular dichroism spectra.* J Mol Biol, 1992. **225**(4): p. 1075-93.
112. LeVine, H., 3rd, *Thioflavine T interaction with synthetic Alzheimer's disease beta-amyloid peptides: detection of amyloid aggregation in solution.* Protein Sci, 1993. **2**(3): p. 404-10.
113. Danielsson, J., et al., *High-resolution NMR studies of the zinc-binding site of the Alzheimer's amyloid beta-peptide.* FEBS J, 2007. **274**(1): p. 46-59.
114. Hamley, I.W., *The amyloid beta peptide: a chemist's perspective. Role in Alzheimer's and fibrillization.* Chem Rev, 2012. **112**(10): p. 5147-92.
115. Faller, P., C. Hureau, and G. La Penna, *Metal ions and intrinsically disordered proteins and peptides: from Cu/Zn amyloid-beta to general principles.* Acc Chem Res, 2014. **47**(8): p. 2252-9.
116. Truex, N.L., Y. Wang, and J.S. Nowick, *Assembly of Peptides Derived from beta-Sheet Regions of beta-Amyloid.* J Am Chem Soc, 2016. **138**(42): p. 13882-13890.
117. Buchete, N.V. and G. Hummer, *Structure and dynamics of parallel beta-sheets, hydrophobic core, and loops in Alzheimer's A beta fibrils.* Biophys J, 2007. **92**(9): p. 3032-9.
118. Tarus, B., J.E. Straub, and D. Thirumalai, *Dynamics of Asp23-Lys28 salt-bridge formation in Abeta10-35 monomers.* J Am Chem Soc, 2006. **128**(50): p. 16159-68.
119. Stroud, J.C., et al., *Toxic fibrillar oligomers of amyloid-beta have cross-beta structure.* Proc Natl Acad Sci U S A, 2012. **109**(20): p. 7717-22.

120. Meisl, G., et al., *Modulation of electrostatic interactions to reveal a reaction network unifying the aggregation behaviour of the Abeta42 peptide and its variants.* Chem Sci, 2017. **8**(6): p. 4352-4362.
121. Ahmed, M., et al., *Structural conversion of neurotoxic amyloid-beta(1-42) oligomers to fibrils.* Nat Struct Mol Biol, 2010. **17**(5): p. 561-7.
122. Matsunaga, Y., et al., *Conformational changes preceding amyloid-fibril formation of amyloid-beta and stefin B; parallels in pH dependence.* Curr Med Chem, 2002. **9**(19): p. 1717-24.
123. Murphy, R.M., *Kinetics of amyloid formation and membrane interaction with amyloidogenic proteins.* Biochim Biophys Acta, 2007. **1768**(8): p. 1923-34.
124. Kim, W. and M.H. Hecht, *Generic hydrophobic residues are sufficient to promote aggregation of the Alzheimer's Abeta42 peptide.* Proc Natl Acad Sci U S A, 2006. **103**(43): p. 15824-9.
125. Streltsov, V.A., et al., *Crystal structure of the amyloid-beta p3 fragment provides a model for oligomer formation in Alzheimer's disease.* J Neurosci, 2011. **31**(4): p. 1419-26.
126. Arosio, P., T.P. Knowles, and S. Linse, *On the lag phase in amyloid fibril formation.* Phys Chem Chem Phys, 2015. **17**(12): p. 7606-18.
127. Favrin, G., A. Irback, and S. Mohanty, *Oligomerization of amyloid Abeta16-22 peptides using hydrogen bonds and hydrophobicity forces.* Biophys J, 2004. **87**(6): p. 3657-64.
128. Narayanan, C. and C.L. Dias, *Hydrophobic interactions and hydrogen bonds in beta-sheet formation.* J Chem Phys, 2013. **139**(11): p. 115103.
129. Colvin, M.T., et al., *Atomic Resolution Structure of Monomorphic Abeta42 Amyloid Fibrils.* J Am Chem Soc, 2016. **138**(30): p. 9663-74.
130. Buchete, N.V., R. Tycko, and G. Hummer, *Molecular dynamics simulations of Alzheimer's beta-amyloid protofilaments.* J Mol Biol, 2005. **353**(4): p. 804-21.
131. Garai, K. and C. Frieden, *Quantitative analysis of the time course of Abeta oligomerization and subsequent growth steps using tetramethylrhodamine-labeled Abeta.* Proc Natl Acad Sci U S A, 2013. **110**(9): p. 3321-6.
132. Cohen, S.I., et al., *Proliferation of amyloid-beta42 aggregates occurs through a secondary nucleation mechanism.* Proc Natl Acad Sci U S A, 2013. **110**(24): p. 9758-63.
133. Xue, W.F., et al., *Fibril fragmentation enhances amyloid cytotoxicity.* J Biol Chem, 2009. **284**(49): p. 34272-82.
134. Xue, W.F., et al., *Fibril fragmentation in amyloid assembly and cytotoxicity: when size matters.* Prion, 2010. **4**(1): p. 20-5.
135. Knowles, T.P., M. Vendruscolo, and C.M. Dobson, *The amyloid state and its association with protein misfolding diseases.* Nat Rev Mol Cell Biol, 2014. **15**(6): p. 384-96.
136. Biancalana, M. and S. Koide, *Molecular mechanism of Thioflavin-T binding to amyloid fibrils.* Biochim Biophys Acta, 2010. **1804**(7): p. 1405-12.
137. Naiki, H., et al., *Fluorometric determination of amyloid fibrils in vitro using the fluorescent dye, thioflavin T1.* Anal Biochem, 1989. **177**(2): p. 244-9.
138. Noel, S., et al., *The benzazole scaffold: a SWAT to combat Alzheimer's disease.* Chem Soc Rev, 2013. **42**(19): p. 7747-62.
139. Zeineddine, R. and J.J. Yerbury, *The role of macropinocytosis in the propagation of protein aggregation associated with neurodegenerative diseases.* Front Physiol, 2015. **6**: p. 277.
140. Fandrich, M., M. Schmidt, and N. Grigorieff, *Recent progress in understanding Alzheimer's beta-amyloid structures.* Trends Biochem Sci, 2011. **36**(6): p. 338-45.
141. Kirschner, D.A., C. Abraham, and D.J. Selkoe, *X-ray diffraction from intraneuronal paired helical filaments and extraneuronal amyloid fibers in Alzheimer disease indicates cross-beta conformation.* Proc Natl Acad Sci U S A, 1986. **83**(2): p. 503-7.
142. Luhrs, T., et al., *3D structure of Alzheimer's amyloid-beta(1-42) fibrils.* Proc Natl Acad Sci U S A, 2005. **102**(48): p. 17342-7.

143. Schmidt, M., et al., *Peptide dimer structure in an Abeta(1-42) fibril visualized with cryo-EM.* Proc Natl Acad Sci U S A, 2015. **112**(38): p. 11858-63.
144. Gremer, L., et al., *Fibril structure of amyloid-beta(1-42) by cryo-electron microscopy.* Science, 2017. **358**(6359): p. 116-119.
145. Cizas, P., et al., *Size-dependent neurotoxicity of beta-amyloid oligomers.* Arch Biochem Biophys, 2010. **496**(2): p. 84-92.
146. Bitan, G., et al., *Amyloid beta -protein (Abeta) assembly: Abeta 40 and Abeta 42 oligomerize through distinct pathways.* Proc Natl Acad Sci U S A, 2003. **100**(1): p. 330-5.
147. Zhang-Haagen, B., et al., *Monomeric Amyloid Beta Peptide in Hexafluoroisopropanol Detected by Small Angle Neutron Scattering.* PLoS One, 2016. **11**(2): p. e0150267.
148. Nag, S., et al., *Nature of the amyloid-beta monomer and the monomer-oligomer equilibrium.* J Biol Chem, 2011. **286**(16): p. 13827-33.
149. Larson, M.E. and S.E. Lesne, *Soluble Abeta oligomer production and toxicity.* J Neurochem, 2012. **120 Suppl 1**: p. 125-39.
150. Lambert, M.P., et al., *Diffusible, nonfibrillar ligands derived from Abeta1-42 are potent central nervous system neurotoxins.* Proc Natl Acad Sci U S A, 1998. **95**(11): p. 6448-53.
151. Amar, F., et al., *The amyloid-beta oligomer Abeta*56 induces specific alterations in neuronal signaling that lead to tau phosphorylation and aggregation.* Sci Signal, 2017. **10**(478).
152. Kreutzer, A.G., et al., *X-ray Crystallographic Structures of a Trimer, Dodecamer, and Annular Pore Formed by an Abeta17-36 beta-Hairpin.* J Am Chem Soc, 2016. **138**(13): p. 4634-42.
153. Sakono, M. and T. Zako, *Amyloid oligomers: formation and toxicity of Abeta oligomers.* FEBS J, 2010. **277**(6): p. 1348-58.
154. Wolff, M., et al., *Abeta42 pentamers/hexamers are the smallest detectable oligomers in solution.* Sci Rep, 2017. **7**(1): p. 2493.
155. Klein, W.L., G.A. Krafft, and C.E. Finch, *Targeting small Abeta oligomers: the solution to an Alzheimer's disease conundrum?* Trends Neurosci, 2001. **24**(4): p. 219-24.
156. Aggett, P.J., *Physiology and metabolism of essential trace elements: an outline.* Clin Endocrinol Metab, 1985. **14**(3): p. 513-43.
157. Sensi, S.L., et al., *Zinc in the physiology and pathology of the CNS.* Nat Rev Neurosci, 2009. **10**(11): p. 780-91.
158. Lovell, M.A., et al., *Copper, iron and zinc in Alzheimer's disease senile plaques.* J Neurol Sci, 1998. **158**(1): p. 47-52.
159. Huang, X., et al., *Alzheimer's disease, beta-amyloid protein and zinc.* J Nutr, 2000. **130**(5S Suppl): p. 1488S-92S.
160. Faller, P., C. Hureau, and O. Berthoumieu, *Role of metal ions in the self-assembly of the Alzheimer's amyloid-beta peptide.* Inorg Chem, 2013. **52**(21): p. 12193-206.
161. Atrian-Blasco, E., A. Conte-Daban, and C. Hureau, *Mutual interference of Cu and Zn ions in Alzheimer's disease: perspectives at the molecular level.* Dalton Trans, 2017. **46**(38): p. 12750-12759.
162. Alies, B., et al., *Zinc(II) Binding Site to the Amyloid-beta Peptide: Insights from Spectroscopic Studies with a Wide Series of Modified Peptides.* Inorg Chem, 2016. **55**(20): p. 10499-10509.
163. Guo, J., et al., *Kinetic Insights into Zn(2+)-Induced Amyloid beta-Protein Aggregation Revealed by Stopped-Flow Fluorescence Spectroscopy.* J Phys Chem B, 2017. **121**(16): p. 3909-3917.
164. Noy, D., et al., *Zinc-amyloid beta interactions on a millisecond time-scale stabilize non-fibrillar Alzheimer-related species.* J Am Chem Soc, 2008. **130**(4): p. 1376-83.
165. Sharma, A.K., et al., *The effect of Cu(2+) and Zn(2+) on the Abeta42 peptide aggregation and cellular toxicity.* Metallomics, 2013. **5**(11): p. 1529-36.

166. Tougu, V., et al., *Zn(II)- and Cu(II)-induced non-fibrillar aggregates of amyloid-beta (1-42) peptide are transformed to amyloid fibrils, both spontaneously and under the influence of metal chelators.* J Neurochem, 2009. **110**(6): p. 1784-95.
167. Solomonov, I., et al., *Zn2+-Abeta40 complexes form metastable quasi-spherical oligomers that are cytotoxic to cultured hippocampal neurons.* J Biol Chem, 2012. **287**(24): p. 20555-64.
168. Abelein, A., A. Graslund, and J. Danielsson, *Zinc as chaperone-mimicking agent for retardation of amyloid beta peptide fibril formation.* Proc Natl Acad Sci U S A, 2015. **112**(17): p. 5407-12.
169. Xu, L., et al., *Coupling of Zinc-Binding and Secondary Structure in Nonfibrillar Abeta40 Peptide Oligomerization.* J Chem Inf Model, 2015. **55**(6): p. 1218-30.
170. Rezaei-Ghaleh, N., et al., *Effect of zinc binding on beta-amyloid structure and dynamics: implications for Abeta aggregation.* Biophys J, 2011. **101**(5): p. 1202-11.
171. Wise-Scira, O., et al., *Structures and free energy landscapes of aqueous zinc(II)-bound amyloid-beta(1-40) and zinc(II)-bound amyloid-beta(1-42) with dynamics.* J Biol Inorg Chem, 2012. **17**(6): p. 927-38.
172. Miller, Y., B. Ma, and R. Nussinov, *Zinc ions promote Alzheimer Abeta aggregation via population shift of polymorphic states.* Proc Natl Acad Sci U S A, 2010. **107**(21): p. 9490-5.
173. Demattos, R.B., et al., *A plaque-specific antibody clears existing beta-amyloid plaques in Alzheimer's disease mice.* Neuron, 2012. **76**(5): p. 908-20.
174. Brody, D.L. and D.M. Holtzman, *Active and passive immunotherapy for neurodegenerative disorders.* Annu Rev Neurosci, 2008. **31**: p. 175-93.
175. Schenk, D., et al., *Immunization with amyloid-beta attenuates Alzheimer-disease-like pathology in the PDAPP mouse.* Nature, 1999. **400**(6740): p. 173-7.
176. Nicoll, J.A., et al., *Neuropathology of human Alzheimer disease after immunization with amyloid-beta peptide: a case report.* Nat Med, 2003. **9**(4): p. 448-52.
177. Winblad, B., et al., *Safety, tolerability, and antibody response of active Abeta immunotherapy with CAD106 in patients with Alzheimer's disease: randomised, double-blind, placebo-controlled, first-in-human study.* Lancet Neurol, 2012. **11**(7): p. 597-604.
178. Hull, M., et al., *Long-Term Extensions of Randomized Vaccination Trials of ACC-001 and QS-21 in Mild to Moderate Alzheimer's Disease.* Curr Alzheimer Res, 2017. **14**(7): p. 696-708.
179. Gallardo, G. and D.M. Holtzman, *Antibody Therapeutics Targeting Abeta and Tau.* Cold Spring Harb Perspect Med, 2017. **7**(10).
180. Honig, L.S., et al., *Trial of Solanezumab for Mild Dementia Due to Alzheimer's Disease.* N Engl J Med, 2018. **378**(4): p. 321-330.
181. Sevigny, J., et al., *The antibody aducanumab reduces Abeta plaques in Alzheimer's disease.* Nature, 2016. **537**(7618): p. 50-6.
182. Hung, S.Y. and W.M. Fu, *Drug candidates in clinical trials for Alzheimer's disease.* J Biomed Sci, 2017. **24**(1): p. 47.
183. Kumar, D., et al., *Secretase inhibitors for the treatment of Alzheimer's disease: Long road ahead.* Eur J Med Chem, 2018. **148**: p. 436-452.
184. Willem, M., et al., *Control of peripheral nerve myelination by the beta-secretase BACE1.* Science, 2006. **314**(5799): p. 664-6.
185. Artavanis-Tsakonas, S., M.D. Rand, and R.J. Lake, *Notch signaling: cell fate control and signal integration in development.* Science, 1999. **284**(5415): p. 770-6.
186. Lai, E.C., *Notch signaling: control of cell communication and cell fate.* Development, 2004. **131**(5): p. 965-73.
187. Hopkins, C.R., *ACS chemical neuroscience molecule spotlight on semagacestat (LY450139).* ACS Chem Neurosci, 2010. **1**(8): p. 533-4.
188. Doody, R.S., et al., *A phase 3 trial of semagacestat for treatment of Alzheimer's disease.* N Engl J Med, 2013. **369**(4): p. 341-50.

189. Bursavich, M.G., B.A. Harrison, and J.F. Blain, *Gamma Secretase Modulators: New Alzheimer's Drugs on the Horizon?* J Med Chem, 2016. **59**(16): p. 7389-409.
190. Kennedy, M.E., et al., *The BACE1 inhibitor verubecestat (MK-8931) reduces CNS beta-amyloid in animal models and in Alzheimer's disease patients.* Sci Transl Med, 2016. **8**(363): p. 363ra150.
191. Egan, M.F., et al., *Randomized Trial of Verubecestat for Mild-to-Moderate Alzheimer's Disease.* N Engl J Med, 2018. **378**(18): p. 1691-1703.
192. Lansbury, P.T., Jr., *Inhibition of amyloid formation: a strategy to delay the onset of Alzheimer's disease.* Curr Opin Chem Biol, 1997. **1**(2): p. 260-7.
193. Blanchard, B.J., et al., *Efficient reversal of Alzheimer's disease fibril formation and elimination of neurotoxicity by a small molecule.* Proc Natl Acad Sci U S A, 2004. **101**(40): p. 14326-32.
194. Lakey-Beitia, J., et al., *Polyphenols as therapeutic molecules in Alzheimer's disease through modulating amyloid pathways.* Mol Neurobiol, 2015. **51**(2): p. 466-79.
195. Thapa, A., S.D. Jett, and E.Y. Chi, *Curcumin Attenuates Amyloid-beta Aggregate Toxicity and Modulates Amyloid-beta Aggregation Pathway.* ACS Chem Neurosci, 2016. **7**(1): p. 56-68.
196. Hyung, S.J., et al., *Insights into antiamyloidogenic properties of the green tea extract (-)-epigallocatechin-3-gallate toward metal-associated amyloid-beta species.* Proc Natl Acad Sci U S A, 2013. **110**(10): p. 3743-8.
197. Cheng, B., et al., *Inhibiting toxic aggregation of amyloidogenic proteins: a therapeutic strategy for protein misfolding diseases.* Biochim Biophys Acta, 2013. **1830**(10): p. 4860-71.
198. Chen, D., et al., *Dissociation of haemolytic and oligomer-preventing activities of gramicidin S derivatives targeting the amyloid-beta N-terminus.* Chem Commun (Camb), 2017. **53**(100): p. 13340-13343.
199. Hoyer, W., et al., *Stabilization of a beta-hairpin in monomeric Alzheimer's amyloid-beta peptide inhibits amyloid formation.* Proc Natl Acad Sci U S A, 2008. **105**(13): p. 5099-104.
200. Richman, M., et al., *In vitro and mechanistic studies of an antiamyloidogenic self-assembled cyclic D,L-alpha-peptide architecture.* J Am Chem Soc, 2013. **135**(9): p. 3474-84.
201. Wiesehan, K., et al., *Selection of D-amino-acid peptides that bind to Alzheimer's disease amyloid peptide abeta1-42 by mirror image phage display.* Chembiochem, 2003. **4**(8): p. 748-53.
202. Brener, O., et al., *QIAD assay for quantitating a compound's efficacy in elimination of toxic Abeta oligomers.* Sci Rep, 2015. **5**: p. 13222.
203. van Groen, T., et al., *Reduction of Alzheimer's disease amyloid plaque load in transgenic mice by D3, A D-enantiomeric peptide identified by mirror image phage display.* ChemMedChem, 2008. **3**(12): p. 1848-52.
204. van Groen, T., et al., *In vitro and in vivo staining characteristics of small, fluorescent, Abeta42-binding D-enantiomeric peptides in transgenic AD mouse models.* ChemMedChem, 2009. **4**(2): p. 276-82.
205. van Groen, T., et al., *Treatment with D3 removes amyloid deposits, reduces inflammation, and improves cognition in aged AbetaPP/PS1 double transgenic mice.* J Alzheimers Dis, 2013. **34**(3): p. 609-20.
206. Liu, H., S.A. Funke, and D. Willbold, *Transport of Alzheimer disease amyloid-beta-binding D-amino acid peptides across an in vitro blood-brain barrier model.* Rejuvenation Res, 2010. **13**(2-3): p. 210-3.
207. Jiang, N., et al., *Blood-brain barrier penetration of an Abeta-targeted, arginine-rich, d-enantiomeric peptide.* Biochim Biophys Acta, 2016. **1858**(11): p. 2717-2724.
208. Elfgen, A., et al., *Surprisingly high stability of the Abeta oligomer eliminating all-d-enantiomeric peptide D3 in media simulating the route of orally administered drugs.* Eur J Pharm Sci, 2017. **107**: p. 203-207.

209. Aileen Funke, S., et al., *Oral treatment with the d-enantiomeric peptide D3 improves the pathology and behavior of Alzheimer's Disease transgenic mice.* ACS Chem Neurosci, 2010. **1**(9): p. 639-48.
210. Funke, S.A. and D. Willbold, *Mirror image phage display--a method to generate D-peptide ligands for use in diagnostic or therapeutical applications.* Mol Biosyst, 2009. **5**(8): p. 783-6.
211. Bartnik, D., et al., *Differently selected D-enantiomeric peptides act on different Abeta species.* Rejuvenation Res, 2010. **13**(2-3): p. 202-5.
212. Ziehm, T., et al., *Increase of Positive Net Charge and Conformational Rigidity Enhances the Efficacy of d-Enantiomeric Peptides Designed to Eliminate Cytotoxic Abeta Species.* ACS Chem Neurosci, 2016. **7**(8): p. 1088-96.
213. Olubiyi, O.O. and B. Strodel, *Structures of the amyloid beta-peptides Abeta1-40 and Abeta1-42 as influenced by pH and a D-peptide.* J Phys Chem B, 2012. **116**(10): p. 3280-91.
214. van Groen, T., et al., *The Abeta oligomer eliminating D-enantiomeric peptide RD2 improves cognition without changing plaque pathology.* Sci Rep, 2017. **7**(1): p. 16275.
215. Schemmert, S., et al., *Abeta Oligomer Elimination Restores Cognition in Transgenic Alzheimer's Mice with Full-blown Pathology.* Mol Neurobiol, 2018.
216. Liu, J., et al., *Analytical Ultracentrifugation and Its Role in Development and Research of Therapeutical Proteins.* Methods Enzymol, 2015. **562**: p. 441-76.
217. Brown, P.H. and P. Schuck, *Macromolecular size-and-shape distributions by sedimentation velocity analytical ultracentrifugation.* Biophys J, 2006. **90**(12): p. 4651-61.
218. *Analytical Ultracentrifugation*. 2017 [cited 2017 13 February]; Available from: https://www.ncl.ac.uk/nuppa/services/analytical-utracentrifugation/#overview.
219. Ralston, G.B. and I. Beckman Instruments, *Introduction to Analytical Ultracentrifugation*. 1993: Beckman.
220. Kingsbury, J.S. and T.M. Laue, *Fluorescence-detected sedimentation in dilute and highly concentrated solutions.* Methods Enzymol, 2011. **492**: p. 283-304.
221. Uchiyama, S., M. Noda, and E. Krayukhina, *Sedimentation velocity analytical ultracentrifugation for characterization of therapeutic antibodies.* Biophys Rev, 2018. **10**(2): p. 259-269.
222. Correia, J.J. and W.F. Stafford, *Sedimentation Velocity: A Classical Perspective.* Methods Enzymol, 2015. **562**: p. 49-80.
223. Baldwin, R.L., *Boundary spreading in sedimentation-velocity experiments. V. Measurement of the diffusion coefficient of bovine albumin by Fujita's equation.* Biochem J, 1957. **65**(3): p. 503-12.
224. Erickson, H.P., *Size and shape of protein molecules at the nanometer level determined by sedimentation, gel filtration, and electron microscopy.* Biol Proced Online, 2009. **11**: p. 32-51.
225. Schuck, P., et al., *Basic Principles of Analytical Ultracentrifugation*. 2016: CRC Press.
226. Brautigam, C.A., *Using Lamm-Equation modeling of sedimentation velocity data to determine the kinetic and thermodynamic properties of macromolecular interactions.* Methods, 2011. **54**(1): p. 4-15.
227. Brown, P.H., A. Balbo, and P. Schuck, *Characterizing protein-protein interactions by sedimentation velocity analytical ultracentrifugation.* Curr Protoc Immunol, 2008. **Chapter 18**: p. Unit 18 15.
228. Schuck, P., *Analytical Ultracentrifugation as a Tool for Studying Protein Interactions.* Biophys Rev, 2013. **5**(2): p. 159-171.
229. Schuck, P., et al., *Size-distribution analysis of proteins by analytical ultracentrifugation: strategies and application to model systems.* Biophys J, 2002. **82**(2): p. 1096-111.
230. Taylor, I.A., K. Rittinger, and J.F. Eccleston, *Sedimentation equilibrium studies.* Methods Mol Biol, 2015. **1278**: p. 205-22.

231. Taylor, I.A., J.F. Eccleston, and K. Rittinger, *Sedimentation equilibrium studies.* Methods Mol Biol, 2004. **261**: p. 119-36.
232. Harding, S.E., R.B. Gillis, and G.G. Adams, *Assessing sedimentation equilibrium profiles in analytical ultracentrifugation experiments on macromolecules: from simple average molecular weight analysis to molecular weight distribution and interaction analysis.* Biophys Rev, 2016. **8**(4): p. 299-308.
233. Schuck, P. *Sedfit*. Analytical Ultracentrifuge; Available from: http://www.analyticalultracentrifugation.com/sedfit.htm.
234. Demeler, B. *UltraScan*. 2015 April 26, 2015; Available from: http://ultrascan.uthscsa.edu/index.php.
235. Braun, D. and A. Libchaber, *Trapping of DNA by thermophoretic depletion and convection.* Phys Rev Lett, 2002. **89**(18): p. 188103.
236. Seidel, S.A., et al., *Microscale thermophoresis quantifies biomolecular interactions under previously challenging conditions.* Methods, 2013. **59**(3): p. 301-15.
237. Jerabek-Willemsen, M., et al., *Molecular interaction studies using microscale thermophoresis.* Assay Drug Dev Technol, 2011. **9**(4): p. 342-53.
238. Jerabek-Willemsen, M., et al., *MicroScale Thermophoresis: Interaction analysis and beyond.* Journal of Molecular Structure, 2014. **1077**: p. 101-113.
239. Duhr, S. and D. Braun, *Why molecules move along a temperature gradient.* Proc Natl Acad Sci U S A, 2006. **103**(52): p. 19678-82.
240. Asmari, M., et al., *Thermophoresis for characterizing biomolecular interaction.* Methods, 2018.
241. Platten, J.K., *The Soret Effect: A Review of Recent Experimental Results.* Journal of Applied Mechanics, 2005. **73**(1): p. 5-15.
242. Wienken, C.J., et al., *Protein-binding assays in biological liquids using microscale thermophoresis.* Nat Commun, 2010. **1**: p. 100.
243. Kelly, S.M., T.J. Jess, and N.C. Price, *How to study proteins by circular dichroism.* Biochim Biophys Acta, 2005. **1751**(2): p. 119-39.
244. Greenfield, N.J., *Circular dichroism analysis for protein-protein interactions.* Methods Mol Biol, 2004. **261**: p. 55-78.
245. Greenfield, N.J., *Using circular dichroism spectra to estimate protein secondary structure.* Nat Protoc, 2006. **1**(6): p. 2876-90.
246. Kelly, S.M. and N.C. Price, *The use of circular dichroism in the investigation of protein structure and function.* Curr Protein Pept Sci, 2000. **1**(4): p. 349-84.
247. *Circular Dichroism (CD) Spectroscopy*. Available from: http://www.proteinchemist.com/cd/cdspec.html.
248. Greenfield, N.J., *Analysis of the kinetics of folding of proteins and peptides using circular dichroism.* Nat Protoc, 2006. **1**(6): p. 2891-9.
249. Greenfield, N.J., *Circular dichroism (CD) analyses of protein-protein interactions.* Methods Mol Biol, 2015. **1278**: p. 239-65.
250. Drolle, E., et al., *Atomic force microscopy to study molecular mechanisms of amyloid fibril formation and toxicity in Alzheimer's disease.* Drug Metab Rev, 2014. **46**(2): p. 207-23.
251. Ruggeri, F.S., et al., *AFM-Based Single Molecule Techniques: Unraveling the Amyloid Pathogenic Species.* Curr Pharm Des, 2016. **22**(26): p. 3950-70.
252. Mastrangelo, I.A., et al., *High-resolution atomic force microscopy of soluble Abeta42 oligomers.* J Mol Biol, 2006. **358**(1): p. 106-19.
253. Arimon, M., et al., *Fine structure study of Abeta1-42 fibrillogenesis with atomic force microscopy.* FASEB J, 2005. **19**(10): p. 1344-6.
254. Small, S.A. and K. Duff, *Linking Abeta and tau in late-onset Alzheimer's disease: a dual pathway hypothesis.* Neuron, 2008. **60**(4): p. 534-42.

255. Selkoe, D.J., *Alzheimer's disease results from the cerebral accumulation and cytotoxicity of amyloid beta-protein.* Journal of Alzheimer's disease : JAD, 2001. **3**(1): p. 75-80.
256. Nisbet, R.M., et al., *Tau aggregation and its interplay with amyloid-beta.* Acta Neuropathol, 2015. **129**(2): p. 207-20.
257. Smith, L.M. and S.M. Strittmatter, *Binding Sites for Amyloid-beta Oligomers and Synaptic Toxicity.* Cold Spring Harb Perspect Med, 2017. **7**(5): p. a024075.
258. Hara, T., et al., *Physiological roles of zinc transporters: molecular and genetic importance in zinc homeostasis.* J Physiol Sci, 2017. **67**(2): p. 283-301.
259. Prakash, A., K. Bharti, and A.B. Majeed, *Zinc: indications in brain disorders.* Fundam Clin Pharmacol, 2015. **29**(2): p. 131-49.
260. Wang, P. and Z.Y. Wang, *Metal ions influx is a double edged sword for the pathogenesis of Alzheimer's disease.* Ageing Res Rev, 2016. **35**(May 2017): p. 265-290.
261. Li, L.B. and Z.Y. Wang, *Disruption of brain zinc homeostasis promotes the pathophysiological progress of Alzheimer's disease.* Histol Histopathol, 2016. **31**(6): p. 623-7.
262. Takeda, A. and H. Tamano, *Significance of the degree of synaptic Zn(2)(+) signaling in cognition.* Biometals, 2016. **29**(2): p. 177-85.
263. Branch, T., et al., *Kinetic Analysis Reveals the Identity of Abeta-Metal Complex Responsible for the Initial Aggregation of Abeta in the Synapse.* ACS Chem Neurosci, 2017. **8**(9): p. 1970-1979.
264. Syme, C.D. and J.H. Viles, *Solution 1H NMR investigation of Zn2+ and Cd2+ binding to amyloid-beta peptide (Abeta) of Alzheimer's disease.* Biochim Biophys Acta, 2006. **1764**(2): p. 246-56.
265. Bush, A.I., et al., *Modulation of A beta adhesiveness and secretase site cleavage by zinc.* J Biol Chem, 1994. **269**(16): p. 12152-8.
266. Clements, A., et al., *Aggregation and metal-binding properties of mutant forms of the amyloid A beta peptide of Alzheimer's disease.* Journal of neurochemistry, 1996. **66**(2): p. 740-7.
267. Tougu, V., A. Karafin, and P. Palumaa, *Binding of zinc(II) and copper(II) to the full-length Alzheimer's amyloid-beta peptide.* Journal of neurochemistry, 2008. **104**(5): p. 1249-59.
268. Garai, K., et al., *Zinc lowers amyloid-beta toxicity by selectively precipitating aggregation intermediates.* Biochemistry, 2007. **46**(37): p. 10655-63.
269. Tougu, V., A. Tiiman, and P. Palumaa, *Interactions of Zn(II) and Cu(II) ions with Alzheimer's amyloid-beta peptide. Metal ion binding, contribution to fibrillization and toxicity.* Metallomics, 2011. **3**(3): p. 250-61.
270. Matheou, C.J., N.D. Younan, and J.H. Viles, *The Rapid Exchange of Zinc(2+) Enables Trace Levels to Profoundly Influence Amyloid-beta Misfolding and Dominates Assembly Outcomes in Cu(2+)/Zn(2+) Mixtures.* J Mol Biol, 2016. **428**(14): p. 2832-46.
271. Clever, H., M. Derrick, and S. Johnson, *The solubility of some sparingly soluble salts of Zinc and Cadmium in water and aqueous electrolyte solutions.* J.Phys.Chem.Ref.Data, 1992. **21**(5): p. 941-1004.
272. Ehrnhoefer, D.E., et al., *EGCG redirects amyloidogenic polypeptides into unstructured, off-pathway oligomers.* Nat Struct Mol Biol, 2008. **15**(6): p. 558-66.
273. Schuck, P., *Size-distribution analysis of macromolecules by sedimentation velocity ultracentrifugation and lamm equation modeling.* Biophys J, 2000. **78**(3): p. 1606-1619.
274. Brautigam, C.A., *Calculations and Publication-Quality Illustrations for Analytical Ultracentrifugation Data.* Methods Enzymol, 2015. **562**: p. 109-33.
275. Steger, C., *An Unbiased Detector of Curvilinear Structures.* IEEE Trans. Pattern Anal. Mach. Intell., 1998. **20**(2): p. 113-125.
276. Nasica-Labouze, J., et al., *Amyloid beta Protein and Alzheimer's Disease: When Computer Simulations Complement Experimental Studies.* Chem Rev, 2015. **115**(9): p. 3518-63.

277. Ono, K., et al., *Phenolic compounds prevent amyloid beta-protein oligomerization and synaptic dysfunction by site-specific binding.* J Biol Chem, 2012. **287**(18): p. 14631-43.
278. Roychaudhuri, R., et al., *C-terminal turn stability determines assembly differences between Abeta40 and Abeta42.* J Mol Biol, 2013. **425**(2): p. 292-308.
279. Patel, T.R., D.J. Winzor, and D.J. Scott, *Analytical ultracentrifugation: A versatile tool for the characterisation of macromolecular complexes in solution.* Methods, 2016. **95**: p. 55-61.
280. Demeler, B., E. Brookes, and L. Nagel-Steger, *Analysis of heterogeneity in molecular weight and shape by analytical ultracentrifugation using parallel distributed computing.* Methods Enzymol, 2009. **454**: p. 87-113.
281. Chou, C.Y., Y.H. Hsieh, and G.G. Chang, *Applications of analytical ultracentrifugation to protein size-and-shape distribution and structure-and-function analyses.* Methods, 2011. **54**(1): p. 76-82.
282. Schuck, P. and P. Rossmanith, *Determination of the sedimentation coefficient distribution by least-squares boundary modeling.* Biopolymers, 2000. **54**(5): p. 328-41.
283. Pachahara, S.K., et al., *Hexafluoroisopropanol induces self-assembly of beta-amyloid peptides into highly ordered nanostructures.* J Pept Sci, 2012. **18**(4): p. 233-41.
284. Takano, K., *Amyloid beta conformation in aqueous environment.* Curr Alzheimer Res, 2008. **5**(6): p. 540-7.
285. Ding, F., et al., *Mechanism for the alpha-helix to beta-hairpin transition.* Proteins, 2003. **53**(2): p. 220-8.
286. Guo, J., et al., *Kinetic Insights into Zn2+-Induced Amyloid beta-Protein Aggregation Revealed by Stopped-Flow Fluorescence Spectroscopy.* J Phys Chem B, 2017. **121**(16): p. 3909-3917.
287. Shi, H., B. Kang, and J.Y. Lee, *Zn(2+) effect on structure and residual hydrophobicity of amyloid beta-peptide monomers.* J Phys Chem B, 2014. **118**(35): p. 10355-61.
288. Dong, J., et al., *Modulating amyloid self-assembly and fibril morphology with Zn(II).* J Am Chem Soc, 2006. **128**(11): p. 3540-2.
289. Coskuner, O., *Divalent copper ion bound amyloid-beta(40) and amyloid-beta(42) alloforms are less preferred than divalent zinc ion bound amyloid-beta(40) and amyloid-beta(42) alloforms.* J Biol Inorg Chem, 2016. **21**(8): p. 957-973.
290. Chen, W.T., et al., *Distinct effects of Zn2+, Cu2+, Fe3+, and Al3+ on amyloid-beta stability, oligomerization, and aggregation: amyloid-beta destabilization promotes annular protofibril formation.* J Biol Chem, 2011. **286**(11): p. 9646-56.
291. Li, W., et al., *Effects of zinc binding on the conformational distribution of the amyloid-beta peptide based on molecular dynamics simulations.* J Phys Chem B, 2007. **111**(49): p. 13814-21.
292. Gurry, T. and C.M. Stultz, *Mechanism of amyloid-beta fibril elongation.* Biochemistry, 2014. **53**(44): p. 6981-91.
293. Xu, L., X. Wang, and X. Wang, *Characterization of the internal dynamics and conformational space of zinc-bound amyloid beta peptides by replica-exchange molecular dynamics simulations.* Eur Biophys J, 2013. **42**(7): p. 575-86.
294. Mithu, V.S., et al., *Zn(++) binding disrupts the Asp(23)-Lys(28) salt bridge without altering the hairpin-shaped cross-beta Structure of Abeta(42) amyloid aggregates.* Biophys J, 2011. **101**(11): p. 2825-32.
295. Wallace, J.A. and J.K. Shen, *Probing the strand orientation and registry alignment in the propagation of amyloid fibrils.* Biochemistry, 2010. **49**(25): p. 5290-8.
296. Wolff, M., et al., *Amyloid beta Oligomeric Species Present in the Lag Phase of Amyloid Formation.* PloS one, 2015. **10**(5): p. e0127865.
297. Uversky, V.N., *Introduction to intrinsically disordered proteins (IDPs).* Chem Rev, 2014. **114**(13): p. 6557-60.

298. Dyson, H.J. and P.E. Wright, *Intrinsically unstructured proteins and their functions.* Nat Rev Mol Cell Biol, 2005. **6**(3): p. 197-208.
299. Korsak, M. and T. Kozyreva, *Beta Amyloid Hallmarks: From Intrinsically Disordered Proteins to Alzheimer's Disease.* Adv Exp Med Biol, 2015. **870**: p. 401-21.
300. Selkoe, D.J. and J. Hardy, *The amyloid hypothesis of Alzheimer's disease at 25 years.* EMBO Mol Med, 2016. **8**(6): p. 595-608.
301. Roche, J., et al., *Monomeric Abeta(1-40) and Abeta(1-42) Peptides in Solution Adopt Very Similar Ramachandran Map Distributions That Closely Resemble Random Coil.* Biochemistry, 2016. **55**(5): p. 762-75.
302. Schumacher, T.N., et al., *Identification of D-peptide ligands through mirror-image phage display.* Science, 1996. **271**(5257): p. 1854-7.
303. Sun, N., S.A. Funke, and D. Willbold, *Mirror image phage display--generating stable therapeutically and diagnostically active peptides with biotechnological means.* J Biotechnol, 2012. **161**(2): p. 121-5.
304. Borgia, A., et al., *Extreme disorder in an ultrahigh-affinity protein complex.* Nature, 2018. **555**(7694): p. 61-66.
305. Chaturvedi, S.K., et al., *Use of fluorescence-detected sedimentation velocity to study high-affinity protein interactions.* Nat Protoc, 2017. **12**(9): p. 1777-1791.
306. Zhao, H., M.L. Mayer, and P. Schuck, *Analysis of protein interactions with picomolar binding affinity by fluorescence-detected sedimentation velocity.* Anal Chem, 2014. **86**(6): p. 3181-7.
307. Schuck, P., *Diffusion of the reaction boundary of rapidly interacting macromolecules in sedimentation velocity.* Biophys J, 2010. **98**(11): p. 2741-51.
308. Schuck, P., *Sedimentation patterns of rapidly reversible protein interactions.* Biophys J, 2010. **98**(9): p. 2005-13.
309. Linse, S., *Monomer-dependent secondary nucleation in amyloid formation.* Biophys Rev, 2017. **9**(4): p. 329-338.
310. Tornquist, M., et al., *Secondary nucleation in amyloid formation.* Chem Commun (Camb), 2018. **54**(63): p. 8667-8684.
311. Habchi, J., et al., *An anticancer drug suppresses the primary nucleation reaction that initiates the production of the toxic Abeta42 aggregates linked with Alzheimer's disease.* Sci Adv, 2016. **2**(2): p. e1501244.
312. Arosio, P., et al., *Chemical kinetics for drug discovery to combat protein aggregation diseases.* Trends Pharmacol Sci, 2014. **35**(3): p. 127-35.
313. Meisl, G., et al., *Molecular mechanisms of protein aggregation from global fitting of kinetic models.* Nat Protoc, 2016. **11**(2): p. 252-72.
314. Zhang, Z., S. Witham, and E. Alexov, *On the role of electrostatics in protein-protein interactions.* Phys Biol, 2011. **8**(3): p. 035001.
315. Liu, J., et al., *Study on the efficiency and interaction mechanism of a decapeptide inhibitor of beta-amyloid aggregation.* Biomacromolecules, 2014. **15**(3): p. 931-9.
316. Dogan, J., S. Gianni, and P. Jemth, *The binding mechanisms of intrinsically disordered proteins.* Phys Chem Chem Phys, 2014. **16**(14): p. 6323-31.
317. Ganguly, D., et al., *Electrostatically accelerated coupled binding and folding of intrinsically disordered proteins.* J Mol Biol, 2012. **422**(5): p. 674-684.
318. Cox, D., et al., *Small Heat-shock Proteins Prevent alpha-Synuclein Aggregation via Transient Interactions and Their Efficacy Is Affected by the Rate of Aggregation.* J Biol Chem, 2016. **291**(43): p. 22618-22629.
319. Assarsson, A., et al., *Charge dependent retardation of amyloid beta aggregation by hydrophilic proteins.* ACS Chem Neurosci, 2014. **5**(4): p. 266-74.

320. Walti, M.A., et al., *Probing the mechanism of inhibition of amyloid-beta(1-42)-induced neurotoxicity by the chaperonin GroEL.* Proc Natl Acad Sci U S A, 2018. **115**(51): p. E11924-E11932.
321. Nick, M., et al., *A long-lived Abeta oligomer resistant to fibrillization.* Biopolymers, 2018. **109**(8): p. e23096.
322. Fu, Z., et al., *Mechanism of Nucleated Conformational Conversion of Abeta42.* Biochemistry, 2015. **54**(27): p. 4197-207.
323. Hasecke, F., et al., *Origin of metastable oligomers and their effects on amyloid fibril self-assembly.* Chem Sci, 2018. **9**(27): p. 5937-5948.
324. Paravastu, A.K., et al., *Molecular structural basis for polymorphism in Alzheimer's beta-amyloid fibrils.* Proc Natl Acad Sci U S A, 2008. **105**(47): p. 18349-54.
325. Liao, Q., et al., *Abeta under stress: the effects of acidosis, Cu(2+)-binding, and oxidation on amyloid beta-peptide dimers.* Chem Commun (Camb), 2018. **54**(56): p. 7766-7769.
326. Liu, H., et al., *Residue-Specific Dynamics and Local Environmental Changes in Abeta40 Oligomer and Fibril Formation.* Angew Chem Int Ed Engl, 2018. **57**(27): p. 8017-8021.
327. Gu, L., C. Liu, and Z. Guo, *Structural insights into Abeta42 oligomers using site-directed spin labeling.* J Biol Chem, 2013. **288**(26): p. 18673-83.
328. Novo, M., S. Freire, and W. Al-Soufi, *Critical aggregation concentration for the formation of early Amyloid-beta (1-42) oligomers.* Sci Rep, 2018. **8**(1): p. 1783.
329. Scheuermann, T.H., et al., *On the acquisition and analysis of microscale thermophoresis data.* Anal Biochem, 2016. **496**: p. 79-93.
330. Cole, J.L., et al., *Analytical ultracentrifugation: sedimentation velocity and sedimentation equilibrium.* Methods Cell Biol, 2008. **84**: p. 143-79.
331. Choi, T.S., et al., *Molecular Insights into Human Serum Albumin as a Receptor of Amyloid-beta in the Extracellular Region.* J Am Chem Soc, 2017. **139**(43): p. 15437-15445.
332. Carrotta, R., et al., *Inhibiting effect of alpha(s1)-casein on Abeta(1-40) fibrillogenesis.* Biochim Biophys Acta, 2012. **1820**(2): p. 124-32.
333. Algamal, M., et al., *Atomic-resolution map of the interactions between an amyloid inhibitor protein and amyloid beta (Abeta) peptides in the monomer and protofibril states.* J Biol Chem, 2017. **292**(42): p. 17158-17168.
334. Durchschlag , H. and P. Zipper, *Calculation of the partial volume of organic compounds and polymers*, in *Progress in Colloid & Polymer Science* 1994, Springer. p. 20-39.
335. Durchschlag , H., *Determination of the partial specific volume of conjugated proteins.* Colloid and Polymer Science, 1989. **267**(12): p. 1139–1150.
336. Hess, B., et al., *GROMACS 4: Algorithms for Highly Efficient, Load-Balanced, and Scalable Molecular Simulation.* J Chem Theory Comput, 2008. **4**(3): p. 435-47.
337. Jorgensen, W.L., D.S. Maxwell, and J. Tirado-Rives, *Development and Testing of the OPLS All-Atom Force Field on Conformational Energetics and Properties of Organic Liquids.* Journal of the American Chemical Society, 1996. **118**(45): p. 11225-11236.
338. Kaminski, G.A., et al., *Evaluation and Reparametrization of the OPLS-AA Force Field for Proteins via Comparison with Accurate Quantum Chemical Calculations on Peptides.* The Journal of Physical Chemistry B, 2001. **105**(28): p. 6474-6487.
339. Qiu, D., et al., *The GB/SA Continuum Model for Solvation. A Fast Analytical Method for the Calculation of Approximate Born Radii.* The Journal of Physical Chemistry A, 1997. **101**(16): p. 3005-3014.
340. Anton, F.K., H. Berk, and B.H.J. C., *Improving efficiency of large time-scale molecular dynamics simulations of hydrogen-rich systems.* Journal of Computational Chemistry, 1999. **20**(8): p. 786-798.
341. Bussi, G., D. Donadio, and M. Parrinello, *Canonical sampling through velocity rescaling.* J Chem Phys, 2007. **126**(1): p. 014101.

342. Xavier, D., et al., *Peptide Folding: When Simulation Meets Experiment.* Angewandte Chemie International Edition, 1999. **38**(1 - 2): p. 236-240.
343. Abraham, M.J., et al. *GROMACS User Manual version 2018*. 2018; Available from: www.gromacs.org.
344. Jorgensen, W.L., J. Chandrasekhar, and J.D. Madura, *Comparison of simple potential functions for simulating liquid water.* The Journal of Chemical Physics, 1983. **79**(2): p. 926-935.
345. Allen, M.P. and D.J. Tildesley, *Computer Simulation of Liquids*. 1987, Oxford, UK,: Clarendon Press.
346. Parrinello, M. and A. Rahman, *Polymorphic transitions in single crystals: A new molecular dynamics method.* Journal of Applied Physics, 1981. **52**(12): p. 7182-7190.
347. Essmann, U., L. Perera, and M.L. Berkowitz, *A smooth particle mesh Ewald method.* The Journal of Chemical Physics, 1995. **103**(19): p. 8577-8593.
348. Darden, T., D. York, and L. Pedersen, *Particle mesh Ewald: An N·log(N) method for Ewald sums in large systems.* The Journal of Chemical Physics, 1993. **98**(12): p. 10089-10092.
349. Hess, B., et al., *LINCS: A linear constraint solver for molecular simulations.* Journal of Computational Chemistry, 1997. **18**(12): p. 1463-1472.
350. Ortega, A., D. Amoros, and J. Garcia de la Torre, *Prediction of hydrodynamic and other solution properties of rigid proteins from atomic- and residue-level models.* Biophys J, 2011. **101**(4): p. 892-8.
351. Voss, N.R., et al., *The geometry of the ribosomal polypeptide exit tunnel.* J Mol Biol, 2006. **360**(4): p. 893-906.
352. Humphrey, W., A. Dalke, and K. Schulten, *VMD: Visual molecular dynamics.* Journal of Molecular Graphics, 1996. **14**(1): p. 33-38.
353. Kabsch, W. and C. Sander, *Dictionary of protein secondary structure: pattern recognition of hydrogen-bonded and geometrical features.* Biopolymers, 1983. **22**(12): p. 2577-637.
354. Luo, J., et al., *Cellular polyamines promote amyloid-beta (Abeta) peptide fibrillation and modulate the aggregation pathways.* ACS Chem Neurosci, 2013. **4**(3): p. 454-62.
355. Hellstrand, E., et al., *Amyloid beta-protein aggregation produces highly reproducible kinetic data and occurs by a two-phase process.* ACS Chem Neurosci, 2010. **1**(1): p. 13-8.
356. Whitmore, L. and B.A. Wallace, *DICHROWEB, an online server for protein secondary structure analyses from circular dichroism spectroscopic data.* Nucleic Acids Res, 2004. **32**(Web Server issue): p. W668-73.
357. Lobley, A., L. Whitmore, and B.A. Wallace, *DICHROWEB: an interactive website for the analysis of protein secondary structure from circular dichroism spectra.* Bioinformatics, 2002. **18**(1): p. 211-2.
358. Compton, L.A. and W.C. Johnson, Jr., *Analysis of protein circular dichroism spectra for secondary structure using a simple matrix multiplication.* Anal Biochem, 1986. **155**(1): p. 155-67.
359. Sreerama, N. and R.W. Woody, *Estimation of protein secondary structure from circular dichroism spectra: comparison of CONTIN, SELCON, and CDSSTR methods with an expanded reference set.* Anal Biochem, 2000. **287**(2): p. 252-60.
360. Wood, S.J., et al., *Physical, morphological and functional differences between ph 5.8 and 7.4 aggregates of the Alzheimer's amyloid peptide Abeta.* J Mol Biol, 1996. **256**(5): p. 870-7.
361. Straub, J.E. and D. Thirumalai, *Toward a molecular theory of early and late events in monomer to amyloid fibril formation.* Annu Rev Phys Chem, 2011. **62**: p. 437-63.
362. Sengupta, U., A.N. Nilson, and R. Kayed, *The Role of Amyloid-beta Oligomers in Toxicity, Propagation, and Immunotherapy.* EBioMedicine, 2016. **6**: p. 42-49.
363. Choi, M.L. and S. Gandhi, *Crucial role of protein oligomerization in the pathogenesis of Alzheimer's and Parkinson's diseases.* FEBS J, 2018. **285**(19): p. 3631-3644.

364. Elfgen, A., et al., *Metabolic resistance of the D-peptide RD2 developed for direct elimination of amyloid-beta oligomers.* Sci Rep, 2019. **9**(1): p. 5715.
365. Leithold, L.H., et al., *Pharmacokinetic properties of tandem d-peptides designed for treatment of Alzheimer's disease.* Eur J Pharm Sci, 2016. **89**: p. 31-8.
366. Sreerama, N., S.Y. Venyaminov, and R.W. Woody, *Estimation of protein secondary structure from circular dichroism spectra: inclusion of denatured proteins with native proteins in the analysis.* Anal Biochem, 2000. **287**(2): p. 243-51.
367. Ziehm, T., A.K. Buell, and D. Willbold, *Role of Hydrophobicity and Charge of Amyloid-Beta Oligomer Eliminating d-Peptides in the Interaction with Amyloid-Beta Monomers.* ACS Chem Neurosci, 2018. **9**(11): p. 2679-2688.
368. Balbo, A. and P. Schuck, *Analytical ultracentrifugation in the study of protein self-association and heterogeneous protein-protein interactions*, in *Protein-Protein Interactions*, E. Golemis and P.D. Adams, Editors. 2005, Cold Spring Harbor Laboratory Press: Cold Spring Harbor, New York.
369. Olubiyi, O.O., et al., *Amyloid aggregation inhibitory mechanism of arginine-rich D-peptides.* Curr Med Chem, 2014. **21**(12): p. 1448-57.
370. Salvadores, N., et al., *Detection of misfolded Abeta oligomers for sensitive biochemical diagnosis of Alzheimer's disease.* Cell Rep, 2014. **7**(1): p. 261-8.
371. Hayden, E.Y. and D.B. Teplow, *Amyloid beta-protein oligomers and Alzheimer's disease.* Alzheimers Res Ther, 2013. **5**(6): p. 60.
372. Serrano-Pozo, A., et al., *Neuropathological alterations in Alzheimer disease.* Cold Spring Harb Perspect Med, 2011. **1**(1): p. a006189.
373. Ramakrishnan, M., et al., *Surface plasmon resonance binding kinetics of Alzheimer's disease amyloid beta peptide-capturing and plaque-binding monoclonal antibodies.* Biochemistry, 2009. **48**(43): p. 10405-15.
374. Salloway, S., et al., *Two phase 3 trials of bapineuzumab in mild-to-moderate Alzheimer's disease.* N Engl J Med, 2014. **370**(4): p. 322-33.
375. Doody, R.S., et al., *Phase 3 trials of solanezumab for mild-to-moderate Alzheimer's disease.* N Engl J Med, 2014. **370**(4): p. 311-21.
376. O'Nuallain, B., et al., *Human plasma contains cross-reactive Abeta conformer-specific IgG antibodies.* Biochemistry, 2008. **47**(47): p. 12254-6.
377. Crisostomo, A.C., et al., *Kinetic analysis of IgG antibodies to beta-amyloid oligomers with surface plasmon resonance.* Anal Biochem, 2015. **481**: p. 43-54.
378. Brockhaus, M., et al., *Thermodynamic studies on the interaction of antibodies with beta-amyloid peptide.* J Phys Chem B, 2007. **111**(5): p. 1238-43.
379. Arndt, J.W., et al., *Structural and kinetic basis for the selectivity of aducanumab for aggregated forms of amyloid-beta.* Sci Rep, 2018. **8**(1): p. 6412.
380. Teplyakov, A., G. Obmolova, and G.L. Gilliland, *A coiled conformation of amyloid-beta recognized by antibody C706.* Alzheimers Res Ther, 2017. **9**(1): p. 66.
381. Crespi, G.A., et al., *Crystallization and preliminary X-ray diffraction analysis of the Fab portion of the Alzheimer's disease immunotherapy candidate bapineuzumab complexed with amyloid-beta.* Acta Crystallogr F Struct Biol Commun, 2014. **70**(Pt 3): p. 374-7.
382. Crespi, G.A., et al., *Molecular basis for mid-region amyloid-beta capture by leading Alzheimer's disease immunotherapies.* Sci Rep, 2015. **5**: p. 9649.
383. Miles, L.A., et al., *Bapineuzumab captures the N-terminus of the Alzheimer's disease amyloid-beta peptide in a helical conformation.* Sci Rep, 2013. **3**: p. 1302.
384. La Porte, S.L., et al., *Structural basis of C-terminal beta-amyloid peptide binding by the antibody ponezumab for the treatment of Alzheimer's disease.* J Mol Biol, 2012. **421**(4-5): p. 525-36.
385. Jin, M., et al., *An in vitro paradigm to assess potential anti-Abeta antibodies for Alzheimer's disease.* Nat Commun, 2018. **9**(1): p. 2676.

386. Schuck, P. and H. Zhao, *The role of mass transport limitation and surface heterogeneity in the biophysical characterization of macromolecular binding processes by SPR biosensing.* Methods Mol Biol, 2010. **627**: p. 15-54.
387. MacGregor, I.K., A.L. Anderson, and T.M. Laue, *Fluorescence detection for the XLI analytical ultracentrifuge.* Biophys Chem, 2004. **108**(1-3): p. 165-85.
388. Krayukhina, E., et al., *Analytical ultracentrifugation with fluorescence detection system reveals differences in complex formation between recombinant human TNF and different biological TNF antagonists in various environments.* MAbs, 2017. **9**(4): p. 664-679.
389. Kroe, R.R. and T.M. Laue, *NUTS and BOLTS: applications of fluorescence-detected sedimentation.* Anal Biochem, 2009. **390**(1): p. 1-13.
390. Dam, J., et al., *Sedimentation velocity analysis of heterogeneous protein-protein interactions: Lamm equation modeling and sedimentation coefficient distributions c(s).* Biophys J, 2005. **89**(1): p. 619-34.
391. Brown, P.H., A. Balbo, and P. Schuck, *Characterizing protein-protein interactions by sedimentation velocity analytical ultracentrifugation.* Curr Protoc Immunol, 2008. **Chapter 18**: p. 18.15.1-18.15.39.
392. Skamris, T., et al., *Monoclonal Antibodies Follow Distinct Aggregation Pathways During Production-Relevant Acidic Incubation and Neutralization.* Pharm Res, 2016. **33**(3): p. 716-28.
393. Kwon, H., et al., *Anti-abeta oligomer IgG and surface sialic acid in intravenous immunoglobulin: measurement and correlation with clinical outcomes in Alzheimer's disease treatment.* PLoS One, 2015. **10**(3): p. e0120420.
394. Finke, J.M., et al., *Antibody blood-brain barrier efflux is modulated by glycan modification.* Biochim Biophys Acta Gen Subj, 2017. **1861**(9): p. 2228-2239.
395. Reyes Barcelo, A.A., F.J. Gonzalez-Velasquez, and M.A. Moss, *Soluble aggregates of the amyloid-beta peptide are trapped by serum albumin to enhance amyloid-beta activation of endothelial cells.* J Biol Eng, 2009. **3**: p. 5.
396. Luo, J., et al., *Non-chaperone proteins can inhibit aggregation and cytotoxicity of Alzheimer amyloid beta peptide.* J Biol Chem, 2014. **289**(40): p. 27766-75.
397. Kim, S.A., et al., *Sedimentation Velocity Analysis with Fluorescence Detection of Mutant Huntingtin Exon 1 Aggregation in Drosophila melanogaster and Caenorhabditis elegans.* Biochemistry, 2017. **56**(35): p. 4676-4688.
398. Yan, Y. and C. Wang, *Abeta42 is more rigid than Abeta40 at the C terminus: implications for Abeta aggregation and toxicity.* J Mol Biol, 2006. **364**(5): p. 853-62.
399. Brannstrom, K., et al., *The N-terminal region of amyloid beta controls the aggregation rate and fibril stability at low pH through a gain of function mechanism.* J Am Chem Soc, 2014. **136**(31): p. 10956-64.
400. Munke, A., et al., *Phage display and kinetic selection of antibodies that specifically inhibit amyloid self-replication.* Proc Natl Acad Sci U S A, 2017. **114**(25): p. 6444-6449.
401. Lee, M.C., et al., *Zinc ion rapidly induces toxic, off-pathway amyloid-beta oligomers distinct from amyloid-beta derived diffusible ligands in Alzheimer's disease.* Sci Rep, 2018. **8**(1): p. 4772.
402. Tjernberg, L.O., et al., *Arrest of beta-amyloid fibril formation by a pentapeptide ligand.* J Biol Chem, 1996. **271**(15): p. 8545-8.
403. Pallitto, M.M., et al., *Recognition sequence design for peptidyl modulators of beta-amyloid aggregation and toxicity.* Biochemistry, 1999. **38**(12): p. 3570-8.
404. Jiang, N., et al., *Preclinical Pharmacokinetic Studies of the Tritium Labelled D-Enantiomeric Peptide D3 Developed for the Treatment of Alzheimer s Disease.* PLoS One, 2015. **10**(6): p. e0128553.

405. Ziehm, T., A.K. Buell, and D. Willbold, *Role of Hydrophobicity and Charge of Amyloid-Beta Oligomer Eliminating d-Peptides in the Interaction with Amyloid-Beta Monomers.* ACS Chem Neurosci, 2018.
406. Brock, K., et al., *Optimization of electrostatic interactions in protein-protein complexes.* Biophys J, 2007. **93**(10): p. 3340-52.